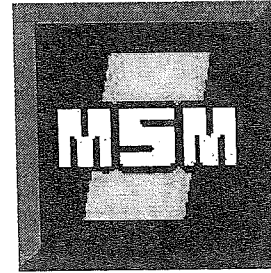




Département MSM
1, chemin des Chevreuils
B 4000 Liège
Belgium
Anne.Habraken@ulg.ac.be



CONTRIBUTIONS TO CONSTITUTIVE LAWS

OF METALS:

MICRO-MACRO AND DAMAGE MODELS

Parts A and B

Thèse présentée en vue de l'obtention du grade d'Agrégé de l'Enseignement Supérieur
par Anne-Marie HABRAKEN

Année académique 2000-2001

Membres du comité de Lecture

Université de Liège

Mme LECOMTE Jacqueline,
M. CESCOTTO Serge,
M. COHEUR Jean-Pierre,
M. FONDER Ghislain,
M. HOGGE Michel.

Membres extérieurs

Professeur Paul VAN HOUTTE
Departement Metaalkunde en Toegepaste Materiaalkunde
Katholieke Universiteit Leuven

Professeur Jean-Claude GELIN
Université de Franche Comté
Laboratoire de Mécanique Appliquée

Professeur Eric VAN DER GIESSEN
University of Groningen
Dept. of Applied Physics

*A Jean-Luc, pour que chaque étape contribue à te renforcer face au caillou suivant et te laisse
découvrir un fleuve tranquille.*

*To Jean Luc - that each step contribute to reinforcing you for the next stone you encounter, letting you discover a
tranquil river.*

A Tanguy, pour que tu trouves l'équilibre entre l'intelligence et la sensibilité qui t'habitent.

To Tanguy - that you find the balance between the intelligence and the sensitivity you possess.

*A Maëlle, pour que tu exploites avec bonheur ta faculté d'adaptation, l'harmonie entre ton corps et
ton esprit.*

To Maëlle - that you successfully exploit your ability to adapt, the harmony between your body and mind.

A Yann, pour que ta joie de vivre continue à éclabousser ton entourage et te rende heureux.

To Yann - that your joy for life may always dazzle your entourage and bring you happiness.

A Aude, tu nous es arrivée avec beaucoup de racines, puissions nous t'aider à découvrir tes ailes.

To Aude - you came to us with many roots; with hopes that we can help you discover your wings.

Foreword

This thesis is the culmination of nearly four years of work, which began during a stay in Clermont-Ferrand in August 1997. It was interrupted many times and often delayed because of technical contingencies; among these, the departure and arrivals of team researchers, work on urgent contracts to be completed, personal matters, i.e., pregnancy, childcare and other family problems, including an untimely death. On a positive note, these delays enabled me to take some distance with regard to the subject matter.

Acknowledgements

I would like to thank all those who helped me to pursue my work in the face of professional and other difficulties.

I am grateful to my husband for his patience, his encouragement and time spent with the children, which allowed me to finish this work. If the children are right, their mother will have a bit more time and be calmer, now that the thesis is finished...

I also express my heartfelt thanks to:

- Professor Serge Cescotto, for his theoretical as well as moral assistance in the daily management of the team, for his friendship and for so often lending a needed ear;
- Ghislain Fonder, for his practical assistance in dealing with administrative tasks and his personal warmth;
- Philippe Boeraeve, Etienne Rondia, Michel Bechoux and Michel Basteys, for their patience and efficiency in meeting my requests for experiments out of the usual context;
- the doctoral students and researchers who have contributed to my work; their scientific participation is defined more precisely in part A, but I acknowledge here the numerous chores that they carried out, which enabled me to concentrate on my thesis;
- Colette Verbist and Virginie Bertrand, for their help in the manuscript layout and corrections of the initial text;
- Gérard Franquet, for his precious assistance with a very large number of figures;
- Emile Lemaire for his good humor and ability to solve numerous computer related problems and Pierre Villers for his efficient help in managing the graphic post processors and the web;
- the members of the thesis committee who accepted to read this voluminous manuscript.

I also wish to thank the *Fonds National de la Recherche Scientifique* which has allowed me to pursue a professional career in research. Finally, I thank the academic authorities of the University of Liege for providing a pleasant work framework and a pluralistic environment that is as open as possible.

PART A

INTRODUCTION

Thèse présentée en vue de l'obtention du grade d'Agrégé de l'Enseignement
Supérieur
par Anne Marie HABRAKEN

Année académique 2000-2001

CONTENTS

1. Objectives and thesis contents	1
1.1. The general context of the thesis	1
1.2. The historical context and the contents of the thesis	1
2. Scientific work	3
2.1. Remeshing technique	3
2.2. Phase transformation	5
2.3. Contact modeling	5
2.4. Continuous casting model	7
2.5. Texture and plasticity models	8
2.6. Damage models	10
2.7. Forging models	11
2.8. Recrystallization model	13
3. Activities as research associate	13

1. OBJECTIVES AND THESIS CONTENTS

1.1. The general context of the thesis

The researcher status differs depending on country, employer and time as new regulations and new requirements frequently appear to adjust to the society evolution.

In Belgium, the National Fund for Scientific Research (FNRS) offers jobs in scientific research. A Ph.D. thesis is required from candidates for the first permanent position, Research Associate. To access the next steps in the career, Senior Research Associate and Research Director, an "Aggregation in Higher Education" is necessary. This degree requires :

- a main thesis accompanied by three additional contributions;
- an oral presentation of this thesis in front of one's entire faculty and several foreign scientists;
- a public lecture on an imposed topic.

The format of the thesis was described in 1931 and has become quite obsolete. The most widely accepted interpretation is based on the probable subsequent career as Research Director and, eventually, University Professor. Contrarily to the Ph.D. Thesis which must demonstrate the ability to do research at the personal level, the Aggregation thesis must demonstrate the ability to conduct research, to take a broad view of a research subject and to diffuse one's experience in research; originality is, of course, not to be neglected.

1.2. The historical context and the contents of the thesis

My thesis is divided into four parts.

The first (part A), which is very short summarizes my work since March 1987, when I obtained my own Ph.D. Since that time, two Ph.D. theses have been completed under a shared supervision of professor Cescotto and myself. Four others Ph.D. theses are in progress. These four Ph.D students have already achieved their master theses. I have taken an active part in three additional theses and directed numerous final projects and research contracts leading to progress reports, final reports and publications. All the developments have been introduced in the Finite Element code LAGAMINE, set up in the MSM Department to simulate the forming of metals. More information about the work of my team can be found in section 2 of Part A. In fact, a collection of papers resulting from these researches could have been presented as the Aggregation thesis.

Part B of the thesis is devoted to micro-macro approaches. It is an extensive state-of-the-art on the subject, presented in a unified way.

Part C is devoted to damage modeling. It also begins as a state of the art review but it is progressively focused towards the models that I have developed with my team.

As shown in section 2 of Part A, damage models and micro-macro approaches represent an important part of my contribution to the modeling of metal behavior modeling. Since Yongyi Zhu and Professor Cescotto had already developed the problematic of damage in the MSM Department, I have exploited and extended their work. I also had the opportunity to introduce micro-macro approaches in LAGAMINE thanks to a European project and a research project supported by the Région Wallonne. The development of this topic in the MSM Department results from my personal involvement.

As explained in the introductions of Parts B and C, research on micro-macro and damage approaches has been possible in the frame of different projects and thanks to the work of many different research engineers that I have supervised to the best of my ability. So, summarizing the behavior laws proposed by my team in one consistent text is of interest for researchers using them as code-users, or interested in implementing them into other codes. In order to choose the best orientations for further personal research, it is important to establish an extensive bibliographic review. This finally results in writing third cycle courses that could help future Ph.D. students of my team or other research groups worldwide. This goal was in itself an incitement to write this thesis. From this point of view, Part B is more complete, since I have already taught micro-macro approaches in February 2000 at the Graduate School in Computational and Experimental Mechanics. Part C, written for the most part in 1998 and 1999, already requires some updating.

Part D concerns the future : it concludes and offers perspectives for the continuation of the work.

The three papers joined as annex theses provide information about subjects not covered in the main text but to which I have significantly contributed. The first two present results of research performed with my co-workers using thermal-mechanical-metallurgical models. The last one is an article summarizing my contribution to contact between two bodies.

As much of my energy is devoted to metals at hot temperature, thermal-mechanical-metallurgical studies represent indeed another topic which should have been included in a consistent presentation and an up-dated literature review. When I began this thesis, I was confident that this would be summarized by two of my Ph.D. students. One of them, Jean-François Charles, left before completing a thesis; therefore the recrystallization model implemented in LAGAMINE is described only by articles in conference proceedings and internal reports. However, the developed macroscopic thermo-elasto-visco-plastic law has been extensively described by Frédéric Pascon in his DEA thesis (master's thesis). As the number of engineers having developed this field with me is limited, a coherent presentation seems less crucial than for damage and micro-macro approaches. Note that an Aggregation thesis would never end if one did

not decide to stop at a certain moment ! I am sure that my future work will be full of exciting new topics.

2. SCIENTIFIC WORK

My Ph.D. thesis (Habraken,1989) was entitled “Contribution à la modélisation du formage des métaux par la méthode des éléments finis”, which, without surprise, can be translated as “Contribution to metal forming modeling by the Finite Element Method”. This broad title was chosen for historical reasons; two very different topics were studied:

- The remeshing technique, adapted to a large displacement and deformation Lagrangian code and applied to simulations of forging processes.
- A thermal-mechanical-metallurgical model predicting phase volume fractions (austenite, cementite, ferrite, pearlite, bainite, martensite), stress, strain and temperature history during the cooling of steel parts. This work has been used by ARBED (Luxemburg steel industry) to study the Quenching-Self-Tempering of hot rolled steel beams.

Of course, since March 1989, I have developed the topics of this thesis but others as well (listed hereafter). These were chosen to fulfill industrial contracts or to develop new long-term research subjects that should help my department to continue its assistance mission for metal industries.

2.1. Remeshing technique

At the end of my Ph.D. thesis, a semi-automatic remeshing technique became available in LAGAMINE. The decision to remesh relies on geometric criteria or error criteria of the Zienkiewicz type. A semi-automatic mesh generator requiring some topological data from the user creates a new mesh. Then the stresses and internal variables are transferred from the old mesh to the new one and, finally, the simulation restarts. This approach is published in:

- An Automatic remeshing technique for finite element simulation of forming processes. Habraken, A.M., Cescotto, S., *Int. J. for Numerical Method. in Engineering*, (Dec. 1990), **30/8**, 1503-1525.

This remeshing technique became fully automatic with the help of Marek Dyduch, a Ph.D. student supervised by Professor Cescotto and myself. Error criteria are developed, based on the comparisons between the stress and strain rate fields directly computed by the code or the superconvergent ones. His research shows that an error criterion based on stresses can be applied to take the remeshing decision and an error criterion based on strain rates helps to define the variable nodal density in the new

mesh. Marek Dyduch adapts the evaluation of superconvergent meshes to get the stresses and internal values in the new mesh. The particular case of anti-hourglass stresses in mixed type elements is also studied. On the basis of these considerations, three research engineers, Zhou Ding Wu, Zhu Yongyi and André Godinas developed an automatic mesh generator starting from the old mesh data and the strain rate error indicator. A description of this work can be found in:

- Adaptive methods in finite element simulation of metal forming processes, Dyduch, M., Thèse de Doctorat en Sciences Appliquées, Université de Liège, (1995-1996).
- Automatic adaptive remeshing for numerical simulations of metalforming, Dyduch, M. Habraken, A.M., Cescotto, S. *Computer methods in applied mechanics and engineering*, **101**, (1992), 283-293.
- Error estimates and indicators for adaptive analysis of bulk forming, Dyduch, M., Cescotto, S., Habraken, A.M., *Computational Plasticity. Fundamentals and Applications*, edited by Owen, D.R.J. and Onate, E. at Pineridge Press, (1995), 1355-1367.
- Efficient Error Estimates for Adaptive Remeshing in 2D Metal Forming Modelling, Dyduch, M., Cescotto, S., Habraken A.M., NUMIFORM 95, *Simulation of Materials Processing: Theory, Methods and Applications*, edited by Shen & Dawson, at BALKEMA, (1995), 419-424.

Joëlle Pierry and Jean-Dominique Barnichon, from Professor Charlier's soil mechanics team, further improved the remeshing modules. This second group in the MSM department also works with the LAGAMINE code and maintains close ties with Professor Cescotto and myself. Jean-Dominique Barnichon implemented a classical method to interpolate the variables in the new mesh. For each new interpolation point, he localizes the old element where it belongs and uses the old element values to perform the interpolation. With the help of André Godinas for the mesh generator, Jean-Dominique Barnichon extended the whole remeshing method to multi-domain bodies. In soil mechanics, the different soil layers require such a tool. This research is summarized in Jean-Dominique Barnichon's thesis:

- Finite element modelling in structural and petroleum geology, Barnichon, J.D., Thèse de Doctorat en Sciences Appliquées, Université de Liège, (1998).

Finally, Sylvie Castagne, one of the research engineers whom I supervise, applied many of the above-described modules to study the surface layer of a rolled zinc sheet. Our goal was to investigate the 50 μm surface layer, which shows one peak in texture intensity in industrial zinc sheets; this property can be correlated with the crack resistance of the sheet. A specialized mesh generator is developed and the final strain rate and temperature fields present maximums in the surface layer zone that could explain the experimental observations. These results are published at the 2nd ESAFORM (European Scientific Association in material FORMing) conference.

-
- Study of the Surface Layer of a Rolled Zinc Sheet, Castagne, S., Habraken, A.M., Wégria, J., *2nd ESAFORM Conference on Metal Forming*, Guimaraes, Portugal, Covas J.A. Editor, (13-16 April 1999), 77-80.

2.2. Phase transformation

The model developed in my Ph.D. thesis was applied to optimize the Quenching-Self-Tempering process in ARBED (Luxemburg steel industry). Its description is published together with an application performed by ARBED in:

- Coupled thermo-mechanical-metallurgical analysis during the cooling of steel pieces, Habraken, A.M., Bourdouxhe, M., *"European Journal of Mechanics", A/Solids*, 11/3, (1992), 381-402.

I did not have the opportunity to keep working in this direction until September 2000. However during conferences and as jury member of Ph.D. theses, I followed the developments of FEM models to simulate phase transformations. Thanks to one current project funded by the Région Wallonne, I can again apply my thermal-metallurgical model. As an industrial interest is clearly present, I soon hope to up-date and apply again this thermal-mechanical-metallurgical model.

2.3. Contact modeling

Whatever the forming process, forging, rolling, extrusion or deep drawing, the contact between the tools and the workpiece has to be simulated. During my research, I first had the opportunity to work with Professor Charlier on a two-dimensional contact element between a rigid tool called foundation and a deformable specimen. This research based on the penalty method is described by:

- Numerical modelisation of contact with friction phenomena by the finite element method, Charlier, R., Habraken, A.M., *Computers and Geotechnics*, 9, (1990) 59-72.

I later extended the contact FEM element to the case of 2 deformable bodies, studying convergence according to the choice of weak or strong coupling between bodies in the stiffness matrix. This work, completed in 1992, was finally published in 1998:

- Contact between deformable solids, the fully coupled approach, Habraken, A.M., Cescotto, S., *Mathematical and Computer Modelling*, 28/4-8, (1998), 153-169.

The efficiency of the method allows treating quite complex cases as, for instance, the swaging process during the installation of swaged bolts (see Figures 1-1 and 1-2).

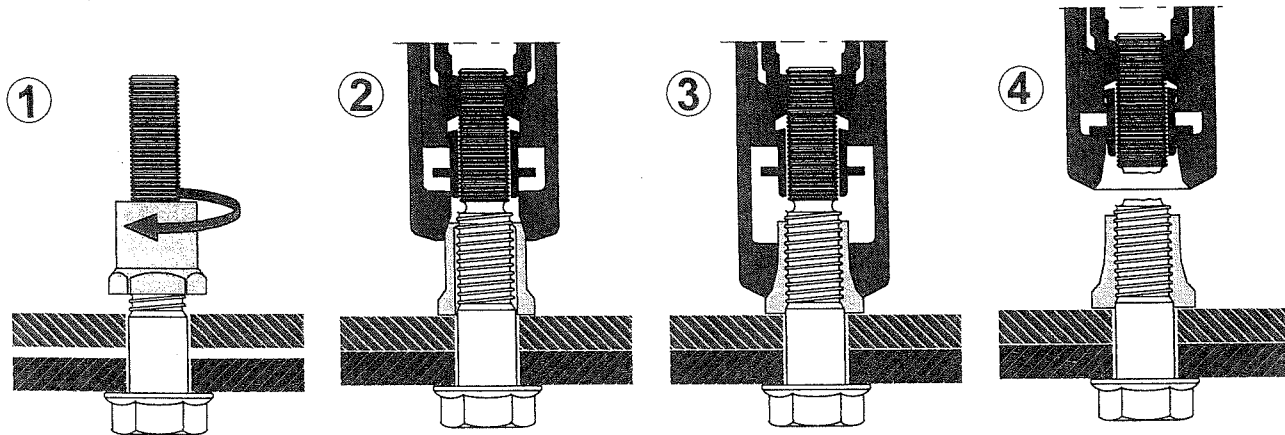


Figure 1-1 Installation of swaged bolts from “Swaged bolts: Modelling of the installation process and numerical analysis of the mechanical behaviour” by M. Dréan, A.-M. Habraken, A. Bouchaïr and J.-P. Muzeau, published in 5th International Conference on COMPUTATIONAL STRUCTURES TECHNOLOGY Leuven, Belgium, 6-8 September 2000

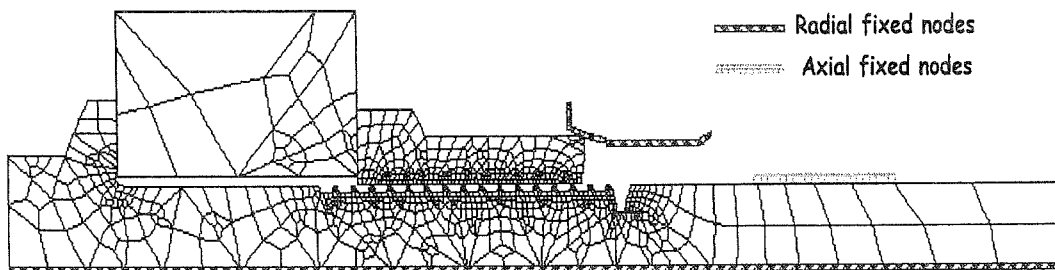


Figure 1-2 Axisymmetrical mesh used to model the second step of swaging process, from Dréan *et al.*, *Construction métallique*, 4, (1999), 21-34.

Realized in collaboration with Michel Dréan, a Ph.D. student from CUST (Clermont-Ferrand, France), this application was published in a well-known French journal and presented at several conferences.

- Modélisation de la mise en œuvre des boulons sertis précontraints, Dréan, M., Habraken, A.M., Bouchaïr, A., Muzeau, J.P., *Construction métallique*, 4, (1999), 21-34.

I have implemented the concept of “pilot nodes” in LAGAMINE. These nodes define the translational and/or rotational degrees of freedom of a rigid tool in contact with a workpiece. This approach is necessary to apply a blank holder force during a deep

drawing simulation. I have adapted this Pilot Node approach in three dimensions and implemented the analytical stiffness matrix to keep CPU time low. This is described in:

- Numerical approach of contact with friction between two bodies in large deformations, Habraken, A.M., Radu, J.P., Charlier, R., *Contact Mechanics, Int. Symposium*, edited by Curnier A., sponsored by Fondation LATSIS, Presses Polytechniques et Universitaires Romandes, (7-10 October 92), 391-408

The contact element used in LAGAMINE is a thermal-mechanical element where the thermal flow depends on the contact state. It is briefly described in:

- Dynamic Recrystallization during Zinc Rolling, Habraken, A.M., Charles, J.F., Wégria, J., Cescotto, S., *Int. J. of Forming Processes*, 1, (1998), 53-73.

Some limited investigation has been conducted on an augmented Lagrangian approach, in collaboration with Professor Charlier and Jean-Philippe Bille.

- Numerical Approach of Contact Using an Augmented Lagrangian Method. Bille, J.P., Habraken, A.M., Charlier R., *3e Congrès National belge de mécanique théorique et appliquée*, (30-31 May 1994), Liège.

2.4. Continuous casting model

In collaboration with ARBED, two research projects have been conducted to simulate the continuous casting process with the LAGAMINE code. The first approach, which I performed in 1989, included 2 different behavior models for liquid and solid states. A mixture law was applied in the mushy zone. The experiments performed were not sufficient at that time to identify the model parameters; besides the model stability and convergence were quite poor. However this model has helped ARBED to optimize the mold taper, but no publication describes it.

Nearly 10 years later, a second project on continuous casting was initiated with a Ph.D. student, Frédéric Pascon. This time, an important experimental part of the research (performed at SIDMAR the research center, North Belgian steel industry) allows us to adjust our behavior law. The constitutive model adopted to simulate solid, mushy or liquid states is a thermal-elasto-visco-plastic law of the Norton type. First developed with Jean-François Charles to model zinc and steel rolling, this law has been greatly improved during this research. The convergence difficulties of the continuous casting model stimulated us to study all the details. Finally, the integration scheme as well as the loading-unloading criterion have been improved, and we have reached a quite stable and robust law. This research is described in Frédéric Pascon's DEA (master thesis) presented in September 2000, and published in international conference proceeding or journal:

- Finite element modeling of contact between the strand and the mould in continuous casting, Pascon, F., Diplôme d'études approfondies en Sciences Appliquées, Université de Liège, (September 2000).
- Thermo-mechanical model of a strand in the mould of a continuous casting plant, Pascon, F., Habraken, A.M., Bourdouxhe, M., Labory, F., *European Congress on Computational Methods in Applied Sciences and Engineering, ECCOMAS 2000*, Barcelona, 11-14 September 2000. CD-Rom with 979 papers. Our article is in section Computational Solid and Structural Mechanics, alphabetic classification on article title, (15 pages).
- Modélisation des phénomènes thermomécaniques dans une lingotière de coulée continue. Pascon, F., Habraken, A.M., Bourdouxhe, M., Labory, F., *Mécanique & Industrie*, 1, (2000), 61-70.

2.5. Texture and plasticity models

This research began in 1994, thanks to a European COST project. Exchanges between our team and Professor van Houtte of Katholieke Universiteit of Leuven afforded us the possibility to implement a first yield locus based on texture data in LAGAMINE. Serge Munhoven and I tested this first plastic surface based on 4-dimensional spline functions. It shows bad convergence and continuity problems. A second method, developed by Jan Winter and based on a 6th order series expansion in deviatoric stress space, gives satisfaction, enabling both teams to present FEM simulations on sheet behavior at the international conference, NUMIFORM 95.

- Anisotropic finite element simulation of plane strain tests. Winters, J., Van Bael, A., Munhoven, S., Habraken, A.M., Mols, K., Van Houtte, P., NUMIFORM, *Simulation of Materials Processing: Theory, Methods and Applications*, Shen & Dawson editors, BALKEMA (18-21 June, 1995); 357-362.
- Application of an anisotropic yield locus based on texture to a deep drawing simulation, Munhoven, S., Habraken, A.M., Winters, J., Schouwenaars, R., Van Houtte, P., NUMIFORM, *Simulation of Materials Processing: Theory, Methods and Applications*, , Shen & Dawson editors, BALKEMA (18-21 June, 1995), 767-772.

The Leuven Taylor's module to predict texture evolution was implemented in Liège and applied on aluminum extrusion by our team. Our results are close to those computed by a Norwegian team partner in the COST project:

- Texture prediction and aluminum extrusion, Degueudre, A., Habraken, A.M., Munhoven, S., Aukrust, T., Van Bael, A., Karhausen, K., *General Workshop COST 512, MMSP 96 Davos: Modelling in Materials Science and Processing*, edited by Rappaz M. and Kadro M. for the COST 512, Action Management

Committee. Published by the European Commission Directorate General XII Science Research Development, B-1048 Brussels, 260-265.

A project funded by the Région Wallonne partly devoted to the effect of texture evolution on yield locus shape started in September 1996. The fitting of a 6th order series, thanks to texture information, was considered too expensive (both in CPU time and memory storage requirement) to take into account texture evolution. It requires about 70000 calls to Taylor's module. Thus, it was decided to develop a description of a part of the yield locus requiring only 5 or 6 calls to Taylor's module. A so-called hyperplane approach was implemented in LAGAMINE and presented at NUMIFORM 98 conference:

- Comparison of Anisotropic Elastoplastic Laws Applied to Steel Sheet, Habraken, A.M., Radu, J.P., Duchêne, L., Wauters, M., Munhoven, S., NUMIFORM 98, *Simulation of Materials Processing: Theory, Methods and Applications*, edited by Huetink, Baaijens at Balkema, Enschede, The Netherlands, (22-25 June 1998), 769-774.

At that time, the lack of long-term involvement of engineers in this project severely slowed down the project but my long-term position allowed me to safeguard the information. Recently, the research could go on with the help of a Ph.D. student, Laurent Duchêne. Poor continuity of the hyperplane development is responsible for poor convergence; an improved approach called the interpolation method was proposed with André Godinas, Laurent Duchêne and myself and published in January 1999:

- Elastoplastic Anisotropic Model Based on Texture Analysis to Simulate Steel Sheet Behaviour, Duchêne, L., Habraken, A.M., Cescotto, S., *7th Int. Symp. on Plasticity*, Cancun, Mexico, edited by Akthar S. Khan at Neat Press, (5-13 January 1999), 325-328.

Our progress with this method has also been presented in the well-known ICOTOM and NUMISHEET conferences:

- Texture effects on steel sheet behaviour under large strain simulations, Duchêne, L., Godinas, A., Habraken, A.M., *12th Int. Conf. on Textures of Materials (ICOTOM-12)*, Montreal, Canada, edited by Szpunar, J.A., at NRC Research Press Ottawa, (9-13 August 1999), 286-291.
- Metal Plastic Behaviour linked to Texture Analysis and FEM Method. Duchêne, L., Godinas, A., Habraken, A.M., NUMISHEET '99, *4th Int. Conf. and Workshop on Numerical Simulation of 3D Sheet Forming Processes*, Besançon, France, edited by Gélén, J.C., Picart, P., Université de Franche-Comté et ENSMM, (13-17 September 1999), 97-102.

It has been extensively described in Laurent Duchêne's DEA final paper:

-
- Implementation of a yield locus interpolation method in the finite element code Lagamine, Duchêne, L., Diplôme d'études approfondies en Sciences Appliquées, Université de Liège, (September 2000).

This method is now in its validation phase as Laurent Duchêne's Ph.D. thesis should soon lead to more comparisons between experiments and simulations. At the ESAFORM 2001 conference that I organized in Liège, I proposed a further study of a NUMISHEET 99 benchmark in order to compare different anisotropic constitutive laws for steel sheet behavior.

2.6. Damage models

The models developed by my team belong to the Lemaître & Chaboche French school of ductile rupture (Lemaître, J., Chaboche, J.L. 1985 *Mécanique des matériaux solides*, Dunod, Paris). They are macroscopic approaches of damage, where damage evolution is measured by the decreasing value of the apparent Young's modulus and, possibly, of Poisson's ratio.

I have supervised the implementation of a coupled isotropic elastoplastic damage model in the LAGAMINE code by Yongyi Zhu, a Ph.D. student with Professor Cescotto:

- Contribution to the local approach of fracture in solid dynamics, Zhu, Y., Thèse de Doctorat en Sciences Appliquées, Université de Liège, (1992).

This model has been applied on zinc sheets and aluminum rods in the graduation works written by Anne-France Cambron and Sylvie Castagne to get their Physician Engineer Degree.

With Wang Xiao Chuan, I have extended Zhu Yongyi's formulation to an elasto-viscoplastic model. For an aluminum alloy, the identification of the model was performed in our laboratory. So, accurate measurements of Young's modulus were developed; different experiments for the model validation were created. As the available geometry of the material was limited, we had to imagine non-classical experiments. Finally, the model has been applied to a rotative forging process for aluminum rods.

- An Elastic-visco-plastic Damage Model: from Theory to Application, Wang, X.C., Habraken, A.M., *Local Approach to Fracture* Fontainebleau (9-11 September 1996), *Supplément au Journal de Physique C*, **6**, (October 1996), 86-96.

As a large set of experiments on these aluminum rods were performed in our laboratory, with Li Hong Zhang, I have tried to go further in their exploitation. Additional comparisons of the elasto-visco-plastic damage model with experimental results were thus performed:

-
- A new elastic-visco-plastic damage model for annealed aluminum: theory, calibration and validation, Habraken, A.M., Zhang, L.H., Wang, X.C., Cescotto, S., *Symposium Continuous Damage and Fracture*, 23-27 October 2000, Cachan, France, *Continuous Damage and Fracture*, edited by Benallal, A., at Elsevier France, 341-352.

With Sylvie Castagne, the damage elasto-plastic model from Zhu Yongyi was also applied to these experiments. It appeared that some improvement was necessary to get correlation between model predictions and reality. The following paper has been accepted for publication:

- Application of a damage model to an aluminum alloy, Castagne, S., Habraken, A.M., Cescotto, S., to appear in *Int. Journal of Damage*.

In his Ph.D. thesis, Zhu Yongyi had also developed an anisotropic elastoplastic damage model, but his work did not include an experimental approach to identify model parameters and validation step. Michaël Wauters, a Ph.D. student of mine, has applied this model on two steel sheets, and a set of accurate sheet tests was developed in order to check Young's modulus decrease in anisotropic steel sheets. His experiments rapidly demonstrated that the simple linear hardening proposed by Yongyi Zhu leads to the prediction of a non-realistic behavior. Consequently Michaël Wauters has improved the model and performed different experiments to identify its parameters, validate its basic assumptions and validate its prediction. A first summary of this work can be found in:

- A fully coupled elasto-plastic damage model applied to anisotropic materials, materials, Wauters, M., Habraken, A.M., Duchêne, L., *14th Engineering Mechanics Conference*, May 21-24, Austin, Texas, USA, CD Rom Compiled by D. R. Maniar, edited by J.L. Tassoulas, The University of Texas at Austin (6 pages).
- Calibration of an anisotropic elastoplastic damage model for sheet metal forming, Wauters, Michaël, *Diplôme d'études approfondies en Sciences Appliquées*, Université de Liège, (June 2000).

Michaël Wauters's Ph.D. thesis should be completed later on.

2.7. Forging models

A strong cooperation with FORCAST, a forging industry producing cylinders for rolling mills, induced both experimental and numerical progresses. On the numerical front, in 1996, we developed a strategy to model their forging process as a generalized plane state. A comparison of the stress and strain states produced by a few strokes of different hammer and anvil geometries have helped to make some progress in the

understanding of physical events occurring during the process. An account of this work is given in:

- Procédés Intelligents de Mise en Œuvre par Forgeage Dynamique, Programme Mobilisateur Multimatériaux de la Région Wallonne, Rapport Final, Habraken A.M., Wang, X.C., (1996).

After further investigations and discussions, it appeared that three-dimensional simulations were necessary to represent the industrial reality. Again a set of simulations compared results of different tool shapes, helping engineers in decision-making. The efficient thermal-elasto-visco-plastic law of the Norton type, developed with Jean-François Charles and Frédéric Pascon, enabled investigation of the cooling effect during forging. A lot of computations were done; the following publication summarizes some of these:

- Numerical modeling of the forging process of rolls for rolling mills, Charles, J.F., Castagne, S., Zhang, L.H., Habraken, A.M., Cescotto, S., *8th int. Conf. on Metal Forming 3-7 September 2000, Metal Forming 2000* edited by Pietrzyk, M., Kusiak, J., Majta, J., Hartley, P., Pillinger, I. at Balkema, (2000), 625-631.

Jean-François Charles also developed experimental hot compression tests with the help of Philippe Boeraeve and technicians of the department laboratory. The goal was to identify the parameters of Norton's law. These tests are performed at "constant" temperature and "constant" strain rate. In fact, for rapid tests, the radiant furnace cannot compensate the adiabatic heat and the test does not take place at constant temperature. A subsequent development by Christophe Martin allows measuring this temperature variation during the test. The press, in the strain rate range of 10^{-4} to 10 sec^{-1} , correctly follows the constraint of constant strain rate. An Excel post processor provides the stress-strain curves from the measured force and displacement. This use of tests to reach stress-strain curves does not completely neglect the barreling effect that prevents homogeneous stress and strain states, but simply applies Orowan's formula. From these data, another Excel treatment computes Norton's parameters:

- Modelling of Elasto-Visco-Plastic Behaviour of Steels at High Temperatures, Charles, J.F., Habraken, A.M., Lecomte, J., NUMIFORM, *Simulation of Materials Processing : Theory, Methods and Applications*, 22-25 June 1998, edited by Huetink, Baaijens, at Balkema., Enschede, The Netherlands, 277-282.

Jean-François Charles also developed a first inverse approach, neglecting the variation temperature during the tests. A initial set of Norton's parameters is used in a set of FEM simulations modeling the different experiments. Then comparisons between predicted and measured force-displacement curves and an optimization approach provide a new set of Norton's parameters and a new iteration is computed. When the difference between predicted and measured force-displacement curves reaches a minimum, it is

assumed that the Norton's parameter set is the good one. Of course, local minimums can appear. This point as well as the effect of temperature must still be investigated.

2.8. Recrystallization model

Thanks to an industrial project for Union Minière devoted to zinc rolling simulation, Jean-François Charles and I have implemented a dynamic recrystallization model in the LAGAMINE code. This model uses the strain rate, temperature and strain level computed by the FEM code to follow the recrystallization phenomena. It is a post-processor activated inside the constitutive law, so the FEM simulation results give the recrystallized fraction of the final state product. The research is described in the following article:

- Dynamic Recrystallization during Zinc Rolling, Habraken, A.M., Charles, J.F., Wégria, J. Cescotto, S. , *Int. J. of Forming Processes*, 1, (1998), 53-73.

A second model, where recrystallization affects mechanical behavior, has been proposed. Applying Sellars's approach, each material point is subdivided into substructures defined by their volume fraction. Their hardening degree is directly linked to the recrystallization process and the macroscopic strain.

The problem with such models is not really their numerical implementation, even if this is not so simple for the coupled one. The difficult point is the parameters identification. Coupling the hot compression tests described above with microscopic observations performed by the Service de Métallurgie Sidérurgie of ULG, we have tried to follow the dynamic recrystallisation process. However, a delay still exists between the hot deformation and the quench process that freezes the microscopic state. So some doubts remain about the information. It could cover meta-dynamic or even fast static recrystallization. Nevertheless, first results have been published in:

- Numerical modeling of the forging process of rolls for rolling mills, Charles, J.F., Castagne, S., Zhang, L.H., Habraken, A.M., Cescotto, S., *8th int. Conf. on Metal Forming 3-7 September 2000, Metal Forming 2000* edited by Pietrzyk, M., Kusiak, J., Majta, J., Hartley, P., Pillinger, I. at Balkema, (2000), 625-631.

This research is currently in progress. Parameters identification should also be improved by the use of inverse modeling.

3. ACTIVITIES AS RESEARCH ASSOCIATE

The above description of my technical activity gives an idea of my work which includes applying for projects with the industry, the University, the Région Wallonne and the

European Research organization. Then I hire, instructs and guide engineers to do the research or, in very rare cases, I handle the project alone.

I also attend conferences, where I present the research of my group and try to follow the scientific progress in the metal forming field. As member of twelve Ph.D. thesis juries, I have had opportunity to follow the research of other European teams in a very accurate and timely way. As a member of the Board of Directors of ESAFORM (European Scientific Association for material FORMING), I have organized its 2001 international conference, which has attracted more than 250 participants.

I actively participate in the educational process at the University by advising Ph.D. students and engineering students writing their final papers. As an elected member of the scientific staff of the Engineering Faculty, I participate to its daily life : this means belonging to various committees. For the last four years, I have been a member of the University Research Council. This decision-making group, composed of the University authorities, one professor and one scientist from each faculty, selects the research projects to be financed by the University or submitted to other institutions (Région Wallonne, French Community, etc.).

PART B

MODELING THE PLASTIC ANISOTROPY OF METALS
BY FINITE ELEMENT METHOD

GraSMech Course
February 2000

Thèse présentée en vue de l'obtention du grade d'Agrégé de l'Enseignement
Supérieur
par Anne-Marie HABRAKEN

Année académique 2000-2001

Part B - Introduction

This section consists of a postgraduate course that I taught in February 2000 within the frame of the Graduate School in Computational and Experimental Mechanics (GraSMech). My GraSMech students were supposed to attend an introduction to micromechanics by Professor Paul van Houtte during the first semester. His course contents are referenced as van Houtte, 1995. This is why this reference often appears in my own course.

I propose an important state-of-the-art review in the field of polycrystal micro-macro models implemented in Finite Element Method (FEM) as well as a summary of my personal research on this topic. My goal in doing such an important literature survey is to optimize further guidance of my research group.

Since 1994, my co-workers and I have been working on the development of a FEM approach, which couples plasticity and texture models. In fact, this research has been developed within the frame of 2 projects:

- a European COST 512 project, entitled "Integration of Micromechanical Models for the Plastic Deformation of Polycrystalline Materials with FE modeling of Forming Process"
- a Région Wallonne project entitled "Integration of Micro-Macro Interactions in Finite Element Modeling of Metal Forming".

An intensive collaboration with the team of Paul van Houtte, professor at the Katholieke Universiteit of Leuven, has helped us to tackle this field. Paul van Houtte is a very well-known scientist in the field of texture research (van Houtte 1988, van Houtte 1992, van Houtte 1995, van Bael *et al.* 1994, van Bael *et al.* 1996, Winters *et al.* 1996). Besides Professor van Houtte, I am particularly grateful to Jan Winters, Bert van Bael and Eric Hoferlin, who kindly and patiently transmitted the practical knowledge needed for using the numerical tools exchanged between our teams.

Numerous colleagues from the MSM Department such as Serge Munhoven, Jean-Pol Radu, André Godinas, Najj El Masri and Laurent Duchêne, have participated in this research. In the text, their specific work will be identified in the referenced list of authors or by explicit mention of their name. The research is currently in progress with the Ph.D. thesis of Laurent Duchêne, which should be completed on next academic year (2001-2002).

References

- Van Bael, A., Winters, J. , Van Houtte, P. (1994) The effect of strain hardening on R-value measurements. In *Numerical Predictions of Deformation Processes and the Behaviour of Real Materials (Proc. 15th Riso International Symposium*

- on *Materials Science*), Andersen S.I., Bilde-Sørensen J.B., Lorentzen T., Pedersen O.B. & Sørensen N.J. Eds, Roskilde, Denmark, Risø Laboratory, 225-230.
- Van Bael, A., Winters, J., Van Houtte, P. (1996) A semi-analytical approach for incorporating crystallographic data into elasto-plastic finite element formulations, *Textures of Materials*, Proceedings of the 11th Int. Conf. on Textures of Materials, vol. 1, ICOTOM-11, Sept. 16-20, Liang Z., Zuo L., Chu Y. Eds.
- Van Houtte, P. (1988) A comprehensive mathematical formulation of an extended Taylor-Bishop-Hill model featuring relaxed constraints, the Renouard-Wintenberger theory and a strain rate sensitivity model, *Textures and Microstructures*, **8-9**, 313-350.
- Van Houtte, P. (1992) Anisotropic Plasticity, *Numerical Modelling of Material Deformation Processes, Research, Development and Applications*, Hartley, P., Pillinger, I., editors, Springer-Verlag.
- Van Houtte, P. (1995) Micromechanics of polycrystalline materials, Chaire Francqui, Université de Liège.
- Winters, J. (1996) Implementation of a texture-based yield locus into an elastoplastic finite element code. Application to sheet forming. Katholieke Universiteit Leuven, MTM department, Ph. D thesis.

CONTENTS

Notations	B-1
Symbols	
Abbreviations	B-3
Latin letters	B-3
Greek letters	B-11
1. Introduction	1.1
References	1.3
2. Anisotropic phenomenological yield loci	2.1
2.1 Initial shape of yield loci	2.1
2.1.1 Hill's approach	2.2
2.1.2 Barlat's and Karafillis's approach	2.6
2.1.3 A polar-coordinate representation of an orthotropic yield locus	2.14
2.1.4 Vegter's approach	2.17
2.1.5 Summary	2.20
2.2. Updated yield loci	2.21
References	2.23
3. Hardening models	3.1
3.1 Basic knowledge on crystal events	3.1
3.2 Crystallographic texture	3.3
3.3 Introduction to hardening models	3.5
3.4 Simple macroscopic isotropic hardening approaches	3.9
3.5 Macroscopic approaches with microscopic roots	3.10
3.5.1 Bergström-van Liempt-Vegter's model	3.10
3.5.2 Follansbee & Kocks's model	3.15
3.5.3 Schmitz's model	3.18
3.5.4 Miller -Mc Dowell's model	3.18
3.5.5 Teodosiu's model	3.24
3.6 Conclusion	3.30
References	3.31
4. Microscopic models and micro-macro approaches	4.1
4.1 Taylor's single crystal plasticity model	4.1
4.1.1 Description	4.1
4.1.2 Taylor's factor	4.4
4.2 Strain rate sensitivity approach for single crystal plasticity model	4.4
4.3 Evolution rule for CRSS value	4.5
4.4 Mechanical frame for single crystal plasticity	4.6
4.5 Polycrystal plasticity models	4.9
4.5.1 Description	4.9
4.5.2 Average Taylor's factor	4.11

4.6 Link between the evolution of the reference CRSS and macroscopic strain hardening	4.13
4.7 Summary	4.14
References	4.14
5. FEM Micro-Macro models without yield locus	5.1
5.1 Introduction	5.1
5.2 Microscopic FEM computations to model macroscopic behavior	5.1
5.2.1 Teodosiu et al. 1992	5.1
5.2.2 Acharya & Beaudoin's model	5.5
5.3 Macroscopic FEM simulations relying on discrete set of crystals	5.9
5.3.1 Taylor's model + Polycrystal models	5.10
5.3.2 Self-consistent approach + Polycrystal models	5.19
5.3.3 Homogenization approach + Polycrystal models	5.20
5.4 Macroscopic FEM simulations with microscopic models	5.24
5.5 FEM analysis applied on both ODF evolution and macroscopic process	5.26
5.5.1 Crystal orientation representation	5.27
5.5.2 Micro-Macro Links	5.28
5.5.3 Evolution rule of Orientation Distribution Function	5.29
5.5.4 Computation of the reorientation velocity field	5.30
5.5.5 Texture prediction under monotonic deformations	5.31
5.5.6 Application to aluminum rolling	5.32
5.5.7 Conclusion	5.33
5.6 Conclusion	5.35
References	5.35
6. FEM Micro-Macro models with yield locus	6.1
6.1 Introduction	6.1
6.2 Macroscopic models imbued from single crystal plasticity	6.2
6.2.1 3G model	6.2
6.2.2 Khan & Cheng's model	6.9
6.2.3 Aifantis' models	6.10
6.2.4 Conclusion	6.17
6.3 Analytical yield loci computed from texture data	6.17
6.3.1 Polycrystal yield locus obtained by Taylor's approach	6.17
6.3.2 Proposals applying concepts from Montheillet	6.19
6.3.3 Arminjon, Bacroix, Imbault... 's potential formulation	6.24
6.3.4 Van Houtte's potential formulation	6.29
6.3.5 Conclusion	6.38
6.4 Models developed by MSM	6.39
6.4.1 First steps in coupling FEM with texture codes	6.39
6.4.2 Texture updating coupled with FEM simulations	6.48
6.4.3 Hyperplane model	6.51
6.4.4 Interpolation approach	6.60

6.4.5 Conclusion	6.70
6.5 Validations of our models	6.70
6.5.1 Discrete sets of crystallographic orientations	6.70
6.5.2 π -sections of the yield locus computed by local and non local methods	6.72
6.5.3 Lankford coefficient prediction	6.74
6.5.4 Academic rolling validation with texture updating	6.76
6.5.5 Conclusions of validation step	6.79
6.5.6 Conclusion	6.80
References	6.80
7. Conclusions	7.1

Notations

Second order tensors are underlined once or noted with their 2 subscripts and fourth order tensor are identified by four subscripts or underlined twice. Capital Latin letters or Greek letters are used for these tensors. Einstein's summation on identical indices is always assumed unless otherwise specified.

The simple contracted tensor product is identified by ".".

$$\underline{C} = \underline{A} \cdot \underline{B} \Leftrightarrow C_{ij} = A_{ik} B_{kj}$$

The tensorial product is :

$$\underline{\underline{C}} = \underline{A} \otimes \underline{B} \Leftrightarrow C_{ijkl} = A_{ij} B_{kl}$$

The double contracted tensor product is noted by ":"

$$s = \underline{A} : \underline{B} \Leftrightarrow s = A_{ij} B_{ij} \quad \underline{C} = \underline{\underline{S}} : \underline{B} \Leftrightarrow C_{ij} = S_{ijkl} B_{kl}$$

$$s = \underline{A} : \underline{\underline{S}} : \underline{B} \Leftrightarrow s = A_{ij} S_{ijkl} B_{kl}$$

The tensorial norm is defined by :

$$|\underline{A}| = \sqrt{\underline{A} : \underline{A}}$$

$$|\underline{\underline{S}}| = \sqrt{S_{ijkl} S_{ijkl}}$$

The inverse operator is defined by the superscript -1 :

$$\underline{A}^{-1} \underline{A} = \underline{I} \Leftrightarrow A_{ik}^{-1} A_{kj} = \delta_{ij}$$

with \underline{I} the unit second order tensor, δ_{ik} Kronecker symbol.

The transverse operator is defined by the subscript T :

$$(A^T)_{ij} = A_{ji}$$

Vectors are also underlined once, but small Latin letters are used. They can also be noted with one subscript. The vector operations are :

$$\underline{s} = \underline{v} \cdot \underline{u} \Leftrightarrow s = v_i u_i$$

$$\underline{C} = \underline{v} \otimes \underline{u} \Leftrightarrow C_{ij} = v_i u_j$$

$$|\underline{v}| = \sqrt{\underline{v} \cdot \underline{v}} = \sqrt{v_i v_i}$$

If \underline{v} is a vector and \underline{A} a second order tensor :

$$\underline{u} = \underline{A} \cdot \underline{v} \Leftrightarrow u_i = A_{ij} v_j$$

Scalars are not underlined.

The superscript * characterises unit vector :

$$\underline{u}^* \Rightarrow |\underline{u}^*| = 1$$

Abbreviations

<i>CRSS</i>	Critical Resolved Shear Stress characterizing one slip system
<i>FEM</i>	Finite Element Method
<i>FLD</i>	Forming Limit Diagram
<i>MK</i>	Marciniak Kuczynski
<i>MSM</i>	department of Mechanics of Structures and Materials
<i>ODF</i>	Orientation Distribution Function
<i>RVE</i>	Representative Volume Element

Latin letters

a	exponent in the yield surfaces proposed by Hill, Hosford, Barlat, Karafillis
a, b	material constants in Tourki's model
a, A, B, C, D, E	material constants in 3G model
a_m	annihilation of mobile dislocations
a_i	annihilation of immobile dislocations
$a_{1b}, a_{2b}, a_{3b}, a_{1n}, a_{2n}, a_{3n}$	functions of dislocation density in constitutive relations of Aifantis's model
a^{su}	matrix taking into account various types of dislocation interactions in Teodosiu's micro model
\underline{a}	unit vector oriented in the crystal direction in Aifantis' model
$\underline{\underline{a}}$	vector (1 1 1 1 1) in the 5 dimensional space (interpolation approach)
$\underline{a}, \underline{b}$	intermediate vectors in interpolation approach
A	constant representing the rate of annihilation of mobile dislocations in Bergström's model
A	constant in Miller & Mac Dowell's model
A	surface region in Acharya & Beaudoin's model
$A A_1 A_2 A_3$	material constants in Follansbee & Kocks' model
A, B, C	material constants in the yield surfaces proposed by Hill, Hosford, Barlat, Karafillis, Tourki
\underline{A}	macroscopic tensor in Aifantis' model equivalent to \underline{A}^s tensor at microscopic level
$A_{ij}^s \underline{A}^s$	symmetric part of Schmid's tensor K_{ij}^s
\underline{A}_i^s	symmetric part of Schmid's tensor associated to texture component i

b_α, b_R	shape-control parameter in Khan & Cheng's model
\underline{b}	Burgers' vector in crystalline plasticity, b is its magnitude
\underline{b}^c	cumulative Burgers vector of all dislocations threading the region A in Acharya & Beaudoin's model
\underline{b}^s	unit vector in the slip direction for the slip system s
c	creation of dislocations in Bergström's model
\hat{c}	variation of dislocation density in Aifantis's model
C	constant in the expression of dislocation density for constant strain rate tensile tests
C	constant in the first Miller & Mac Dowell's model and function in their second model
C	curve bounding a surface region A in Acharya & Beaudoin's model
C^*	constant in second Miller & Mac Dowell's model
C_α	saturation rate of back stress (Teodosiu's macro model)
C_p	polarization rate of the persistent dislocation structures (Teodosiu's macro model)
C_s	saturation rate of S_D "direct" directional strength (Teodosiu's macro model)
C_i^{uv}	Fourier's coefficients in the series expansion representing the ODF
\underline{C}^e	elastic tangent matrix
\underline{C}^{tan}	non linear tangent matrix
dt, dG_{ij}, \dots	increment of time, increment of shear strain, ...
dV	elementary volume
D	grain size
$\underline{\underline{D}}^{micro}$	stiffness 4 th order tensor relating stress and strain rate in visco-plastic approach in Kumar & Dawson's model
e_i, e_j, e_k	basis of a rectangular Cartesian coordinate system
$\underline{\dot{e}} \text{ or } \dot{e}_p \quad p = 1,5$	vector representation of plastic strain rate tensor in van Houtte's model
E	visco-plastic potential in strain rate space of Arminjon's model
E	earing percentage in cup drawing
E_c	complementary visco-plastic potential in stress space of Arminjon's model
f	statistical crystallite orientation distribution function, its variables are g , the set of Euler angles in Bunge's approach, r in Kumar & Dawson's approach or \underline{a} in Aifantis' approach.

f_i	volume fraction of crystals belonging to texture component i
\hat{f}	source term in momentum exchange between dislocations and lattice in Aifantis's model
F	function in strain rate space which after scaling, gives the plastic multiplier $\dot{\lambda}$ in Arminjon's model
F_p	function describing the yield surface
$F_{p_1 p_2 \dots p_N}$	coefficients of the series expansion in strain rate space of the yield locus in van Houtte's model
F, G, H, N, L, M	material anisotropic constants of Hill's 1948 yield locus
\underline{F}	deformation gradient tensor
$\tilde{\underline{F}}$	fluctuation field in deformation gradient tensor of the RVE in Miehe's approach
\underline{F}^*	elastic deformation gradient tensor
\underline{F}^*	elastic distortion + rigid rotation of the lattice, applied on the isoclinic configuration to recover the real configuration
\underline{F}^p	plastic deformation gradient tensor
g	function in Tourki's model, Follansbee & Kock's model or Teodosiu's macro model
g	orientation of one crystal, expressed by Euler angles
$g^j \quad j=R, \alpha$	function in Miller & Mac Dowell's model for isotropic hardening R and kinematic hardening α
G	shear modulus
$G_{12} \ G_{23} \ G_{31} \ \text{or} \ G_{ij}$	shear strain in maximal shear planes (3G model)
$G_{p_1 p_2 \dots p_N}$	coefficients of the series expansion in stress space of the yield locus in van Houtte's model
h	cup height used to determine the earing percentage
h	material parameter in Barlat's 1989 model
h_0	material parameter in hardening function in Anand's micro model
$h_1 \ h_2 \ h_3$	parameters related to grain size D in Nakamachi's model
h^{su}	hardening matrix in CRSS evolution rule
h^u	function in the CRSS evolution rule
H_0	material parameter in Voce type law in Dawson's micro model
H_{ij}	Hessian matrix, second derivative of the yield surface
\underline{I}	second order unit tensor

$j_b j_n$	size of the dislocation flux in glide or climb directions in Aifantis' model
\underline{j}	dislocation flux in Aifantis' model
$J(\underline{r}_0, t)$	determinant of the mapping corresponding to the trajectories of crystals through orientation space due to plastic deformation
J_1	first stress invariant = $\frac{1}{3}tr(\underline{\hat{\sigma}} - \underline{\alpha})$
J_2	second stress invariant = $\frac{1}{2}(\underline{\hat{\sigma}} - \underline{\alpha}) : (\underline{\hat{\sigma}} - \underline{\alpha})$
k	Boltzman's constant
k	scalar factor often used in interpolation approach to keep unit vector property
k, m, n, p, q	material constant in Tourki's model
$k_0 k_1$	material constants in Acharya & Beaudoin's model
k_2	recovery function in Acharya & Beaudoin's model
K	material constant in the flow rule of the 3G model
K_{ij}^s	geometrical matrix describing the slip system s , generally called Schmid's tensor
$\underline{\underline{K}}$	fourth order texture tensor in Aifantis' average procedure
L_{ij}^s	plastic velocity gradient generated by a particular slip system s
\underline{L}^{micro}	velocity gradient applied to a crystal, its decomposition neglects elasticity
$\underline{\underline{L}}$	fourth order tensor describing material anisotropy in yield locus approach or in self-consistent scheme
$\underline{\underline{L}}^*$	4 th rank interaction tensor in elastic self-consistent approach
$\underline{\underline{L}}^H$	4 th rank Hill's constraint tensor in elasto-vico-plastic self-consistent approach
m	material constant defining the fraction of isotropic hardening in Teodosiu's macro model
$m^j \quad j=R, \alpha$	material parameter in g function of Miller & Mac Dowell's model
M	Taylor's factor for one crystal having an orientation g and submitted to a strain mode
$M_i^*(\underline{\hat{\epsilon}}^p)$	function integral of Taylor's factor and harmonic functions describing the ODF in Arminjon's approach

M_i^{**}	approximated value of $M_i^*(\dot{\underline{\epsilon}}^p)$ to identify β_k^i coefficients
\overline{M}	average Taylor's factor for a polycrystal
n	material rate-sensitivity exponent in a viscoplastic model
n'	strain hardening exponent in elastoplastic model
n_L	exponent in the rate function of latent strength of the persistent dislocation structures (Teodosiu's macro model)
\underline{n} and \hat{N}	unit normal vector and its associated skew symmetric tensor in Acharya & Beaudoin's model
\underline{n}	axis of rotation in Rodrigues's representation of crystal orientation
\underline{n}^γ	outward normal of the deformed configuration of the RVE
\underline{n}^T	outward normal of the initial configuration of the RVE with sometimes + or - superscript to localize its direction
\underline{n}^s	unit vector normal to the slip plane for the slip system s
N	dimension of the space
N_v	number of inclusions per unit of volume
$\underline{N}_{\dot{\epsilon}^p}$	direction of the plastic strain rate tensor in Teodosiu's macro model
p	material parameter in Barlat's 1989 model
p^{su}	parameter of dynamic recovery due to cross slip in Nakamachi's micro model of CRSS evolution
\underline{P}	tensor associated to the polarity of the dislocation structures (Teodosiu's macro model)
q	material parameter weighting direct and latent part of directional strength S_D, S_L (Teodosiu's macro model)
q	parameter of non-uniformity of any scalar field
$q^j \quad j = R, \alpha$	material parameter in g function of Miller & Mac Dowell's model
q^{su}	interaction matrix of self and latent hardening in Nakamachi's micro model of CRSS evolution
$Q(u_p)$	approximate polynomial function of average Taylor's factor in van Houttes's model
$Q(\underline{s}^*)$	polynomial function describing stress yield locus in van Houtte's model

r	effective distance between the adjacent slip systems in Nakamachi's micro model
r	re-mobilization of immobile dislocations
r	Lankford coefficient, ratio of the transverse to the thickness strain during an uniaxial tensile test
\underline{r}	orientation vector of a crystal in Rodrigues' parametrization adopted by Kumar & Dawson's model
r_α	Lankford coefficient measured by a tensile test which longitudinal axis does an angle of α with the Rolling Direction
$\bar{r} = r_0 + r_{90} + 2r_{45}$	average Lankford coefficient for an anisotropic sheet
\underline{r}_0	Rodrigues' vector to define crystal orientation in initial reference texture
R	isotropic hardening variable, increase of plastic stress in Miller & Mac Dowell's model
$R_0 R_2$	saturated values of isotropic hardening in Khan & Cheng's model
$R_{sat}^{(0)}$	(initial) saturation value of R variable
\underline{R}	rotation matrix
\underline{R}_i^Φ	rotation matrix about the i -axis by the angle Φ
$\underline{R}^{elastic}$	crystal elastic rotation tensor in Acharya & Beaudoin's model
s	size of a deviatoric stress on the yield locus, also called stress radius
s	mean free path or average distance covered by mobile dislocations
s	slip system
$s_1 s_2 s_3$	parameters related to grain size D in Nakamachi's micro model
s_0	parameters related to dislocation density decrease due to glide work and thermomechanical effect in Nakamachi's micro model of CRSS evolution
s^s	mean free path or average distance covered by mobile dislocations in slip system s
s^{su}	softening matrix in Nakamachi's micro model of CRSS evolution
\underline{s} or s_p $p = 1,5$	vector representation of deviatoric stress tensor in van Houtte's or hyperplane or interpolation approach
$\underline{s}^{(k)}$ or $s_p^{(k)}$	nodal stress point k of the yield locus used to build an hyperplane facet

$\underline{s}^{(i)}$	non unit stress vector associated to a unit direction in strain rate space $\underline{u}^{*(i)}$
$\underline{s} = s\underline{s}^*$	vector description of a deviatoric stress point on the yield locus in van Houtte's model
\underline{s}^*	unit vector defining a deviatoric stress direction
\underline{s}^{*0}	unit vector defining a deviatoric stress direction, center of a local description of the yield locus
$\underline{s}^{*(i)}$	unit vector representing a perturbed direction i around \underline{s}^{*0} , called domain limit vector (interpolation approach)
\underline{s}^{*0}	unit vector in the direction of vector (1 1 1 1 1) in stress space
$\underline{s}^{*0(i)}$	unit vector representing a perturbed direction i around \underline{s}^{*0}
\underline{SS}^i	contravariant vector associated to vector $\underline{s}^{*(i)}$
$\underline{SS}^{*(i)}$	contravariant vector associated to vector $\underline{s}^{(i)}$
\underline{s}_A	stress vector at the step beginning
\underline{s}_B	stress vector at the step end
\underline{s}_{Btrial}	elastic stress predictor vector at the step end
S_D	scalar related to the strength of the dislocation structures associated with currently active slip systems, "direct" directional strength (Teodosiu's macro model)
S_{sat}	saturation value of S_D
S_L	norm of latent strength of the persistent dislocation structures
\underline{S}_L	latent strength of the persistent dislocation structures
\underline{S}	directional strength of dislocation structures (Teodosiu's macro model)
t	time
t_A, t_b, t_n	functions of dislocation density, interaction forces between dislocations in constitutive relations of Aifantis's model
\underline{t}	traction at the boundary in Miehe's proposal
T	absolute temperature in Kelvin degree
$\overset{uv}{T}_l$	harmonic function of Euler angle in the series expansion representing the ODF
\underline{u} or u_p	strain rate mode $\underline{U}_{\varepsilon p}$ in its vector notation

\underline{u}'	all possible strain rate modes $\underline{U}_{\dot{\epsilon}^p}$ in minimization process
\underline{u}^*	unit vector, direction of a strain rate vector
$\underline{u}^{*(i)}$	unit vector in strain rate space representing a perturbed direction i around a central direction \underline{u}^{*0}
U	rate of immobilization or annihilation of mobile dislocations
$\underline{U}_{\dot{\epsilon}^p}$	strain rate mode tensor
$\underline{U}'_{\dot{\epsilon}^p}$	unit strain rate mode tensor
$\underline{U}^X_{\dot{\epsilon}^p}$	strain rate mode in principal strain rate axes
\underline{v}	unit vector in the 5 dimensional space, direction of the vector identified by coordinates (1 1 1 1 1)
\underline{v}	reorientation velocity vector in ODF conservation relation.
V	volume
V^*	volume fraction of crystals in a subset of orientation space Ω^* in Kumar & Dawson's model
\tilde{W}	fluctuation field applied on the RVE in Miehe's model
W	viscosity constant in 3G model
W^p	plastic work
\dot{W}^p	plastic work rate
$x_1 x_2$	transformation of principal stress axes in Tourki's work
\underline{x}	coordinates in the final configuration
\underline{x}^*	coordinates in the isoclinic configuration
$X_0 X_1 X_2$	saturated values of hardening in Kan & Cheng's model
X_k	4rth order strain rate term in Arminjon's description
$X_P Y_P Z_P$	cartesian coordinates of P point
\underline{X}	coordinates in the initial configuration
y_c	characteristic length associated to the annihilation process of dislocation dipoles
$Z_{ij}^s \underline{Z}^s$	anti-symmetric part of Schmid's tensor K_{ij}^s

Greek Letters

α	orientation angle between rolling direction and tensile direction in experimental test
α	material constant in relationship between uniaxial flow stress and dislocation density (Bergström's model) or CRSS and dislocation density
α	ratio between the CRSS associated to a particular slip system and a common reference CRSS
α_k	material coefficient in polynomial formulation of the plastic multiplier in Arminjon's approach
$\alpha_1 \alpha_2$	angles measuring the deviation of G_{12} gliding planes from the directions at 45° to principal stresses in 3G model
$\alpha_{sat}^{(0)}$	(initial) saturation value of the back stress norm (Miller & Mac Dowell's model, Teodosiu's macro model)
$\underline{\alpha}$	back-stress in kinematic hardening (Teodosiu's macro model, Miller & Mc Dowell's model...) also called dislocation stress in Aifantis's model
$\alpha \quad \beta$	material coefficients in Montheillet's yield function
β	variable in Bezier formula in Vegter's criterion
β	orientation of the principal stress directions with the Rolling Direction (Hill's model, Tourki's model, 3G model)
β	parameter defining the size of one hyperplane facet or of the interpolation domain
$\beta_1 \beta_2 \beta_3 \beta_4$	set of 4 angles to represent a strain mode tensor
$\beta_1 \beta_2 \beta_3$	Euler angles defining the orientation of principal strain rate mode directions
β_4	deviation of the current strain rate mode with respect to an axisymmetric compression along the 3 rd principal axis
β_k^i	linear coefficient between parameter α_k of Arminjon's approach and texture coefficients C_i
$\gamma^{macro \text{ or } micro}$	deformed configuration in Mische's model
$\dot{\gamma}^s$	slip rate associated to a slip system s
$\dot{\gamma}_0$	reference slip rate in microscopic viscoplastic flow rule
$\dot{\gamma}_{scaled}^s$	slip rate per unit equivalent strain rate
Γ	total slip in one crystal
$\Gamma^{macro \text{ or } micro}$	initial configuration in Mische's model

$\bar{\dot{\Gamma}}$	total average polycrystal slip rate
δ_{ij}	Kroneker symbol
Δ	angle step used to discretize Euler's space (Darrieulat & Piot)
ΔG	activation enthalpy
$\underline{\underline{\Delta}}$	measure of lattice incompatibility in Acharya & Beaudoin 1999
$\underline{\underline{\underline{\Delta}}}$	Eshelby's 4 th order tensor
$\varepsilon_1 \varepsilon_2 \varepsilon_3$	principal strains
ε_{ps}	prestrain applied in one direction before a second loading
$\varepsilon_{eq}(\varepsilon_{eq}^p)$	equivalent von Mises (plastic) strain $\sqrt{\frac{2}{3}\varepsilon_{ij}\varepsilon_{ij}}$
ε_e^p	integrated equivalent plastic strain (hardening internal variable computed from the integral of $d\varepsilon_{eq}^p$)
ε_m	mean strain
$\dot{\varepsilon}_0$	limit strain rate for thermally activated motion
$\dot{\varepsilon}_{eq}^{(p)}$	(plastic) von Mises equivalent plastic strain rate
$\dot{\varepsilon}_{eqa}^p$	anisotropic equivalent plastic strain rate associated to anisotropic equivalent stress to recover plastic dissipation
$\underline{\underline{\varepsilon}}$ or ε_{ij}	strain tensor
$\underline{\underline{\varepsilon}}^{p\ micro}$	strain tensor at microscopic level (in one crystal)
$\underline{\underline{\dot{\varepsilon}}}_i^{p\ micro}$	plastic strain rate tensor associated to the texture component i in Darrieulat's model
$\underline{\underline{\varepsilon}}^{macro}$ or $\bar{\underline{\underline{\varepsilon}}}$	strain tensor at macroscopic level
$\underline{\underline{\varepsilon}}^e$	elastic strain tensor
$\underline{\underline{\varepsilon}}^p$	plastic strain tensor
$\hat{\underline{\underline{\varepsilon}}}$	deviatoric strain tensor
ζ	material parameter in plastic spin function (Miller & Mac Dowell's model)
η	isoparametric coordinate in a reference plane in FEM formulation
η_i	one of the 5 η -coordinates used in stress space or in strain rate space in the interpolation approach
θ	polar angle associated with the polar-coordinate description used by Tourki, Ferron
θ	angle between central direction and domain limit vectors in interpolation approach

θ	scalar defining the implicit character of an integration scheme $0 \leq \theta \leq 1$
θ_{0k}	hardening rate due to dislocation accumulation in Voce's law (Follansbee-Kocks, Acharya-Beaudoin)
λ	plastic multiplier
λ^k	slip lattice incompatibility corresponding to system k in Acharya & Beaudoin's model
ξ	isoparametric coordinate in a reference plane in FEM formulation
$\rho_{(0)}$	(initial) total dislocation density
ρ_i	density of immobile dislocations
ρ_m	density of mobile dislocations
ρ^s	dislocation density related to slip system s
$\hat{\sigma}$	internal variable in Follansbee & Kocks' model, flow stress at 0°K associated to a defined dislocation substructure
$\sigma_1 \sigma_2 \sigma_3$	principal stresses
$\sigma_0 \sigma_{45} \sigma_{90} \sigma_\alpha$	yield stress under uniaxial tension in one direction doing an angle 0, 45, 90, α with the Rolling Direction
σ_0	initial elastic limit (Bergström's model, Miller & Mac Dowell's model, Teodosiu's macro model...)
$\sigma_{0\text{sta}}$	static yield stress of a dislocation free material (Vegter's model)
$\sigma_{0\text{dyn}}$	dynamic part of the flow stress (Vegter's model)
σ_a	athermal stress component associated with interaction of dislocations with long range obstacles in Follansbee & Kocks' model
σ_b	yield value under equibiaxial plane sollicitation
σ_{eq}	von Mises equivalent stress $\sqrt{\frac{3}{2} \hat{\sigma}_{ij} \hat{\sigma}_{ij}}$
σ_{eqa}	anisotropic equivalent stress
σ_F	yield stress under uniaxial tension in a reference direction
σ_m	hydrostatic (mean) stress $(1/3) \sigma_{ii}$
σ_{sat}	stress at zero strain hardening rate, called saturation stress (Follansbee & Kocks' model, Schmitz's model)
σ_{sat0}	saturation stress at 0°K (Follansbee & Kocks' model)
$\sigma_x \sigma_y \sigma_z \tau_{xy} \tau_{xz} \tau_{yz}$	stress components in the material orthotropic axes
$\underline{\sigma}$	Cauchy stress tensor

$\underline{\sigma}^{effective} = \underline{\sigma} - \underline{\alpha}$	macroscopic effective stress in Aifantis' model
$\underline{\hat{\sigma}}$	deviatoric Cauchy stress tensor
$\nabla \underline{\hat{\sigma}}$	Jaumann deviatoric stress rate
$\underline{\sigma}^{micro}$	microscopic stress tensor, no <i>micro</i> superscript means macroscopic stress, sometimes superscript <i>macro</i> is effectively recalled
$\underline{\sigma}_i^{micro}$	microscopic stress tensor of texture component <i>i</i> in Darrieulat's approach
τ	yield stress in a pure shear test parallel to material orthotropic axes (Hill's yield locus),
τ	stress limit in Tresca's criterion, ($2\tau = \sigma_F$ yield stress in uniaxial tensile test)
τ^s	resolved shear stress acting on the slip system <i>s</i>
$\tau_{effective}^s$	resolved shear stress in Aifantis' model where 1 slip system is assumed and a cinematic hardening approach is applied at the microscopic level
τ_n	resolved climb component in Aifantis' model
$\tau_{c(0)}^s$	(initial) critical resolved shear stress acting on the slip system <i>s</i> often called CRSS
$\tau_{c(0)}$	(initial) common reference value assumed for CRSS in one crystal
τ_{sat}	saturation value of common reference CRSS
$\tau_{12} \tau_{23} \tau_{13}$	shear stress associated to shear strains $G_{12} G_{23} G_{13}$ (model 3G)
$\bar{\tau}_c$	average common reference CRSS in a polycrystal
$\underline{\tau}^{micro \text{ or } macro}$	first Piola Kirschhoff stress used in Miehe's model
Φ	amplitude of rotation in Rodrigues' description of crystal orientation
$\Phi_i(\xi, \eta)$	interpolation function in classical geometric space in isoparametric finite element
$\Phi_i(\xi_1, \xi_1, \xi_1, \xi_1)$	interpolation function in a reference stress space in the hyperplane discretization of the yield locus
$\Phi \Phi_1 \Phi_2$	functions in Karafillis' model used to define the yield function
$\varphi_1 \phi \phi_2$	set of Euler's angle
Ψ_k	strain rate function used in polynomial description of plastic multiplier in Arminjon's approach
ω_0	scattering width angle with an ideal texture component

Ω	probability for re-mobilization or annihilation of immobile dislocations in Bergström's model
Ω^*	subset domain in crystal orientation space in Rodrigues space
Ω'	whole domain in crystal orientation space of in Rodrigues space (Kumar & Dawson's model)
$\underline{\Omega}$	antisymmetric part of the velocity gradient tensor or total spin
$\underline{\Omega}^{micro}$	microscopic spin decomposed into the plastic spin and the rate of crystal lattice rotation
$\underline{\Omega}^p$	plastic spin
$\underline{\Omega}^L$	rate of crystal lattice rotation used to update texture
$\underline{\Omega}^t$	texture spin due to grain boundary effects in Aifantis' model

1. INTRODUCTION

If we look at the anisotropic plastic models proposed in the literature, 2 types of models exist: the phenomenological ones (chapter 2) and the micro-macro ones (chapters 5 and 6) based on polycrystalline and texture approach. The first ones do not need additional knowledge to be understood by a classical mechanical scientist; it is not the case for the models issued from texture approach. Therefore some basic information will be recalled for the non-specialist reader (chapter 4); however for shortness sake, this will be limited. For a deeper understanding, I recommend the lecture of Van Houtte 1995, Teodosiu 1997, Bunge & Esling 1997.

Roughly speaking, chapter 2 is dedicated to the initial shape of the yield locus. Then chapter 3 describes the hardening models. First, simple macroscopic hardening approaches are recalled; then, more complex formulations with microscopic roots are presented. Chapter 5 summarizes micro-macro approaches without yield locus which use homogenization techniques based on crystal computations (Beaudoin *et al.* 1995, Kumar & Dawson 1996, Anand & Kothari 1996, Nakamachi *et al.* 1999). Chapter 6 presents the other trends of yield locus computations, based on texture and crystal plasticity (Lequeu *et al.* 1987, Imbault 1993, van Houtte 1994, Duchêne *et al.* 1999). The advantages and drawbacks of the different proposals will be defined as well as the model identification procedure since this is a key factor for practical applications.

The reason of the strong interest in the initial and up-dated shape of the yield locus or in the micro-macro approaches is related to the accuracy of the model predictions. The reliability of Finite Element Method simulations in deep drawing computations (Figure 1-1, Figure 1-2, Figure 1-3) as well as of Marciniak Kuczynski's (MK) predictions of Forming Limit Diagrams (FLD) (Figure 1-4, Figure 1-5) easily explain the reasons to improve the description of the yield locus or to use polycrystal models.

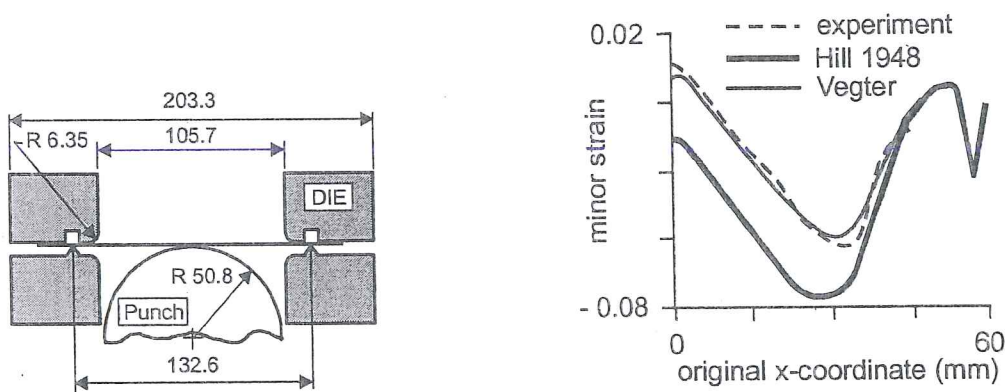


Figure 1-1 Simulated and measured minor strains along a symmetry axis of a Limiting Dome Height test, benchmark of the Numisheet 96 conference with draw quality mild IF steel (models with phenomenological description of yield locus, Pijlman *et al.* 1998).

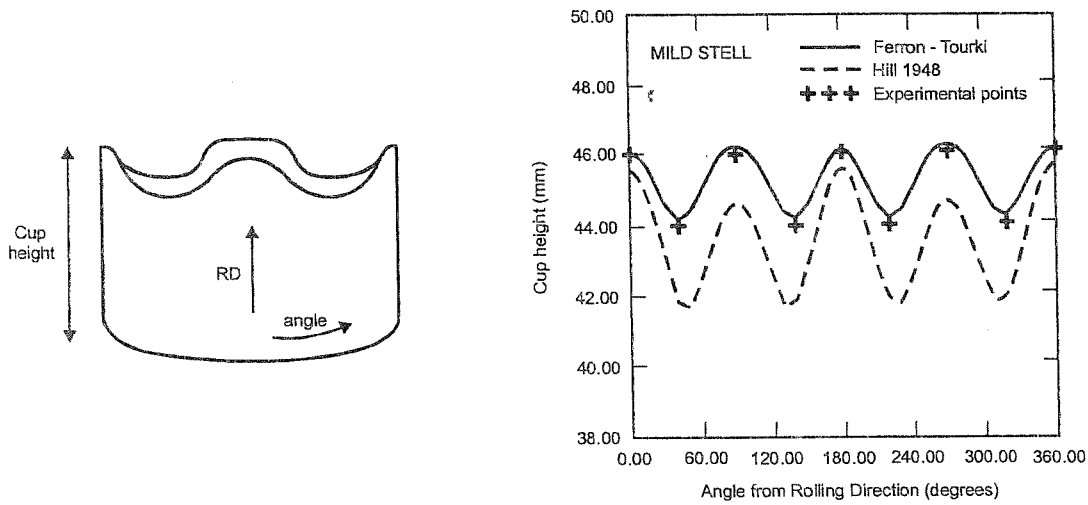


Figure 1-2 Deep drawing of a cylindrical cup : comparison between experimental and calculated earing profiles, mild steel supplied by SOLLAC (models with phenomenological description of yield locus, Tourki *et al.* 1996).

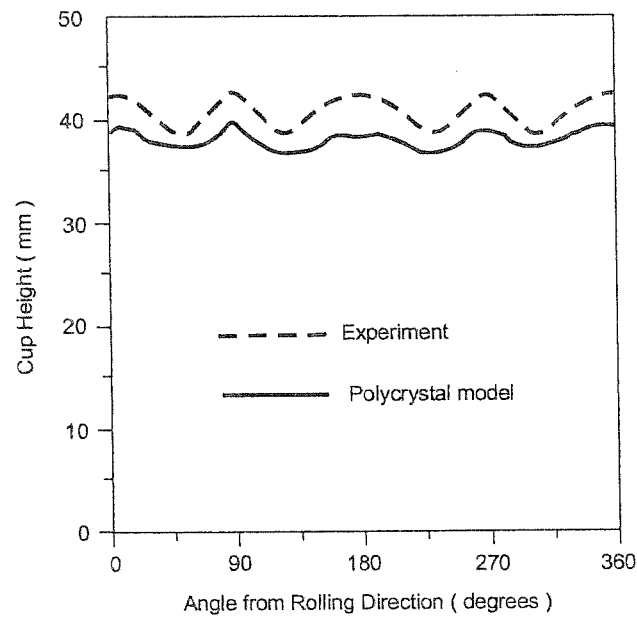


Figure 1-3 Deep drawing of a cylindrical cup: comparison between experimental and computed earing profiles for Al2008-T4 sheet (polycrystal model, Anand *et al.* 1997).

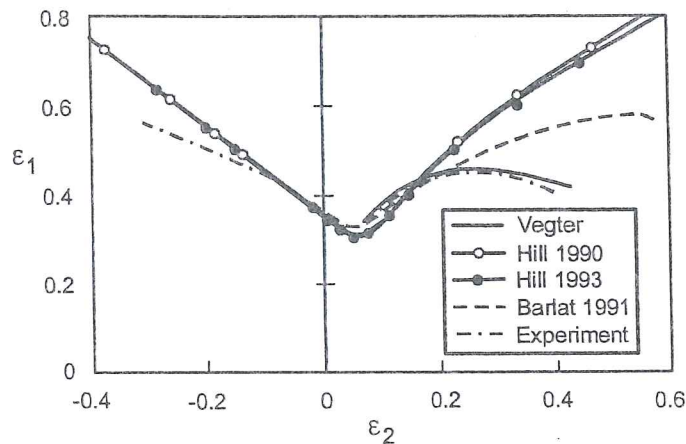


Figure 1-4 FLD predictions applied on bi-axial pre-strained specimens of an IF steel, using different yield loci and comparison with experiments (models with phenomenological description of yield locus, Vegter *et al.* 1999).

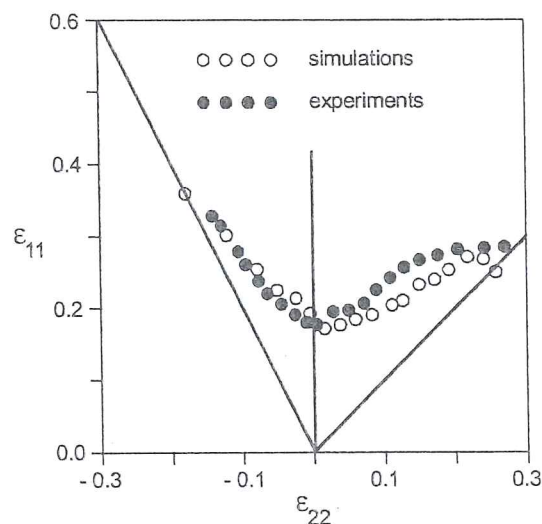


Figure 1-5 Polycrystal model predicted and measured FLD for as received AA6111-T4-C (polycrystal model, Wu *et al.* 1998).

Barlat 1987 has shown that the theoretical sheet forming limit strain at necking for balanced biaxial stretching is roughly 5 times larger for a material the yield surface of which is described by the von Mises criterion than for a material which follows the Tresca criterion, when all other properties are identical. This theoretical result, as well as the above figures and Marciniak Kuczynski's predictions, underline the importance of the yield locus shape.

References

- Anand, L., Kothari, M. (1996) A Computational Procedure for Rate-Independent crystal plasticity, *J. Mech. Phys. Solids*, 44/4, 525-558.
 Anand, L., Balasubramanian S., Kothari, M. (1997) Constitutive Modeling of

- Polycrystalline Metals at Large Strains : Application to Deformation Processing, *Large plastic deformation of crystalline aggregates*, International Centre for Mechanical Sciences, Courses and Lectures n° 376, Springer Ed, 109-172.
- Barlat, F., Becker, R.C., Hayashida, Y., Maeda, Y., Yanagawa, M., Chung, K., Brem, J.C., Lege, D.J., Matsui, K., Murtha, S.J., Hattori, S. (1997) Yielding description for solution strengthened aluminium alloys, *Int. J. of Plasticity*, **13-4**, 385-401.
- Beaudoin, A.J., Dawson, P.R., Mathur, K.K., Kocks, U.F. (1995) A hybrid finite element formulation for polycrystal plasticity with consideration of macrostructural and microstructural linking, *Int. J. Plasticity*, **11/5**, 501-521.
- Bunge, H.J., Esling, C. (1997) Texture et anisotropie des matériaux, *Techniques de l'ingénieur*, M 605/9, 1-39.
- Duchêne L., Godinas A., Habraken, A.M. (1999) Metal Plastic Behaviour linked to Texture Analysis and FEM Method, NUMISHEET '99, 4th Int. Conf. and Workshop on Numerical Simulation of 3D Sheet Forming Processes, Besançon, France, 13-17 September 1999, Edité par J.C. Gélín, P. Picart, Université de Franche-Comté et ENSMM, 97-102.
- Imbault, D. (1993) Un modèle micro-macro analytique pour la plasticité des polycristaux anisotropes, thèse de docteur de l'Institut National Polytechnique de Grenoble.
- Kumar, A., Dawson, P.R. (1996) The simulation of texture evolution with finite elements over orientation space, I. Development, *Comp. Methods Appl. Mech. Eng.*, **130**, 227-246.
- Lequeu, Ph., Gilormini, P., Montheillet, F., Bacroix, B., Jonas, J.J. (1987) Yield surfaces for textured polycrystals, I. Crystallographic Approach, *Acta Metall.*, **35/2**, 439-451.
- Nakamachi, E., Xie C.L., Hiraiwa, K., Harimoto, M. (1999) Development of elastic/crystalline viscoplastic finite element analysis code based on the meso-phenomenological material modeling, Numisheet'99, 13-17 September 1999, vol. 1, Besançon, France, 79-84.
- Pijlman, H.H., Huetink, J., Carleer, B.D., Vegter, H. (1998) Application of the Vegter yield criterion and a physically based hardening rule on simulation of sheet forming, *Simulation of Materials Processing : Theory, Methods and Applications*, Balkema, Huetink & Baaijens Eds.
- Teodosiu, C. (1997) Dislocation modelling of crystal plasticity, *Large plastic deformation of crystalline aggregates*, International Centre for Mechanical Sciences, Courses and Lectures n° 376, Springer Ed, 21-80
- Tourki, Z., Zeghloul, A., Ferron, G. (1996) Sheet metal forming simulations using a new model for orthotropic plasticity, *Computational Materials Science*, **5**, 255-262.
- Van Houtte, P. (1994) Application of plastic potentials to strain rate sensitive and insensitive anisotropic materials, *Int. J. Plasticity*, **10**, 719-748.
- Van Houtte, P. (1995) Micromechanics of polycrystalline materials, Chaire Francqui, Université de Liège.
- Vegter, H., An Y., Pijlman H.H., Huetink J. (1999), Different approaches to describe

the plastic material behaviour of steel and aluminium-alloys in sheet forming, 2nd ESAFORM Conference on Material Forming, Guimaraes, Portugal, Covas J.A. Ed.

Wu, P.D., Neale, K.W., Van Der Giessen, E. (1998) Effects of strain paths on sheet metal limit strains, *Material Instabilities in Solids*, John Wiley&Sons Ltd, de Borst R.&Van der Giessen E., Eds.

2. ANISOTROPIC PHENOMENOLOGICAL YIELD LOCI

2.1. Initial shape of yield loci

The yield locus is the boundary between the elastic and plastic domains. It is a continuous surface in stress space, $F_p(\sigma_{ij}) = 0$, corresponding to all stress states that cause yielding. During plastic deformation, the updated yield locus will expand or contract, translate and distort. In this section, the initial shape of the yield locus associated with the first yielding is analyzed. Experimental evidence and theoretical considerations concerning the plastic behavior of materials have led to some restrictions on the mathematical representation of a yield surface. Following Bridgman's experimental observations (Bridgman 1923, 1952), hydrostatic pressure (25000 bars) does not induce plasticity in metals. More recently, Barlat *et al.* 1991 have measured a relative density change due to plastic deformation of the order of 10^{-3} . Extrapolating an approximate limit analysis of a porous medium, Gurson's model 1977 proposes a plastic behavior law affected by pressure. His goal is fracture prediction and far from rupture, the pressure effect is limited. In a hot sintering process, the initial porosity can be very high and the pressure effect is important. However, in general cases of sound classical metals characterized by low porosity, yield surfaces are taken to be pressure independent. Drucker (1951) showed that, based on a stability postulate, the yield surface must be convex. If the yield function is smooth with no vertex, convexity ensures the uniqueness of the plastic strain rate for a given stress state.

Mathematically, the yield surface F_p is convex if, for given stresses σ_{ij} and plastic strain rates $\dot{\epsilon}_{ij}^p$, any stress state σ_{ij}^* inside or on the yield surface obeys the following relationship:

$$(\sigma_{ij} - \sigma_{ij}^*) \dot{\epsilon}_{ij}^p \geq 0 \quad (2-1)$$

If the function F_p is twice differentiable, its Hessian matrix H is defined by :

$$H_{ij} = \frac{\partial^2 F_p}{\partial \sigma_i \partial \sigma_j} \quad (2-2)$$

F_p is convex if the H matrix is semi-definite, that is, if its eigenvalues are positive or zero. Another consequence of Drucker's 1951 postulate is that the flow rule for stable materials is associated. The yield surface is the same as the plastic potential, so the strain rate vector is orthogonal to the yield surface. The associated flow rule is:

$$\dot{\epsilon}_{ij}^p = \dot{\lambda} \frac{\partial F_p}{\partial \sigma_{ij}} \quad (2-3)$$

Hecker 1976 or Phillips 1986, who reviewed numerous critical experiments to assess the yield surface shape, found that the normality rule was never violated. This is also confirmed by the work of Hayakawa & Murakami 1998 in damage mechanics. Indeed, all the yield surfaces listed hereafter respect these 3 characteristics. Table 1 summarizes the evolution of the well-known Hill's 1948 equation. Then Table 2 introduces Barlat's and Karafillis' models. Ferron-Tourki's model is presented next. Finally, Vegter's models are presented since they seem to be well validated and adapted to FEM computations. In addition to these tables, some comments help to understand the origin of the presented models, their parameters identification method as well as their experimental validation. Let us note that except for Karafillis' model and Vegter's model, all the others are restricted to anisotropic materials exhibiting orthotropic symmetry, i.e. to materials which possess 3 mutually orthogonal planes of symmetry at every point. Actually, most scientists agree that this restriction is not a very significant constraint because most mechanically processed materials are orthotropic in their initial state. Typical examples are rolled sheets or plates. Hereafter, when an angle α defines a direction, the reference is always the Rolling Direction (RD). For instance, the notation σ_α means the current yield stress in uniaxial tension along a direction at an angle α with the Rolling Direction. An anisotropic plastic model defined by $F(\sigma_{ij}) = 0$ can be used only if the reference axes are defined. They are often chosen as the material orthotropic directions : $x = \text{Rolling Direction} = \text{RD}$, $y = \text{Transverse Direction} = \text{TD}$, $z = \text{Thickness or Normal Direction} = \text{ND}$.

Other reviews of phenomenological anisotropic models can be found in Vial *et al.* 1983, Kobayashi *et al.* 1985, Barlat 1987, Arminjon *et al.* 1994, Mahmudi 1995, Kuwabara & van Bael 1999, Banabic 2000. Note that the present work and Banabic's 2000 review were conducted separately but at the same moment. Both reviews have selected nearly identical models as the most appropriate to simulate metal sheet behavior.

2.1.1. Hill's approach

Table 1 is dedicated to Hill's research. The classical quadratic yield criterion, Hill 1948 (Table 1), is well suited to specific metals and textures, but lacks flexibility. As mentioned in Vial *et al.* 1983, Hill's old criterion gives a better correlation with metals having an average Lankford's coefficient \bar{r} greater than 1 but is less acceptable when \bar{r} is less than 1. This average value is computed by:

$$\bar{r} = \frac{1}{4}(r_0 + 2r_{45} + r_{90}) \quad (2-4)$$

This proposal has advantages that explain its intensive use:

- it improves the simple assumption of neglecting anisotropy,
- it is simple to implement in a FEM code and available in numerous commercial codes,
- only 3 tensile tests at 0° , 45° , 90° are required to determine the material parameters.

Law Name	Description	Characteristics	References
Hill 1948	$F(\sigma_y - \sigma_z)^2 + G(\sigma_z - \sigma_x)^2 + H(\sigma_x - \sigma_y)^2 + 2L\tau_{yz}^2 + 2M\tau_{zx}^2 + 2N\tau_{xy}^2 = 2\sigma_F^2$	General quadratic equation with 6 parameters, crude approximation of the yield surface shape computed from polycrystal models.	Hill 1948, Vial 1997, Barlat <i>et al.</i> 1991, Vial & Hosford 1983, ...
Hill 1979	$F \sigma_y - \sigma_z ^a + G \sigma_z - \sigma_x ^a + H \sigma_x - \sigma_y ^a + A 2\sigma_x - \sigma_y - \sigma_z ^a + B 2\sigma_y - \sigma_z - \sigma_x ^a + C 2\sigma_z - \sigma_x - \sigma_y ^a = \sigma_F^a$	Hill with variable exponent (non integer) and no shear stress term so that orthotropic material axes and principal stress axes must be superimposed.	Vial 1997, Barlat <i>et al.</i> 1991, Suh <i>et al.</i> 1996, Vial & Hosford 1983.
Hill 1990	$\left \sigma_1 + \sigma_2 \right ^a + \frac{\sigma_b^a}{\tau^a} \left \sigma_1 - \sigma_2 \right ^a + \left \sigma_1^2 + \sigma_2^2 \right ^{\frac{a-1}{2}}$ $\left\{ -2A(\sigma_1^2 - \sigma_2^2) + B(\sigma_1 - \sigma_2)^2 \cos 2\beta \right\} = (2\sigma_b)^2$	Extension of Hill 79 that suppresses its limitation in loading directions but is only defined for plane stress case.	Hill 1990 Barlat <i>et al.</i> 1991, Vegter <i>et al.</i> 1999, Kuwabare & van Bael 1999.
Hill 1993	$\frac{\sigma_x^2}{\sigma_0^2} - C \frac{\sigma_x \sigma_y}{\sigma_0 \sigma_{90}} + \frac{\sigma_y^2}{\sigma_0^2} + \left\{ (A + B) - \frac{A\sigma_x + B\sigma_y}{\sigma_b} \right\} \frac{\sigma_x \sigma_y}{\sigma_0 \sigma_{90}} = 1$	Expression enabling to model different τ_0 and τ_{90} values, when uniaxial stresses in rolling σ_0 and transversal σ_{90} direction are almost equal. Only defined for plane stress case and loads applied along orthotropic axes (no shear component).	Hill 1993, Banabic 1996, Banabic, <i>et al.</i> 1999, Vegter <i>et al.</i> 1999.

Notations :

$A, B, C, F, G, H, L, M, N, a$ = material parameters

$\sigma_x, \sigma_y, \sigma_z, \tau_{xy}, \tau_{xz}, \tau_{yz}$ = stress components in the material orthotropic axes

σ_1, σ_2 = principal stress components oriented by an anticlockwise angle β with the RD axis

σ_b = yield value under plane equibiaxial stress state

τ = yield stress in pure shear test parallel to orthotropic axes (plane stress case)

σ_F = yield stress under uniaxial tension in a reference direction

Table 1 Hill's models.

Hill's 1979 equation (Table 1) is a proposal that adds linear combinations of the deviatoric stresses affected by a *non integer exponent* a . As checked by various authors (see Table 1), this law offers sufficient flexibility when orthotropy and loading are co-axial. This is however a strong limitation.

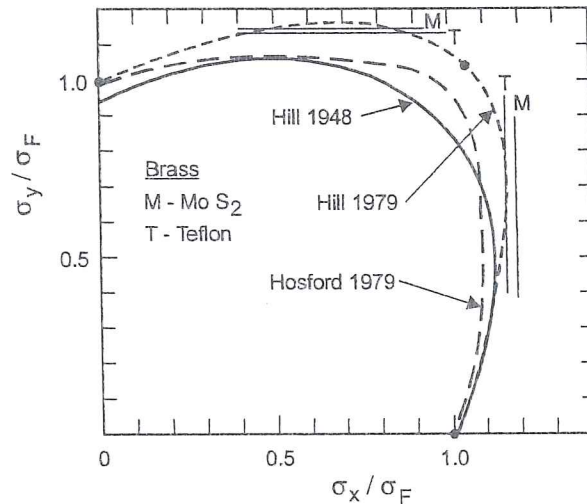


Figure 2-1 Comparison of experimental data with predicted yield loci normalized by uniaxial tension at a strain of 0.1. Experimental data are indicated by solid points and by horizontal and vertical tangents obtained from plane-strain tests (from Vial *et al.* 1983).

When applied to plane stress state and in-plane isotropy, Hill's 1979 proposal reduces to :

$$|\sigma_1 + \sigma_2|^a + (1 + 2\bar{r}) |\sigma_1 - \sigma_2|^a = 2(1 + \bar{r})\sigma_F^a \quad (2-5)$$

So, 3 tensile tests at 0°, 45°, 90° are necessary to reach \bar{r} and Wagoner 1980 proposes a method for calculating a by comparing plane-strain and uniaxial stress-strain curves. Suh *et al.* 1996 have checked that using a variable value of a for 2008-T4 aluminum enables to improve Hill's 1979 predictions.

In Suh's study, the exponent used to simulate the behavior of 70/30 brass with Hill's 1979 model has shown minor change, so that a constant value gives quite accurate results. In fact, a variable a exponent is one way to relax the isotropic hardening assumption.

In 1990, Hill proposes a new yield criterion (Hill 1990 Table 1) adapted to in-plane anisotropy and to any loading orientation. It reduces to Hill 1948 when $a=2$ and recovers Hill 1979 when both A and B vanish. It can be checked that the relation defined in Table 1 is equivalent to a homogeneous function of degree a if the stress components are expressed in the orthotropic axes. If the exponent a is known, the material parameters A and B are computed from the results $\sigma_0, \sigma_{45}, \sigma_{90}$ of uniaxial

tests in directions 0° , 45° and 90° and from the yield stress σ_b under equibiaxial tension:

$$A = \frac{1}{4} \left[\left(\frac{2\sigma_b}{\sigma_{90}} \right)^a - \left(\frac{2\sigma_b}{\sigma_0} \right)^a \right] \quad B = \frac{1}{2} \left[\left(\frac{2\sigma_b}{\sigma_0} \right)^a + \left(\frac{2\sigma_b}{\sigma_{90}} \right)^a \right] - \left(\frac{2\sigma_b}{\sigma_{45}} \right)^a \quad (2-6)$$

The following relation can be used to replace the ratio σ_b^a / τ^a :

$$1 + 2r_{45} = - \frac{\sigma_b^a}{\tau^a} \quad (2-7)$$

Hill does not explicitly define a calibration method. However, the 3 preceding equations, coupled with the predicted yield stress σ_α for uniaxial tensions performed in directions doing an angle α with the rolling direction:

$$\left(\frac{2\sigma_b}{\sigma_\alpha} \right)^a = 1 + \frac{\sigma_b^a}{\tau^a} - 2A \cos 2\alpha + B \cos^2 2\alpha \quad (2-8)$$

allow to reach the 5 parameters : σ_b , τ , A , B , a .

Hill's 1993 proposal aims to model materials characterized by extreme properties such as $\sigma_0 = \sigma_{90}$ together with $r_0 \neq r_{90}$, or by $r_0 = r_{90}$ together with $\sigma_0 \neq \sigma_{90}$. The equation is defined in Table 1 and the 3 constants A, B, C can be reached thanks to the following relations (Hill 1993), which require results from uniaxial tests in directions 0° and 90° and from equibiaxial tension:

$$\frac{C}{\sigma_0 \sigma_{90}} = \frac{1}{\sigma_0^2} + \frac{1}{\sigma_{90}^2} + \frac{1}{\sigma_b^2} \quad (2-9)$$

$$\left(\frac{1}{\sigma_0} + \frac{1}{\sigma_{90}} - \frac{1}{\sigma_b} \right) A = \frac{2r_0(\sigma_b - \sigma_{90})}{(1+r_0)\sigma_0^2} - \frac{2r_{90}\sigma_b}{(1+r_{90})\sigma_{90}^2} + \frac{C}{\sigma_0} \quad (2-10)$$

$$\left(\frac{1}{\sigma_0} + \frac{1}{\sigma_{90}} - \frac{1}{\sigma_b} \right) B = \frac{2r_{90}(\sigma_b - \sigma_0)}{(1+r_{90})\sigma_{90}^2} - \frac{2r_0\sigma_b}{(1+r_0)\sigma_0^2} + \frac{C}{\sigma_{90}} \quad (2-11)$$

The parameters are very easy to reach and, as checked by Banabic *et al.* 99, Hill 93 provides a quite good correlation with experimental results (Figure 2-2).

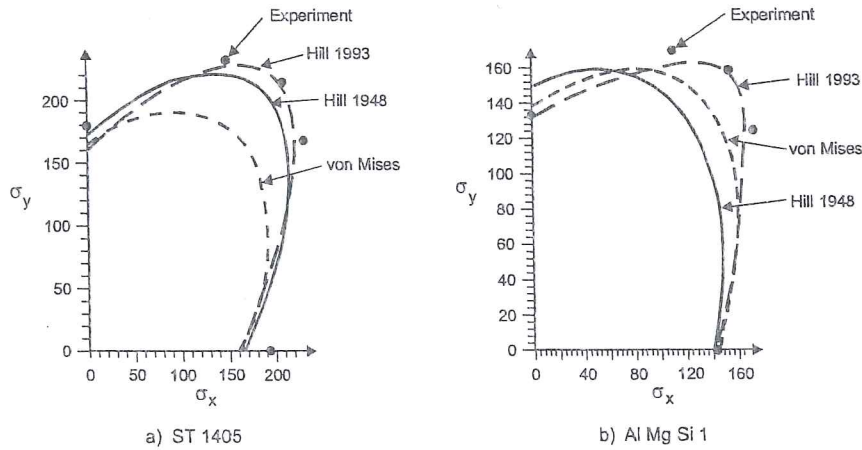


Figure 2-2 Yield loci obtained from biaxial tensile tests and compared with computed yield functions; stresses in MPa (from Banabic *et al.* 1999).

Vegter *et al.* 1999 show an application of Hill 1990 and Hill 1993 criteria (Figure 2-3).

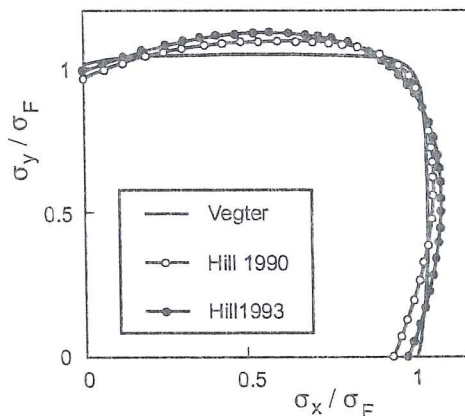


Figure 2-3 Comparison of yield loci : Vegter's line passes through the experimental points for Al-6000 (from Vegter *et al.* 1999).

2.1.2. Barlat's and Karafillis' approach

The presentation of Karafillis *et al.* 1993 is reproduced here as it provides a nice general frame to explain his proposal as well as Barlat's 1989 and 1991. First looking at isotropic yield surfaces, Karafillis recalls that Mendelson 1968 has shown the existence of bounds in an isotropic yield surface of a material with a fixed yield stress in uniaxial tension. These bounds are derived from symmetry and convexity considerations. The lower bound coincides with the limiting maximum shear stress yield surface as described by Tresca's 1864 criterion, whereas the upper bound was proposed by Hosford 1972. In the deviatoric plane section of the yield surface, the lower bound is inscribed in the von Mises' yield circle which, in turn, is inscribed in the upper bound hexagon (Figure 2-4). This deviatoric plane, also called Π plane, is perpendicular to the line representing hydrostatic pressure states and contains the

stress origin point. The relations to compute the projection of a stress state onto the Π plane can be found in van Bael 1994 or Khan & Huang 1995.

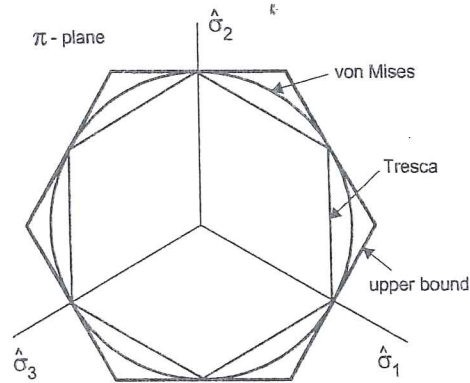


Figure 2-4 The upper bound, the lower bound and the von Mises' yield surface in the Π -plane (from Karafillis *et al.* 1993).

Isotropic yield surfaces lying between the bounds defined by von Mises' yield surface and Tresca's yield surface can be mathematically described by **Hosford's 1972 criterion**. His proposal is a modification of the von Mises' mathematical description of a yield surface, where an exponent other than 2 is used:

$$(\hat{\sigma}_1 - \hat{\sigma}_2)^{2a} + (\hat{\sigma}_2 - \hat{\sigma}_3)^{2a} + (\hat{\sigma}_3 - \hat{\sigma}_1)^{2a} = 2\sigma_F^{2a} \quad (2-12)$$

with a integer >1 , $\hat{\sigma}_1, \hat{\sigma}_2, \hat{\sigma}_3$ the principal values of the deviatoric stress tensor $\hat{\sigma}$ and σ_F the yield stress under uniaxial tension. This relation is equivalent to von Mises' equation when $a=1$ and to Tresca's equation when $a=\infty$. Intermediate values of a describe all the yield surfaces lying between the two proposals (Figure 2-5). Equation (2-12) is identical to relation "Karafillis 1993 (a)" in Table 2 if $\hat{\sigma}$ is substituted by \underline{s} .

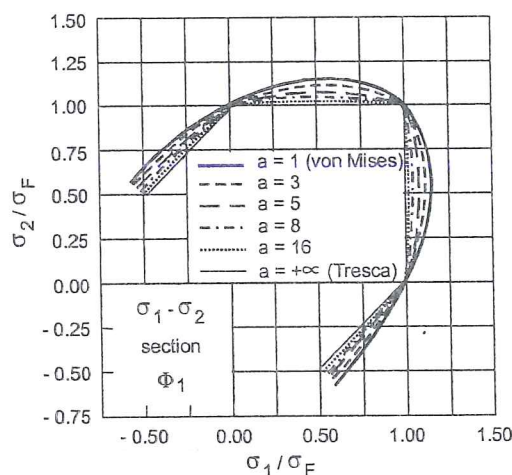


Figure 2-5 Different isotropic yield surfaces between the von Mises' yield surface and the lower bound (Tresca), sections in principal stress plane (from Karafillis *et al.* 1993).

Law Name	Description	Characteristics	References
Barlat 1989	$A K_1 + K_2 ^a + A K_1 - K_2 ^a + (2 - A) 2K_2 ^a = 2\sigma_F^a$ $K_1 = (\sigma_x + h\sigma_y)/2$ $K_2 = \sqrt{[(\sigma_x - h\sigma_y)/2]^2 + (p\sigma_y)^2}$	Generalization of isotropic Hosford's (1972) equation with a shear term, defined by 4 parameters, a, h, p, A plane stress case.	Vial 1997, Barlat & Lian 1989, Berg <i>et al.</i> 1998, Moshfegh <i>et al.</i> 1998, Andersson <i>et al.</i> 1999.
Barlat 1991	$ s_1 - s_2 ^a + s_2 - s_3 ^a + s_3 - s_1 ^a = 2\sigma_F^a$ <p>with $\underline{s} = \underline{L} \underline{\sigma}$</p> $\underline{L} = \begin{bmatrix} (c_2 + c_3)/3 & -c_3/3 & -c_2/3 & 0 & 0 & 0 \\ -c_3/3 & (c_3 + c_1)/3 & -c_1/3 & 0 & 0 & 0 \\ -c_2/3 & -c_1/3 & (c_1 + c_3)/3 & 0 & 0 & 0 \\ 0 & 0 & 0 & c_4 & 0 & 0 \\ 0 & 0 & 0 & 0 & c_5 & 0 \\ 0 & 0 & 0 & 0 & 0 & c_6 \end{bmatrix}$	Generalization of isotropic Hosford's (1972) equation with a shear term, defined by 6 anisotropy coefficients c_1 to c_6 + exponent m adapted for general stress state and orthotropic symmetric material. The 4 th order tensor can be represented by a 6x6 matrix in the axis of orthotropic symmetry (RD, TD, ND).	Barlat <i>et al.</i> 1991, Hayashida <i>et al.</i> 1995, Suh <i>et al.</i> 1996, Vegter <i>et al.</i> 1999.
Karafillis 1993	$\Phi_1 = s_1 - s_2 ^{2a} + s_2 - s_3 ^{2a} + s_3 - s_1 ^{2a} = 2\sigma_F^{2a}$ $\Phi_2 = s_1^{2a} + s_2^{2a} + s_3^{2a} = \frac{2^{2a} + 2}{3^{2a}} \sigma_F^{2a}$ $\Phi = (1 - C)\Phi_1 + C \frac{3^{2a}}{2^{2a-1} + 1} \Phi_2 = 2\sigma_F^{2a}$ $\underline{s} = \underline{L} \underline{\sigma} \text{ with } \underline{L} \text{ tensor 4}^{th} \text{ order}$	Generalization of Barlat's 91 work to non orthotropic material.	Karafillis & Boyce 1993, Andersson <i>et al.</i> 1999, Barlat <i>et al.</i> 1997.
Barlat 1997	$\Phi = A s_1 - s_2 ^a + B s_2 - s_3 ^a + C s_3 - s_1 ^a = 2\sigma_F^a$ <p>with \underline{s} and \underline{L} defined as in Barlat 1991.</p>	Extension of Barlat 1991 to model high pure shear yield stress and to better fit r_0 and r_{90} (plane stress case).	Barlat <i>et al.</i> 1997, Vegter <i>et al.</i> 1999.

s_1, s_2, s_3 = eigenvalues of tensor \underline{s}
 $\underline{\sigma}$ = stress tensor in orthotropic axes
 \underline{L} = linear operator
 $\sigma_x, \sigma_y, \sigma_{xy}$ = stress components on the orthotropic axes
 σ_F = uniaxial plastic stress in a reference direction

Table 2 Barlat's and Karafillis' models.

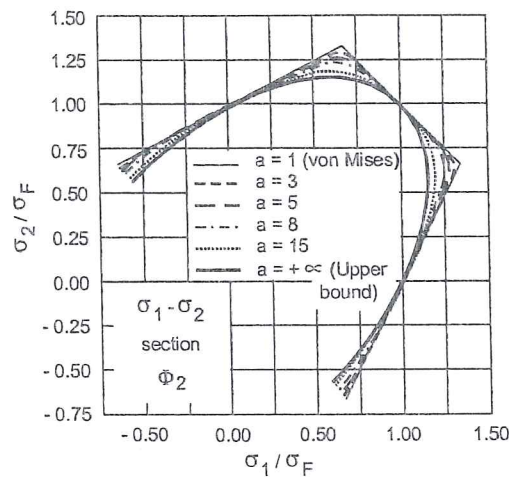


Figure 2-6 Different isotropic yield surfaces between the von Mises' yield surface and the upper bound : sections in principal stress plane (from Karafillis *et al.* 1993).

In fact, the surfaces lying between von Mises' yield surface and the upper bound (Figure 2-6) are described by "Karafillis 1993 (b)" in Table 2 if \underline{s} is substituted by $\underline{\hat{\sigma}}$. When $a=1$ the yield surface corresponds to von Mises' yield surface whereas when $a=\infty$ the upper bound yield surface is recovered. So to describe a generic isotropic yield surface lying between the lower bound and the upper bound, a generalized mathematical relation mixing Karafillis 1993 relations (a) and (b) in Table 2 is needed. It is the goal of relation (c) where the constant C belong to $[0,1]$. If $a=15$ is chosen, Φ_1 and Φ_2 describe yield surfaces very close to the lower and the upper bound respectively. By varying the value of the mixing factor C , a family of yield surfaces is created which spans the space between the 2 bounds, set by the selection of a (Figure 2-7).

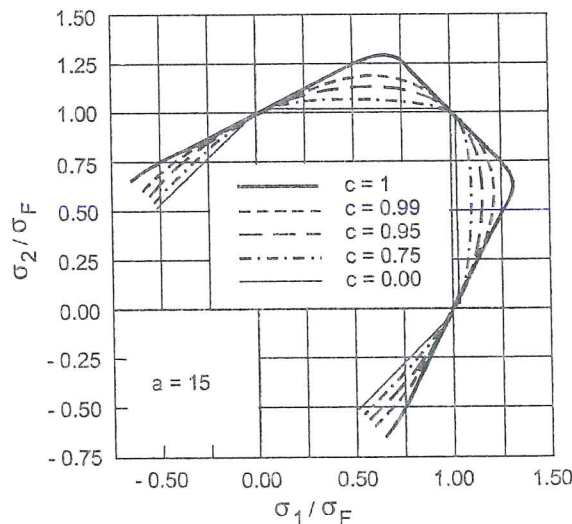


Figure 2-7 Different isotropic yield surfaces between the lower bound (Tresca) and the upper bound : sections in principal stress plane (from Karafillis *et al.* 1993).

Barlat *et al.* 1991 use a linear transformation of the 6 components of a stress state (Barlat 1991b, Table 2). The obtained transformed stress state is then used in Hosford's 1972 yield criterion (2-12). The 6 parameters describing anisotropy can be deduced from uniaxial yield stresses measured at 0°, 45°, 90° from the rolling direction. The exponent a can take any real value larger than 1 but practically, a should be larger than 6, depending on the anisotropy induced by texture and on the crystal type. In fact, a can be tuned to optimize the predictions of the yield locus shape.

Barlat's 1989 work already contains the same type of approach but is limited to plane stress state (see Table 2). This formulation has the advantage of clearly showing the effect of the shear component which modifies the sections of the yield locus (Figure 2-8, Figure 2-9, Figure 2-10). The 4 parameters A, h, p, a of Barlat's 1989 model are determined as explained by Barlat & Lian 1989 or Berg *et al.* 1998: $a=6$ for b.c.c. metals; $a=8$ for f.c.c. metals (from numerous polycrystal model comparisons)

$$A = 2 - 2\sqrt{\frac{r_0}{1+r_0} \frac{r_{90}}{1+r_{90}}} \quad h = \sqrt{\frac{r_0}{1+r_0} \frac{r_{90}}{1+r_{90}}} \quad (2-13)$$

$$p = \frac{\sigma_F}{\tau} \left(\frac{2}{2A + 2^a(2-A)} \right)^{1/a} \quad (2-14)$$

where σ_F is the yield stress in uniaxial tension, τ is the yield stress for pure shear. In practice, p varies since the ratio $\frac{\sigma_F}{\tau}$ is not a constant function of the equivalent strain. This affects the shape of the yield surface as demonstrated by Berg *et al.* 1998. It is worth mentioning that Barlat 1991 does not reduce to Barlat 1989 in the plane stress case because the linear transformations of stresses are different in these two cases.

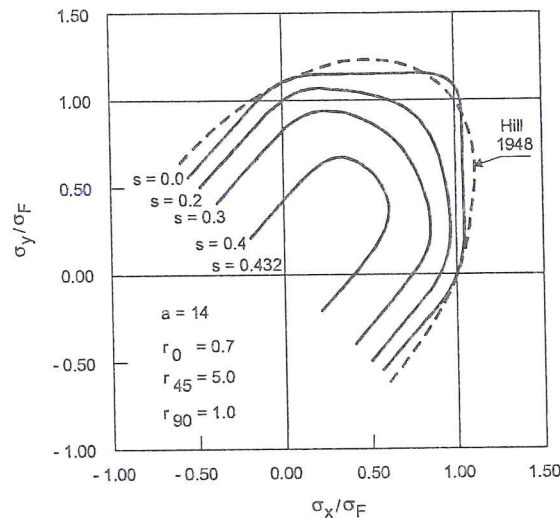


Figure 2-8 Plane stress yield surface proposed by Barlat & Lian 1989 where $a=14$, A, h, p are calculated with $r_0=0.7, r_{90}=1, r_{45}=5$ and $S = \sigma_{xy} / \sigma_F$; (material containing 50% brass texture and 50% of randomly distributed grains), adapted from Barlat & Lian 1989.

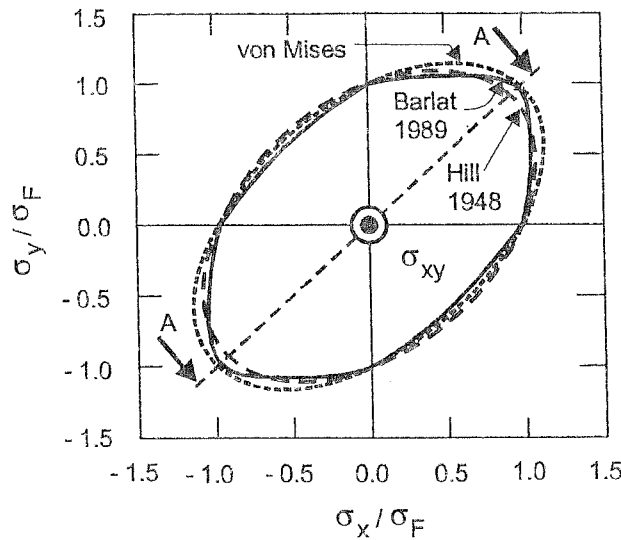


Figure 2-9 Comparison of yield surfaces of Al 2024 aluminium alloy for $\sigma_{xy} = 0$ (from Berg *et al.* 1998).

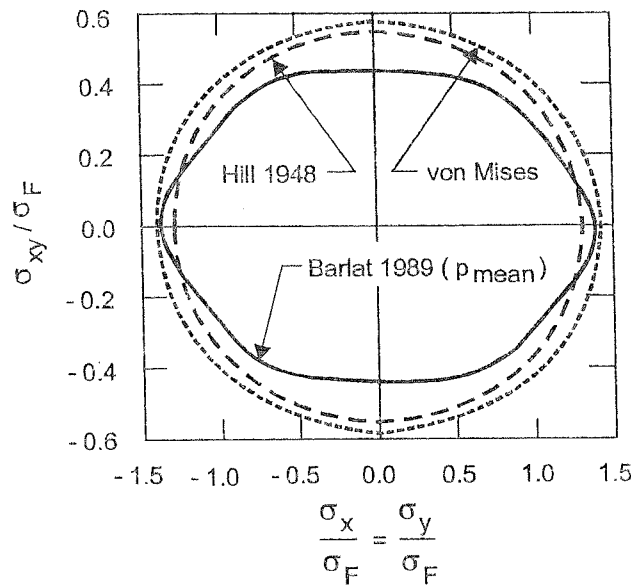


Figure 2-10 Cross section A_A of the yield surfaces of Figure 2-9, (from Berg *et al.* 1998).

For anisotropic material, Barlat 1991 as well as Karafillis *et al.*, 1993 consider a tensor \underline{s} , resulting of a linear transformation \underline{L} of the actual stress tensor $\underline{\sigma}$. In the case of isotropic material, this linear transformation simply yields the deviatoric stress tensor of the actual material stress state. This explains why, in the general anisotropic case, Karafillis calls the transformed tensor \underline{s} “*isotropic plasticity equivalent deviatoric stress tensor*”. Then, as in Barlat’s 1991 proposal, Karafillis introduces his transformed tensor \underline{s} in an isotropic yield criterion. Of course he chooses the general one described above. The fourth order tensor \underline{L} used by

Karafillis to transform the stress is more flexible than the simple choice made by Barlat and can be associated with material symmetries which range from the lowest level of triclinic symmetry to the highest level of full symmetry (Table 3).

Material symmetry	Rotations which leave \underline{L} invariant	Number of independent elements of \underline{L}
Triclinic	No rotation	15
Monoclinic	R_2^π	8
Orthotropic	R_1^π, R_2^π	6
Trigonal	$R_3^{2\pi/3}, R_1^\pi$	4
Tetragonal	$R_3^{\pi/2}, R_1^\pi$	4
Transversely isotropic	all R_3^ϕ, R_1^π	3
Cubic	$R_1^{\pi/2}, R_2^{\pi/2}, R_3^{\pi/2}$	2
Isotropic	All rotations	1

R_i^ϕ denotes a rotation about the i -axis by the angle ϕ .

Table 3 Characteristics of \underline{L} tensor according to material symmetry from Karafillis *et al.* 1993.

This provides a potential for the representation of any anisotropic state of the material. More details on symmetry properties and constraints applied to \underline{L} can be found in Karafillis *et al.* 1993. Finally, for orthotropic materials, 3 uniaxial tensile tests of specimens cut at 0°, 45°, 90° with respect to rolling direction allow to completely determine C and \underline{L} . Remark that, in this orthotropic case, Karafillis' transformation tensor \underline{L} reduces to Barlat's 1991 (Table 2). Figure 2-11 and Figure 2-12 show Karafillis' results compared with other models and experiments.

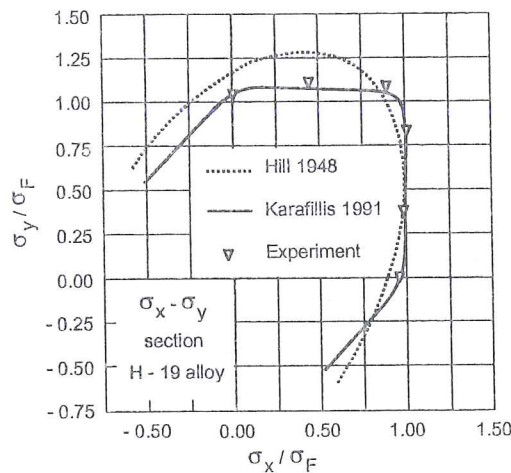


Figure 2-11 The yield surface of the H-19 can stock aluminum alloy in the orthotropic stress axes (from Karafillis *et al.* 1993).

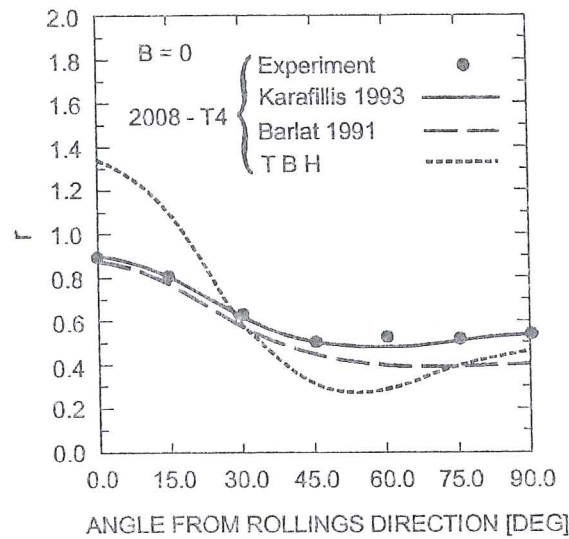


Figure 2-12 Lankford coefficient as a function of the angle with the rolling direction for 2008-T4 aluminum alloy, TBR = Taylor 1938-Bishop & Hill 1951 polycrystal model, (from Karafillis *et al.* 1993).

Hill 1948 (Table 1), Barlat 1989 and Karafillis 1993 (Table 2) were implemented in the commercial code LS-DYNA3D. Andersson *et al.* 1999 use it to simulate deep drawing tests of aluminum sheets and compare their FEM results to experiments. Their results show that Karafillis' model yields the best agreement with the experimental results and that CPU times are in the same range: Hill 1948 =1, Barlat 1989 =1.5 and Karafillis 1993 =1.1. Andersson *et al.* 1999 describe also the optimization code, they have developed, to identify Karafillis 1993 parameters from tensile tests in 3 different directions.

Barlat's 1997 proposal (Table 2) generalizes his 1991 model, as Barlat has checked that the additional coefficient C proposed by Karafillis is an isotropic constant which does not help to reproduce the behavior of an Al-Mg sheet with 80% cold reduction. For the plane stress case, only 6 independent coefficients characterize anisotropy. They can be deduced from 4 tests: uniaxial tension at 0° , 45° , 90° to the rolling direction and equal biaxial bulge test. The proposed yield surface appears to fit nicely to experiments (Figure 2-13). However, if it is used to predict r ratios, it agrees with r_0 and r_{90} , but r_{45} is significantly under-estimated. This observation suggests that an additional parameter could be introduced in the formulation to accommodate r_{45} .

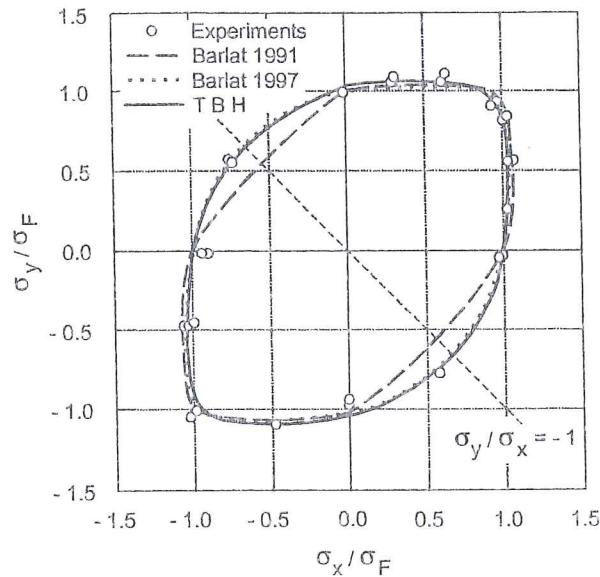


Figure 2-13 Yield surface for material : Al-2.5%Mg, 150 μm grain size, 80% cold reduction before annealing; experiments and yield function predictions from 3 models: Taylor-Bishop-Hill polycrystal, Barlat 1991 and Barlat 1997 (from Barlat *et al.* 1997).

2.1.1.3. A polar-coordinate representation of an orthotropic yield locus

Ferron *et al.* 1994, Tourki *et al.* 1994, Tourki *et al.* 1996 investigate the form taken by the constitutive equations when orthotropic plasticity under plane stress is analyzed by using a polar coordinate representation of the yield surface in the principal stress space. They assume a parametric representation :

$$x_1 = \frac{\sigma_1 + \sigma_2}{2\sigma_b} = g(\theta, \beta) \cos \theta \quad x_2 = \frac{\sigma_1 - \sigma_2}{2\sigma_b} = g(\theta, \beta) \sin \theta \quad (2-15)$$

where σ_b is the equibiaxial yield stress, β is an angle defining the orientation of the principal axes of the stress tensor with respect to the in-plane material anisotropy axes, $g(\theta, \beta)$ represents the length of the radius for a point on the yield locus in (x_1, x_2) axes, θ is the polar angle associated with the above polar coordinate description. This formulation is an extension of the one proposed by Budiansky 1984 in case of planar isotropy where the angle β is immaterial.

Looking at orthotropic symmetry, convexity and consistency of the yield function, Ferron *et al.* 1994 propose a form of the $g(\theta, \beta)$ function. Then, they build a new criterion as an extension of Drucker's 1949 isotropic yield criterion expressed under plane stress in polar coordinate form. Their yield criterion for planar isotropy is :

$$(1-k)g(\theta)^6 = F(\theta) = (\cos^2 \theta + A \sin^2 \theta)^3 - k \cos^2 \theta (\cos^2 \theta - B \sin^2 \theta)^2 \quad (2-16)$$

where A and B are dimensionless and positive constants. In case of planar anisotropy, it becomes :

$$(1-k)^{m/6} g(\theta, \beta)^{-m} = F(\theta)^{m/6} + 2a \sin \theta \cos^{2n-1} \theta \cos 2\beta + b \sin^{2p} \theta \cos^{2q} 2\beta \quad (2-17)$$

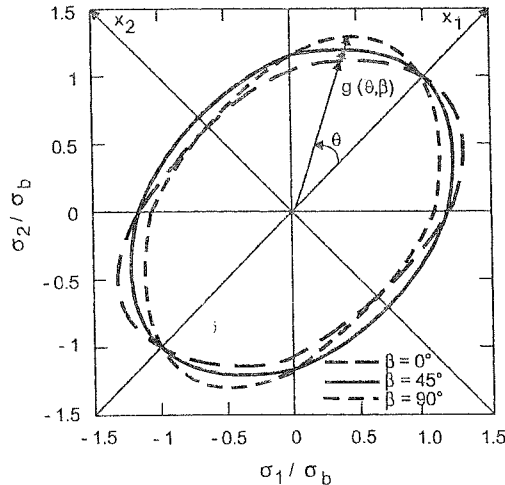


Figure 2-14 Polar coordinate representation of the yield surface in principal stress space (σ_1, σ_2) , the yield loci are parameterized by angle β , (from Ferron *et al.* 1994).

This yield function involves 9 parameters: the 3 parameters k, A, B introduced to account for planar isotropy and the 6 parameters m, n, p, q, a, b depicting the orientation dependence of yielding. Remark that Hill 1948 is retrieved with $k=0, m=2$ and $n=p=q=1$. The effect of increasing k from 0 to some positive value, defining the limit for convexity, is to produce a flattening of the yield locus near pure shear and plane strain tension/compression. One property of the yield function (2-17) is to be able to accommodate a ratio of equibiaxial yield stress to uniaxial yield stress independently of the measured r -value in uniaxial tension. Increasing the exponents n and p leads to a decrease of the width of the annulus generated by the yield locus in (σ_1, σ_2) space when β varies (see Figure 2-14).

In practice, according to Ferron *et al.* 1994, a good fit of experimental or theoretical crystallographic data is generally obtained with $m=n=p=2$ and $q=1$, which leaves 5 parameters to identify. The appendix of this article accurately describes the way to determine these 5 material parameters. The 3 parameters k, A, B of the isotropic yield criterion can be deduced from 3 measurements : pure shear yield stress, equibiaxial yield stress and Lankford coefficient. However a simplified approach using only uniaxial tension tests is available. For the anisotropic case, it is proposed first to determine k, A, B from a test performed for $\beta = \pi/4$, then to compute a and b from the experimental values of r_0 and r_{90} and of the parameters m, n, p, q .

Experimental validation for a mild steel is shown on Figure 1-2. Comparisons with Taylor-Bishop-Hill computations for a 2008-T4 aluminum alloy are presented on Figure 2-15, Figure 2-16, Figure 2-17. For this material, the parameters were identified as : $k=0.55$, $A=2.2$, $B=3.71$, $m=n=p=2$, $q=1$, $a=0.24$, $b=0.47$.

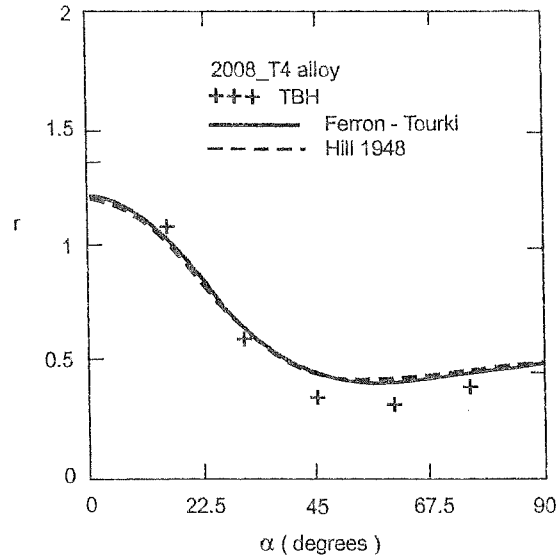


Figure 2-15 Orientation dependence of the Lankford coefficient for a 2008-T4 aluminum alloy according to Taylor-Bishop-Hill's approach, Hill's 1948 yield criterion or Ferron & Tourki's yield criterion (from Ferron *et al.* 1994).

These results confirm that shear or normal strains as well as stresses are well described by this model. Angle α characterizes the angle between the uniaxial tensile direction and the rolling direction.

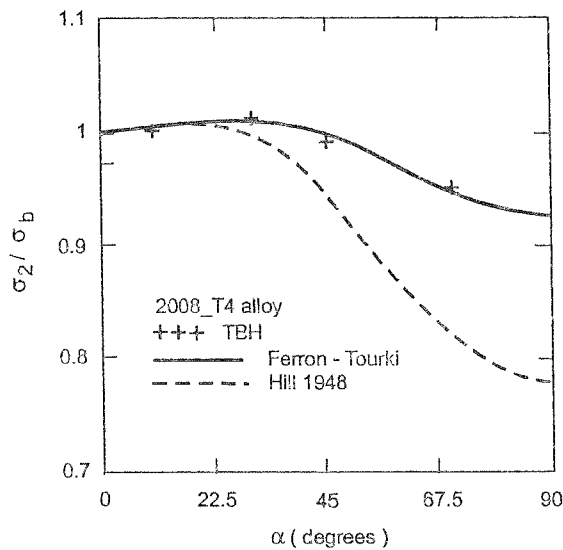


Figure 2-16 Orientation dependence of the normalized uniaxial yield stress for a 2008-T4 aluminum alloy according to Taylor-Bishop-Hill's approach, Hill's 1948 yield criterion or Ferron & Tourki's yield criterion (from Ferron *et al.* 1994).

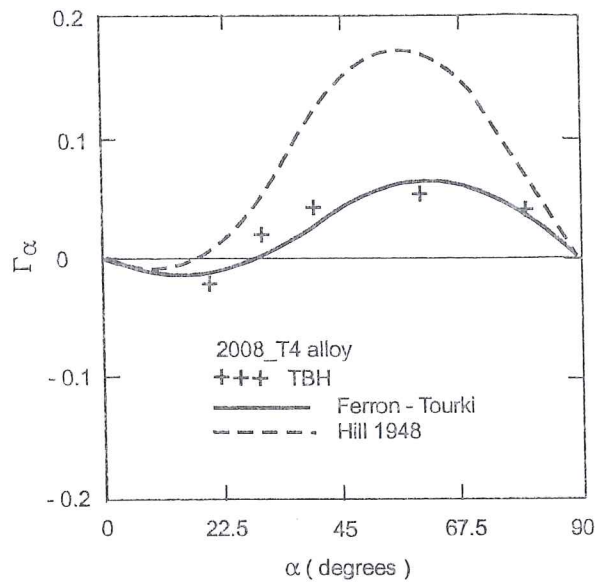


Figure 2-17 Orientation dependence of the shear parameters $\Gamma_\alpha = \dot{\epsilon}_{12} / \dot{\epsilon}_{11}$ in uniaxial tension for a 2008-T4 aluminum alloy according Taylor-Bishop-Hill's approach, Hill's 1948 yield criterion or Ferron & Tourki's yield criterion (from Ferron *et al.* 1994).

2.1.4. Vegter's approach

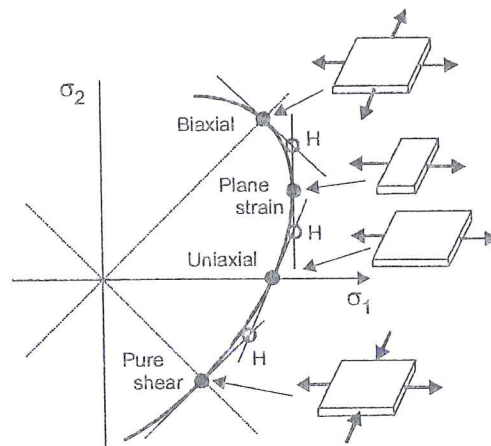


Figure 2-18 Vegter's yield locus in the principal stress space, reference points (black circles) defined by experiments and hinge points (white circle), adapted from Carleer *et al.* 1997

Vegter's approach (Carleer *et al.* 1997, Vegter 1998, Vegter *et al.* 1999a,b, Pijlam *et al.* 1998) proposes a yield criterion directly based on data of the pure shear test, the uniaxial test, the plane strain test and the biaxial test. Figure 2-18 clearly summarizes this criterion for a planar isotropic material behavior. A complete yield surface is described by 12 Bezier interpolation functions. When σ_1 and σ_2 are defined in such a way that $\sigma_1 \geq \sigma_2$, only the part of the surface beneath the line $\sigma_1 = \sigma_2$ is needed. As

the material is assumed to behave identically in tension and compression, the part of the surface beneath the line $\sigma_1 = -\sigma_2$ can be derived from the part above that line. As a result, the complete yielding of the material can be described using the measurements for a quarter of the yield surface. Vegter's yield function is restricted to plane stress state. It is defined as :

$$\sigma_{veg}(\sigma_x, \sigma_y, \sigma_{xy}) - \sigma_{yield} = 0 \quad (2-18)$$

where σ_{veg} is a kind of equivalent stress depending on the stress components in orthotropic axes $\sigma_x, \sigma_y, \sigma_{xy}$ and σ_{yield} is the yield stress.

In case of planar isotropic material behavior, σ_{yield} is the uniaxial yield stress σ_F . The second order Bezier interpolations allow to describe the normalized yield surface.

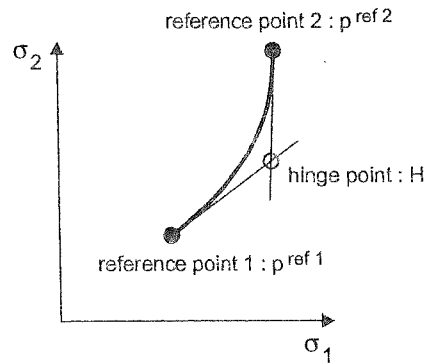


Figure 2-19 Bezier curve in Vegter's yield locus, adapted from Carleer *et al.* 1997.

For a part going from reference point 1 to reference point 2 with hinge point H (Figure 2-19), one has :

$$\frac{\sigma_1}{\sigma_{veg}} = (1-\beta)^2 p_1^{ref1} + 2\beta(1-\beta)p_1^{hinge} + \beta^2 p_1^{ref2} \quad (2-19a)$$

$$\frac{\sigma_2}{\sigma_{veg}} = (1-\beta)^2 p_2^{ref1} + 2\beta(1-\beta)p_2^{hinge} + \beta^2 p_2^{ref2} \quad (2-19b)$$

where σ_1, σ_2 are principal stresses, β is a curvilinear coordinate increasing from 0 to 1 and representing the location on the curve between the reference points, p_i^{refj} and p_i^{hinge} are respectively the components i of the reference point j and the hinge point. Both equations (2-19a) and (2-19b) give an expression for σ_{veg} . Equating these expressions allows to find β as a solution of a second order equation. This solution is chosen to satisfy the condition $0 \leq \beta \leq 1$. The expression of σ_{veg} is then found by substituting β into (2-19a) or (2-19b).

For planar anisotropy, the 4 tests (pure shear, uniaxial, plane strain and biaxial tests) are performed for directions of $0^\circ, 45^\circ, 90^\circ$ from the Rolling Direction and an

interpolation function $\underline{p}^{ref}(\alpha)$ is used to find interpolated reference points from the measured points $\underline{p}_\alpha^{ref}$:

$$\underline{p}^{ref}(\alpha) = \frac{\underline{p}_0^{ref} + 2\underline{p}_{45}^{ref} + \underline{p}_{90}^{ref}}{4} + \frac{\underline{p}_0^{ref} - \underline{p}_{90}^{ref}}{2} \cos 2\alpha + \frac{\underline{p}_0^{ref} - 2\underline{p}_{45}^{ref} + \underline{p}_{90}^{ref}}{4} \cos 4\alpha \quad (2-20)$$

Here α is the angle of the principal stresses to the Rolling Direction. The function $\underline{p}^{ref}(\alpha)$ can be regarded as a Fourier series with only 3 terms; it can be extended if orthotropic properties are not respected. So, with the new interpolated reference points, Vegter's yield criterion can be constructed.

This description of the yield locus shape is coupled with a strain hardening model based on the development of the dislocation cell structure with strain (Bergström 1969, see section 3.5.1.).

Figure 1-1 and Figure 1-4 show the quality of this model. However its experimental identification is quite expensive: pure shear, uniaxial, plane strain and biaxial tests in one direction in case of planar isotropy or in 3 directions for planar anisotropy. As pointed by Vegter *et al.* 1999b, it is important to reach high experimental accuracy and to correct experimental results if non homogeneity or non isothermal conditions happen. Piljman *et al.* 1999 use FEM to study a multiaxial test equipment and demonstrate that the deformation state cannot be directly related to the displacements of the clamps.

An important characteristic of Vegter's model is its flexibility. For instance, Figure 2-20 shows a variant called Vegter-flat, in which the reference point corresponding to plane strain is very close to the hinge point located between plane strain and biaxial states. The agreement with the measured Forming Limit Diagram shown on Figure 2-21 is significantly improved. This last effect shows the extreme sensitivity of the FLD prediction to the shape of the yield locus.

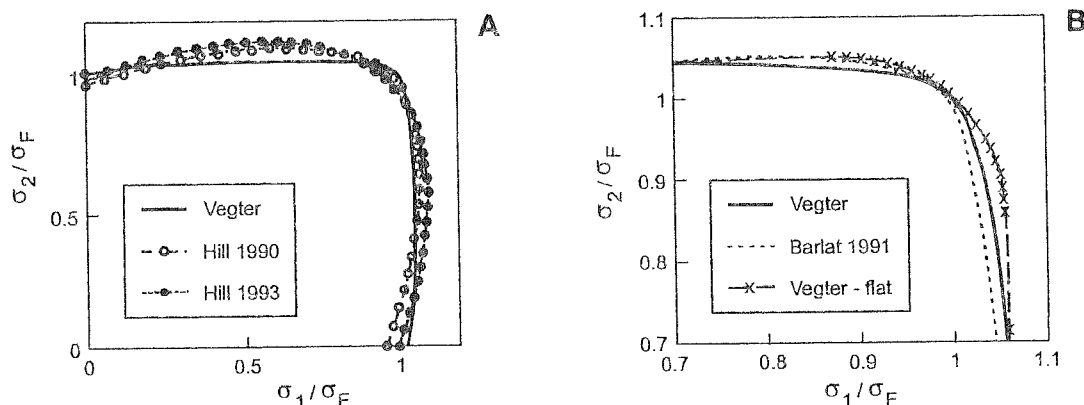


Figure 2-20 Comparison of different yield loci descriptions for Al-6000 (from Vegter *et al.* 1999).

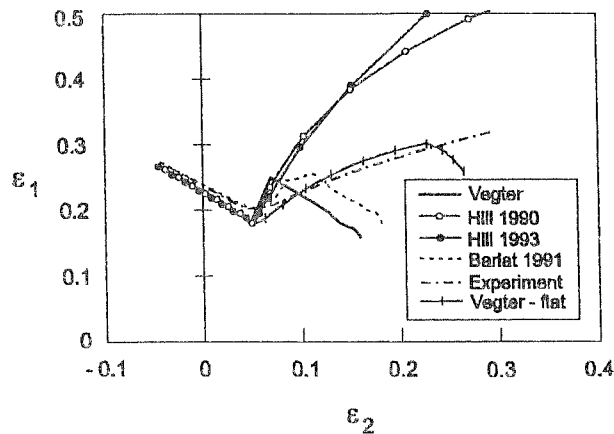


Figure 2-21 FLD predictions for the Al-6000 (90° to RD) using different yield criteria and comparison with experiments (from Vegter *et al.* 1999).

2.1.5. Summary

To conclude this section devoted to the initial shape of yield loci, it can be said that scientists have found new formulations of anisotropic yield loci that seem closer to experimental evidence. However the number of parameters used to determine these new criteria increases with their flexibility. So, according to the requested accuracy, the available experimental equipment and the criteria implemented in the used FEM code, one has to make his own choice to describe anisotropic material behavior.

The Table 4 summarizes the parameter number and the experimental tests necessary to identify the yield loci listed above, in their initial shape, without hardening description. Note that some tests give different information like yield stress and Lankford coefficient for a uniaxial tensile test. According to the parameters identification process and to the model purpose and flexibility, both results are required or just one is used. Choosing stress value or Lankford coefficient to identify the model parameters is not equivalent. Without surprise, one can provide two sets of parameters for one model starting from identical tests. One set of parameters recovers stress information and the other strain information. This apparent difficulty comes from the approximations of these phenomenological models, unable to reproduce physics with perfect accuracy.

Yield loci	Parameter number	Experiments	Described state
Hill 1948	6 parameters	3 uniaxial tests 0; 45; 90°	3D State
Hill 1979	7 parameters	3 uniaxial tests + plane strain test	3D State
Hill 1990	5 parameters	3 uniaxial tests + equibiaxial tensile test	Plane Stress State
Hill 1993	5 parameters	2 uniaxial tests 0;90° + equibiaxial tensile test	Plane Stress State
Karafillis 93	6 + 2 parameters	3 uniaxial tests	3D State
Barlat 1989	4 parameters	2 uniaxial tests + pure shear test	Plane Stress State
Barlat 1991	6 + 1 parameters	3 uniaxial tests	3D State
Barlat 1997	6 + 1 parameters	3 uniaxial tests + equibiaxial bulge	Plane Stress State
Vegter 1998	12 parameters	12 tests: pure shear test, uniaxial test, plane strain test, equibiaxial test repeated in 0; 45; 90°	Plane Stress State

Table 4 - Phenomenological yield loci for orthotropic case; initial shape description.

2.2. Updated yield loci

It is a fundamental issue of the physics of metal plasticity that any particular yield surface is the product of microstructural and textural evolutions imposed by the specific strain path or loading history undergone by the material element of interest. Starting with a given material piece, the initial shape of the yield locus is easily identified by stress states that initiate plastic strains, as the changes in texture during such tests will be imperceptible. It is quite harder to find a general agreement on how to measure an updated yield locus. One possibility used by a lot of authors (Vial *et al.* 1983, Tourki *et al.* 1996, Kuwabara & van Bael 1999) is to determine work contours instead of updated yield loci. They generate a new locus by joining stress states - for example (σ_1, σ_2) points - for which an equal amount of (plastic) work has been spent per unit volume. Usually, radial stress paths (i.e. constant σ_1 / σ_2 ratio) are chosen. As stated by Hill 1993, it cannot be a yield locus when it connects states with different textures. In fact, these different stress states cannot possibly lie on a neutral loading path.

In practice, the initial phenomenological yield criteria described in the preceding section must be associated with a hardening rule to model plastic deformation beyond plasticity initiation. As described in next section, these hardening models

depend on internal variables and allow to compute the new size, shape and position of the yield locus. So, the updated yield locus must connect points representing stress states characterized by identical values of internal variables. For simple macroscopic hardening models, the *plastic work* is often taken as the only internal state variable, which validates the use of the work contours mentioned above, even though this surface connects stress points related to different material textures. This plastic work is easily computed by:

$$W^P = \int \underline{\sigma} : d\underline{\varepsilon}^P \quad (2-21)$$

Another simple approach is to use an *integrated equivalent plastic strain* as the only internal variable. So, the updated yield locus is related to stress states with identical integrated plastic strain. Let us note that this *integrated equivalent plastic strain* is computed by :

$$\varepsilon_e^P = \int d\varepsilon_{eq}^P \text{ with } d\varepsilon_{eq}^P = \frac{2}{\sqrt{3}} \left(\frac{1}{2} d\underline{\varepsilon}^P : d\underline{\varepsilon}^P \right)^{1/2} \quad (2-22)$$

This value should not be confused with the equivalent plastic strain:

$$\varepsilon_{eq}^P = \frac{2}{\sqrt{3}} \left(\frac{1}{2} \underline{\varepsilon}^P : \underline{\varepsilon}^P \right)^{1/2} \quad (2-23)$$

As pointed out by Khan & Huang 1995, for von Mises' yield locus, the *strain hardening hypothesis* ($\varepsilon_e^P =$ internal variable) and the *work hardening hypothesis* ($W^P =$ internal variable) are equivalent. For anisotropic yield loci, if the above definition of integrated equivalent plastic strain is used, the *strain hardening hypothesis* and the *work hardening hypothesis* are of course not equivalent. However, in general, the equivalence is retained because the definition of the integrated equivalent plastic strain is adapted : it is now computed by the integration of $\dot{\varepsilon}_{eqa}^P$, the *anisotropic equivalent plastic strain rate*, directly deduced from the plastic dissipation:

$$\sigma_{eqa} \dot{\varepsilon}_{eqa}^P = \sigma_{ij} \dot{\varepsilon}_{ij}^P \text{ with } \sigma_{eqa} = \sqrt{\sigma_{ij} L_{ijkl} \sigma_{kl}} \quad (2-24)$$

where tensor $\underline{\underline{L}}$ represents the material anisotropy when assuming that the yield locus can be expressed by a function

$$F_p = \sqrt{\sigma_{ij} L_{ijkl} \sigma_{kl}} - \sigma_p = 0 \quad (2-25)$$

This 4th order tensor $\underline{\underline{L}}$ can be directly deduced in Hill's approach or in some texture based yield locus (see chapter 6).

The $\underline{\underline{L}}$ tensor used in Barlat's or Karafillis' approaches (see Table 2) describes also the material anisotropy but does not fit with relation (2-25). The same notations were chosen however, because both tensors translate material anisotropy.

So, hereafter, $\dot{\epsilon}_{eq}^P$ represents the rate of the equivalent plastic strain given by (2-23) while $\dot{\epsilon}_{eqa}^P$ and σ_{eqa} are defined by (2-24) and L_{ijkl} by (2-25) since no more discussion on Barlat's or Karafillis' model appears. Note that, in presence of kinematic hardening, the stress is replaced by the overstress in σ_{eqa} .

For hardening approaches with strong microscopic roots, the equality of internal hardening state variables effectively implies that all the points connected by the yield locus are related to the same material state. This is closer to the microscopic concept of hardening and constitutes an incitement to measure actual updated yield loci rather than work contours.

Beyond the elastic-plastic transient zone (Aernoudt et al., 1987), the yield loci directly deduced from the measured updated material texture should be good approximations of the actual shape of updated yield loci. However their size often depends on isotropic hardening variables, which are a too crude representation of the reality.

In conclusion, this paragraph shows the prominent role of the hardening approach to determine updated yield locus.

References

- Aernoudt, E., Gil-Sevillano J. & Van Houtte, P. (1987) Constitutive Relations and Their Physical Basis, S.I. Andersen et al. Eds, RisØ National Laboratory, Roskilde, Denmark, 1-38.
- Andersson, A., Ohlsson C-A, Mattiasson, K. and Persson B. (1999) Implementation and Evaluation of the Karafillis-Boyce Material Model for Anisotropic Metal Sheets, Numisheet'99, 13-17 September 1999, 1, Besançon, France, 115-121.
- Arminjon, M., Bacroix, B., Imbault, D. and Raphanel, J.K. (1994) A fourth-order plastic potential for anisotropic metals and its analytical calculation from texture function, *Acta Mechanica*, **107**, 33.
- Banabic, D. (1996) Forming limit diagrams predicted by using the new Hill's yield criterion, *Proceedings of the 3rd Int. Conf. Numisheet'96 Numerical Simulation of 3-D Sheet Metal Forming Processes – Verification of Simulations with Experiments*, Lee, Kinzel, Wagoner Eds., the Ohio State University.
- Banabic, D. (1997) Sheet metal formability predicted by using the new Hill's yield criterion, *Advanced Methods in Materials Processing Defects*, Predeleanu M. & Gilormini P., 257-264.
- Barlat, F. (1987) Crystallographic texture, anisotropic yield surfaces and forming limits of sheet metal. *Materials Science and Engineering*, **91**, 55.
- Barlat, F. and Lian, J. (1989) Plastic behaviour and stretchability of sheet metals. Part 1 : a yield function for orthotropic sheets under plane stress conditions, *Int. J. of Plasticity*, **5**, 51.
- Barlat, F., Lege, D.J., Brem, J.C. (1991) A six-component yield function for

- anisotropic materials. *Int. J. of Plasticity*, 7, 693.
- Barlat, F., Becker, R.C., Hayashida, Y., Maeda, Y., Yanagawa, M., Chung, K., Brem, J.C., Lege, D.J., Matsui, K., Murtha, S.J., Hattori, S. (1997) Yielding description for solution strengthened aluminium alloys, *Int. J. of Plasticity*, 13/4, 385-401.
- Berg, H., Hora, P., Reissner, J. (1998) Simulation of sheet metal forming processes using different anisotropic constitutive models, *Simulation of materials processing : theory, methods and applications*, Huetink & Baaijens Eds, Balkema.
- Bergstrom, Y. (1969/70) A dislocation model for the stress strain behaviour of polycrystalline α -Fe with special emphasis on the variation of the densities of mobile and immobile dislocations, *Mat. Sci. Eng.*, 5, 179-192.
- Bishop, J.W.F., Hill, R. (1951) A theory of the plastic distortion of a polycrystalline aggregate under combined stresses and a theoretical derivation of the plastic properties of polycrystalline face-centered metals, *Philos. Mag.*, 42, 414-427, 1298-1307.
- Bridgman, P.W. (1923) The compressibility of thirty metal as a function of pressure and temperature, *Proc. Am. Acad. Arts Sci*, 58, 165.
- Bridgman, P.W. (1952) Studies in large plastic flow and fracture. *Metallurgy and Metallurgical Engineering Series*, New-York, McGraw-Hill.
- Budianski, B. (1984) Anisotropic plasticity of plane-isotropic sheets, *Mechanics of Material Behaviour*, Dvorak G.J. and Shield R.T. Eds, Elsevier, 15.
- Carleer, B.D., Meinders, T., Pijlman, H.H., Huetink, J., Vegter, H. (1997) A planar anisotropic yield function based on multi axial stress states in finite elements, *Computational plasticity – fundamentals and applications*, Owen, Onate and Hinton Eds.
- Drucker, D.C. (1951) A more fundamental approach to plastic stress-strain relations, in *Proc. First US Nat. Congr. Applied Mechanics*, ASME, New-York, 487-491.
- Ferron, G., Makkouk, R., Morreale J. (1994) A parametric description of orthotropic plasticity in metal sheets. *Int. J. of Plasticity*, 10/5, 431-449.
- Gurson, A.L. (1977) Continuum theory of ductile rupture by void nucleation and growth. *J. Engng. Materials Technology* 99, 2-15.
- Hayakawa, K., Murakami, S., (1998) Space of damage conjugate force and damage potential of elastic-plastic-damage materials, *Damage Mechanics in Engineering Materials*, Voyiadjis, G.Z., Ju, J.W., Chaboche J.L. Eds, 27-44.
- Hayashida, Y., Maeda, Y., Matsui, K., Hashimoto, N., Hattori S., Yanagawa M., Chung, K., Barlat F., Brem J.C., Lege D.J., Murtha, S.J. (1995) FEM analysis of punch stretching and cup drawing tests for aluminium alloys using a planar anisotropic yield function, *Simulation of Materials Processing : Theory, Methods and Applications*, Shen&Dawson Eds, Balkema, 717.
- Hecker, S.S. (1976) Experimental studies of yield phenomena in biaxially loaded metals, in Strick-Lin, J.A., Saczalski, K.J. Eds, *Constitutive equations in viscoplasticity : computational and engineering aspects*, ASME, New-York, 1-33.
- Hill, R. (1948) A theory of the yielding and plastic flow of anisotropic materials.

- Proc. Royal Soc. London, A193, 281-297.
- Hill, R. (1990) Constitutive Modelling of Orthotropic Plasticity in Sheet Metals, *J. Mech. Phys. Solids*, 38/3, 405-417.
- Hill, R. (1993) A user-friendly theory of orthotropic plasticity in sheet metals, *Int. J. Mech. Sci.*, 35/1, 19-25.
- Holt, D.L. (1970) Dislocation cell formation in metals, *J. Appl. Phys.*, 41, 3197-3201.
- Hosford W.F. (1972) A generalized isotropic yield criterion, *J. Appl. Mech. Trans. ASME*, 39, 607-609.
- Karafillis, A.P., Boyce, M.C. (1993) A general anisotropic yield criterion using bounds and a transformation weighting tensor, *J. Mech. Phys. Solids*, 41/12, 1859-1886.
- Khan A.S., Huang S. (1995) Continuum theory of plasticity, Wiley & Sons Eds.
- Kobayashi, S., Caddell, R.M. and Hosford, W.F. (1985) Examination of Hill's latest yield criterion using experimental data for various anisotropic sheet metals. *Int. J. of Mech. Sci.*, 27, 509.
- Kuwabara, T., Van Bael, A. (1999) Measurement and Analysis of Yield Locus of Sheet aluminium Alloy 6XXX, Numisheet'99, 13-17 September 1999, 1, Besançon, France, 85-90.
- Mahmudi (1995) Yield loci of anisotropic aluminium sheets, *Int. J. of Mech. Sci.*, 37, 919.
- Mendelson A. (1968) Plasticity : Theory and Application, MacMillan, New-York, 87.
- Moshfegh, R., Nilsson, L., Jensen M.R., Danckert J. (1998) Finite Element Simulation of the Hydromechanical Deep Drawing Process, 1st ESAFORM Conference on Material Forming, Sophia-Antipolis (France), 17-20 March 1998, J.L. Chenot, J.F. Agassant, P. Montmittonet, B. Vergnes, N. Billon Eds.
- Phillips, A. (1986) A review of quasi-static experimental plasticity and viscoplasticity, *Int. J. of Plasticity*, 2, 315.
- Pijlman, H.H., Brinkman J., Huetink, J., Vegter, H. The Vegter Yield Criterion Based on Multi-Axial Measurements, Numisheet'99, 13-17 September 1999, vol. 1, Besançon, France, 109-114.
- Suh, Y.S., Saunders, F.I., Wagoner, R.H. (1996) Anisotropic yield functions with plastic-strain induced anisotropy, *Int. J. of Plasticity*, 12/3, 417-438.
- Taylor, G.I. (1938) Plastic strains in metals, *J. Inst. Metals*, 62, 307-324.
- Tourki, Z., Makkouk R., Zeghloul A., Ferron G. (1994) Orthotropic plasticity in metal sheets : a theoretical framework, *J. Mater. Process. Technol.*, 45, 453-458.
- Tourki, Z., Zeghloul, A., Ferron, G. (1996) Sheet metal forming simulations using a new model for orthotropic plasticity, *Computational Materials Science*, 5, 255-262.
- Van Bael, A. (1994) Anisotropic yield loci derived from crystallographic data and their application in finite element simulations of plastic forming processes, proefschrift voorgedragen tot het behalen van het doctoraat in de toegepaste wetenschappen, Katholieke Universiteit Leuven.
- Vegter, H., An Y., Pijlman J.J., Carlee B.D., Huetink J. (1998), Advanced Material

- Models in Simulation of Sheet Forming Processes and Prediction of Forming Limits, *1st ESAFORM Conference on Material Forming*, Sophia Antipolis, Chenot, Agassant, Montmitonnet, Vergnes, Billon Eds.
- Vegter, H., An Y., Pijlman H.H., Huetink J. (1999a), Different approaches to describe the plastic material behaviour of steel and aluminium-alloys in sheet forming, *2nd ESAFORM Conference on Material Forming*, Guimaraes, Portugal, Covas J.A. Ed.
- Vegter, H., An Y., Pijlman H.H., Huetink J. (1999b), Advanced Mechanical Testing on Aluminium Alloys and Low Carbon Steels for Sheet Forming, Numisheet'99, 13-17 September 1999, **1**, Besançon, France, 3-8.
- Vial, C., Caddell, R.M. and Hosford, W.F. (1983) Yield loci of anisotropic sheet metals, *Int. J. of Mech. Sci.*, **25**, 899.
- Vial-Edwards, C. (1997) Yield loci of FCC and BCC sheet metals, *Int. J. of Plasticity*, **13/5**, 521-531.
- Wagoner, R.H. (1980) Measurement and analysis of plane strain work hardening, *Metall. Trans. A*, **11A**, 165.

3. HARDENING MODELS

3.1. Basic knowledge on crystal events

Ewing & Rosenhain 1900 have established that the plastic deformation of a crystal occurs by slipping on some crystallographic planes (*slip or glide planes*), by slipping in some crystallographic directions (*slip or glide direction*) or by twinning, another crystallographic phenomenon.

However, the elementary theoretical estimation of the shear strength of a perfect crystal given by Frenkel 1926 yields values of the order of $10^{-1} G$ (G =shear modulus of the crystal). Knowing that the observed shear strength is of the order of $10^{-6} \approx 10^{-4} G$, scientists have proposed the concept of crystal defects, called dislocations, that reduce the strength of the crystal. Figure 3-1 and Figure 3-2 present two basic types of dislocations, the edge and screw dislocations, and show the *dislocation line* AB. The motion of dislocations results in crystal shearing.

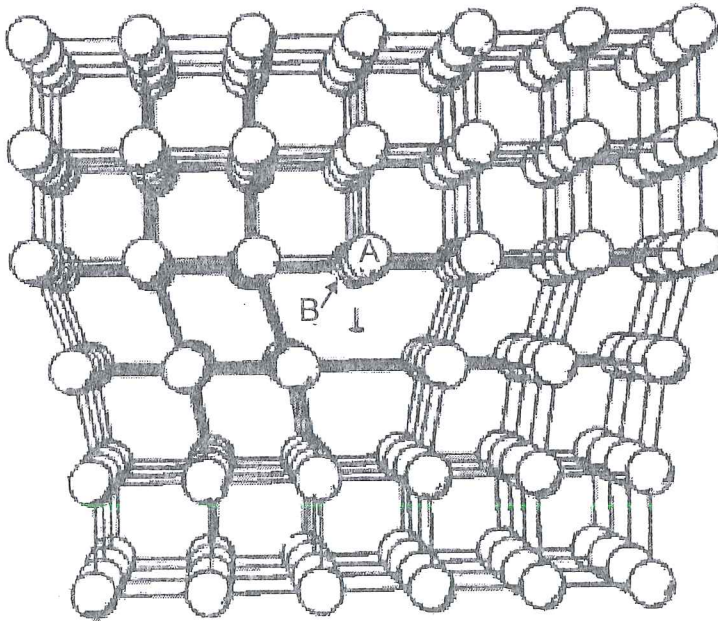


Figure 3-1 Edge dislocation (from Magnée, 1994).

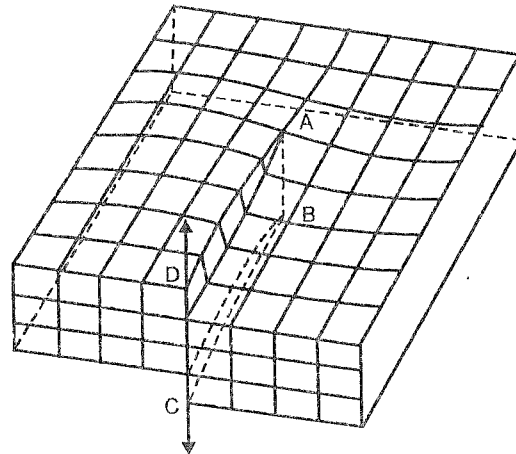


Figure 3-2 Screw dislocation (from Khan & Huang, 1995).

Burgers' vector \underline{b} is introduced to describe the slip direction of a dislocation. It is determined by Burgers' circuit, a closed path involving two lattice directions and surrounding the dislocation line (Figure 3-3).

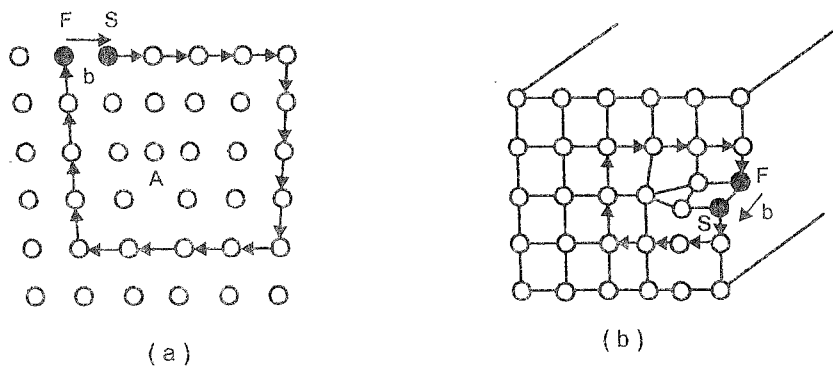


Figure 3-3 Burgers' circuit for edge (a) and screw (b) dislocation defining Burgers' vector \underline{b} (from Khan & Huang, 1995).

It should be pointed out that, for screw dislocation, Burgers' vector is parallel to its dislocation line, while for edge dislocation, Burgers' vector is perpendicular to the dislocation line.

A slip or glide system is characterized by the combination of a slip plane and a slip direction. Experimental observations show that, in most metals, the slip planes are usually those planes with the closest atomic packing, while the slip directions are always the closest packed directions on the slip planes. Once reference axes are defined, a slip system is described by its geometrical matrix K_{ij}^s also called Schmid's tensor :

$$K_{ij}^s = b_i^s n_j^s \tag{3-1}$$

n_j^s unit vector normal to the slip plane for the slip system s ;

b_j^s unit vector in the slip direction for the slip system s .

A_{ij}^s and Z_{ij}^s are respectively the symmetric and the anti-symmetric parts of K_{ij}^s .

Another approach to characterize one slip system is to use Miller's indices to represent the slip planes and directions. For instance, for b.c.c metals, 24 $\{110\}\langle 111\rangle$ and $\{112\}\langle 111\rangle$ slip systems are available and, for f.c.c metals, 12 $\{111\}\langle 110\rangle$ are generally assumed (van Houtte 1995).

The *critical resolved shear stress CRSS* τ_c^s is the shear stress to apply in order to sustain the long range propagation of a dislocation according to a slip system s , under the superposed effects of all coexisting structural features which represent obstacles of different strengths. In practice, the *resolved shear stress* τ^s acting on a slip system s can be derived by projecting the microscopic stress $\underline{\sigma}^{micro}$ on the slip plane with the help of the corresponding A_{ij}^s matrix. This determination can be checked, if one computes the energy dissipated by the strain rate tensor $\underline{\dot{\epsilon}}^p$ associated to a single shear of one active slip system:

$$\dot{\gamma}^s \tau^s = \dot{\epsilon}_{ij}^p \sigma_{ij}^{micro} = A_{ij}^s \dot{\gamma}^s \sigma_{ij}^{micro}$$

$$\tau^s = A_{ij}^s \sigma_{ij}^{micro} \quad (3-2):$$

The slip s occurs according to Schmid's law if the shear stress τ^s reaches the CRSS τ_c^s . This defines the yield locus of a single crystal:

$$-\tau_c^s \leq \tau^s \leq \tau_c^s \quad (3-3)$$

Equals signs hold for plastic deformation, while inequalities apply to the elastic domain. In this elastoplastic formulation, the detection of active slip systems can be done either by Bishop-Hill's approach or by Taylor's approach. These methods are dual ones and are well summarized in van Houtte 1988. Taylor's approach will be summarized in Chapter 4.

3.2. Crystallographic texture

In a polycrystalline sample, each crystal is characterized by its volume fraction dV and by its orientation, symbolically designated by g . More specifically, the set of Euler's angles $(\varphi_1, \phi, \varphi_2)$, describing the orientation of the crystal reference system with respect to the sample (external) reference system, is most often used (Bunge, 1982).

Figure 3-4 shows the physical meaning of $\varphi_1, \phi, \varphi_2$. With $dV(g)/V$ as the volume fraction of crystals having their orientation within dg around g , the *statistical crystallite orientation distribution function* (ODF) $f(g)$ is then defined as :

$$\frac{dV(g)}{V} = f(g)dg \quad \text{with} \quad dg = \frac{1}{8\pi^2} \sin \phi \, d\phi_1 \, d\phi \, d\phi_2 \quad (3-4)$$

It provides a quantitative description of the crystallographic texture of the polycrystal; high values indicate preferred orientations, and $f(g) \equiv 1$ a completely random texture.

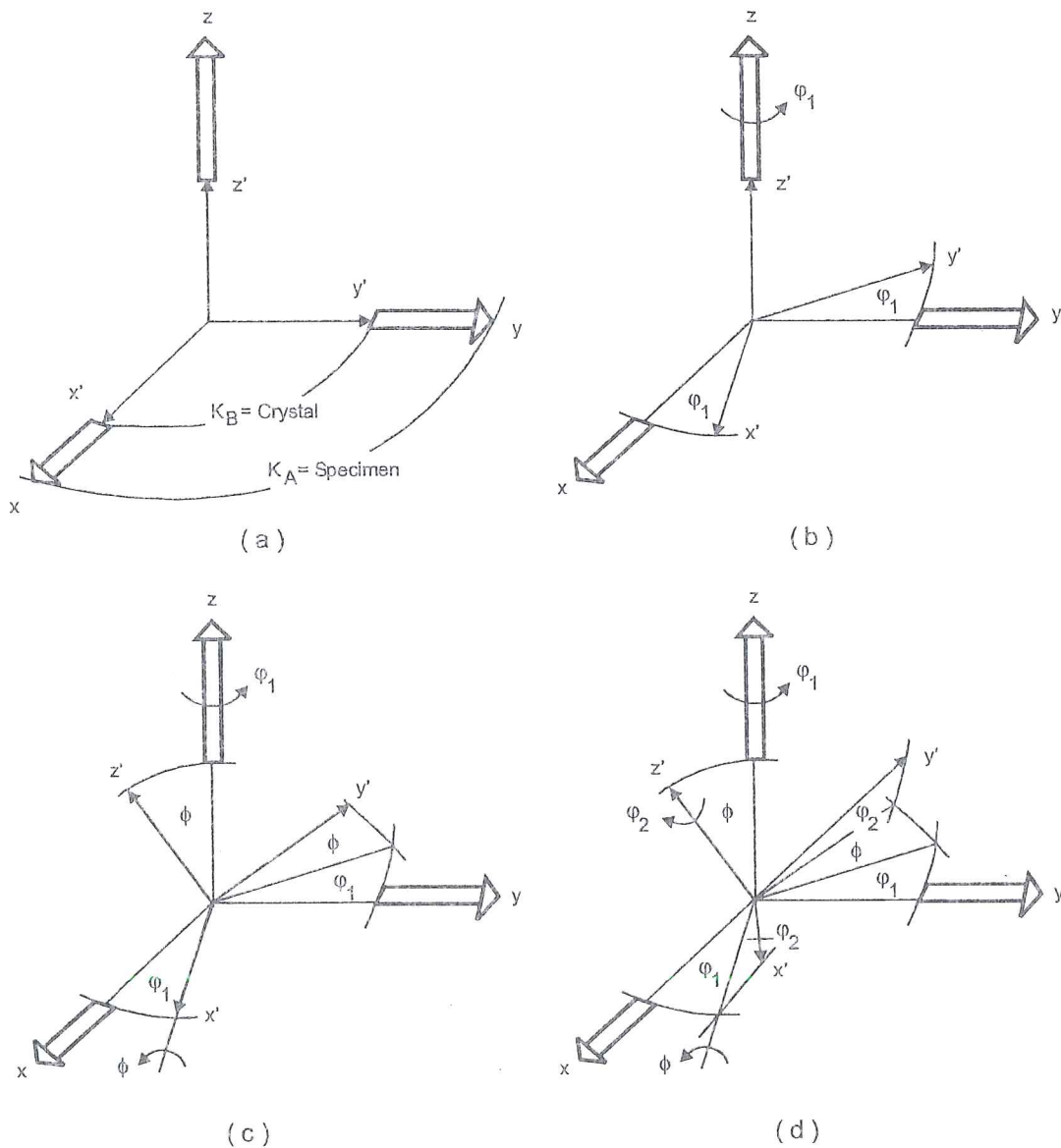


Figure 3-4 Definition of Euler's angles (from van Houtte 1995).

Because of the crystal symmetry, several symmetrically equivalent choices exist for a crystal reference system. The classical ranges for the three Euler's angles, $0 \leq \phi_1 \leq 2\pi$, $0 \leq \phi \leq \pi$ and $0 \leq \phi_2 \leq 2\pi$, may therefore be reduced. Besides, symmetries in the forming process may lead to an initial texture with similar statistical symmetries. This so-called sample symmetry allows again for a reduction

of the part of Euler's space to be considered. For example, in the case of cubic crystals without sample symmetry, the ranges $[0,2\pi] \times [0,\pi/2] \times [0,\pi/2]$ are to be used; with additional orthorhombic sample symmetry, $[0,\pi/2] \times [0,\pi/2] \times [0,\pi/2]$ will be sufficient (Van Bael 1994).

Using the harmonic method proposed by Bunge 1982, the ODF $f(g)$ can be represented by a series expansion :

$$f(g) \equiv \sum_{l=0}^{l_{\max}} \sum_{\mu=1}^{\mu_{\max}^{(l)}} \sum_{\nu=1}^{\nu_{\max}^{(l,\mu)}} C_l^{\mu\nu} \dot{T}_l^{\mu\nu}(g) \quad (3-5)$$

with l_{\max} the maximum degree of the series expansion, $\dot{T}_l^{\mu\nu}(g)$ harmonic functions of Euler's angles and $C_l^{\mu\nu}$ their Fourier's coefficients describing the texture. For instance, truncating at $l_{\max} = 22$, a ODF for cubic crystals and orthorhombic sample symmetry is represented by a set of 185 $C_l^{\mu\nu}$ - coefficients (355 in the absence of sample symmetry). These can for example be obtained, after appropriate mathematical processing, from a set of X-ray diffraction pole figures, measured on a sample with the help of a texture goniometer (Bunge, 1982).

3.3. Introduction to hardening models

From a microscopic point of view, hardening is often presented as **material** and **geometric** (Miller & McDowell 1996). The dislocations remaining inside a volume element modify its state through the elastic field they produce. They also constitute obstacles to the production and motion of further dislocation, a phenomenon which is perceived as the material (strain) hardening of the crystal. The geometric (textural) hardening is related to the effect of lattice rotation, which can either raise or lower the stress required for yielding. In tension and compression, texturing generally increases the yield stress while in torsion its value is reduced. In Chapter 4, presenting the microscopic models used in micro-macro analysis, these 2 components clearly appear in hardening models. However, in most hardening models linked to phenomenological yield loci, the geometric hardening is neglected. In the models presented hereafter, it is the case for Bergström-van Liempt-Vegter's model, Follansbee-Kocks' model, Schmitz's model and Teodosiu's model. However Miller's model tries to take both phenomena into account.

From a macroscopic point of view, **isotropic** and **kinematic** hardening models are usually considered. Let us recall that isotropic hardening assumes that the subsequent yield surface is obtained by a uniform expansion of the initial yield surface. So, the centers of the initial and updated yield loci are the same and the shape modification of the yield locus induced by plastic deformations is neglected. Kinematic hardening assumes that, during the process of plastic loading, the yield surface translates in stress space while its shape and size remain unchanged. This model is motivated by the Bauschinger effect in the uniaxial tension-compression experiments (Figure 3-5).

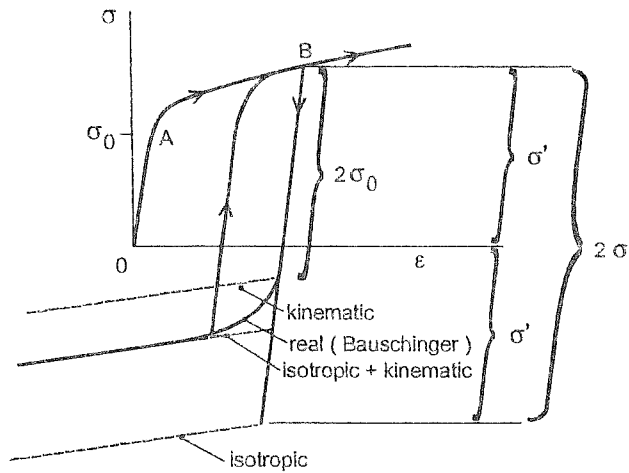


Figure 3-5 The Bauschinger effect, isotropic and kinematic hardening (adapted from Huétink *et al.* 1995)

Assuming an isotropic hardening rule, all the yield surfaces presented in section 2 can be written in the form :

$$F(\underline{\sigma}, \alpha_k, \underline{L}) = f(\underline{\sigma}, \underline{L}) - \sigma_F(\alpha_k) \quad (3-6)$$

with α_k : hardening scalar internal variables;
 \underline{L} : a material tensor characterizing material anisotropy;
 σ_F : a threshold value, function of the internal variables.

The different approaches of isotropic hardening depend on the choice of the internal variables α_k and of the threshold function σ_F .

Due to kinematic hardening in the process of plastic deformation, the general formulation of the yield surface hereabove takes the form :

$$F(\underline{\sigma}, \underline{\alpha}, \alpha_k, \underline{L}) = f(\underline{\sigma} - \underline{\alpha}, \underline{L}) - \sigma_F(\alpha_k) \quad (3-7)$$

where $\underline{\alpha}$ is a tensorial hardening parameter, usually called *back stress*, which represents the center of the yield surface in the stress space. The first proposal by Prager 1955 implies that the yield surface moves along the direction of the plastic strain rate:

$$d\underline{\alpha} = c d\underline{\varepsilon}^p \quad (3-8)$$

where c is a material constant. This formulation does not give consistent results for 3-dimensional and 2-dimensional stress states and predicts softening in transverse direction due to uniaxial tension. To overcome these shortcomings, Ziegler 1959 proposed the following modification of Prager's model :

$$d\underline{\alpha} = (\underline{\sigma} - \underline{\alpha}) d\mu \quad (3-9)$$

where $d\mu$ is a proportionality scalar constant determined thanks to the consistency

condition (Khan & Huang 1995) :

$$d\mu = \frac{\partial f / \partial \underline{\sigma} : d\underline{\sigma}}{\partial f / \partial \underline{\sigma} : (\underline{\sigma} - \underline{\alpha})} \quad (3-10)$$

The schematic representations of Prager's and Ziegler's models are shown in Figure 3-6.

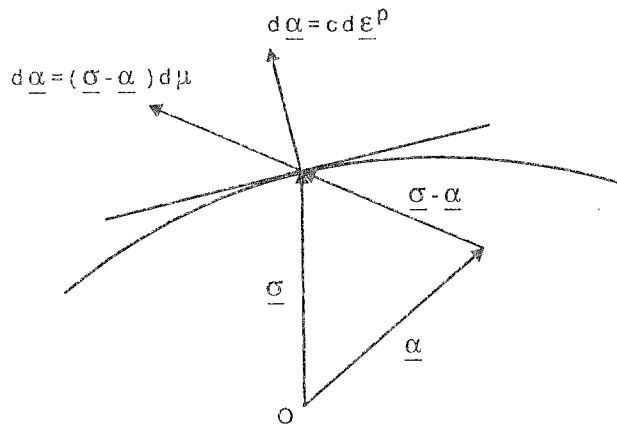


Figure 3-6 Prager's and Ziegler's kinematic hardening models (from Khan & Huang 1995).

The attempts to model the response of engineering materials under symmetric, unsymmetric or random cyclic loading, reversal or successive different directional deformations paths show the limits of the classical isotropic or kinematic hardening models. Two ways are possible to improve the macroscopic models:

- the use of multi-surfaces model shortly summarized hereafter;
- the use of internal variables closely linked to the underlying physics, described in section 3.5.

Multi-surface models have been introduced by Mroz 1967, Dafalias & Popov 1975. In Mroz' model, the nonlinearity of the stress-strain curve is introduced by defining a set of hardening moduli associated with several initially concentric surfaces which can translate rigidly and expand uniformly. In Dafalias & Popov's model, the nonlinearity is described by modeling the continuous variation of a hardening modulus based on the concept of 2 surfaces : the yield locus and the bounding locus. These two surfaces allow to define a distance d in the stress space, representing the difference between the current loading state and the bounding state. This variable distance has been found very important to define the variation of the hardening modulus. This approach has met a great success and other double yield surfaces models have been developed (Krieg 1975, Philips & Lee 1979).

This basic concept is explained with Huétink's *et al.* 1995 proposal. These authors use a classical Hill's yield surface translated by kinematic hardening, called "kinematic yield surface", and a fictitious yield surface, referred hereafter as the "isotropic yield surface" (Figure 3-7). The latter surface corresponds to the

application of isotropic hardening on the initial yield locus. It keeps the memory of the maximum stress reached during the deformation path.

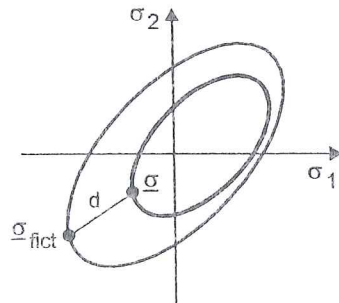


Figure 3-7 Kinematic and isotropic yield surfaces and definition of the distance d between the current stress point $\underline{\sigma}$ and a stress point $\underline{\sigma}_{fict}$ on the fictitious isotropic yield surface (from Huétink *et al.* 1995).

Their hypothesis is that the rate of hardening depends on distance d . The fictitious isotropic yield surface (re)starts growing when the kinematic surface touches the isotropic yield surface. Let us follow a cyclic loading experiment ($A \rightarrow B \rightarrow C \rightarrow D \rightarrow E$) as defined on Figure 3-8.

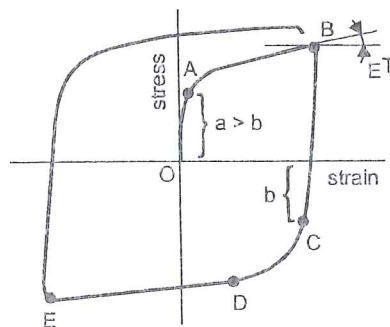


Figure 3-8 Stress-strain relation during an experiment of cyclic loading (from Huétink *et al.* 1995).

When starting with virgin material, the isotropic and kinematic yield surfaces coincide, as depicted in Figure 3-9^a. During the deformation process, the fictitious isotropic yield surface grows due to the accumulated strain and the kinematic yield surface translates in such a way that $\underline{\sigma}$ remains on both the isotropic and the kinematic yield surfaces, as illustrated by Figure 3-9^b ($A \rightarrow B$). In this case, the distance d is zero and the hardening rate is equal to the slope of the monotonic stress-strain curve E^T (Figure 3-8). When the deformation direction changes ($B \rightarrow$), the stress $\underline{\sigma}$ lies inside the kinematic yield surface and the material is elastic.

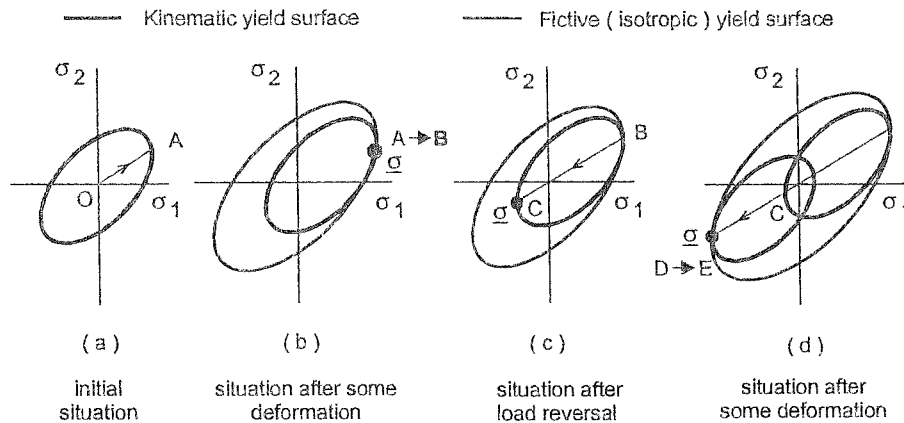


Figure 3-9 Yield surfaces, kinematic and isotropic hardening (from Huétink *et al.* 1995).

After a further increase of the load in the reversed direction, $\underline{\sigma}$ moves to the opposite side of the yield surface, see Figure 3-9^c, and plasticity starts to occur again. At this moment, the distance d is important and a relatively fast hardening occurs. The hardening rate decreases when the kinematic yield surface approaches the fictitious isotropic yield surface (point D in Figure 3-9^d). After $\underline{\sigma}$ touches the isotropic yield surface, hardening is controlled by the growth of the isotropic yield surface, see Figure 3-9^d. The mathematical description can be found in Huétink *et al.* 1995.

Some proposals of hardening rules associated with models using only one yield surface are now listed. Section 3.4 presents purely macroscopic models while section 3.5 proposes macroscopic models strongly linked to the microscopic events. As it will be seen, even with strong microscopic roots, such models can still be compatible with phenomenological descriptions of the yield locus and give a fair description of the experimental behavior.

3.4. Simple macroscopic isotropic hardening approaches

As used in Hill's or Barlat's relations (see Tables 1 and 2 of Chapter 2), the threshold value is defined by σ_F , the yield stress deduced from uniaxial tension. Different equations have been proposed for this tensile stress-strain curve $\sigma_F = f(\varepsilon)$:

$$\begin{aligned} \sigma_F &= \sigma_0 + H\varepsilon^n && \text{Ludwick 1909} \\ \sigma_F &= H\varepsilon^n && \text{Hollomon 1944} \\ \sigma_F &= \sigma_0 + (\sigma_s - \sigma_0) [1 - \exp(-n'\varepsilon)] && \text{Voce 1948} \\ \sigma_F &= H(\varepsilon_s + \varepsilon)^n && \text{Swift 1947} \\ \sigma_F &= \sigma_0 \tanh\left(\frac{E\varepsilon}{\sigma_0}\right) && \text{Prager 1938} \end{aligned}$$

$$\varepsilon = \frac{\sigma_F}{E} + H \left(\frac{\sigma_F}{E} \right)^{n'} \quad \text{Ramberg \& Osgood 1943} \quad (3-11)$$

where σ_F, ε refer to Cauchy's stress and the logarithmic strain respectively, $E, H, n', \sigma_0, \sigma_s, \varepsilon_s$ are material constants and must be determined experimentally. For this uniaxial test, the strain is additionally decomposed into an elastic part ε^e and a plastic one ε^p .

$$\varepsilon = \varepsilon^e + \varepsilon^p \quad (3-12)$$

The link between this uniaxial state and the actual three dimensional stress-strain state relies on the chosen internal variables α_k .

3.5. Macroscopic approaches with strong microscopic roots

3.5.1. Bergström - van Liempt - Vegter's model

Bergström 1969 proposes a model which intends to describe slow constant strain-rate tensile tests on polycrystalline α -Fe at room temperature. It considers only the homogeneous deformation, i.e. the deformation that occurs up to the point where necking begins. This model starts from the well known relationship between the uniaxial flow stress σ_F and the total dislocation density ρ (total length of dislocations per volume unit):

$$\sigma_F = \sigma_0 + \alpha G b \sqrt{\rho} \quad (3-13)$$

where σ_0 is the elastic limit, G the shear modulus, b the magnitude of Burgers' vector and α a material constant.

Then, it establishes the relation between dislocation density ρ and strain ε . Only the average behavior of a large number of dislocations is considered and it is assumed that :

- ρ is composed of a mobile dislocation density ρ_m and an immobile dislocation density ρ_i ,
- ρ_m is a constant, hence strain independent,
- The variation of ρ_i with ε is determined by 4 processes, namely creation, immobilization, re-mobilization and annihilation of dislocations (see Figure 3-10),
- The effects of changes in dislocation structure can be neglected.

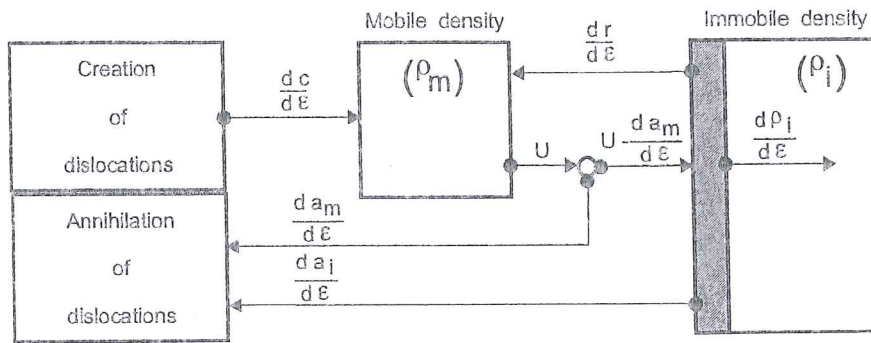


Figure 3-10 Illustration of the dislocation model (adapted from Bergström 1969)

As the density of mobile dislocations ρ_m is constant, the processes causing an increase of ρ_m , creation ($dc/d\varepsilon$) and re-mobilization ($dr/d\varepsilon$), are balanced by the processes of annihilation ($da_m/d\varepsilon$) and immobilization ($U - (da_m/d\varepsilon)$), causing a decrease of ρ_m . The term $da_i/d\varepsilon$ covers the annihilation of immobile dislocations. The density of immobile dislocations ρ_i increases with strain ε .

Three main parameters are introduced :

- $U(\varepsilon)$: a function measuring the rate at which mobile dislocations are immobilized or annihilated.
- Ω : a constant measuring the probability for re-mobilization or annihilation of immobile dislocations at room temperature; it is assumed $\ll 1$.
- A : a constant measuring the rate at which mobile dislocations annihilate by reacting with other mobile dislocations, grain boundaries, specimen surface, etc.

According to Figure 3-10 and the parameters introduced hereabove, the variation of the total dislocation density with strain is obtained:

$$\frac{d\rho}{d\varepsilon} = \frac{d\rho_i}{d\varepsilon} = U(\varepsilon) - \frac{da_m}{d\varepsilon} - \left(\frac{dr}{d\varepsilon} + \frac{da_i}{d\varepsilon} \right) = U(\varepsilon) - A - \Omega\rho \quad (3-14)$$

Since U is proportional to v (average velocity of mobile dislocations) and to ρ_m , and inversely proportional to s (mean free path or average distance covered by mobile dislocations), following relation is obtained:

$$U(t) = \frac{v\rho_m}{s(t)} \quad (3-15)$$

where the time t is the variable. Then, using the proportion:

$$\dot{\varepsilon} \div \overline{M} b \rho_m v \quad (3-16)$$

where \overline{M} is the average Taylor's factor depending on the orientation of crystals which will be defined in section 4.5.2, relation (3-15) becomes :

$$U(\varepsilon) = \frac{1}{Mb s(\varepsilon)} \quad (3-17)$$

if strain ε is used as variable.

In constant strain rate tensile tests, it has been found that the total dislocation density ρ , for strains up to approximately 10%, varies with strain as:

$$\rho = C\varepsilon + \rho_0 \quad (3-18)$$

in which C and ρ_0 are experimental constants. The previous relations (3-14) and (3-18) imply $(U-A)=C$ if, as assumed above, $\Omega \ll 1$. So the assumption that A is strain independent implies that it is also the case for U in the strain range in which relation (3-18) is valid. Beyond this range, a dislocation cell structure develops in the α -Fe "which changes little on further deformation". This strong hypothesis is not valid at large strains and is a limit of Bergström's model. The experimental observation that the dislocation density within the cells is very low supports the assumption that when a dislocation moves, it does so from one cell wall to the other. This suggests that the mean free path s is proportional to the size of the cells. So, according to relation (3-17), U does not change as long as the cell diameter and the crystal orientations remain constant.

Assuming U to be independent of strain, relation (3-14) can be integrated with the limit condition $\rho = \rho_0$ at $\varepsilon = 0$ and the following expression is obtained:

$$\rho = \frac{U - A}{\Omega} (1 - e^{-\Omega\varepsilon}) + \rho_0 e^{-\Omega\varepsilon} \quad (3-19)$$

Finally, Bergström proposes the following stress-strain relationship deduced from equations (3-13) and (3-19):

$$\sigma_f = \sigma_0 + \alpha G b \left\{ \frac{U - A}{\Omega} (1 - e^{-\Omega\varepsilon}) + \rho_0 e^{-\Omega\varepsilon} \right\} \quad (3-20)$$

In this case, σ_0 is the flow stress of the undeformed polycrystal.

This model presents an horizontal asymptote in the stress-strain curve. If the relation (3-20) is fitted on experimental data, the work hardening rate vanishes at strains greater than the experimental strain range. It is however reported in the literature, that work hardening persists up to very high strains. One possibility to improve this model is to maintain relation (3-17) but with a mean free path of mobile dislocations s which varies with strain. This has been proposed by van Liempt 1994, who keeps the idea of a mean free path s proportional to the cell size and assumes an evolution rule for the cell size at large strains:

- cells shrink in size during plastic deformation as the average cell diameter is inversely proportional to $\sqrt{\rho}$;
- cells will be strained with the bulk of material;

- for cells deformed in plane strain, the cell thickness is proportional to $\frac{1}{\sqrt{\rho}} e^{-\beta\varepsilon}$

where β is a material constant and ε is the macroscopic strain.

The experimental observation of the cell size (van Liempt 1994) allows to reach a constant value of $\beta = 0.18$. Finally, van Liempt's proposal for the differential equation of dislocation density is :

$$\frac{d\rho}{d\varepsilon} = B\sqrt{\rho} e^{\beta\varepsilon} - \Omega\rho \quad (3-21)$$

where B is assumed constant but takes into account the average Taylor's factor.

The introduction of relation (3-21) in relation (3-13) produces the following form of the stress strain relation:

$$\sigma_F = \sigma_0 + \alpha G b \left[\frac{B}{\Omega + 2\beta} \left\{ e^{(\frac{\Omega}{2} + \beta)\varepsilon} - 1 \right\} + \sqrt{\rho} \right] e^{-\Omega\varepsilon/2} \quad (3-22)$$

So, instead of reaching a saturation level, this equation behave exponentially at high strains. Rietman *et al.* 1997 present finite element simulations using this model.

Vegter 1991 uses Bergström's theory to describe the interaction processes between dislocations and cell structures as well as the influence of the change of shape of the dislocation cell with large strains proposed by van Liempt 1994. To these two concepts, Vegter 1991 adds a modification for the flow stress at high strains and temperature different from room temperature. He derives the following relation for the uniaxial reference flow stress (Pijlman *et al.* 1998) :

$$\sigma_F = \sigma_0 + \Delta\sigma_m \left[\beta \cdot (\varepsilon_0 + \varepsilon) + \left\{ 1 - e^{-\Omega(\varepsilon_0 + \varepsilon)} \right\}^{n'} \right] \quad (3-23)$$

with :

σ_0 the initial yield stress, which depends on strain rate and temperature;

ε the uniaxial strain;

ε_0 predeformation parameter;

$\Delta\sigma_m$ a constant representing the stress increase by strain hardening;

β a constant describing the change of shape of the dislocation cells, necessary for large strain behavior;

Ω a constant describing the annihilation of dislocations, necessary for low strain behavior;

n' the strain hardening exponent.

As parameter σ_0 depends on the effect of strain rate and temperature, according to Kabriell and Dahl 1982, it can be split into 2 terms :

$$\sigma_0 = \sigma_{0\text{ stat}} + \sigma_{0\text{ dyn}} \quad (3-24)$$

with:

- $\sigma_{o\ sta}$ the static yield stress of a dislocation free material;
- $\sigma_{o\ dyn}$ the dynamic part of the flow stress.

Krabiell and Dahl 1982 derived the relation of the dynamic part of the flow stress $\sigma_{o\ dyn}$ with strain rate and temperature, based on the thermally activated motion of dislocations over obstacles. In case of steel, these obstacles are mainly the hills and valleys in the slip plane (Peierls' force). This leads to the following equation for the activation enthalpy:

$$\Delta G = -kT \ln \left(\frac{\dot{\epsilon}}{\dot{\epsilon}_o} \right) \quad (3-25)$$

with:

- k Boltzman's constant;
- T absolute temperature in K°;
- $\dot{\epsilon}$ the strain rate;
- $\dot{\epsilon}_o$ the limit strain rate for thermally activated motion.

Using the latter relation (3-25), Vegter 1991 derives the contribution of the strain rate to the flow stress:

$$\begin{aligned} \sigma_{o\ dyn} &= \sigma_o^* \left\{ 1 - \frac{\Delta G}{\Delta G_{max}} \right\}^{m'} \quad \text{with } 0 < \Delta G < \Delta G_{max} \\ \sigma_{o\ dyn} &= \sigma_o^* \quad \text{with } \Delta G < 0 \\ \sigma_{o\ dyn} &= 0 \quad \text{with } \Delta G > \Delta G_{max} \end{aligned} \quad (3-26)$$

with:

- σ_o^* the limit dynamic flow stress;
- m' the exponent for the dynamic stress;
- ΔG the activation enthalpy;
- ΔG_{max} the maximum activation enthalpy.

The final relation for the flow stress as a function of the strain and strain rate is obtained by combining (3-24), (3-25), (3-26) :

$$\sigma_F = \sigma_{o\ sta} + \Delta \sigma_m \left[\beta \cdot (\epsilon_o + \epsilon + \{1 - e^{-\Omega(\epsilon_o + \epsilon)}\}^{a'}) \right] + \sigma_o^* \left\{ 1 + \frac{kT}{\Delta G_{max}} \ln \left(\frac{\dot{\epsilon}}{\dot{\epsilon}_o} \right) \right\}^{m'} \quad (3-27)$$

In this relation :

- ϵ_o is 0.005 for steel and 0 for aluminum, which corresponds to the amount of pre-deformation during the skin pass.
- n' : strain hardening exponent is fixed at 0,75 (Vegter 1991). The fit on a stress

strain curve is not sufficiently discriminating for the determination of this exponent. The reason for this choice is based on the evaluation of the diameter of the dislocation cells. If they remain constant (in volume), the value of n' is 0,5; if they decrease according to Holt 1970, the value of n' is 1. The value 0.75 is just a pragmatic choice in between.

- $\Delta G_{max}, \dot{\epsilon}_0, m', \sigma_0^*$: strain rate and temperature constants are deduced from tensile tests at strain rates ranging from 10^{-4} to 1 s^{-1} . Such tests are available in Vegter 1991; and some values are proposed in table 5 from Vegter *et al.* 1999.
- $\sigma_{0 sta}, \Delta\sigma_m, \beta, \Omega$: strain hardening constants are derived from tensile tests which yield a planar isotropic flow stress.

material	Strain hardening constants						Strain rate constants			
	$\sigma_{0 sta}$ (MPa)	$\Delta\sigma_m$ (MPa)	β	Ω	ϵ_0	n'	σ_0^* (MPa)	ΔG_0 (eV)	m'	ϵ_0^* (s^{-1})
IF-steel	96.2	271.0	0.25	9.27	0.005	0.75	600.0	0.8	2.2	10^8
Al-6000	107.1	179.6	0.25	8.07	0.000	0.75	20.0	0.8	1.0	10^8

Table 5 Material parameters for the Vegter's final flow stress function (from Vegter *et al.* 1999).

3.5.2. Follansbee & Kocks's model

This model uses a single internal variable to describe the flow stress reference curve over a wide range of strain rates (for instance, 10^{-4} to 10^{+4} s^{-1}). It has been developed and validated for pure copper by Follansbee & Kocks 1988, but it has been used later for other metals like tantalum, tantalum - tungsten alloys (Maudlin *et al.* 1999). The foundation of the model is the separation of the phenomena related to the constant dislocation structure and the phenomena related to the structure evolution. The basic assumptions are:

- the plastic deformation occurs by accumulation and motion of dislocations,
- the mechanism controlling the rate of deformation is the interaction of dislocations with defects: grain boundaries, forest dislocations, (dislocations not parallel to the glide plane of the moving dislocation), solute atoms, ...
- for pure f.c.c metals, the dominant short range obstacles are the forest dislocations.

The internal variable is called the mechanical threshold stress $\hat{\sigma}$: it represents the flow stress at 0° K and depends on the dislocation structures present in the material. The flow stress proposal is defined by :

$$\sigma_F = \sigma_a + (\hat{\sigma} - \sigma_a) \left\{ 1 - \left[\frac{kT \ln(\dot{\epsilon}_0 / \dot{\epsilon})}{g_0 G b^3} \right]^{1/q} \right\}^{1/p} \quad (3-28)$$

where σ_a is the athermal component characterizing the (rate independent) interactions of dislocations with long range barriers such as grain boundaries; in practice, it is chosen as the yield stress of the undeformed material. The second component characterizes the rate dependent interactions of dislocations with short range obstacles such as forest dislocation, solute atoms... Thermal activation reduces this component. k is Boltzmann's constant, $\dot{\epsilon}_0$ a reference constant strain rate, g_0 a normalized activation energy for dislocation/dislocation interactions, G the shear modulus, b the magnitude of Burgers' vector, p and q constants characterizing the statistically averaged shape of the obstacle profile ($0 \leq p \leq 1, 1 \leq q \leq 2$). In the method of parameter identification, p and q are chosen in such a way that realistic g_0 are obtained. The second term of (3-28) shows some similitude with the third term of Vergter's model (3-27), also related to thermal and strain rate effects. The evolution of the mechanical threshold stress $\hat{\sigma}$ attempts to model the evolution of the dislocation structure considered as the balance between dislocation accumulation and dynamic recovery :

$$\frac{d\hat{\sigma}}{d\epsilon} = \theta_0 - \theta_0 \frac{\hat{\sigma} - \sigma_a}{\sigma_{sat} - \sigma_a} \quad (3-29)$$

where θ_0 represents the hardening rate due to the dislocation accumulation and the second term covers the dislocation annihilation processes. σ_{sat} is the stress at zero strain hardening rate, often called: the saturation stress. This linear variation of the strain hardening rate with stress is often termed as Voce behavior. Estrin & Ecking 1984 have given physical significance to this relation by considering the competition between dislocations. However another function, close to the previous one, produces better experimental fits for copper :

$$\frac{d\hat{\sigma}}{d\epsilon} = \theta_0 \left(1 - g \left(\frac{\hat{\sigma} - \sigma_a}{\sigma_{sat} - \sigma_a} \right) \right) \quad (3-30)$$

Relations for g , θ_0 , σ_{sat} are specific for each material. For copper, Follansbee & Kocks 1988 use:

$$g = \frac{\tanh(2X)}{\tanh(2)} \quad \text{with } X = \frac{\hat{\sigma} - \sigma_a}{\sigma_{sat} - \sigma_a} \quad (3-31.a)$$

$$\ln \frac{\dot{\epsilon}}{\dot{\epsilon}_0} = \frac{Gb^3 A}{kT} \ln \left(\frac{\sigma_{sat}}{\sigma_{sat_0}} \right) \quad (3-31.b)$$

$$\theta_0 = A_1 + A_2 \ln \dot{\epsilon} + A_3 \dot{\epsilon} \quad (3-31.c)$$

where $\dot{\epsilon}_0$, A , A_1 , A_2 , A_3 are material constants, σ_{sat_0} is the saturation stress for deformation at 0° K. The relation (3-31.c), deduced from experiments, is related to the « increased strain rate sensitivity » of the flow stress found in copper and other f.c.c. metals at high strain rates ($> 10^3 \text{ s}^{-1}$). In fact, a constant initial strain hardening

$\theta_0 = A_1$ means that dislocations are immobilized after traveling a distance proportional to the average distance between dislocations. However, at very high strain rates, it might be speculated that the distance before dislocation immobilization is simply the distance that a dislocation can move during the imposed time duration of the deformation. This explains the second and third terms of relation (3-31.c).

As shown by Figure 3-11, with a single set of material parameters, this model is able to predict stress strain curves at various constant levels of strain rate.

Figure 3-12 shows that this model can predict effects of strain rate modifications if they happen at low strain but not at high strain.

Follansbee & Kocks 1988 provide a good description of their method to identify the material parameters : $A, A_1, A_2, A_3, \sigma_{sat_0}, \sigma_a, G, b, g_0, p, q, \theta_0, \dot{\epsilon}_0$.

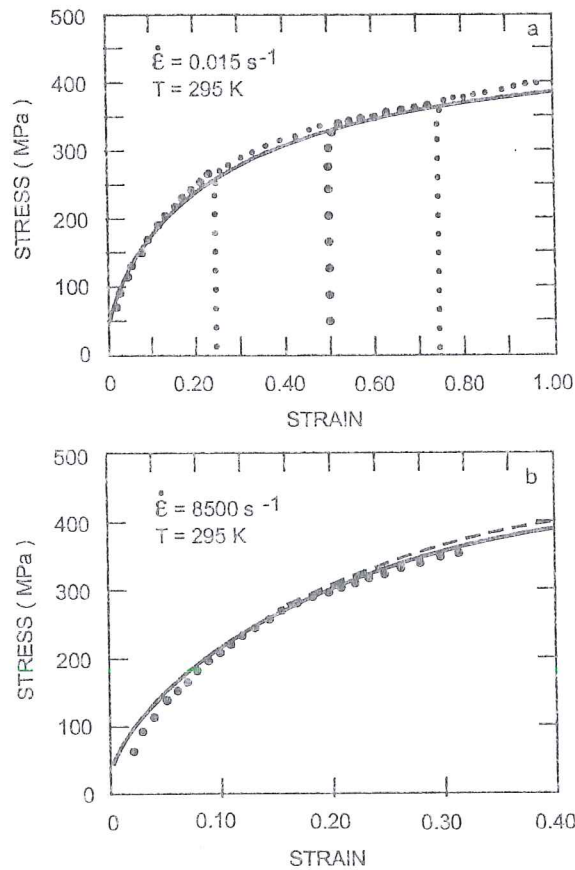


Figure 3-11 Follansbee & Kocks' model predictions for isothermal (---) or adiabatic (—) assumptions compared to experiments (...) on copper (from Follansbee & Kocks 1988).

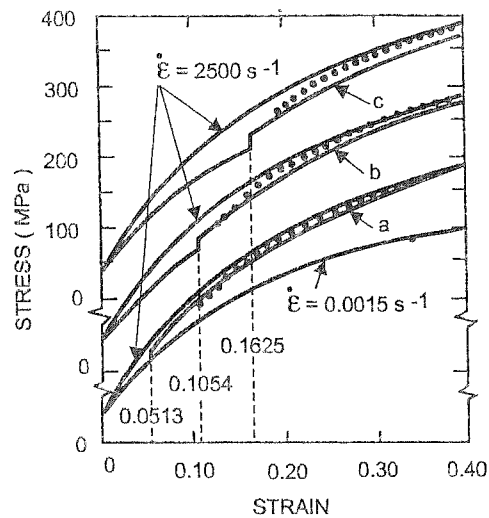


Figure 3-12 Follansbee & Kocks' model predictions compared to 3 experimental results for a strain rate change from $\dot{\epsilon} = 0.0015 \text{ s}^{-1}$ to $\dot{\epsilon} = 2500 \text{ s}^{-1}$ at strain of $\epsilon = 0.0513$; 0.1054 and 0.1625 (from Follansbee & Kocks 1988).

3.5.3. Schmitz's model

Another example of macroscopic hardening law based on dislocation analysis combined with some phenomenological approach is proposed by Schmitz 1995. His goal is to simulate the behavior of a ferritic steel at high temperature for a model of the rolling process. He finally uses an isotropic von Mises' surface the size of which is defined by the following reference stress :

$$\frac{d\sigma_F}{d\epsilon} = \frac{k}{\sigma_{sat}} \left(\frac{\sigma_{sat}^2}{\sigma_F} - \sigma_F \right) \quad (3-32)$$

$$Z = \dot{\epsilon} \exp\left(\frac{Q}{RT}\right) = B \exp(\beta\sigma_{sat}) \quad (3-33)$$

with

- σ_{sat} saturation stress;
- Z Zener Hollomon temperature compensated strain rate;
- Q activation energy for deformation;
- R universal gas constant;
- K, B, β material constant.

3.5.4. Miller-Mc Dowell's model

Experimental observations and physical explanations

If von Mises' equivalent stress is plotted versus von Mises' equivalent strain for experimental data obtained from free-end torsion tests and compression tests, it is

typically observed (Figure 3-13) that the curve corresponding to torsion is lower.

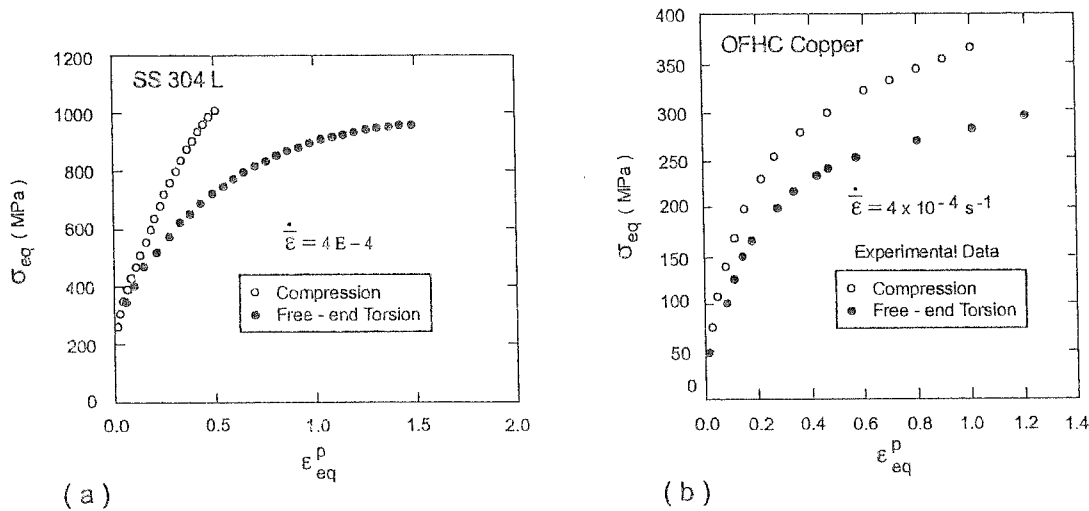


Figure 3-13 Experimental data deduced from compression and free-end torsion tests
 (a) 304L stainless steel (from Miller & Mc Dowell 1996)
 (b) OFHC copper (from Miller & Mc Dowell 1994).

For a f.c.c crystal structure and an initially isotropic material, on the basis of *average Taylor's factors* \overline{M} for torsion and tension, the effective yield stress in torsion is expected to be 7 % lower than in tension (Miller & Mc Dowell 1996). The exact mathematical definition of this average Taylor's factor is given in Chapter 4. Physically, it represents an average of the slip rates on active slip systems for each crystal. This factor depends on the texture of the metal (i.e. the orientation of its crystals) and on the type of deformation. It has been argued that the stress level difference becomes more significant at larger strains, since the textures formed in compression and tension tend to increase the average Taylor's factor \overline{M} above the isotropic value (textural hardening) while the textures formed in torsion tend to decrease the average Taylor's factor \overline{M} (texture softening). However, a polycrystal model explicitly taking the texture effect into account and using a hardening rule linked only to microscopic equivalent plastic strain ($\epsilon_{eq}^{p\ macro}$) is not able to reproduce experimental observations. So geometric (textural) hardening alone does not explain the reality. In practice, a larger average Taylor's factor \overline{M} implies more crystallographic slip activity to accommodate the same macroscopic equivalent strain. This leads to an increased slip system hardening in compression as compared to torsion. In conclusion, in addition to textural hardening, slip-dependent strain-hardening must be invoked to explain the stress level difference observed on Figure 3-13.

So, a polycrystal model with a hardening rule taking into account both $\epsilon_{eq}^{p\ macro}$ and \overline{M} can reproduce the above reported difference between compression and torsion (Miller *et al.* 1995).

During torsion tests at large strains, second order effects are induced. Depending on the boundary conditions at the ends of the gage length, these effects produce either an induced axial stress (fixed-end) or an axial extension (free-end), the latter being called the Swift effect. Such phenomena cannot be explained with the assumption of an isotropic material submitted to a pure torsion state. The hypothesis of deformations induced by a material becoming anisotropic helps to understand these effects.

Figure 3-14 presents the effect of different modes of deformation as well as axial extension during free-end torsion tests.

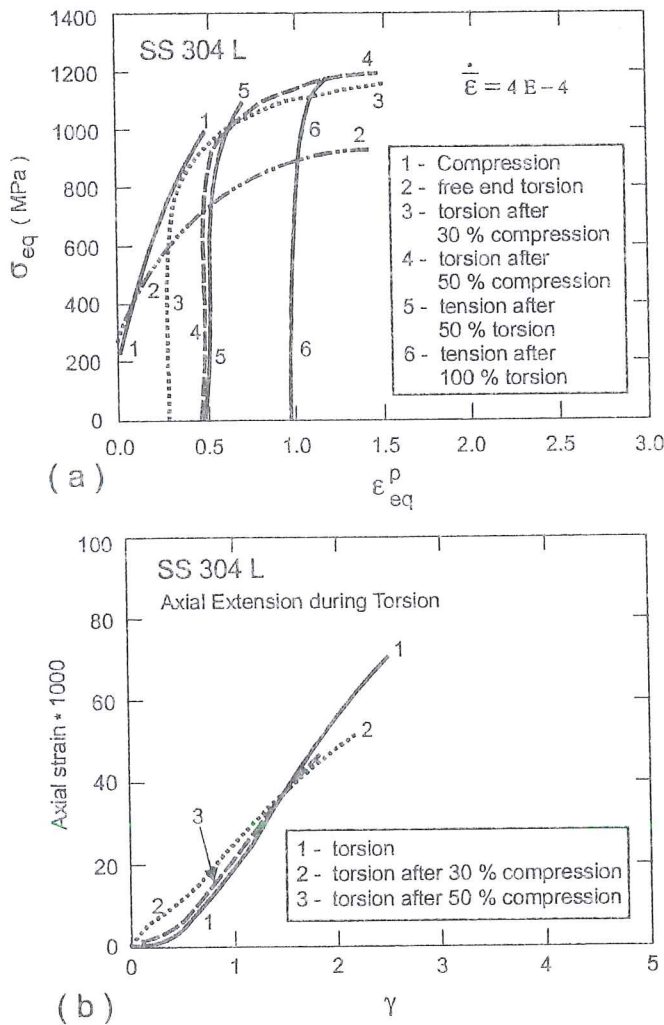


Figure 3-14 Experimental results from compression, free-end torsion and sequential tests conducted on SS 304L (a) equivalent stress-strain response, (b) axial strain response for torsional test (from Miller&Mc Dowell 1996).

First macroscopic model

A macroscopic model using a yield function F_p based only on the equivalent stress (here the von Mises' yield surface) and employing a purely isotropic hardening will predict the same $(\sigma_{eq}, \epsilon_{eq}^p)$ curves for torsion and compression.

$$F_p = \sigma_{eq} - \sigma_0 - R \quad (3-34)$$

$$\dot{R} = C (R_{sat} - R) \dot{\epsilon}_{eq}^p$$

with

- σ_0 initial plastic stress; R_{sat} saturation value of R ;
- R increase of plastic stress; C material constant.
- $\dot{\epsilon}_{eq}^p$ plastic strain rate equivalent;

One way to reproduce experimental observations is to introduce a kinematic hardening as well as a plastic spin $\underline{\Omega}^p$. More details on plastic spin concept can be found in Hoferlin 2001. For single crystal approach, the plastic spin is the difference that does exist between the rate of rotation of the crystal substructure and the rotational flow of the continuous medium $\underline{\Omega}$. For the case of polycrystals, Mandel 1971 suggested to use as constitutive spin the average of each single crystal lattice spin. However numerous phenomenological approaches have been proposed. Here is the choice of Miller and Mc Dowel:

$$\overset{\nabla}{\underline{\alpha}} = C \left(\alpha_{sat} \frac{\underline{\hat{\sigma}} - \underline{\alpha}}{|\underline{\hat{\sigma}} - \underline{\alpha}|} - \underline{\alpha} \right) \dot{\epsilon}_{eq}^p \quad (3-35)$$

$$\overset{\nabla}{\underline{\alpha}} = \underline{\dot{\alpha}} - (\underline{\Omega} - \underline{\Omega}^p) \cdot \underline{\alpha} + \underline{\alpha} \cdot (\underline{\Omega} - \underline{\Omega}^p) \quad (3-36)$$

$$\underline{\Omega}^p = \zeta e^{C \epsilon^p} (\underline{\alpha} \cdot \dot{\epsilon}^p - \dot{\epsilon}^p \cdot \underline{\alpha}) \quad (3-37)$$

where (3-36) is Jaumann's objective rate of the back stress, $\underline{\Omega}$ is the antisymmetric part of the total velocity gradient and $\underline{\alpha}$ is the back stress.

During uniaxial compression, $\dot{\epsilon}^p$ and $\underline{\alpha}$ are coaxial; hence the plastic spin is null. During torsion, plastic spin exists and the material parameter ζ is fitted from the axial extension data measured during a free-end torsion experiment.

The kinematic hardening and the plastic spin $\underline{\Omega}^p$ generally allow to reproduce the geometric hardening or texture effect. As explained above, this effect alone cannot reproduce all the physical phenomena and it is not surprising that this von Mises model coupled with kinematic and isotropic hardening fails to predict experimental results.

Improved macroscopic hardening model

The above macroscopic model is modified to include the third invariant of overstress J_3^* in the yield function and in the evolution equations of the hardening variables $\underline{\alpha}$ and R .

$$J_3^* = \frac{1}{3} \text{tr}(\underline{\hat{\sigma}} - \underline{\alpha})^3 \quad (3-38)$$

The value of J_3^* is 0 for a free-end torsion test, $\frac{2}{27}(\sigma_{11} - \alpha_{11})^3$ for a uniaxial tensile test and $-\frac{2}{27}(\sigma_{11} - \alpha_{11})^3$ for a uniaxial compression test. So, an even power of J_3^* can be used to delineate torsion from compression and tension, while an odd power of J_3^* delineates compression from tension. The exact form of the F_p proposal can be found in Miller & Mc Dowell 1996. A simplified version of this hardening model is presented. In fact, the saturation levels (see relations (3-34) and (3-35)) are functions of J_3^* :

$$R_{sat} = R_{sat}^0 g^R \quad (3-39)$$

$$\alpha_{sat} = \alpha_{sat}^0 g^\alpha \quad (3-40)$$

$$g^j = 1 + \frac{m^j}{(q^j + 1)} \frac{27}{4} \left[\frac{J_3^{*2}}{J_2^{*3}} + q^j \left(\frac{J_3^{*2}}{J_2^{*3}} \right)_{max} \right] \quad j = R, \alpha \quad (3-41)$$

with $J_2^* = \frac{1}{2} \text{tr}(\underline{\sigma} - \underline{\alpha})^2$.

The parameter m^R is motivated by the differences in isotropic strain-hardening between torsion and compression as discussed earlier. The quantity $\left(\frac{J_3^{*2}}{J_2^{*3}} \right)_{max}$ and positive values of q^R are motivated by the high hardening level observed in Figure 3-14 during the torsion phase of the compression-followed-by-torsion test compared to the pure torsion test.

The scalar coefficient C_m relation (3-34) is now a function of the degree of coaxiality of the back stress and the inelastic strain rate:

$$C = \frac{C^*}{\left[A + \frac{\alpha}{|\alpha|} : \frac{\dot{\epsilon}^p}{|\dot{\epsilon}^p|} \right]} \quad (3-42)$$

where C^* and A are material constants. This expression is motivated by the nature of directional hardening sources (dislocation substructures, crystallographic texture,

etc). A sudden direction change in the loading path can produce a discontinuous rise of the strain hardening rate. Such an effect appears when evolving from a simple structure like that found in torsion to a more complicated diffuse structure found in uniaxial compression or tension. Remember that slips occur on planes oriented most closely to the plane of maximum shear. There are conceptually an infinite number of such planes during uniaxial compression or tension, but only two during a torsion test.

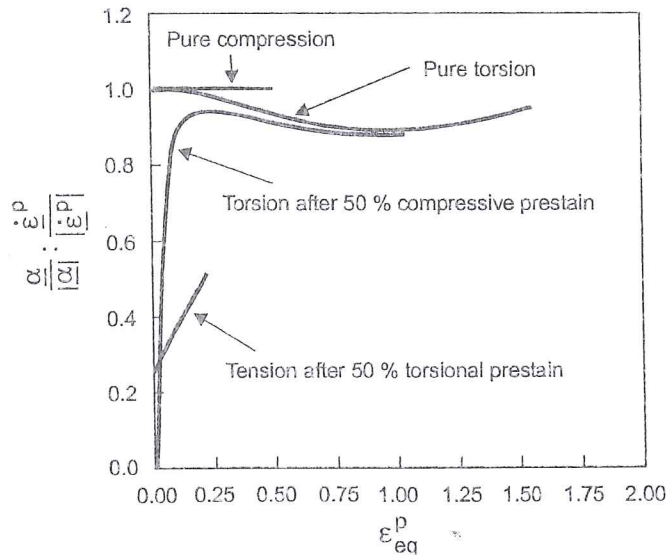


Figure 3-15 Inner product $\frac{\underline{\alpha}}{|\underline{\alpha}|} : \frac{\dot{\underline{\epsilon}}^p}{|\dot{\underline{\epsilon}}^p|}$ for different loading paths (from Miller&Mc Dowell 1996).

The inner product $\frac{\underline{\alpha}}{|\underline{\alpha}|} : \frac{\dot{\underline{\epsilon}}^p}{|\dot{\underline{\epsilon}}^p|}$ is shown on Figure 3-15 for compression (where coaxiality results in unity value), torsion, torsion after 50% compressive prestrain and tension after 50% torsional prestrain. After a compressive prestrain, the direction of $\underline{\alpha}$ quickly evolves to near that of pure torsion. The direction of $\underline{\alpha}$ during tension after torsional prestrain evolves more slowly towards coaxiality. This is consistent with the high initial strain-hardening rate observed on the torsion-followed-by-tension experimental data (Figure 3-14).

This “simplified version” of Miller’s hardening model uses 9 parameters : C^* , A , α_{sat} , R_{sat} , m^R , q^R , m^α , q^α , ζ . In fact the complete version requires 18 parameters as each hardening variable is doubled in order to have 2 hardening sets : the first one reflects the slip interaction phenomena and the second one the deformation induced anisotropy. Details can be found in Miller & Mc Dowell 1996.

These authors apply their model to predict the experimental results shown on Figure 3-14. Simulation and experiment results are very close. From this comparison, one

could believe that this model solves all the problems. However, as underlined in Miller *et al.* 1995, the first invariant J_3^* is 0 for a plane strain compression as for a torsion test while their equivalent stress-strain curves do not coincide (see Figure 3-16). In the same paper, a classical Taylor's polycrystal model has been modified to reproduce this experimental behavior. The average Taylor's factor has been added to the internal variables to modify the hardening functions and this improved model predicts the difference in stress-strain curves.

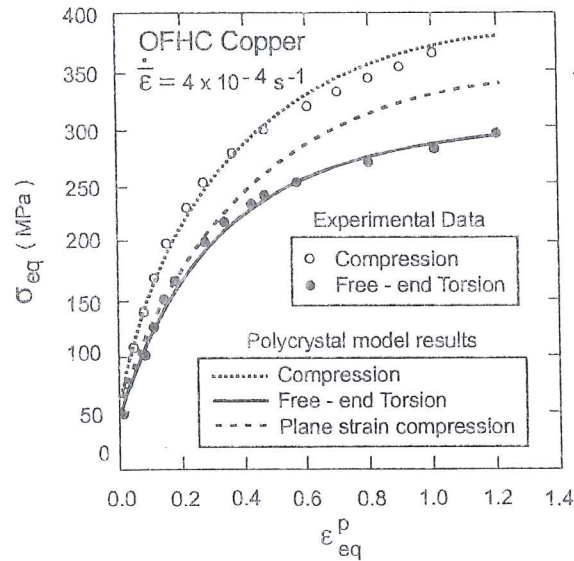


Figure 3-16 Comparison of experimental and simulated stress-strain curves for compression, torsion and plane strain compression (from Miller *et al.* 1995).

3.5.5. Teodosiu's model

Teodosiu & Hu 1998 propose a work-hardening model for cold deformation of metals, able to reproduce experimental observations such as the influence of a pre-deformation on the subsequent work-hardening behavior. For instance, this model can predict the observed work-hardening stagnation under reversed deformation at large strains and the work-softening during a subsequent orthogonal deformation. Dedicated to room temperature behavior, the model neglects viscous effects. Another assumption is that the evolution of the dislocation structure is the predominant effect at moderately large strains, with the influence of the initial texture. The effect of texture evolution is neglected.

This macroscopic model by Teodosiu is different from his microscopic one presented in Chapter 5. So, in the notations table, both Teodosiu's models appear with "micro" or "macro" identification.

Teodosiu and Hu assume that the plastic behavior of metals depends not only on the current state of deformation but also on the deformation history. This influence of the

deformation history can reasonably be represented by the current values of a sufficient number of microstructural parameters, called internal variables.

The complete set of internal state variables of this model is denoted by $(\underline{S}, \underline{P}, \underline{\alpha})$. \underline{S} and $\underline{\alpha}$ have the dimension of stress, \underline{P} has no dimension. \underline{S} is a fourth-order tensor, \underline{P} and $\underline{\alpha}$ are second-order tensors. For a well-annealed material, all their initial values are zero.

The first tensor variable \underline{S} describes the directional strength of an intragranular structure. For instance, after a sufficient amount of monotonic deformation, persistent dislocation structures gradually form. In this stage of work-hardening, plastic slip is mainly carried out by one slip system and the dominant persistent dislocation structures are planar arrays, which are more or less parallel to the main slip plane and which will be called "*dislocation sheets*". The misorientation across a dislocation sheet is closely connected with its polarity. Here the term "*polarity*" means that, on each side of the sheet, there exists an excess of dislocations of the same sign, this sign being different on each side of the sheet.

In the present model, \underline{S} is the most important variable describing the evolution of the dislocation structures. The choice of its order is due to the necessity to describe the anisotropic contribution of persistent dislocation structures to the flow stress.

The second tensor variable \underline{P} is associated with the polarity of the persistent dislocation structures, which is due to the excess of dislocations of the same sign on each side of a dislocation sheet. When a microstructure is not at all polarized, $\underline{P} = \underline{0}$. On the other hand, when a microstructure is completely polarized after a monotonic deformation, then $\underline{P} = \underline{N}_{\dot{\epsilon}^p}$ where $\underline{N}_{\dot{\epsilon}^p}$ is the direction of the plastic strain rate tensor defined by :

$$\underline{N}_{\dot{\epsilon}^p} = \frac{\dot{\underline{\epsilon}}^p}{|\dot{\underline{\epsilon}}^p|} \quad (3-43)$$

therefore, it is assumed, without loss of generality, that $0 < |\underline{P}| < 1$.

The third variable $\underline{\alpha}$ describes the back stress due to microscopic heterogeneous deformation, for instance dislocation pile-ups. It corresponds to the traditional kinematic hardening in the macroscopic framework and allows to describe typical effects of large-amplitude cyclic deformations, including cyclic hardening or softening.

This model is now applied to a yield criterion described by a fourth order tensor \underline{L} representing the initial anisotropy.

Teodosiu assumes that texture is responsible of this anisotropy and neglects texture evolution. So, any phenomenological yield locus defined in Chapter 2 could be used.

$$F_p = \sigma_{eqa} - \sigma_o - m|S| = 0 \quad (3-44)$$

where σ_o is the initial yield stress, $m|S|$ represents the isotropic hardening related to the persistent dislocation structures, and $\hat{\sigma}$ the deviatoric Cauchy stress; σ_{eqa} is the anisotropic equivalent stress defined by $\sqrt{(\hat{\sigma} - \underline{\alpha}) : \underline{L} : (\hat{\sigma} - \underline{\alpha})}$.

For simplicity, a rigid plastic version of the model is presented and all the tensor derivatives are assumed to be objective rates. The plastic deformation rate is given by the associated flow rule :

$$\underline{\dot{\epsilon}}^p = \dot{\lambda} \frac{\partial F_p}{\partial \underline{\sigma}} = \frac{\dot{\lambda}}{\sigma_{eqa}} \underline{L} : (\hat{\sigma} - \underline{\alpha}) \quad (3-45)$$

where $\dot{\lambda}$ is the plastic multiplier and a superposed dot denotes time differentiation. $\dot{\lambda}$ is zero within the rigid region or during rigid unloading. During a plastic loading process, $\dot{\lambda}$ is positive and determined by the consistency condition. The anisotropic equivalent strain rate $\dot{\epsilon}_{eqa}^p$ is defined as the term conjugated with σ_{eqa} to produce the dissipation power :

$$\sigma_{eqa} \dot{\epsilon}_{eqa}^p = (\hat{\sigma} - \underline{\alpha}) : \underline{\dot{\epsilon}}^p \quad (3-46)$$

Using preceding relations, one can check that $\dot{\lambda} = \dot{\epsilon}_{eqa}^p$. Using (3-45) and (3-46), the anisotropic equivalent strain rate can be expressed by :

$$\dot{\epsilon}_{eqa}^p = \dot{\lambda} = \sqrt{\underline{\dot{\epsilon}}^p : \underline{L}^{-1} : \underline{\dot{\epsilon}}^p} \quad (3-47)$$

Finally relations (3-47) and (3-45) yield :

$$\hat{\sigma} - \underline{\alpha} = \sigma_{eqa} \frac{\underline{L}^{-1} : \underline{\dot{\epsilon}}^p}{\sqrt{\underline{\dot{\epsilon}}^p : \underline{L}^{-1} : \underline{\dot{\epsilon}}^p}} = \sigma_{eqa} \frac{\underline{L}^{-1} : \underline{N}_{\dot{\epsilon}^p}}{\sqrt{\underline{N}_{\dot{\epsilon}^p} : \underline{L}^{-1} : \underline{N}_{\dot{\epsilon}^p}}} = \sigma_{eqa} \underline{n} \quad (3-48)$$

which defines tensor \underline{n} .

The evolution laws of the internal variables are written in a work-hardening recovery format which takes into account the mechanisms of formation and dissolution of dislocation structures. For sufficiently large, monotonic strains, all internal variables are supposed to reach some saturation values, which correspond to the balance between work-hardening and recovery.

The evolution of the polarity tensor \underline{P} is described by the evolution equation :

$$\overset{\nabla}{\underline{P}} = C_p (\underline{N}_{\dot{\epsilon}^p} - \underline{P}) \dot{\epsilon}_{eqa}^p \quad (3-49)$$

where C_p characterizes the polarization rate of the persistent dislocation structures

and $\underline{N}_{\dot{\epsilon}^p}$ denotes the current direction of the strain rate tensor. Whatever the initial value of \underline{P} , $|\underline{P}|$ will approach unity and \underline{P} will tend to $\underline{N}_{\dot{\epsilon}^p}$, whenever the strain rate direction $\underline{N}_{\dot{\epsilon}^p}$ remains unchanged for an amount of deformation which is sufficiently large with respect to $1/C_p$.

In the case of cyclic plasticity at small strain amplitudes, Chaboche and Rousselier, 1983 have used a kinematic hardening law of the form :

$$\dot{\underline{\alpha}} = C_\alpha (\alpha_{sat} \underline{N}_{\dot{\epsilon}^p} - \underline{\alpha}) \dot{\epsilon}_{eq}^p \quad (3-50)$$

where C_α characterizes the saturation rate of $\underline{\alpha}$, and α_{sat} is a material parameter characterizing the saturation value of $|\underline{\alpha}|$. In the present model, however, α_{sat} will be considered as a function of the persistent dislocation structures, via the internal variable \underline{S} . Thus, the backstress $\underline{\alpha}$ will describe not only the rapid variations of the flow stress following a change in the strain path, but also the new stationary states that are asymptotically approached after the changes in the strain path.

C_α has a higher value than C_p and $\underline{\alpha}$ approaches its saturation value faster than \underline{P} and \underline{S} after a few percents of strain increment, provided the strain rate tensor remains self-coaxial.

In the anisotropic case, equation (3-50) is generalized to

$$\dot{\underline{\alpha}} = C_\alpha (\alpha_{sat} \underline{n} - \underline{\alpha}) \dot{\epsilon}_{eq}^p \quad (3-51)$$

Taking (3-48) into account, this equation can be rewritten in the form :

$$\dot{\underline{\alpha}} = C_\alpha \left[\frac{\alpha_{sat}}{\sigma_{eqa}} (\hat{\sigma} - \underline{\alpha}) - \underline{\alpha} \right] \dot{\epsilon}_{eq}^p \quad (3-52)$$

which shows that, in the present setting, $\underline{\alpha}$ becomes asymptotically coaxial with $\hat{\sigma}$. α_{sat} is assumed to be given by :

$$\alpha_{sat} = \alpha_{sat}^o + (1-m) \sqrt{S_D^2 + qS_L^2} \quad (3-53)$$

where α_{sat}^o is the initial value of α_{sat} and the second term corresponds to the effect of the planar persistent dislocation structure. $(1-m)$ denotes the contribution of the intergranular structure to kinematic hardening. S_D and S_L are given by the decomposition :

$$\underline{S} = S_D \underline{N}_{\dot{\epsilon}^p} \otimes \underline{N}_{\dot{\epsilon}^p} + \underline{S}_L \quad (3-54)$$

$$S_L = |\underline{S}_L| \quad \text{and} \quad S_D = \underline{N}_{\dot{\epsilon}^p} : \underline{S} : \underline{N}_{\dot{\epsilon}^p} \quad (3-55)$$

So S_D is the strength of the dislocation structure associated with the currently active slip systems whereas S_L is related to the persistent dislocation structure. It is called a latent part of directional strength. q is a material parameter introduced to describe the fact that S_L , the latent dislocation term, has a stronger contribution than S_D , the currently active dislocation term ($q > 1$).

The physical argument for decomposing \underline{S} is explained hereafter. When a metal is deformed from a well-annealed initial state, dislocation sheets or cells develop roughly parallel to the active slip planes. On the other hand, for a severely cold-deformed material subject to a subsequent orthogonal deformation, the strain rate is highly localized. The microbands are parallel to the newly active slip planes and, between them, new dislocation sheets are gradually formed. This experimental evidence strongly suggests that dislocation structures associated with the current direction of the strain rate evolve quite differently from the rest of the persistent dislocation structures.

In order to describe the evolution of S_D , Teodosiu and Hu propose :

$$\dot{S}_D = C_S [g(S_{sat} - S_D) - hS_D] \dot{\epsilon}_{eq}^p \quad (3-56)$$

where C_S characterizes the saturation rate of S_D , S_{sat} denotes the saturation value of S_D . h is a function of $\underline{\alpha} : \underline{N}_{\dot{\epsilon}^p}$ and g is a function of S_D and $\underline{P} : \underline{N}_{\dot{\epsilon}^p}$ describing the influence of the polarity. Neglecting the influence of g and h , i.e. setting $g=1$, $h=0$, the above equation describes a gradual saturation of S_D towards S_{sat} , corresponding to the formation and saturation of planar persistent dislocation structures associated with $\underline{N}_{\dot{\epsilon}^p}$. In order to form dislocation sheets or cell walls, the amount of deformation along which $\underline{N}_{\dot{\epsilon}^p}$ remains unchanged, should be larger than $1/C_S$.

The function h is defined as :

$$h = \frac{1}{2} \left(1 - \frac{\underline{\alpha} : \underline{N}_{\dot{\epsilon}^p}}{\alpha_{sat} \underline{n} : \underline{N}_{\dot{\epsilon}^p}} \right) \quad (3-57)$$

Experimental evidence shows that, for a severely prestrained material under a subsequent reversed deformation, there exists a work-hardening stagnation, followed by a resumption of work-hardening. This phenomenon is described via function g . Specifically, denoting :

$$P_D = \underline{P} : \underline{N}_{\dot{\epsilon}^p} \quad (3-58)$$

it is assumed that :

$$g = \begin{cases} 1 - \frac{C_p}{C_s + C_p} \left| \frac{S_D - P_D}{S_{sat}} \right| & \text{if } P_D \geq 0 \\ (1 + P_D)^{n_p} \left(1 - \frac{C_p S_D}{C_s + C_p S_{sat}} \right) & \text{otherwise} \end{cases} \quad (3-59)$$

Clearly, g is continuous with respect to P_D . Assume that a material is first severely

deformed at a constant strain rate with direction \underline{N}_1 ; then, according to (3-49), at the end of this deformation, the polarity tensor \underline{P} will be practically equal to \underline{N}_1 . If the material is subsequently subject to a reversed deformation, i.e. $\underline{N}_2 = -\underline{N}_1$, then, by (3-58) and (3-59), $P_D = -1$ and $g = 0$. Considering also (3-56), it may be shown that the latter condition corresponds to a stagnation of work-hardening.

Teodosiu and Hu finally discuss the evolution of S_L , which results from the interaction between microbands and preformed microstructures. Two physical mechanisms are possible : the annihilation of dislocations in the preformed structures and the softening of the preformed structure after being sheared by microbands. Both mechanisms reduce the strength of the preformed structures, represented by S_L . Hence the following evolution equation is proposed to describe these phenomena :

$$\dot{\underline{S}}_L = -C_S \left(\frac{S_L}{S_{sat}} \right)^{n_L} \underline{S}_L \dot{\epsilon}_{eq}^P \quad (3-60)$$

where n_L is a positive material parameter.

The factor $(S_L/S_{sat})^{n_L}$ is introduced in order to explain the influence of the amount of prestrain ϵ_{ps} . For a severely deformed material under a subsequent orthogonal deformation, the percentage of grains containing microbands increases with the prestrain ϵ_{ps} . Since the decrease of S_L is mainly due to the interaction between microbands and preformed microstructures, the decreasing rate of $|S_L|$ should increase with ϵ_{ps} . When ϵ_{ps} is very small, $S_L \ll S_{sat}$, hence the evolution of \underline{S}_L is negligible, whereas when ϵ_{ps} is large, S_L approaches S_{sat} , and the evolution of \underline{S}_L is speeded up.

The identification of the model parameters is described in Hu 1992. Only mechanical tests with 3 strain paths are needed to find the 9 parameters :

- monotonic tensile or shear tests allow to fit α_0 , S_{sat} , C_S ($C_P = C_S$ at low homologous temperature), C_α ;
- stress reversal tests are used to reach m , n_p ;
- orthogonal sequences in strain path are needed to get q , n_L .

The validation of the model is checked by comparison of predictions and experiments. Figure 3-17 presents the behavior of a sheet under a monotonic shear until 53 % and a subsequent reversed shear, in the rolling direction. Figure 3-18 shows the shear-plastic work curve for one monotonic shear (first curve), then for 2 cases where the monotonic shear is stopped, unloaded and subsequently followed by a shear test in an orthogonal direction.

The implementation of this model in a Marciniak Kuczynski's model to predict Forming Limit Diagrams has produced results which agree with well-known effects

of strain path modification (Hiwatashi *et al.*, 1998). The coupling of this model with a yield locus described by a texture approach (Hoferlin *et al.*, 1999) has been implemented into a FEM code.

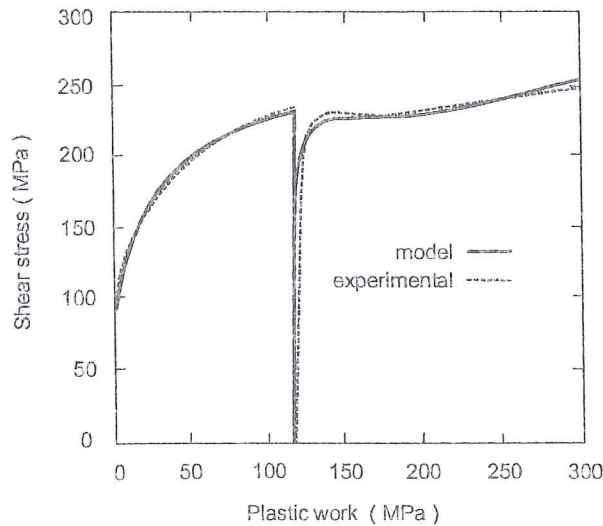


Figure 3-17 Experimental results and model correlation for AKDQ mild steel under reversed shear. The amount of preshear is 53%, from Teodosiu & Hu 1998.

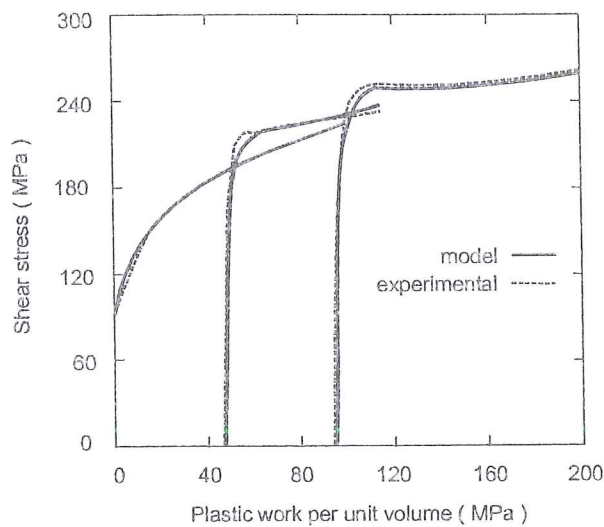


Figure 3-18 Experimental results and model correlation for AKDQ mild steel under orthogonal shear tests, from Teodosiu & Hu 1998.

3.6. Conclusion

The previous hardening models are only a few of those available in the prolific literature on this topic. The choice of one hardening model depends on different factors such as :

- significant strain rate effect or not,
- significant temperature effect or not,
- needed accuracy,
- the model use: description of monotonic loading, or cycles or complex strain paths such as initial shear followed by tension or followed by shear in an orthogonal direction or both...,
- the available tests to identify the model parameters.

The microscopic roots for models such as Teodosiu & Hu's model help to choose physical internal variables. This approach avoids a too high number of variables, as could happen if, starting from a classical isotropic, kinematic hardening model, one tried to improve it in order to describe complex strain paths.

Let us note that according to Vegter *et al.* 1999, Bergström-van Liempt-Vegter's model needs only the identification of 4 parameters, if similar materials have already been identified.

This chapter has presented both hardening types :

- the geometrical one, related to texture evolution, described with more details in chapter 4;
- the material one, related to dislocation density, dislocation cells, which can again be subdivided into direct and latent hardening as these substructures change with deformation.

The respective weight of geometrical and material hardening components depends on the material state, as studied by Winther *et al.* 1997.

Chapters 5 and 6, dealing with behavior models implemented in FEM codes, will show some choices made by scientists working in sheet metal forming simulation.

References

- Bergstrom, Y. (1969/70) A dislocation model for the stress strain behaviour of polycrystalline α -Fe with special emphasis on the variation of the densities of mobile and immobile dislocations, *Mat. Sci. Eng.*, **5**, 179-192.
- Bunge, H.J. (1982) *Texture Analysis in Materials Science*, Butterworths Publishers, London.
- Chaboche, J.L., Rousselier, G. (1983) On the plastic and viscoplastic constitutive equations, Parts I and II, *ASME, J. Pressure Vessel Technol.*, **105**, 153-165.
- Dafalias, Y.F., Popov, E.P. (1975) A model of nonlinearly hardening materials for complex loading, *Acta Mech.*, **21**, 173.
- Estrin Y., Mecking, H., (1984) *Acta Metall.*, **32**, 57.
- Ewing, J.A., Rosenhain, W. (1900) The crystalline structure of metals; *Phil. Trans. R. Soc.*, London, **193**, 353.
- Follansbee, P.S., Kocks, U.F. (1988) A constitutive description of the deformation of copper based on the use of the mechanical threshold stress as an internal state

- variable, *Acta Metall.*, **36/1**, 81-93.
- Frenckel J. (1926) Zur Theorie der Tlastizitätsgrenze und dert gestigkeit kristallinischer Körper, *Z. Phys.*, **37**, 572-609.
- Hiwatashi, S., Van Bael, A., Van Houtte, P., Teodosiu, C. (1998) Prediction of forming limit strains under strain-path changes : application of anisotropic model based on texture and dislocation structure. *Int. J. of Plasticity*, **14/7**, 647-669.
- Hoferlin, E., Van Bael, A., Hiwatashi, S., Van Houtte, P. (1998) Influence of texture and microstructure on the prediction of forming limit diagram, 19th RISO *Symposium on Materials Science*, 7-11 Sept. 1998.
- Hoferlin, E., Van Bael A., Van Houtte P., Teodosiu C. (1999) An accurate model of texture and strain-path induced anisotropy, Numisheet'99, 13-17 September 1999, Besançon, France, 91.
- Hoferlin, E. (2001) Incorporation of an accurate model of texture and strain-path induced anisotropy in simulations of sheet metal forming, Ph.D thesis , Katholieke universiteit Leuven.
- Holt, D.L. (1970) Dislocation cell formation in metals, *J. Appl. Phys.*, **41**, 3197-3201.
- Hu, Z. (1992) Lois de comportement des métaux en grandes transformations tenant compte de l'évolution de la microstructure, Institut National Polytechnique de Grenoble et Université de Paris-Nord, thèse de doctorat.
- Huétink, J., Streppel, A.H., Vreede, P.T. (1995) Development and experimental verification of constitutive equations for anisotropic sheet metal, *Computational Plasticity – Fundamentals and applications*, Proceedings of the fourth international conference held in Barcelona, Spain, 3-6 April 1995, Owen and Onate Eds, Pineridge Press.
- Khan A.S., Huang S. (1995) Continuum theory of plasticity, Wiley & Sons Eds.
- Krabiell, A., Dahl, W. (1982) Zum Einfluss von Temperatur und Dehngeschwindigkeit auf die Streckgrenze von Baustählen unterschiedlicher Festigkeit. *Arch. Eisenhüttenwesen*, **52**, 429-436.
- Krieg, R.D. (1975) A practical two surface plasticity theory. *Journal of applied mechanics*, 641-646.
- Magnée, A. (1994) Physique du solide, notes de cours de la Faculté des Sciences Appliquées, Université de Liège.
- Mandel, J. (1971) Plasticité classique et viscoplasticité (Courses and Lectures **97**), CISM, Udine, Springer, New York.
- Maudlin, P.J., Bingert J.F., House J.W., Chen S.R. (1999) On the modeling of the Taylor cylinder impact test for orthotropic textured materials : experiments and simulations, *Int. J. Plasticity*, **15**, 139-166.
- Miller, M.P., Mc Dowell, D.L. (1994) Stress State Dependent Deformation Behaviour of FCC Polycrystals, in *Numerical Predictions of Deformation Processes and the Behaviour of Real Materials*, Andersen, Bilde-Sorensen, Lorentzen, Pedersen, Sorensen Eds, Riso National Labs, Roskilde, Denmark, 421.
- Miller, M.P., Dawson P.R., Bammann, D.J. (1995) Reflecting microstructural evolution in hardening models for polycrystalline metals, *Simulation of*

-
- Materials Processing : Theory, Methods and Applications*, Shend&Dawson Eds, 1995, Balkema.
- Miller, M.P., Mc Dowell, D.L. (1996) Modeling large strain multiaxial effects in FCC polycrystals, *Int. J. of Plasticity*, 12/7, 875-902.
- Mroz, Z. (1967) On the description of anisotropic work-hardening. *J. Mech. Phys. Solids*, 15, 163.
- Pijlman, H.H., Huétink, J., Carleer, B.D., Vegter, H. (1998) Application of the Vegter yield criterion and a physically based hardening rule on simulation of sheet forming, *Simulation of Materials Processing : Theory, Methods and Applications*, Balkema, Huétink & Baaijens Eds.
- Phillips, A., Lee, C.W. (1979) Yield surfaces and loading surfaces. Experiments and recommendations, *Int. J. Solids & Structures*, 15, 715-729.
- Prager, W. (1955) The theory of plasticity : a survey of recent achievements. *Proc. Inst. Mech. Eng.*, 169, 41.
- Rietman, A.D., Van Liempt, P., Huétink, H. (1997) The modeling of compression tests with a physically based material model using finite elements, *Computational plasticity – fundamentals and applications*, Owen, Onate & Hinton Eds.
- Schmitz A. (1995) Development and experimental validation of a coupled thermal, mechanical and textural model for ferritic hot-rolling of steel, Faculty of Engineering of the Catholic University of Leuven.
- Teodosiu, C., Hu, Z. (1998) Microstructure in the continuum modelling of plastic anisotropy, *Proceedings of the 19th Riso Int. Symp. on Materials Science : Modelling of Structure and Mechanics of Materials from Microscale to Products*, Carstensen, J.V., Leffers, T. Eds.
- Van Bael, A. (1994) Anisotropic yield loci derived from crystallographic data and their application in finite element simulations of plastic forming processes, proefschrift voorgedragen tot het behalen van het doctoraat in de toegepaste wetenschappen, Katholieke Universiteit Leuven.
- Van Houtte, P. (1985) Development of textures by slip and twinning, *Preferred orientation in deformed metals and rocks : an introduction to modern texture analysis*, H.R. Wenk Ed., Academic Press, New-York, 233-258.
- Van Houtte, P. (1988) A comprehensive mathematical formulation of an extended Taylor-Bishop-Hill model featuring relaxed constraints, the Renouard-Wintenberger theory and a strain rate sensitivity model, *Textures and Microstructures*, 8-9, 313-350.
- Van Houtte, P. (1995) Micromechanics of polycrystalline materials, Chaire Francqui, Université de Liège.
- Van Liempt, P. (1994) Workhardening and substructural geometry of metals, *J. Mater. Process. Technol.*, 45, 459-464.
- Vegter, H. (1991), On the plastic behaviour of steel during sheet forming, Dissertation, University of Twente.
- Vegter, H., An Y., Pijlman H.H., Huétink J. (1999), Different approaches to describe the plastic material behaviour of steel and aluminium-alloys in sheet forming, 2nd ESAFORM Conference on Material Forming, Guimaraes, Portugal, Covas J.A. Ed.

- Winther, G., Jensen D.J., Hansen N. (1997) Modelling flow stress anisotropy caused by deformation induced dislocation boundaries, *Acta Mater.*, **45/6**, 2455-2465.
- Ziegler, H. (1959) A modification of Prager's hardening rule. *Quart. Appl. Math.*, **17**, 55.

4. MICROSCOPIC MODELS AND MICRO-MACRO APPROACHES

4.1. Taylor's single crystal plasticity model

4.1.1. Description

At the crystal level, the plastic microscopic velocity gradient generated by a particular slip system s is given by:

$$L_{ij}^s = K_{ij}^s \dot{\gamma}^s \quad (4-1)$$

where Schmid's tensor K_{ij}^s is defined by relation (3-1) and $\dot{\gamma}^s$ is the slip rate acting on this slip system s . In practice, multiple slips occur together. Hence the microscopic velocity gradient applied on a crystal \underline{L}^{micro} is given by :

$$\underline{L}^{micro} = \sum_s \underline{L}^s + \underline{\Omega}^L \quad (4-2)$$

where $\underline{\Omega}^L$ is the rate of crystal lattice rotation.

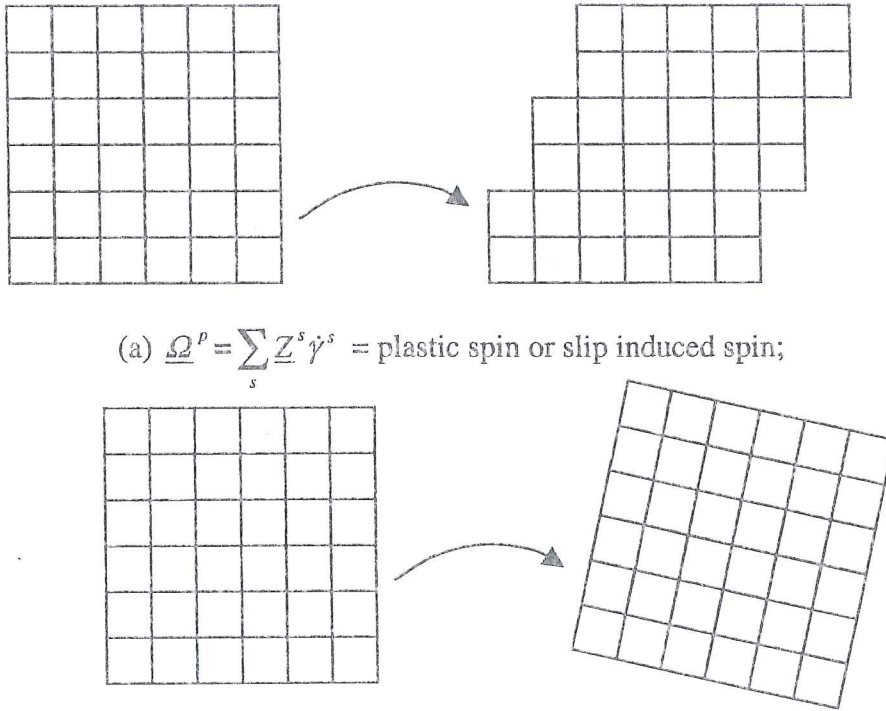
The establishment of this well-known relation is recalled in van Houtte 1995. Its link with the classical formalism of Continuum Mechanics will be summarized in Section 4.4.

Assuming for simplicity that elastic strains are small and can be neglected, as in Asaro & Needleman 1985, Becker 1990, Neale 1993 or Dawson 1997, this microscopic velocity gradient can be split into a microscopic plastic deviatoric strain rate $\underline{\dot{\epsilon}}^{p micro}$ and a microscopic spin $\underline{\Omega}^{micro}$:

$$\underline{\dot{\epsilon}}^{p micro} = sym(\underline{L}^{micro}) = \sum_s \underline{A}^s \dot{\gamma}^s \quad (4-3a)$$

$$\underline{\Omega}^{micro} = skw(\underline{L}^{micro}) = \sum_s \underline{Z}^s \dot{\gamma}^s + \underline{\Omega}^L \quad (4-3b)$$

where \underline{A}^s and \underline{Z}^s are respectively the symmetric and skew-symmetric parts of Schmid's tensor \underline{K}^s . The 2 components of the microscopic spin $\underline{\Omega}^{micro}$ are symbolically represented on Figure 4-1. The first term of (4-3b), $\sum_s \underline{Z}^s \dot{\gamma}^s$, is called plastic spin $\underline{\Omega}^p$.



(a) $\underline{\Omega}^p = \sum_s \underline{Z}^s \dot{\gamma}^s$ = plastic spin or slip induced spin;

(b) $\underline{\Omega}^l$ = rate of crystal lattice rotation as a rigid body, used to update texture.

Figure 4-1 Representation of the 2 terms of the crystal microscopic spin, from the slides presented at NUMISHEET 1999, (Duchêne *et al.* 1999).

Several different combinations of slip rates may achieve the prescribed strain rate. According to Taylor 1938, the one which minimizes the power dissipation is chosen:

$$\dot{W}^p = \sum_s \tau_c^s |\dot{\gamma}^s| = \min \quad (4-4)$$

Taylor roughly assumes that all slip systems have a common value τ_c of their *Critical Resolved Shear Stress* τ_c^s . The CRSS concept has been introduced in section 3.1. This common value τ_c is reasonable for annealed condition. A weaker hypothesis, proposed by van Bael 1994, consists in using proportional CRSS τ_c^s inside a particular crystallite. It is expressed by constant ratios to a *common reference CRSS* τ_c :

$$\alpha^{\pm s} = \tau_c^{\pm s} / \tau_c \quad (4-5)$$

For instance, for b.c.c crystal, van Bael 1994 has :

$$\alpha^{\pm /110 / \langle 111 \rangle} = 1 \quad \alpha^{\pm /112 / \langle 111 \rangle} = 0.95 \quad (4-6)$$

where Miller's indices describe the slip system s . The sign \pm appears because the slip system can be extended to pseudo-slip systems representing twinning. In this

case, slip in anti-twinning direction must be prohibited : $\tau_c^{-s} = \infty$ (van Houtte & Wagner 1985).

The prescribed strain rate $\dot{\underline{\epsilon}}^{p\ micro}$ can be split into a scalar magnitude $\dot{\epsilon}_{eq}^p$ computed by the classical von Mises' formula and a *strain rate mode* $\underline{U}_{\dot{\epsilon}^p}$ very close to the $\underline{N}_{\dot{\epsilon}^p}$ direction of the plastic strain rate in Teodosiu's model (Section 3.5.5) :

$$\underline{U}_{\dot{\epsilon}^p} = \underline{\dot{\epsilon}}^{p\ micro} / \dot{\epsilon}_{eq}^p \quad (4-7)$$

Introducing also the slip rate $\dot{\gamma}_{scaled}^s$ per unit equivalent strain rate :

$$\dot{\gamma}_{scaled}^s = \dot{\gamma}^s / \dot{\epsilon}_{eq}^{p\ micro} \quad (4-8)$$

advantage can be taken of the assumed strain-rate insensitivity to simplify the formulation. Indeed, dividing relation (4-4) by the strain rate magnitude and the reference CRSS τ_c leads to :

$$\frac{\dot{W}^p}{\dot{\epsilon}_{eq}^{p\ micro} \tau_c} = \sum_s \alpha_s |\dot{\gamma}_{scaled}^s| = \text{minimum} \quad (4-9)$$

with, according to equation (4-3a), the minimization constraint :

$$\underline{U}_{\dot{\epsilon}^p} = \sum_s \underline{A}^s \dot{\gamma}_{scaled}^s \quad (4-10)$$

These two equations are called Taylor's equations and may be solved efficiently by means of linear programming (Simplex Method) as explained by van Houtte 1988. This approach has been implemented in the LAGAMINE code by Munhoven 1997. The solution $\dot{\gamma}_{scaled}^s$ depends only on the prescribed strain mode $\underline{U}_{\dot{\epsilon}^p}$ and it does not depend on the magnitude $\dot{\epsilon}_{eq}$ or on the value of the reference CRSS τ_c .

In the Simplex Method, relation (4-9) is called the cost function, to be minimized under the constraint (4-10). This primal problem in the space of slip rates is transformed into a dual problem where the stresses are now the independent variables. In the stress space, the value $\dot{W}^p / \dot{\epsilon}_{eq}^{p\ micro} \tau_c$ (4-9) represents a maximum :

$$\frac{\dot{W}^p}{\dot{\epsilon}_{eq}^{p\ micro} \tau_c} = \underline{U}_{\dot{\epsilon}^p} : \frac{\underline{\sigma}^{micro}}{\tau_c} = \text{maximum} \quad (4-11)$$

This retrieves the approach proposed by Bishop-Hill, which assumes that the admissible stress states satisfy the yield locus constraints expressed by relation (3-3) (see section 3.1) and that the real stress state maximizes the external plastic work. Taylor's and Bishop-Hill's methods are strictly equivalent, that is why they are very often referred to as the *Taylor-Bishop-Hill (TBH) crystal model*.

The Simplex Method produces both slip rates and microscopic stresses at the crystal level. In practice, using the same CRSS τ_c for all slip systems leads to multiple solutions (set of activated slip systems). Each set achieves the prescribed strain rate (4-3a) with the same minimum power dissipation (4-9). Van Houtte 1988 proposes different methods to choose one particular solution. The approach implemented by Munhoven 1997 just stops at the first computed solution. From an energy point of view, all the solutions are equivalent. However, they produce different slip rates, microscopic stresses and hence different crystal lattice rotations. Once the set of active slip systems and the corresponding slip rates are known by the resolution of equations (4-9), (4-10), the crystal rotation $\underline{\Omega}^L$ produced by one imposed velocity gradient can be reached using relation (4-3b). It is expressed by:

$$\underline{\Omega}^L = \underline{\Omega}^{micro} - \sum_s \underline{Z}^s \dot{\gamma}^s \quad (4-12)$$

If a texture is described by a set of representative crystals orientations (Tóth & van Houtte 1992), the rotation of each representative crystal leads to the up-dated texture. Taylor's assumption about an homogeneous velocity gradient:

$$\underline{L}^{macro} = \underline{L}^{micro} \quad (4-13)$$

allows to easily update texture with the help of the previous relations. This will be extensively used in the micro-macro approaches presented hereafter.

This Taylor's model is of common use in scientific works dedicated to micro-macro approaches (van Houtte *et al.* 1989, Hirsch 1991, Winther *et al.* 1997, Aukrust *et al.* 1997)

4.1.2. Taylor's factor

$M(g, \underline{U}_{\epsilon^p})$ is the Taylor's factor associated with a crystal of orientation g for a given strain mode $\underline{U}_{\epsilon^p}$. It is conventionally derived from the plastic power dissipation per unit volume \dot{W}^p by the following relation:

$$M(g, \underline{U}_{\epsilon^p}) = \frac{\dot{W}^p}{\dot{\epsilon}_{eq}^{p,micro} \tau_c} = \sum_s \alpha_s |\dot{\gamma}_{scaled}^s| = \frac{1}{\tau_c} \sigma_{ij}^{micro}(U_{\epsilon^p})_{ij} \quad (4-14)$$

Physically, it represents a certain amount of dislocation glide rate associated to the crystal orientation and to the applied strain rate.

4.2. Strain rate sensitivity approach for single crystal plasticity model

Another approach issued from the theory of thermally activated dislocation glide consists in adopting a viscoplastic flow rule :

$$\dot{\gamma}^s = \dot{\gamma}_0 \left| \frac{\tau^s}{\tau_c^s} \right|^{1/n} \text{sign}(\tau^s) \quad (4-15)$$

where $\dot{\gamma}^s$ is the slip rate on the slip system s , $\dot{\gamma}_0$ is a reference slip rate defined so that $|\dot{\gamma}^s| = \dot{\gamma}_0$ when $|\tau^s| = \tau_c^s$ and the parameter n characterizes the material rate-sensitivity. Under isothermal conditions and in a narrow range of strain rates, the hereabove simple power-law equation has proven its validity. For cold deformation, the rate sensitivity is rather low and the stress dependence on the slip rate can be reasonably approximated with n close to 0. The slip system shear rate $\dot{\gamma}^s$ does not vanish as long as the resolved shear stress τ^s on the corresponding slip system s is not identically zero. It keeps however a low value if τ^s is not close to τ_c^s . This equation applies a posteriori the activation condition defined by Schmid's law by filtering out the inactive systems. It has been widely used (Asaro & Needleman 1985, Anand *et al.* 1997) to overcome the problem of non uniqueness in selecting a set of active systems by the TBH approach.

For cold rolling and biaxial sheet stretching, Neale 1993 asymptotically sets $n \rightarrow 0$ in relation (4-15) to recover the rate independent response. His comparison with the TBH results reveals that:

- the plastic work and active slip systems are identical;
- the unique stress derived from (4-15) and (3-2) corresponds to the average of the active yield surface vertices involved in the Bishop-Hill solutions;
- the active shear rates and lattice spins are identical for situations where no slip system ambiguity results from the TBH analysis.

Anand & Kothari 1996 use FEM simulations of tensile and compression tests to check that both texture and stress results computed by the viscoplastic approach with $n \rightarrow 0$ or by the TBH method are very close to each other.

4.3. Evolution rule for CRSS value

Whatever the solution chosen to model single crystal behavior (TBH model or viscoplastic flow rule), the CRSS τ_c^s appears and evolves in a different way for each individual slip system s . This implies the knowledge of the initial value of τ_c^s as well as its evolution equation. Slip on any slip system generally induces hardening for all slip systems. This is taken into account by adopting an evolution equation of the CRSS of the form :

$$\dot{\tau}_c^s = \sum_u h^{su} \dot{\gamma}^u \quad (4-16)$$

where h^{su} is the so called hardening matrix. Diagonal components of this matrix correspond to the self-hardening effect, while off-diagonal components describe

cross-hardening effects. Franciosi 1988 proposes an evolution rule for the components of this matrix. This rule depends on the pair of slip systems, their shearing rates and their temperature. This approach could seem sophisticated. However, it is still not accurate enough. The fact that hardening defined by one fixed structure of dislocations is affected by structure modification is not taken into account.

Of course, the macroscopic hardening concept, which links the flow stress to the dislocation density and the microstructure (see chapter 3), applies to the CRSS. So, as presented by Anand 1977, the CRSS can be decomposed into two additive components:

- $(\tau_c^s)_t$ representing the resistance to slip due to “thermal” obstacles. This means obstacles that thermal activation can overcome such as solute atoms, forest dislocations, Peierls' resistance;
- $(\tau_c^s)_a$ representing the resistance to slip due to “athermal” obstacles (that thermal energy is unable to overcome) such as dislocation walls and large incoherent precipitates.

Since, for pure b.c.c materials, $(\tau_c^s)_t$ is controlled by the interactions with the Peierls' lattice resistance, it is reasonable to assume that this term is constant. For f.c.c materials, the magnitude of both $(\tau_c^s)_t$ and $(\tau_c^s)_a$ is controlled by the interactions of glide dislocations with forest dislocations, consequently it is difficult to separate the observed strain hardening between $(\tau_c^s)_t$ and $(\tau_c^s)_a$. Nevertheless the variation in $(\tau_c^s)_a$ is expected to be much smaller than that in $(\tau_c^s)_t$. Thus, for b.c.c materials, it is reasonable to assume that:

$$\dot{\tau}_c^s = (\dot{\tau}_c^s)_a = \sum_u h^{su} \dot{\gamma}^u \quad (4-17)$$

and for f.c.c:

$$\dot{\tau}_c^s = (\dot{\tau}_c^s)_t = \sum_u h^{su} \dot{\gamma}^u \quad (4-18)$$

The choice for h^{su} constitutes a distinction between the micro-macro approaches implemented in FEM codes. Khan & Cheng 1996 and Teodosiu 1997 review the different proposals. Some of them will be presented in Chapter 5.

4.4. Mechanical frame for single crystal plasticity

In the frame of Continuum Mechanics, researchers as Asaro 1983, Anand & Kothari 1996 use an *isoclinic* configuration, which is an intermediate conceptual local configuration defined by Figure 4-2, to decompose the deformation gradient tensor:

$$\underline{F} = \frac{\partial \underline{x}}{\partial \underline{X}} = \frac{\partial \underline{x}}{\partial \underline{x}^*} \cdot \frac{\partial \underline{x}^*}{\partial \underline{X}} = \underline{F}^* \cdot \underline{F}^p \quad (4-19)$$

\underline{X} coordinates in the initial configuration expressed in axes \underline{X}_i ;

\underline{x} coordinates in the deformed configuration expressed in axes \underline{x}_i ;

\underline{x}^* coordinates in the isoclinic configuration expressed in axes \underline{X}_i ;

\underline{F}^* sum of an overall “elastic” distortion of the lattice and the rigid rotation of the lattice;

\underline{F}^p “plastic” simple shears that do not disturb the geometry of the lattice.

The lattice in the isoclinic relaxed configuration has the same orientation as the lattice in the reference configuration. The incremental deformation of a crystal is taken as the result of the contributions from two independent atomic mechanisms:

- the sum of an overall “elastic” distortion of the lattice and a rigid rotation of the lattice (\underline{F}^*);
- “plastic” simple shears that do not disturb the lattice geometry (\underline{F}^p).

The microscopic velocity gradient is linked to the deformation gradient tensor:

$$\underline{L}^{micro} = \frac{\partial \dot{\underline{x}}}{\partial \underline{x}} = \frac{\partial \dot{\underline{x}}}{\partial \underline{X}} \cdot \frac{\partial \underline{X}}{\partial \underline{x}} = \dot{\underline{F}} \cdot \underline{F}^{-1} \quad (4-20)$$

$$\underline{L}^{micro} = \dot{\underline{F}}^* \cdot \underline{F}^{*-1} + \underline{F}^* \cdot \dot{\underline{F}}^p \cdot \underline{F}^{p-1} \cdot \underline{F}^{*-1} \quad (4-21)$$

The plastic shear rate is expressed through a certain number of slip systems s (the active ones in the TBH model and all slip systems in the rate sensitive approach):

$$\underline{L}^{micro} = \dot{\underline{F}}^* \cdot \underline{F}^{*-1} + \sum_s \dot{\gamma}^s \underline{K}^{*s} \quad (4-22)$$

Schmid's tensor \underline{K}^{*s} is expressed in deformed configuration, but as the crystal lattice is not affected by \underline{F}^p , one has:

$$\underline{K}^{*s} = \underline{F}^* \cdot \underline{K}^s \cdot \underline{F}^{*-1} \quad (4-23)$$

So in the micro-mechanical frame, one gets (4-22) which can be compared to relation (4-2) of Taylor's model presented in section 4.1 :

$$\underline{L}^{micro} = \underline{\Omega}^L + \sum_s \underline{L}^s \quad (4-2)$$

Since in (4-2), the elastic part of \underline{F}^* has been neglected, the strain rates deduced from (4-22) and (4-2) are different:

$$(4-22) \rightarrow \underline{\dot{\epsilon}} = \text{sym}(\underline{L}^{micro}) = \underline{\dot{\epsilon}}^{elastic} + \underline{\dot{\epsilon}}^{p\ micro} = \underline{\dot{\epsilon}}^{elastic} + \sum_s \underline{A}^{*s} \dot{\gamma}^s \quad (4-24)$$

$$(4-2) \rightarrow \underline{\dot{\epsilon}} = \text{sym}(\underline{L}^{micro}) = \underline{\dot{\epsilon}}^{p\ micro} = \sum_s \underline{A}^{*s} \dot{\gamma}^s \quad (4-25)$$

The skew-symmetric parts of both velocity gradients are identical and are called the spin:

$$\underline{\Omega}^{micro} = \underline{\Omega}^L + \underline{\Omega}^p = \underline{\Omega}^L + \sum_s \underline{Z}^{*s} \dot{\gamma}^s \quad (4-26)$$

where $\underline{\Omega}^L$ is the crystal lattice rotation due to both the global rigid body rotation of the macroscopic body and the particular crystal rotation due to texture updating.

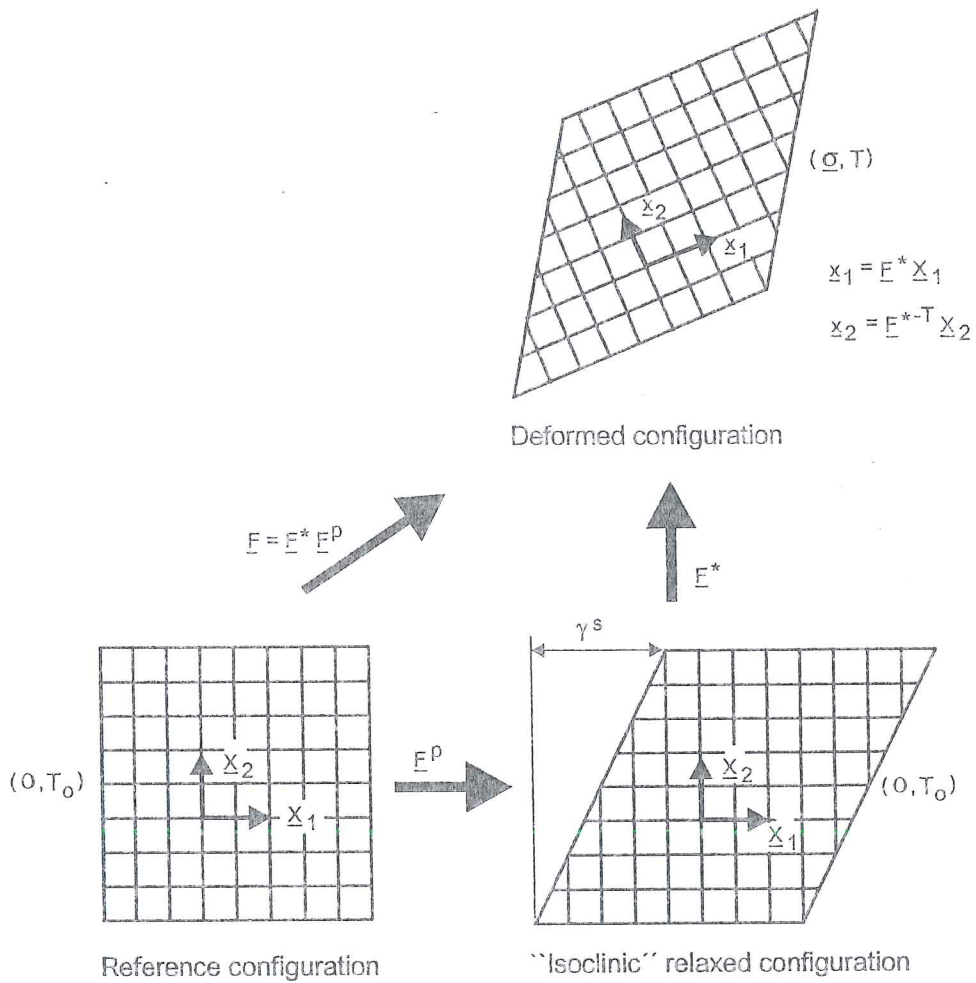


Figure 4-2 Schematic diagram showing the multiplicative decomposition of the deformation gradient tensor $F = F^* F^p$ (adapted from Aasro 1983, Anand & Kothari 1996).

4.5. Polycrystal plasticity models

4.5.1. Description

Starting from the state of individual crystallites, different assumptions have been proposed to deduce the state of the corresponding polycrystal characterized by the macroscopic strain rate tensor $\underline{\dot{\epsilon}}^{macro}$ and the stress tensor $\underline{\sigma}^{macro}$. The most logical approach is a volume average weighted by the ODF function $f(g)$ defined by relation (3-4):

$$\underline{\dot{\epsilon}}^{macro} = \oint \underline{\dot{\epsilon}}^{micro}(g) f(g) dg \quad (4-27)$$

$$\underline{\sigma}^{macro} = \oint \underline{\sigma}^{micro}(g) f(g) dg \quad (4-28)$$

Although the assumption of homogeneous microscopic stress tensor $\underline{\sigma}^{micro}$ and strain rate tensor $\underline{\dot{\epsilon}}^{micro}$ in one single crystal is already a simplification, most macroscopic models are bound by stronger assumptions :

Sachs (1928) applies the loading state (uniaxial tension for instance) at each individual crystallite as if it were a free-standing single crystal, assumed to have only one slip system (van Houtte 1995) This leads to more or less severe violations of geometric compatibility at the grain boundaries and, in general, quite unsatisfactory results (Gil-Sevillano *et al.* 1980). In particular, the predictions of texture evolutions due to deformation do generally not compare favorably with the experimental results.

- **Full Constraint Taylor (1938) (FC)** assumes an homogeneous plastic strain rate distribution:

$$\underline{\dot{\epsilon}}^{p macro} = \underline{\dot{\epsilon}}^{p micro} \quad (4-27)$$

This assumption leads to equilibrium violations at grain boundaries. However this model often computes, for many practical applications, more acceptable results than the previous one. The assumption (4-29) provides an upper bound solution.

- The Full Constraint Taylor's model enforces rigorous geometric compatibility at the expense of stress equilibrium. The so-called *Relaxed Constraint Taylor's (RC)* model drops this strict assumption by relaxing the compatibility of well chosen components of the velocity gradient tensor. In the *lath model* for rolling $L_{(RD)(ND)}$ is not prescribed and the *pancake model* does not enforce the component $L_{(TD)(ND)}$ either, where RD, TD and ND are the rolling, transverse

and normal directions. As shown by van Houtte 1988, these kinds of relaxations can be implemented in an elegant way using pseudo-slip system.

As compared to FC models, RC models sometimes produce better and more detailed results, especially for rolling texture predictions, although their justification is still under debate. The problem of accommodating the strain misfits inherent to RC models leads scientists like Wagner, Lücke, Arminjon, Imbault, van Houtte to propose several more advanced models which try to take these misfits into account. The summary presented in van Houtte 1996 confirms that such models lie between TBH and self-consistent approaches and yield improved results compared to classical FC or RC models.

In general, Taylor type models are quite successful for f.c.c and b.c.c metals where a large number of slip systems ensures that individual crystals can accommodate an arbitrary deformation. However, these types of models are not valid for materials whose crystals have an insufficient number of deformation modes to sustain an arbitrary strain. Such kinematically rank deficient materials are not rare: semi-crystalline polymers, minerals and other geological materials, superconducting ceramics, metals of hexagonal close-packed crystal structure such as zinc, zirconium and titanium. Two proposals adapted to such cases are described in Prantil, Dawson and Chastel 1995. The first one due to Parks & Ashi 1990 is shortly summarized hereafter and the other one due to Chastel is a modified Sachs approach.

- *Taylor hybrid approach* (Parks & Ashi 1990) has been specifically proposed to handle kinematically rank deficient crystals. The crystal strain rate is the macroscopic one from which the components that available slip systems cannot accommodate have been removed. The crystal strain rate computation takes into account an average part from which one can find that the average crystal deformation rate is equal to the macroscopic one. The crystal stress is determined from the active slip systems and by a projection of the macroscopic stress.
- *Self-consistent models* (Berveiller & Zaoui 1979, Canova & Lebensohn 1995 Molinari 1997, Masson & Zaoui 1999) consider a grain as a solid inhomogeneity embedded in a homogeneous infinite matrix subjected to macroscopic loading. All the grains are treated that way one after the other, the matrix behavior results from the weighted average of the individual contributions of all the grains. Both strain rate and stress heterogeneities are allowed, but they are linked by an interaction formula based on Eshelby's 1957 work. For elastic cases, Kröner 1961 uses the interaction formula at the grain level:

$$(\underline{\underline{\sigma}}^{micro} - \underline{\underline{\sigma}}^{macro}) = -\underline{\underline{L}}^* : (\underline{\underline{\epsilon}}^{micro} - \underline{\underline{\epsilon}}^{macro}) \quad (4-28)$$

where $\underline{\underline{L}}^*$ is a 4th rank tensor called the "interaction tensor". The interested reader can find the method to identify $\underline{\underline{L}}^*$ in Van Houtte 1995.

This approach has been extended to elastoplastic states. However, an incremental linearization proposed by Hill 1965 seems to be better adapted:

$$\underline{\dot{\sigma}}^{micro} - \underline{\dot{\sigma}}^{macro} = -\underline{\underline{L}}^H : (\underline{\dot{\epsilon}}^{micro} - \underline{\dot{\epsilon}}^{macro}) \quad (4-29)$$

where $\underline{\underline{L}}^H$ is called the Hill's constraint tensor. It depends on the elastoplastic modulus, on the shape and orientation of the crystals.

Masson & Zaoui 1999 summarizes the scientific controversies on this topic and demonstrates that Hill's conception could be adopted even for elastoviscoplasticity.

Whatever self-consistent approach is used, a rather long iterative solution procedure is required. This is mainly due to the fact that, at the end of the iterative process, the macroscopic values must coincide with the average of the grain response. However, unlike the Taylor's models, the self-consistent models allow to take into account both effects of texture and grain morphology on the mechanical response of the material.

- *Homogenization technique*, used by Smit *et al.* 1998, Miehe *et al.* 1999 or Geers *et al.* 2000, is directly based on a mathematical procedure already applied to find micro-macro links in composite materials. Two levels of finite element models are used: a mesh of the entire structure and a mesh of the Representative Volume Element (RVE). At each interpolation point of the macroscopic mesh, the finite element model of the RVE is called to provide the stress-strain behavior of the material.

The interested reader can find general information on these topics in the course written by van Houtte 1995, except for the Taylor hybrid approach and the homogenization technique. Chapter 5 presents finite element applications of the above micro-macro hypotheses.

4.5.2. Average Taylor's factor

The TBH theory described in section 4.1 for one crystal can directly be applied to polycrystals with Taylor's assumption (4-29). So, plastic strain rate tensors $\underline{\dot{\epsilon}}^p$ are supposed to be homogeneous throughout the polycrystal. In addition, Taylor assumes that the common reference CRSS τ_c (common reference value for all the slip systems in one crystal) is the same for all crystallites in the polycrystal in one representative volume element. It is called the *average common reference CRSS* $\bar{\tau}_c$:

$$\tau_c = \bar{\tau}_c \quad (4-30)$$

This assumption seems acceptable for materials in their annealed state, though it becomes questionable after accumulation of a certain deformation (Bunge *et al.*

1985). With relations (4-29) and (4-32), the average plastic power dissipation in a polycrystal is easily computed from its expression for a single crystal (4-14) and the ODF (3-4):

$$\overline{\dot{W}^p}(\underline{\dot{\epsilon}}^{p\ macro}) = \oint \dot{W}^p(\underline{\dot{\epsilon}}^{p\ micro}, g) f(g) dg = \dot{\epsilon}_{eq}^{p\ macro} \overline{\tau}_c \overline{M}(\underline{U}_{\underline{\dot{\epsilon}}^p}) = \sigma_{eq}^{macro} \dot{\epsilon}_{eq}^{p\ macro} \quad (4-31)$$

with the average Taylor's factor :

$$\overline{M}(\underline{U}_{\underline{\dot{\epsilon}}^p}) = \oint M(\underline{U}_{\underline{\dot{\epsilon}}^p}, g) f(g) dg \quad (4-32)$$

Hereafter any over-lined variable indicates a value which is assumed to be an average for all crystallites belonging to the same elementary volume considered in the macroscopic approach.

The average Taylor's factor only depends on the texture of the polycrystalline material $f(g)$ and on the given strain rate mode $\underline{U}_{\underline{\dot{\epsilon}}^p}$ but not on the strain rate magnitude $\dot{\epsilon}_{eq}^{p\ macro}$.

Relation (4-33) yields the important micro-macro link:

$$\sigma_{eq}^{macro} = \overline{\tau}_c \overline{M}(\underline{U}_{\underline{\dot{\epsilon}}^p}) \quad (4-33)$$

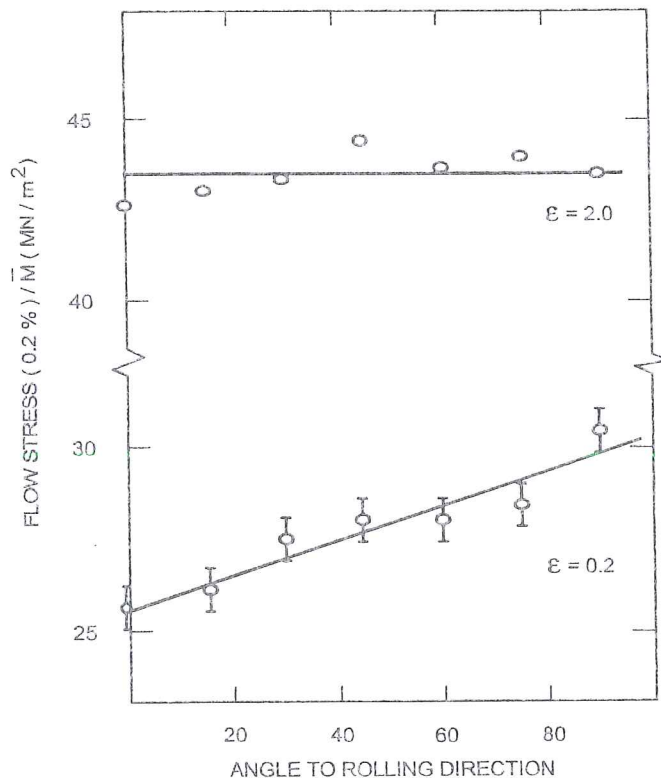


Figure 4-3 Ratio between the tensile yield stress and the corresponding Taylor's factor according to the angle α with the rolling direction (after Jensen & Hansen 1987).

This relation retrieves the physical considerations of Chapter 3 on hardening. Both geometric (textural) hardening related to \bar{M} and material (strain) hardening related to $\bar{\tau}_c$ coexist and appear in a micro-macro approach. Experimental works also demonstrate that the anisotropic behavior cannot be attributed to only one of these factors. For instance, Jensen & Hansen 1987 measured the 0.2% tensile yield stress on specimens cut at different angles α to the Rolling Direction. Their material was a sheet of commercially pure aluminum, which was previously cold-rolled at an equivalent true strain of up to 200%. Textures of the rolled sheet were determined and the average Taylor's factors \bar{M} were computed for different levels of deformation. Figure 4-3 shows the evolution of the ratio $\sigma_{eq}^{macro} / \bar{M}$ corresponding to $\bar{\tau}_c$ according to (4-35), versus the angle α to the rolling direction. At very large strains, $\bar{\tau}_c$ is almost constant, indicating that the observed plastic anisotropy can mainly be attributed to the crystallographic texture. On the contrary, after moderately large monotonic strains, $\bar{\tau}_c$ increases with α , showing a strong influence of the intragranular microstructure on the plastic anisotropy. According to Teodosiu's 1997 review, this conclusion seems true for polycrystalline f.c.c:

- for moderately cold-rolled sheet, plastic anisotropy seems due to the orientation of the dislocation structures (sheets of high dislocation densities more or less parallel to the {111} slip planes);
- for heavily cold-rolled sheets, plastic anisotropy mainly seems due to the crystallographic texture, because dislocations are arranged in thick-walled, equiaxed cells, providing an almost isotropic hardening.

Let us note that the further work of Winther, Jensen and Hansen 1997 studies the combined effect of texture and microstructure on the flow stress anisotropy of metals containing dislocation boundaries with a macroscopic orientation with respect to the sample axes. Assuming that dense dislocation walls and micro-bands resist like ordinary grain boundaries, a value of the CRSS depending on a Petch-Hall equation is adopted. In their approach, Taylor's or Sachs' polycrystal assumption is used on a set of 1152 crystals, representative of the texture. It has been proved that the presence of dislocation boundaries has a significant effect on anisotropic yield.

4.6. Link between the evolution of the reference CRSS and macroscopic strain hardening

Taylor 1938 proposes that the common reference CRSS τ_c evolves as a function of the total slip Γ in each crystal:

$$\Gamma(g) = \int_0^t \dot{\Gamma}(g) dt \quad (4-34)$$

where g defines the crystal orientation. In a similar way, van Bael 1996, assuming constant CRSS-ratios α_s , defines the total slip rate $\dot{\Gamma}$ as :

$$\dot{\Gamma}(g, \dot{\underline{\varepsilon}}^{p\ micro}) = \sum_s \alpha_s |\dot{\gamma}_s| = \dot{\varepsilon}_{eq}^{p\ micro} M(g, \underline{U}_{\dot{\varepsilon}^p}) \quad (4-35)$$

where g defines a crystal orientation, $\dot{\underline{\varepsilon}}^p$ is a strain rate tensor represented by its mode $\underline{U}_{\dot{\varepsilon}^p}$ and magnitude $\dot{\varepsilon}_{eq}^{p\ micro}$.

Using Taylor's assumptions:

- $\dot{\underline{\varepsilon}} = \dot{\underline{\varepsilon}}^{p\ micro} = \dot{\underline{\varepsilon}}^{p\ macro}$
- $\bar{\tau}_c = \tau_c$

the *total polycrystal slip rate* $\bar{\Gamma}$ is defined by:

$$\bar{\Gamma}(\dot{\underline{\varepsilon}}^p) = \int \dot{\Gamma}(g, \dot{\underline{\varepsilon}}^p) f(g) dg = \dot{\varepsilon}_{eq} \bar{M}(\underline{U}_{\dot{\varepsilon}^p}) \quad (4-36)$$

The *total polycrystal slip* $\bar{\Gamma}$ is then computed by integration of the slip rate and an important **micro-macro link** appears:

$$d\bar{\Gamma} = d\bar{\varepsilon}_{eq}^p \bar{M} \quad (4-37)$$

If one works with a uniaxial test where $\varepsilon_{eq}^{p\ macro} = \varepsilon$ and $\sigma_{eq}^{macro} = \sigma$, the macroscopic work hardening can easily be deduced from relations (4-35) and (4-39):

$$\frac{d\sigma}{d\varepsilon} = \bar{M}^2 \frac{d\tau_c}{d\bar{\Gamma}} + \tau_c \frac{d\bar{M}}{d\varepsilon} \quad (4-38)$$

The first term (material hardening) on the right side of equation (4-40) indicates an isotropic hardening at the polycrystal level, since an average is done whatever slip system is activated and for all crystals. The second term (geometrical hardening) is due to the evolution of texture resulting from plastic deformation. It is often neglected in macroscopic models or even in simple micro-macro models (Schmitz 1995, Winters 1996). Relation (4-40) is well known and comments can be found in Aernoudt *et al.* 1987.

4.7. Summary

This chapter has introduced the single crystal plasticity as well as the assumptions to develop a macroscopic plastic model from microscopic models. The physical mechanisms and their models were implemented in finite element codes for validation purpose. They also allow accurate simulations of deep drawing or rolling. Chapters 5 and 6 summarize some applications of this type.

References

- Aernoudt, E., Gil-Sevillano J. & Van Houtte, P. (1987) Constitutive Relations and Their Physical Basis, S.I. Andersen et al. Eds, RisØ National Laboratory, Roskilde, Denmark, 1-38.
- Anand, L., Kothari, M. (1996) A Computational Procedure for Rate-Independent crystal plasticity, *J. Mech. Phys. Solids*, **44/4**, 525-558.
- Anand, L., Balasubramanian S., Kothari, M. (1997) Constitutive Modeling of Polycrystalline Metals at Large Strains : Application to Deformation Processing, *Large plastic deformation of crystalline aggregates*, International Centre for Mechanical Sciences, Courses and Lectures n° 376, Springer Ed, 109-172.
- Asaro, R.J. (1983) Micromechanics of crystals and polycrystals, *Advances in Applied Mechanics*, **23**, 1-115.
- Asaro, R.J., Needleman, A. (1985) Texture development and strain hardening in rate dependent polycrystals, *Acta Metallurgica*, **33**, 923-953.
- Aukrust, I., Tjøtta, S., Vatne, H.E., Van Houtte, P. (1997) Coupled FEM and texture modelling of plane strain extrusion of an Aluminium alloy, *Int. J. of Plasticity*, **13**, 1/2.
- Becker (1990) An analysis of shear localization during bending of a polycrystalline sheet, *Microstructural Evolution in Metal Processing*, **46**.
- Berveiller, M., Zaoui, A. (1979) An extension of the self-consistent scheme to plastically-flowing polycrystals, *J. Mech. Phys. Solids*, **26**, 325-344.
- Bunge, H.J. (1982) Texture Analysis in Materials Science, Butterworths Publishers, London.
- Canova, G.R., Lebensohn, R. (1995) Micro-macro modelling, *Computer Simulation in Materials Science, NATO ASI, Ile d'Oleron, France, June 6-16*.
- Dawson, P.R. & Kumar, A. (1997) Deformation Process Simulations Using Polycrystal Plasticity, *Large plastic deformation of crystalline aggregates*, International Centre for Mechanical Sciences, Courses and Lectures n° 376, Springer Ed, 247.
- Duchêne L., Godinas A., Habraken, A.M. (1999) Metal Plastic Behaviour linked to Texture Analysis and FEM Method, *NUMISHEET '99, 4th Int. Conf. and Workshop on Numerical Simulation of 3D Sheet Forming Processes*, Besançon, France, 13-17 September 1999, Edité par J.C. Gélín, P. Picart, Université de Franche-Comté et ENSMM, 97-102.
- Eshelby, J.D. (1957) The determination of the elastic field of an ellipsoidal inclusion and related problems. *Proc. Roy. Soc. London*, **A241**, 376-396.
- Franciosi, P. (1988) On flow and a work hardening expression correlation in metallic single crystal plasticity, *Revue Phys. Appl.*, **23**, 383-394.
- Geers, M.G.D., Kouznetsova, V., Brekelmans, W.A.M. (2000) Constitutive approaches for the multi-level analysis of the mechanics of microstructures, *5th National Congress on Theoretical and Applied Mechanics, Louvain-La-Neuve, May 23-24, 2000*.
- Hill, R. (1965) Continuum micro-mechanics of elastoplastic polycrystals, *J. Mech. Phys. Solids*, **13**, 89-101.

- Hirsch, J.R. (1990) Correlation of deformation texture and microstructure, *Materials Science and Technology*, **6**, 1048.
- Jensen J., Hansen D.&N. (1987) Relations Between Texture and Flow Stress in Commercially Pure Aluminium, *Constitutive Relations and their Physical Basis*, 8th Riso Int. Symp. on Metallurgy and Mat. Sci., Andersen S.I. et al. Eds, Riso Nat. Lab., Roskilde, 353-360.
- Kalidindi, S.R., Bronkhorst, C.A., Anand, L. (1992) Crystallographic texture evolution during bulk deformation processing of FCC metals, *J. Mech. Phys. Solids*, **40**, 537-579.
- Kalidindi, S.R., Anand, L. (1994) Macroscopic shape change and evolution of crystallographic texture in pre-textured FCC metals, *J. Mech. Phys. Solids*, **42/3**, 459-490.
- Kallend, J.S., Kocks, U.F., Rollett, A.D., Wenk, H.R. (1991) popLA – an integrated software system for texture analysis. *Text. microstruct.*, **14-18**, 1203-1208.
- Khan, A.S., Cheng, P. (1996) An anisotropic elastic-plastic constitutive model for single and polycrystalline metals. I – theoretical developments, *Int. J. Plasticity*, **12/2**, 147-162.
- Kröner, E. (1961) Zur plastischen Verformung des Vielkristalls, *Acta Metall.*, **9**, 155-161.
- Laszlo Tóth, L.S., Van Houtte, P. (1992) Discretization techniques for orientation distribution functions, *Textures and Microstructures*, 1992, 229-244.
- Masson, R., Zaoui, A. (1999) Self-consistent estimates for the rate-dependent elastoplastic behaviour of polycrystalline materials, *J. of Mechanics and Physics of Solids*, **47**, 1543-1568.
- Miehe C., Schröder J., Schotte J. (1999) Computational homogenization analysis in finite plasticity, simulation of texture development in polycrystalline materials, *Computer methods in applied mechanics and engineering*, **171**, 387-418.
- Molinari, A. (1997) Deformation Process Simulations Using Polycrystal Plasticity, *Large plastic deformation of crystalline aggregates*, International Centre for Mechanical Sciences, Courses and Lectures n° 376, Springer Ed, 173-246.
- Munhoven, S. (1997) Taylor ULg A, rapport intermédiaire n° 4, Convention Micro-Macro 2748.
- Neale, K.W. (1993) Use of Crystal Plasticity in Metal Forming Simulations, *Int. J. Mech. Sci.*, **35/12**, 1053-1063.
- Parks, D.M. & Ahzi S. (1990) Polycrystalline plastic deformation and texture evolution for crystals lacking five independent slip systems, *J. Mech. Phys. Solids*, **38/5**, 701-724.
- Prantil, V.C., Dawson, P.R., Chastel, Y.B. (1995) Comparison of equilibrium-based plasticity models and a Taylor-like hybrid formulation for deformations of constrained crystal systems, *Modelling Simul. Mater. Sci. Eng.*, **3**, 215-234.
- Sachs, G. (1928) Zur Ableitung einer Fließbedingung, *Z. Verein Deutscher Ing*, **72**, 734-736.
- Sarma, G.B., Dawson, P.R. (1996) Texture Predictions Using a Polycrystal Plasticity Model Incorporating Neighbor Interactions, *Int. J. of Plasticity*, **12/8**, 1023-1054.

- Schmitz A. (1995) Development and experimental validation of a coupled thermal, mechanical and textural model for ferritic hot-rolling of steel, Faculty of Engineering of the Catholic University of Leuven.
- Sevillano, G., Van Houtte, P., Aernoudt, E. (1980), Large strain work hardening and textures, *Progress in Materials Science*, **25**, 111.
- Smit, R.J.M., Brekelmans, W.A.M., Meijer, H.E.H. (1998) Prediction of the mechanical behavior of nonlinear heterogeneous systems by multi-level finite element modeling, *Comp. Meth. Appl. Mech. Eng.*, **155**, 181-192.
- Taylor, G.I. (1938) Plastic strains in metals, *J. Inst. Metals*, **62**, 307-324.
- Teodosiu, C. (1997) Dislocation modelling of crystal plasticity, *Large plastic deformation of crystalline aggregates*, International Centre for Mechanical Sciences, Courses and Lectures n° 376, Springer Ed, 21-80
- Tóth, L.S., Van Houtte, P. (1992) Discretization techniques for orientation distribution functions, *Textures and Microstructures*, 1992, **19**, 229-244.
- Van Bael, A. (1994) Anisotropic yield loci derived from crystallographic data and their application in finite element simulations of plastic forming processes, proefschrift voorgedragen tot het behalen van het doctoraat in de toegepaste wetenschappen, Katholieke Universiteit Leuven.
- Van Houtte, P. (1988) A comprehensive mathematical formulation of an extended Taylor-Bishop-Hill model featuring relaxed constraints, the Renouard-Wintenberger theory and a strain rate sensitivity model, *Textures and Microstructures*, **8-9**, 313-350.
- Van Houtte, P., Mols, K., Van Bael, A., Aernoudt, E. (1989) Application of yield loci calculated from texture data, *Textures and microstructures*, **11**, 23-39.
- Van Houtte, P. (1995) Micromechanics of polycrystalline materials, Chaire Francqui, Université de Liège.
- Van Houtte, P. (1996) Microscopic strain heterogeneity and deformation texture prediction, *Textures of Materials*, Proceedings of the 11th Int. Conf. on Textures of Materials, vol. 1, ICOTOM-11, Liang Z., Zuo L., Chu Y. Eds.
- Winters, J. (1996) Implementation of a texture-based yield locus into an elastoplastic finite element code. Application to sheet forming. Katholieke Universiteit Leuven, proefschrift voorgedragen tot het behalen van het doctoraat in de toegepaste wetenschappen, Katholieke Universiteit Leuven.
- Winther, G., Jensen D.J., Hansen N. (1997) Modelling flow stress anisotropy caused by deformation induced dislocation boundaries, *Acta Mater.*, **45/6**, 2455-2465.

5. FEM MICRO-MACRO MODELS WITHOUT YIELD LOCUS

5.1. Introduction

The FEM is currently used to simulate the behavior of the materials at the microscopic level. In such cases, a crystal is discretized by one finite element or more as presented in section 5.2. Such simulations aim to validate the microscopic models or to perform parametric studies, that are difficult to do experimentally.

Another use of the FEM coupled with microscopic models concerns accurate macroscopic simulations, where the anisotropic material behavior is taken into account at a microscopic level. In such micro-macro approaches, a lot of averaging methods to extract the macroscopic behavior from microscopic analysis are possible. Some examples are listed in sections 5.3. to 5.5. These examples concern approaches where no macroscopic yield locus is computed. Chapter 6 is dedicated to the macroscopic approximation of yield loci.

5.2. Microscopic FEM computations to model macroscopic behavior

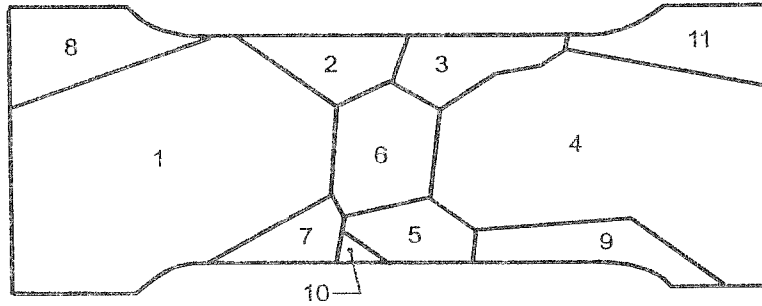
Finite element simulations allow to treat a crystalline aggregate as a continuum, by simply requiring the equilibrium of the stress tensors and the continuity of the displacements across the grain boundaries. Hereafter, two examples (Acharya & Beaudoin 1999, Teodosiu *et al.* 1992) among others (Beaudoin *et al.* 1995, Anand & Kothari 1996, Bertram *et al.* 1997...) are summarized, the first one with specific modeling of grain boundaries and the second one without. These examples demonstrate the interest of such approaches to validate single crystal plasticity models and to investigate microscopic effects by means of a numerical sensitivity analysis. For instance, grain size effect on a macroscopic flow stress is numerically studied in Acharya & Beaudoin 1999.

5.2.1. Teodosiu *et al.* 1992

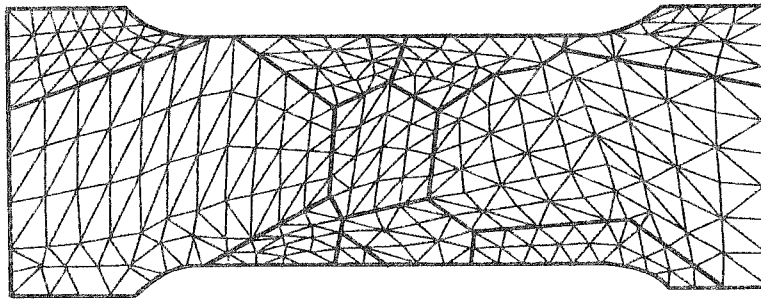
The 3D finite element mesh used to describe a tensile test on a polycrystalline specimen of pure copper is shown on Figure 5-1.

The applied constitutive law takes the elastic anisotropy into account and considers the plastic flow rule at the slip system level thanks to a rate-dependent equation such as (4-15). The hardening law of the CRSS is represented by a relation similar to (4-16), presented in section 4.3. Teodosiu uses neither an average polycrystal common

reference CRSS $\bar{\tau}_c$ nor a single crystal common reference CRSS τ_c but a CRSS defined for each slip system τ_c^s . This CRSS τ_c^s is related to the dislocation density on each slip system, which induces the internal variables choice.



(a)



(b)

Figure 5-1 (a) Front face of the tensile specimen defined by 11 grains
(b) Front view of the single layer of pentahedral finite element mesh, (from Teodosiu *et al.* 1992),

The evolution law of these dislocation densities expresses the balance between work-hardening and recovery :

$$\dot{\rho}^s = \frac{1}{b} \left(\frac{1}{s^s} - 2y_c \rho^s \right) |\dot{\gamma}^s| \quad (5-1)$$

where ρ^s is the dislocation density related to the slip system s , b is the magnitude of Burgers' vector, s^s is the average free path of the dislocations in system s , y_c denotes a characteristic length associated with the annihilation process of dislocation dipoles. Clearly s^s depends on the density of point obstacles encountered in the gliding directions. Taking into account only the dislocation-dislocation interactions yields:

$$s^s = \frac{A}{\sqrt{\sum_{u \neq s} \rho^u}} \quad (5-2)$$

where A is a scalar material parameter. Replacing A by a matrix would translate the influence of different dislocation densities on the average free path in a given slip

system. The CRSS on system s can be related to the dislocation densities by the relation :

$$\tau_c^s = Gb \sqrt{\sum_u a^{su} \rho^u} \quad (5-3)$$

where a^{su} is a matrix which takes into account various types of dislocation interactions. Differentiating relation (5-3) with respect to time and considering equations (5-1) and (5-2) lead to the hardening law proposed in (4-16) where h^{su} is given by:

$$h^{su} = \frac{G}{2} \frac{a^{su}}{\sqrt{\sum_q a^{sq} \rho^q}} \left[\frac{1}{A} \sqrt{\sum_{q \neq u} \rho^q} - 2y_c \rho^u \right] \quad (5-4)$$

The matrix h^{su} depends in an explicit way on the current values of the dislocation densities.

Teodosiu's simulation results show in each crystal: slip line patterns, stress, strain, and dislocation density fields. The parameter of non-uniformity q of any scalar field allows to quantify its heterogeneity. It is defined as the ratio between the maximum and minimum absolute values of that field over the specimen.

Figure 5-3 shows the distribution of the stress component σ_{11} in the elastic range and for average engineering strains of 0.13%, 5.7% and 21%. The direction 1 is the tensile direction. One can check that the patterns differ. In the elastic case (Figure 5-3 a), the q parameter of non-uniformity reaches 2.3. The highest gradients occur in the regions where small grains have high misorientation across the grain boundaries. In plastic cases, the q factor decreases to about 1.4 at the beginning by plastic accommodation (Figure 5-3 b). Later, with progressive deformation, q increases again but finally remains stable at a value of 2.0.

The slip line pattern presented in Figure 5-2 results from the projection on the front face of the specimen of line segments oriented as the most active slip systems within each element. The length of each segment is taken proportional to the accumulated glide in the corresponding slip system or, in some cases, in all coplanar systems having the same trace. The agreement with a Scanning Electron Microscopy (SEM) study is reported to be quite satisfactory. The most striking feature of this correlation is that the simulation can really predict the grains partition into subdomains of different single or multislip activity.

The distribution of dislocation densities has been drawn as well. It is much closer to the stress distribution than to the strain distribution. This confirms the proportionality between the flow stress and the square root of the total dislocation density already reported in the literature and used to develop the crystal model relation (5-3).

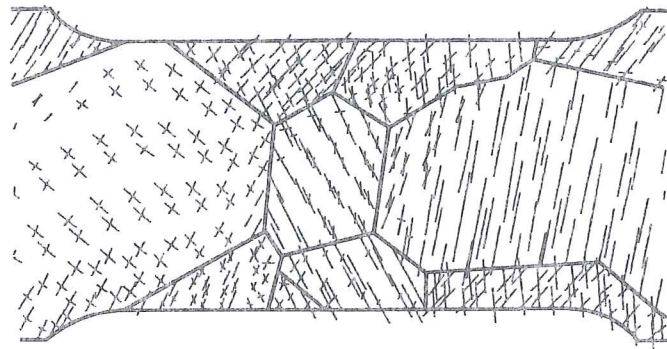


Figure 5-2 Computed slip line pattern at an average engineering strain of 0.13% (from Teodosiu *et al.* 1992).

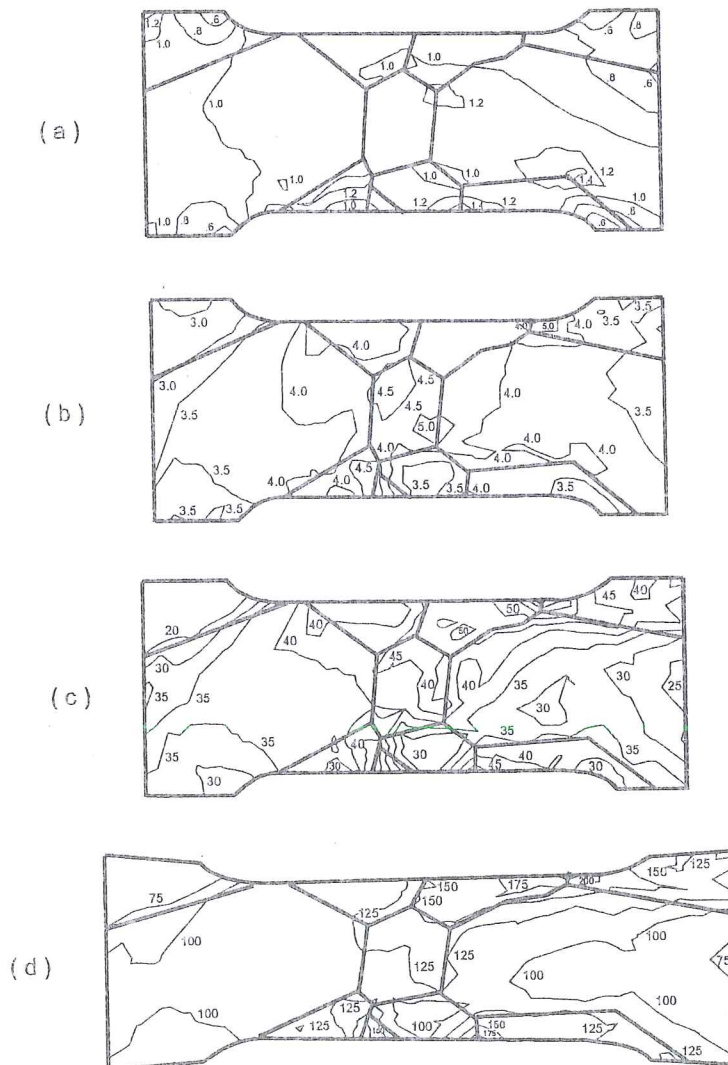


Figure 5-3 Tensile stress in Mpa computed by FEM in the elastic range (a) and for average engineering strains of 0.13% (b), 5.7% (c) and 21% (d) (from Teodosiu *et al.* 1992).

5.2.2. Acharya & Beaudoin's model

Concept

Acharya & Beaudoin 2000 presents a model that is summarized hereafter. Each single crystal undergoes a deformation gradient \underline{F} which is submitted to a multiplicative decomposition:

$$\underline{F} = \underline{F}^* \cdot \underline{F}^p \quad (5-5)$$

where \underline{F}^* is the elastic deformation tensor and \underline{F}^p is the plastic deformation tensor. This approach adopts the isoclinic configuration already introduced in Figure 4.2. As in Teodosiu's approach, a viscoplastic flow rule is applied at the level of each slip system. However a common CRSS for all the slip systems $\tau_c^s = \tau_c$ is used.

When certain types of defect distributions are present in the lattice, the distribution of "isoclinic" configurations cannot constitute a compatible deformation of the current configuration without additional deformation of the material. Consequently, it is reasonable to think of any measure that quantifies this incompatibility in \underline{F}^{*-1} as a measure of certain types of lattice defect distributions.

From mathematical and physical considerations, it can be shown (Acharya & Bassani 2000) that a measure of lattice incompatibility is given by the 3rd order tensor $\underline{\Delta}$, skew symmetric part of the gradient of \underline{F}^{*-1} :

$$\underline{\Delta} = \left(F^{*-1}_{ij,k} - F^{*-1}_{ik,j} \right) \underline{e}_i \otimes \underline{e}_j \otimes \underline{e}_k \quad (5-6)$$

where $(\underline{e}_i, \underline{e}_j, \underline{e}_k)$ is the basis of a rectangular Cartesian coordinate system parametrizing the current configuration. It can also be shown via Stokes' theorem that :

$$\underline{b}^c = \int_C \underline{F}^{*-1} \cdot d\underline{x} = \int_A \underline{\Delta} : \hat{\underline{N}} \, da \quad (5-7)$$

where C is a curve bounding a surface region A with unit normal vector \underline{n} in the current configuration. $\hat{\underline{N}}$ is the unique skew symmetric tensor defined for any vector \underline{a} by:

$$\hat{\underline{N}} \cdot \underline{a} = \frac{1}{2} \underline{n} \wedge \underline{a}. \quad (5-8)$$

If we interpret the expression in the middle of (5-7) as a Burgers' circuit on the deformed lattice in the current configuration, then \underline{b}^c can be thought of as the cumulative Burgers' vector of all dislocations threading the region A on the surface with normal \underline{n} . Consequently, $\underline{\Delta}$ can be interpreted as a fictitious density of lattice incompatibility. When integrated over a surface A , limited by a closed curve in the current configuration, it yields the cumulative Burgers' vector difference between the

beginning and the end points of the image curve in the “intermediate isoclinic configuration”. Since this difference is conceptually equated with the net Burgers' vector of all the dislocations threading the studied surface, then it is reasonable to interpret the continuous field $(\underline{A} : \hat{\underline{N}})$ as a cumulative Burgers' vector per unit area. Therefore, $(\underline{A} : \hat{\underline{N}})/b$, where b is the interatomic spacing for the lattice under consideration or the magnitude of the classical Burgers' vector, yields a continuous field of “dislocation density”.

\underline{A} alone cannot represent the total dislocation density in a phenomenological theory. Nevertheless, given its apparent interpretation as a macroscopic manifestation of certain types of dislocations or lattice defect distributions, it is reasonable to say that the evolution of the total dislocation density is affected by $(\underline{A} : \hat{\underline{N}})/b$. A logical consequence is the use of this measure in an evolution equation for hardening.

This proposal is not comforted by a lot of experimental checks but it is worth mentioning, as it links a microscopic mechanical model to microscopic physics. Such a link could help both physical metallurgists and numerical engineers to develop accurate models.

Common CRSS evolution law

With ρ the total dislocation density, $\dot{\gamma}^k$ the slip system shearing rate on system k , $\underline{\dot{\epsilon}}^{p\ micro}$ the strain rate and T the temperature, Acharya and Beaudoin consider an evolution equation for the dislocation density in a crystal of the form:

$$\dot{\rho} = \sum_k \left\{ k_0 \frac{\lambda^k}{b} + k_1 \sqrt{\rho} - k_2 (\underline{\dot{\epsilon}}^{p\ micro}, T) \rho \right\} |\dot{\gamma}^k| \quad (5-9)$$

where

$$\lambda^k = \sqrt{(\underline{A} : \hat{\underline{N}}^k)(\underline{A} : \hat{\underline{N}}^k)} \quad (5-10)$$

is the slip lattice incompatibility corresponding to system k with unit normal $\hat{\underline{n}}^k$, k_0 is a material constant, k_1 and k_2 are functions defined by relations (5-13) and (5-14).

The first term on the right side of evolution equation (5-9) represents a geometric storage term due to the lattice incompatibility which has been introduced in the previous section. The second term is associated with the dislocation storage through a statistical measure of forest dislocations. The third term is a dynamic recovery rate that renders dislocation segments inactive as they rearrange themselves.

Relation (3-13) defined at the macroscopic level can of course be expressed at the level of the common reference CRSS assumed in a crystal:

$$\tau_c = \tau_{c0} + \alpha G b \sqrt{\rho} \quad (5-11)$$

The time differential of this relation, coupled with relation (5-9), yields:

$$\dot{\tau}_c = \frac{k_o \alpha^2 G^2 b}{2(\tau_c - \tau_{co})} \sum_k \lambda^k |\dot{\gamma}^k| + \left\{ \frac{\alpha G b}{2} k_1 - k_2 \frac{\tau_c - \tau_o}{2} \right\} \sum_k |\dot{\gamma}^k| \quad (5-12)$$

Defining θ_o as the strain-hardening rate that prevails at initial yield and τ_{sat} as the saturation stress ($\dot{\tau}_c(\tau_{sat}) = 0$) which depends on strain-rate and temperature, the following relations are obtained :

$$k_1 = \frac{2\theta_o}{\alpha G b} \quad (5-13)$$

$$k_2(\underline{\dot{\epsilon}}^{p\ micro}, T) = \frac{2\theta_o}{\tau_{sat}(\underline{\dot{\epsilon}}^{p\ micro}, T) - \tau_{co}} \quad (5-14)$$

Substituting relations (5-13) and (5-14) in (5-12), an isotropic, single crystal work hardening model is obtained :

$$\dot{\tau}_c = \frac{k_o \alpha^2 G^2 b}{2(\tau_c - \tau_{co})} \sum_k \lambda^k |\dot{\gamma}^k| + \theta_o \left\{ \frac{\tau_{sat} - \tau_c}{\tau_c - \tau_{co}} \right\} \sum_k |\dot{\gamma}^k| \quad (5-15)$$

It can also be shown that λ^k is invariant under superposed rigid body motions (Acharya & Bassani, 2000); it thus satisfies the invariance requirement for a constitutive assumption.

Numerical applications to predict macroscopic stress-strain behavior

Acharya & Beaudoin use 3D FEM simulations to model aggregates of single crystals where velocity boundary conditions allow to represent uniaxial tensile or compression tests (Figure 5-4).

Simulations were performed with coarse and fine discretizations, the number of elements per grain was 12 and 96 for the 12x12x12 and 24x24x24 meshes respectively. Using the 12x12x12 mesh, simulations were carried out for grain diameters of 200 μ m, 91 μ m, 32 μ m, 20 μ m. Additional grain diameters of 50 μ m and 25 μ m were considered with the finer mesh. Each grain is characterized by its lattice orientation. The hybrid finite element formulation adopted by Beaudoin *et al.* 1995 is used. This model assumes that the plastic part of the velocity gradient is specified by the activation of multiple slip systems as already explained in Taylor's single crystal plasticity (see section 4.1). A viscoplastic flow rule (relation 4-15), coupled with the above CRSS evolution (5-15), links stress and plastic strain rate.

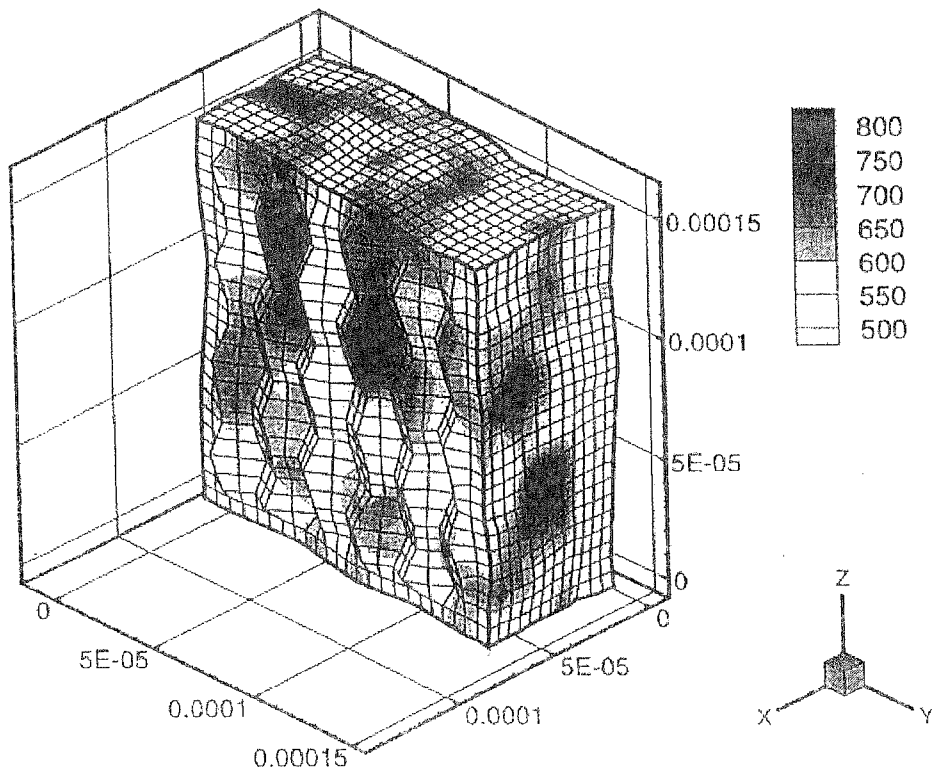


Figure 5-4 Polycrystal aggregate with initial grain diameter of $32\mu\text{m}$ submitted to a tensile strain of 20 %; von Mises equivalent stress is plotted in units of Mpa and dimensions are given in m (from Acharya & Beaudoin 2000).

The model requires the identification of 4 parameters: θ_0 , τ_{sat} , τ_{c0} , k_0 . Thanks to comparisons between experiments and simulation results, a data set can be determined. From computations applied to pure nickel, it appears that the contribution of term λ^k due to "lattice incompatibility", evaluated by relation (5-10), is relatively small for large grain size ($200\mu\text{m}$) but becomes more significant with decreasing grain size.

Whatever the mesh refinement, Figure 5-5 shows a clear relationship between macroscopic yield stress and grain size. Lines fitted to simulation results show a slight deviation from linearity with the inverse of the grain size, in fact $\sigma \propto D^{-4/5}$ is found. Well known scientists, such as Ashby for instance, propose relations where the yield stress is proportional to $D^{-1/2}$, see the review presented in François *et al.* 1992. Acharya & Beaudoin do not comment this difference, as their results are quite close to the experimental ones.

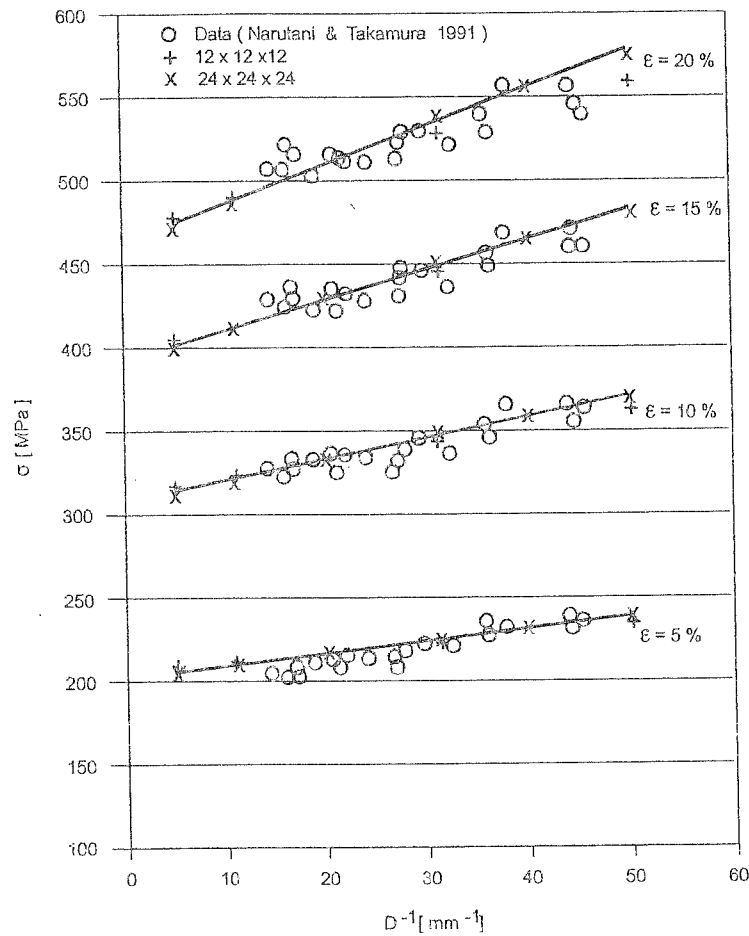


Figure 5-5 Effect of grain size D on volume-averaged stress response of nickel at 77 K° from Acharya & Beaudoin 2000.

5.3. Macroscopic FEM simulations relying on discrete set of crystals

In this type of simulations, the response of each integration point depends on the response of a multitude of single grains, representative of this material point. This can be done only thanks to massive parallel computations. Simulations like hydroforming process, performed by Dawson *et al.* 1992, show that, with powerful computers, this approach can be applied to real problems of limited size. Clearly, in addition to the usual choices in a FEM approach (lagrangian, eulerian formulation, explicit, implicit scheme, ...), the scientist must determine further assumptions:

Step 1 : the micro-macro link (Full Constraint, Relaxed Constraint Taylor's model or one of their variants, self-consistent model, homogenization technique).
It allows to go from a macroscopic velocity gradient to microscopic values and to provide, after computations at microscopic level, the macroscopic stress.

Step 2 : the set of representative crystals.

The number of crystals must be determined as well as their orientation, shape, size, slip system and associated CRSS. The initialization of these crystal data is essential for the accuracy of the results.

Step 3 : the behavior model of each crystal.

In this type of models, elasticity can be neglected or taken into account. The crystal plasticity model defines the link between the resolved shear stress and the slip system rate. The CRSS hardening rule is also a key function that induces differences between the models. As shown hereafter, two different proposals exist: viscoplasticity or rate independent plasticity. Finally, the microscopic stress related to the microscopic velocity gradient is computed.

Of course, all these options interact and have strong effects on the accuracy and computation time. Well-known scientists have proposed various models in order to describe polycrystal models. Some of these models are presented hereafter, together with their advantages and drawbacks.

5.3.1. Taylor's model + Polycrystal models

Such polycrystal models are described for instance in Asro & Needleman 1985, Mathur & Dawson 1989, Becker 1990, Neale 1993, Beaudoin *et al.* 1994, Kalidindi & Anand 1994, Anand *et al.* 1997. The above general choices are clearly identified hereafter.

Micro-Macro Link

Taylor's polycrystal model is used. This implies that the local deformation gradient in each grain is set homogeneous and identical with the macroscopic deformation gradient.

The elasticity is generally neglected in the work performed by Dawson's team (Mathur & Dawson 1989, Beaudoin *et al.* 1994):

$$\underline{F}^{macro} = \underline{F}^{micro} = \underline{R} * \underline{F}^P \quad (5-16)$$

\underline{R}^* being a rotation matrix. But elasticity is taken into consideration by scientists working with Anand (Kalidindi & Anand 1994, Anand *et al.* 1997):

$$\underline{F}^{macro} = \underline{F}^{micro} = \underline{F}^* * \underline{F}^P \quad (5-17)$$

with \underline{F}^* defined by Figure 4-2.

If the N representative grains or crystals have equal volume, a simple average is used to link micro and macro stress tensors (Kalidindi & Anand 1994).

$$\underline{\sigma}^{macro} = \frac{1}{N} \sum_{k=1}^N \underline{\sigma}^{micro(k)} \quad (5-18)$$

Otherwise, a weighted average based on the volume fraction W_k of each crystal orientation is used (Beaudoin *et al.* 1994).

$$\underline{\sigma}^{macro} = \sum_{k=1}^N W^k \underline{\sigma}^{micro(k)} \quad (5-19)$$

Clearly, the average used to reach the macroscopic stress tensor depends on the choice of the representative set of crystals.

Representative set of crystals

Number of crystals : N varies depending on simulations and authors. For instance, 180 or 200 crystals per integration point are used for compression tests (Kalidindi & Anand 1994), 32 for cup-drawing (Anand *et al.* 1997), 256 for hydroforming process (Beaudoin *et al.* 1994), 200 for titanium rolling (Dawson & Kumar, 1997)...

Orientation of crystals: experimental data from X-ray diffraction measurements of crystallographic texture give discrete intensities of diffracted energy as a function of goniometer position angles. This can be transformed into a “*Crystal Orientation Distribution Function*” ODF as explained in section 3.2 and can be used to generate a set of “weighted Euler angles”.

According to “popLA package” (Kallend *et al.* 1991), two approaches are proposed to approximate a texture defined by a continuous density distribution through a set of discrete orientations. In the first approach, all orientations have the same *weight*. Since the crystals are assumed to have the same volume, they are located in the orientation space so that higher density regions are more densely populated. The second approach consists in randomly populating the orientation space with discrete orientations and assigning to each of them an initial weight that minimizes the effect of the density fluctuations arising from the discretization. The weight of each discrete orientation is then multiplied by the actual density in the associated volume of orientation space. This provides a weighted orientation approach generally used by Dawson and his co-workers (see relation (5-19)), while Anand's team generally uses the first approach with identical weights (see relation (5-18)).

This initial set of orientations is updated during the computations. Section 4.4 explains how the computation of the crystal lattice rotation \underline{Q}^L for a single crystal is directly applicable, thanks to Taylor's assumption of identical deformations at microscopic and macroscopic levels (see relations (5-16) and (5-17)).

Slip systems: the slip systems are well known for f.c.c materials like aluminum, copper or b.c.c materials like steel, tantalum, h.c.p. materials like zinc, zircalloy...

CRSS: as explained in section 4.3, the hardening of each CRSS associated to a slip system should be taken into account as well as its initial value. Very often, the values of the initial CRSS of all slip systems are assumed equal or close to each other (van Bael 1994, see relation (4-5)). In an annealed state for f.c.c or b.c.c materials, this seems reasonable. From numerous simulations of homogeneous deformations of f.c.c materials (Kalidindi *et al.* 1992), it has been observed that, after large deformations, the values of the CRSS for the various slip systems in an aggregate are quite close to each other. This common value is estimated from a macroscopic simple compression test.

Shape: this cannot be taken into account in a classical polycrystal Taylor's model.

Behavior model of each crystal

Mathur & Dawson 1989 and Beaudoin *et al.* 1994 neglect elasticity (5-16) and use a rate dependant plasticity model described for each slip system by relation (4-15), recalled here:

$$\dot{\gamma}^s = \dot{\gamma}_0 \left| \frac{\tau^s}{\tau_c^s} \right|^{1/n} \text{sign } \tau_s \quad (4-15)$$

They also adopt a common average value for all CRSS in one crystal:

$$\tau_c^s = \tau_c \quad (5-20)$$

and choose a simple evolution law of Voce's type, already referred to in Follansbee and Kock's model (section 3.5.2.) :

$$\dot{\tau}_c = H_0 \frac{\tau_{sat} - \tau_c}{\tau_{sat} - \tau_{c0}} \quad \text{and} \quad \tau_{sat} = f(\dot{\Gamma}) \quad (5-21)$$

where $\dot{\Gamma}$ = total shear slip on all slip systems of the crystal;
 τ_{sat} = saturation value of the common reference CRSS;
 τ_{c0} = initial value of the common reference CRSS;
 H_0 = material parameter.

In Beaudoin *et al.* 1994, a hydroforming process (Figure 5-6) is chosen to validate the numerical FEM model. This choice seems very well adapted to check the model of the blank behavior :

- applied pressure assures stability;
- contact and friction models do not introduce inaccuracy; punch and blank are in sticking conditions and blank-flange contact is assumed frictionless.

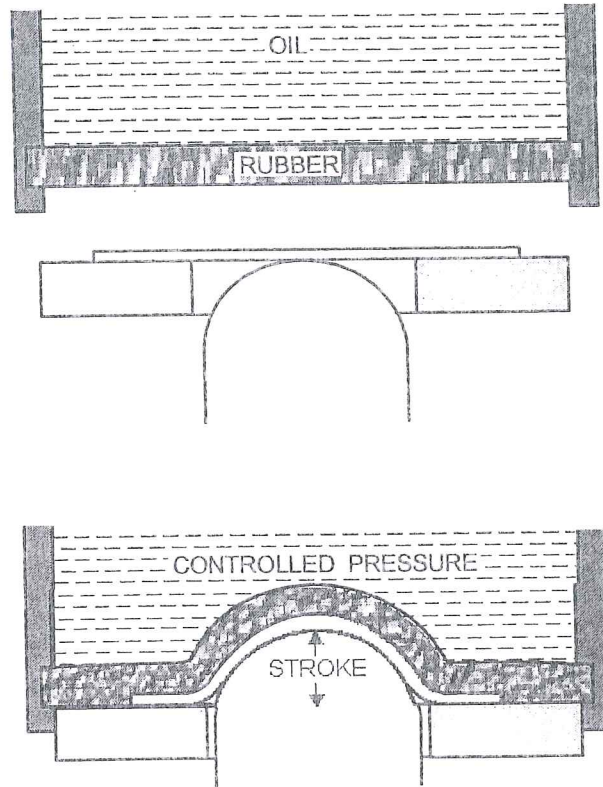


Figure 5-6 Axisymmetrical hydroforming process of an aluminum sheet (adapted from Beaudoin *et al.* 1994).

Consequently the final deformed shape depends on the material anisotropy and is measured by the percentage of earing. As shown in Figure 5-7, numerical results are close to experimental measurements :

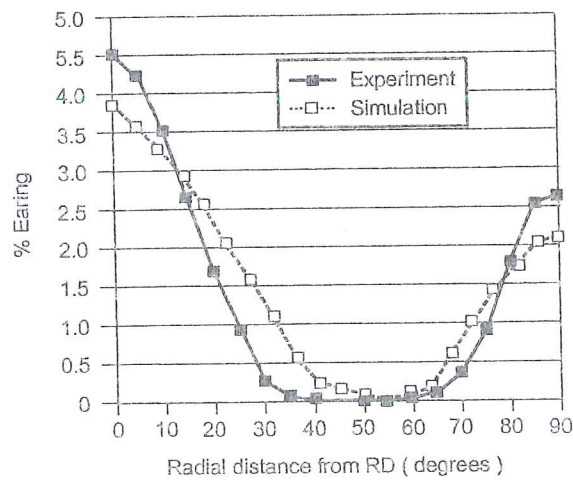


Figure 5-7 Earing measurement and prediction at the final stage of a hydroforming process (from Beaudoin *et al.* 1994).

For this case, it was checked that the texture evolution during the process and its effect on the shape of the yield locus are minimal.

In Anand & Kothari 1996, a viscoplastic flow rule (relation (4-15)) is compared with a rate-independent crystal plasticity model. A robust calculation scheme determines a unique set of active slip systems and the corresponding shear increments in the rate-independent theory. In both models, an evolution rule for the CRSS associated to each slip system τ_c^s is applied. The general form, already presented in section 4.3, is applied :

$$\dot{\tau}_c^s = \sum_u h^{su} \dot{\gamma}^u \quad (4-16)$$

This relation comes from Asro & Needleman 1985 and the chosen hardening matrix h^{su} for the 12 slip systems of f.c.c crystals is:

$$h^{su} = h^u \begin{Bmatrix} A & qA & qA & qA \\ qA & A & qA & qA \\ qA & qA & A & qA \\ qA & qA & qA & A \end{Bmatrix} \quad \text{with } A = \begin{Bmatrix} 1 & 1 & 1 \\ 1 & 1 & 1 \\ 1 & 1 & 1 \end{Bmatrix} \quad (5-22)$$

where systems 1, 2, 3 are coplanar, as systems 4, 5, 6 and 7, 8, 9 and 10, 11, 12 are. For coplanar systems, the ratio of the latent hardening rate to the self hardening rate is equal to unity. For non coplanar systems, it is evaluated by means of factor $q=1.4$. The function h^u is defined by :

$$h^u = h_0 \left(1 - \frac{\tau_c^u}{\tau_{sat}} \right)^a \quad (5-23)$$

where h_0 , a and τ_{sat} are slip system hardening parameters which are taken identical for all slip systems. In fact, τ_{sat} should be an increasing function of strain rate but this can be neglected at low temperature. These parameters are reached by curve-fitting between the results of simple compression tests and numerical simulations using "Taylor's model". By "Taylor's model", one must understand: the TBH model applied at the crystal level with Taylor's assumption of equality between microscopic and macroscopic strain rates. This model uses (4-16) and (5-23) to follow the evolution of the CRSS of each slip system in each crystal. One can check that the initial value of CRSS τ_{c0} influences the initial yield, τ_{sat} the final saturated value of stress, h_0 affects the initial hardening rate and a modifies the shape of the polycrystal stress-strain curve between the initial yield and saturation.

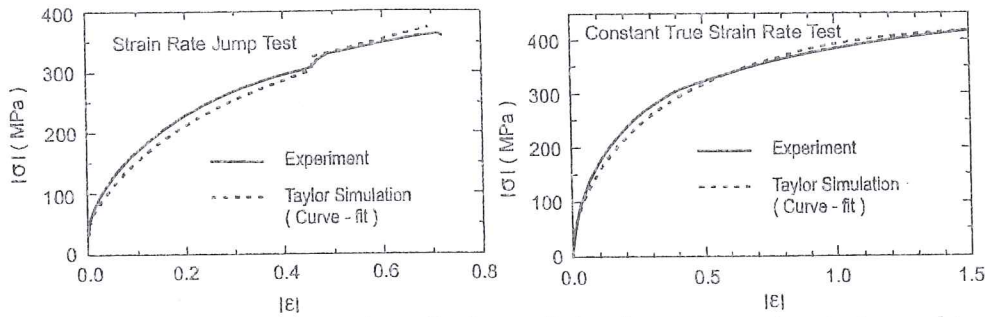


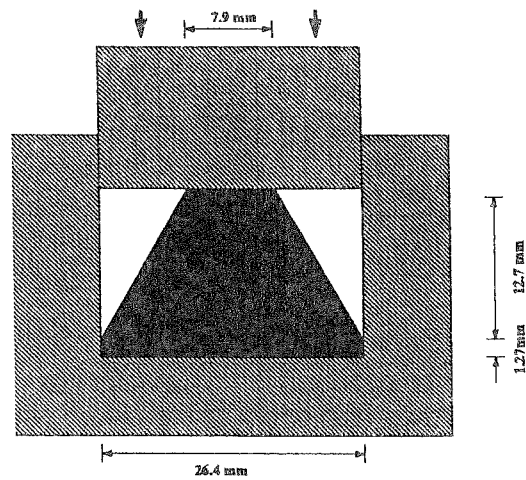
Figure 5-8 Experiments and predictions of simple compression tests used to determine the viscoplastic material parameters in Taylor's model.
 a- Strain rate jump test b- Constant true strain rate test
 (from Kalidindi & Anand 1994).

If the TBH model is replaced by a rate dependent visco-plastic law (relation 4-15), it has two additional parameters: $\dot{\gamma}_0, n$. For copper, according to Kalidindi & Anand 1994, $\dot{\gamma}_0$ is assumed to have a constant value of 0.012 and n is chosen equal to the corresponding macroscopic parameter. This latter is identified thanks to a strain rate jump experiment on a polycrystalline specimen in compression state at room temperature.

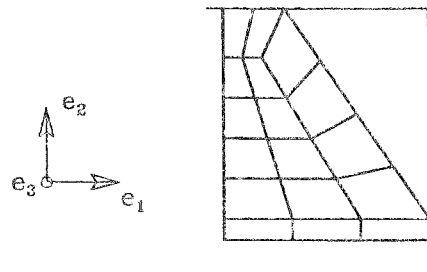
The first "micro-macro model" used here is simply Taylor's assumption of $\dot{\epsilon}^{micro} = \dot{\epsilon}^{macro}$, linked with a TBH model or a visco-plastic approach (4-15). It has no coupling with FEM and allows the identification of $\tau_{co}, \tau_{sab}, h_0, a$ and $\dot{\gamma}_0, n$. All these parameters are necessary to describe the single crystal behavior.

Finally, Figure 5-8 shows the comparison between "Taylor's model" and experiments for a copper with isotropic texture represented by 200 crystals.

Then, Anand and co-workers (Kalidindi & Anand 1994, Anand & Kothari 1996, Anand *et al.* 1997) apply the micro-macro model described above at each interpolation point of a finite element mesh. The behavior of copper and aluminium is simulated by means of Taylor's model. In particular, compression tests of cylindrical specimens, plane strain compression experiments, forging experiments (Figure 5-9), cup drawing experiments (see Figure 1.3) are performed. Experimental and numerical loads, geometric shapes and texture evolutions (Figure 5-10 and Figure 5-11) are compared as well.



(a)



(b)

Figure 5-9 (a) Scheme of a plane strain forging experiment performed on an initially isotropic copper, (b) Coarse mesh used in Abaqus finite element simulation with 180 single crystals per integration point (from Kalidindi & Anand 1994).

The conclusion is that the model gives reasonable accuracy for engineering purpose. Such a model has been successfully applied to high deformation rate of tantalum (Anand *et al.* 1997).

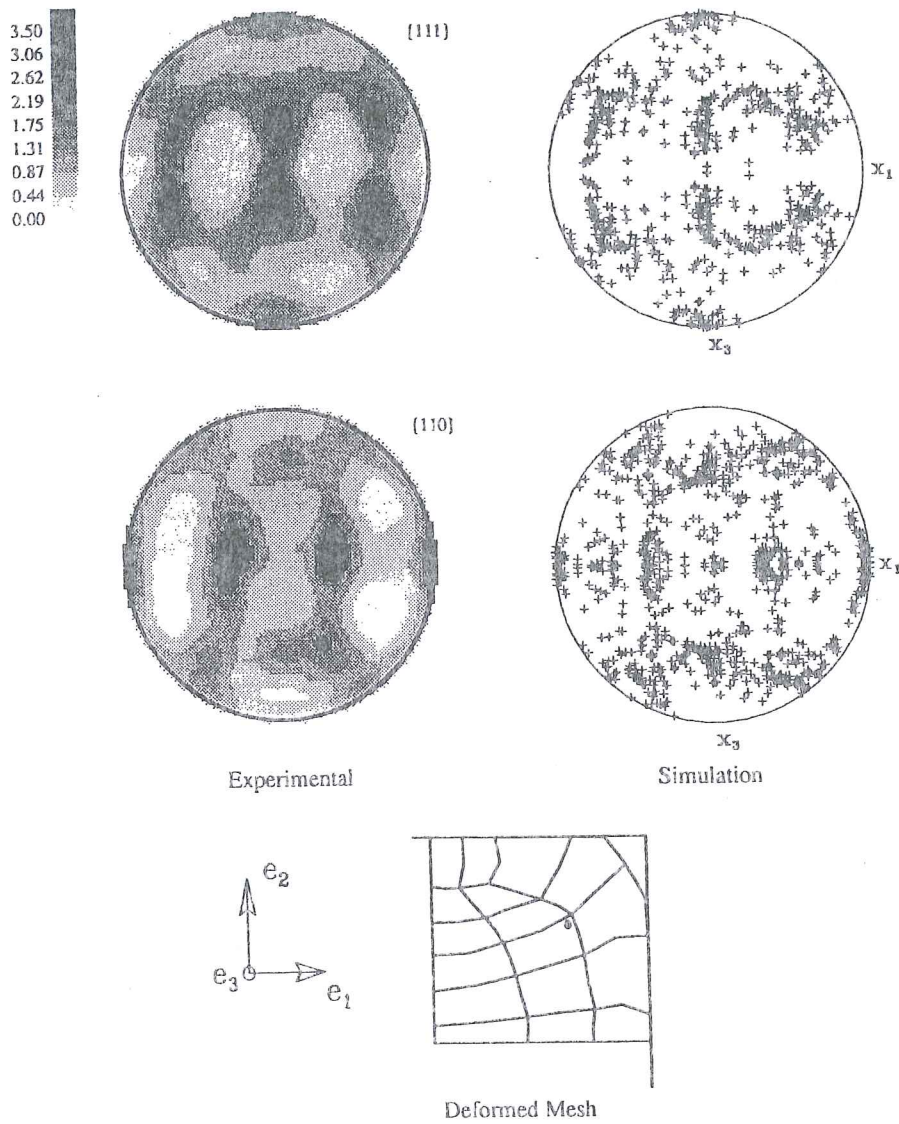


Figure 5-10 Measurement in forging experiment and prediction by FEM simulation of the {111} and {110} pole figures in the deformed specimen at the point indicated in the deformed mesh (from Kalidindi & Anand 1994).

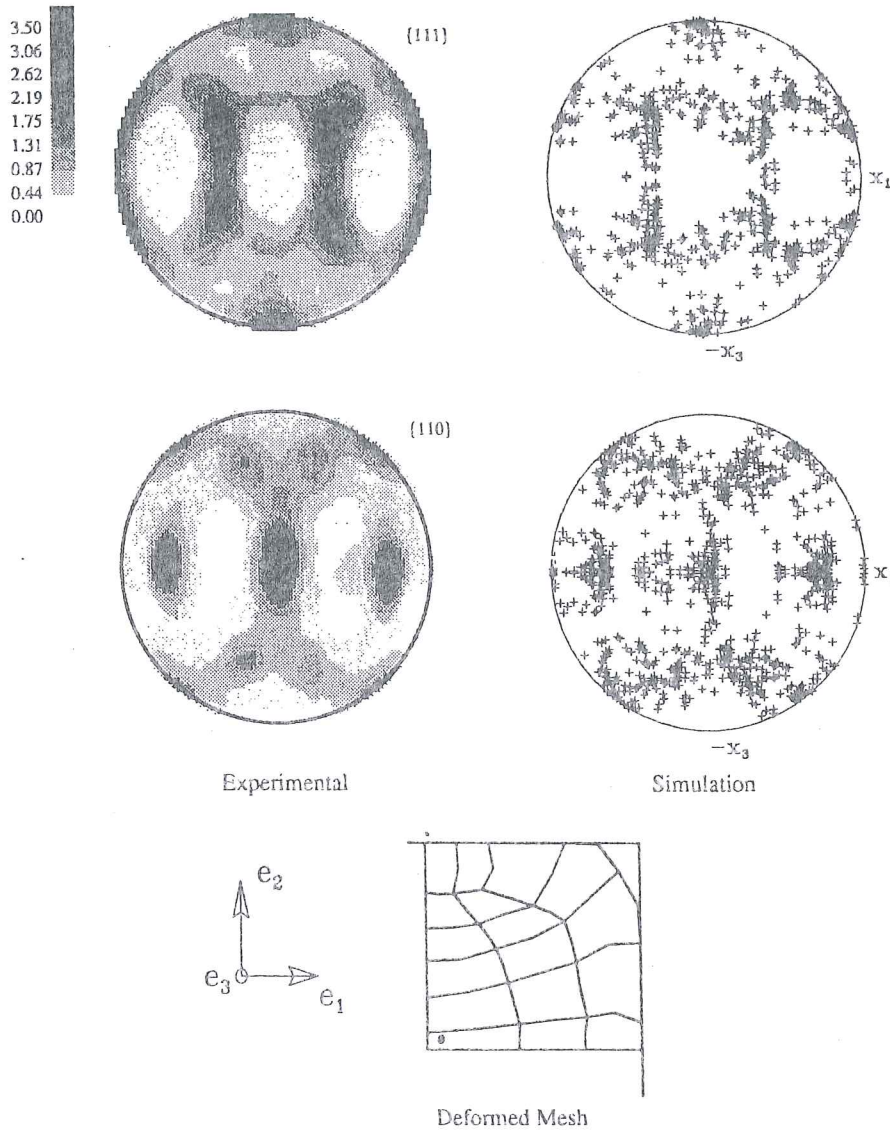


Figure 5-11 Measurement in forging experiment and prediction by FEM simulation of the {111} and {110} pole figures in the deformed specimen at the point indicated in the deformed mesh (from Kalidindi & Anand 1994).

Conclusion

In short, the previous examples using Taylor’s model, coupled with finite elements, show that such approach is feasible and has been validated for b.c.c and f.c.c materials. If a high number of representative crystals at the microscopic level is used, this can provide accurate predictions of texture, geometry and stress history during any cold forming process. The texture evolution is directly implemented in this approach. This means that the “geometrical hardening”, responsible for the shape modification of the yield locus is directly taken into account. This characteristic constitutes an advantage of this type of models with respect to others, such as the phenomenological yield loci coupled with kinematic and isotropic hardening. These

cannot easily represent texture evolution effect. As explained above, this method does not use a global yield locus but an average answer computed from the plastic behavior of a set of representative crystals.

Taylor's model coupled with finite elements requires a high CPU time and memory storage, directly proportional to the number N of crystals associated to one integration point. It is quite surprising that this number N has not been more investigated. Very often, measured pole figures are qualitatively compared to the ones computed from the discrete set of orientations (Anand & Kothary 1996). No further study from a mechanical point of view, such as stress response computed for the same strain and different N values, is performed. For each of the N representative crystals associated with one integration point, one must store:

- the crystal orientation, typically defined by 3 variables;
- hardening variable(s): either one reference CRSS τ_c , as in relation (5-21), if a common reference value for all slip systems is adopted, or one CRSS τ_c^s for each slip systems s as in equation (5-23).

5.3.2. Self-consistent approach + Polycrystal models

As explained in section 4.5, the self-consistent approach respects, on the average, both compatibility and equilibrium between grains. It is intensively used by scientists aiming to understand and predict the macroscopic material behavior thanks to micro-macro models (Canova & Lebensohn 1995, Molinari 1997, Nikolov & Doghri 2000). However, this great advantage is shaded by the increase of computation time. This fact explains why it is seldom used for coupling with FEM models. It is not surprising that self-consistent approach applications appear for hexagonal materials like Zircalloy (Chastel *et al.* 1998) because the low number of deformation modes in such crystals yields inaccurate predictions with Taylor's model.

Chastel *et al.* 1998 present a viscoplastic self-consistent polycrystalline model (Lebensohn & Tomé 1993) coupled to a 3D Eulerian finite element code LAM3 (Hacquain *et al.* 1995), applied to the hot extrusion of Zircalloy. In practice, the finite element calculation starts with an isotropic rheology, which provides a first deformation gradient at each interpolation point. Then, the polycrystalline model is locally activated and provides an anisotropic response of the material which induces subsequent calculation in LAM3. For this case, the final flow patterns reached by the macroscopic approach and by the micro-macro computation are very close to each other as they are mainly fixed by the kinematic boundary computations. Discrepancies between predicted and measured texture evolutions are attributed to the occurrence of recrystallization and/or recovery phenomena, which are not taken into account in the model.

To summarize, such a method allows to consider directly "textural hardening" as Taylor's model coupled with finite elements does. It is more satisfactory from a scientific point of view since, at the microscopic level, both compatibility and equilibrium are approached. The grain shape can be taken into account at the

microscopic level. The case of crystals with a low number of deformation modes seems to require this type of model for accurate predictions. The cost in memory is identical with Taylor's approach. However, the CPU time, which is already a problem with Taylor's model, is even worse here, as an iterative process is needed to find the heterogeneous strain repartition between crystals. This explains why so few macroscopic FEM models are linked to self-consistent microscopic models. Progresses in this direction are on their way. It must be pointed out that with "object programming", it is not a real problem to replace a Taylor's model by a self-consistent one.

5.3.3. Homogenization approach + Polycrystal models

Micro-Macro Link

Proposals by Smit *et al.* 1998, Miehe *et al.* 1999, Geers *et al.* 2000 or Feyel & Chaboche 2000 are directly based on mathematical procedures already applied in composite materials. Two levels of finite element models are used: at every interpolation point of the macroscopic FEM mesh, another microscopic FEM model, simulating a Representative Volume Element (RVE), is called to provide the stress-strain behavior of the material.

In other words, the constitutive law at a macroscopic point results from the global response given by a FEM analysis of a set of representative crystals (RVE) described by a microscopic behavior model. These 2 levels of computation are represented in Figure 5-12.

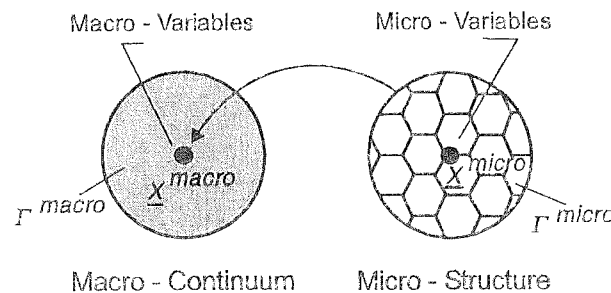


Figure 5-12 Presentation of the macroscopic and microscopic levels (adapted from Miehe *et al.* 1999).

The homogenization approach provides the mathematical background to go from the microscopic level to the macroscopic level. Figure 5-13 presents the mathematical description of the same deformation at macroscopic and microscopic levels.

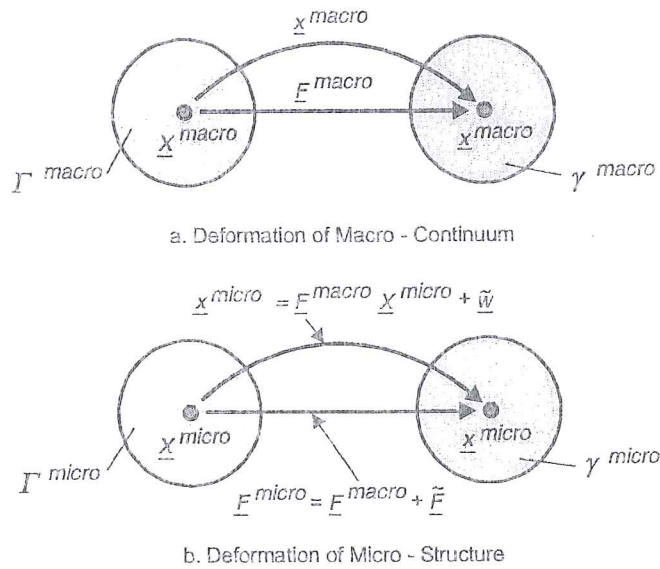


Figure 5-13 Schematic diagram of the deformation at the macroscopic and microscopic levels (adapted from Miehe *et al.* 1999).

In Figure 5-12, Figure 5-13 and Figure 5-14, the superscript *macro* relates to the macroscopic mesh and the superscript *micro* identifies variables attached to the RVE considered at the microscopic simulation level. The following notations are introduced:

$\Gamma^{macro\ or\ micro}$	initial configuration,
$\gamma^{macro\ or\ micro}$	deformed configuration associated to the initial one,
$\underline{X}^{macro\ or\ micro}$	coordinate tensor in the initial configuration,
$\underline{x}^{macro\ or\ micro}$	coordinate tensor in the deformed configuration,
$\underline{F}^{macro} = \frac{\partial \underline{x}^{macro}}{\partial \underline{X}^{macro}}$	macroscopic deformation gradient tensor
$\underline{F}^{micro} = \frac{\partial \underline{x}^{micro}}{\partial \underline{X}^{macro}}$	microscopic deformation gradient tensor,
\underline{n}^Γ	outward normal of the initial configuration of the RVE,
\underline{n}^γ	outward normal of the deformed configuration of the RVE.

The following averaging relations define the macroscopic gradient tensor and the macroscopic first Piola Kirchhoff stress $\underline{\tau}^{macro}$ from their values at a microscopic scale :

$$\underline{F}^{macro} = \frac{1}{V} \int_{\Gamma^{micro}} \underline{F}^{micro} dV \quad (5-24)$$

$$\underline{\tau}^{macro} = \frac{1}{V} \int_{\Gamma^{micro}} \underline{\tau}^{micro} dV \quad (5-25)$$

The application of Gauss' theorem leads to:

$$\underline{F}^{macro} = \frac{1}{V} \int_{\Gamma^{micro}} \underline{F}^{micro} dV = \frac{1}{V} \int_{\partial\Gamma^{micro}} \underline{x}^{micro} \otimes \underline{N}^{\Gamma} dA \quad (5-26)$$

$$\underline{\tau}^{macro} = \frac{1}{V} \int_{\Gamma^{micro}} \underline{\tau}^{micro} dV = \frac{1}{V} \int_{\partial\Gamma^{micro}} \underline{t}^{micro} \otimes \underline{X}^{micro} dA \quad (5-27)$$

where the tension on the boundary $\partial\Gamma^{micro}$ is defined by :

$$\underline{t}^{micro} = \underline{\tau}^{micro} \underline{n}^{\Gamma} \quad (5-28)$$

Figure 5-14 a. illustrates the above theoretical considerations. Figure 5-14 b., c., d. present different microscopic finite element meshes: one element per crystal grain (b.), regular square elements mesh (c), mesh of triangles applied on the crystals (d).

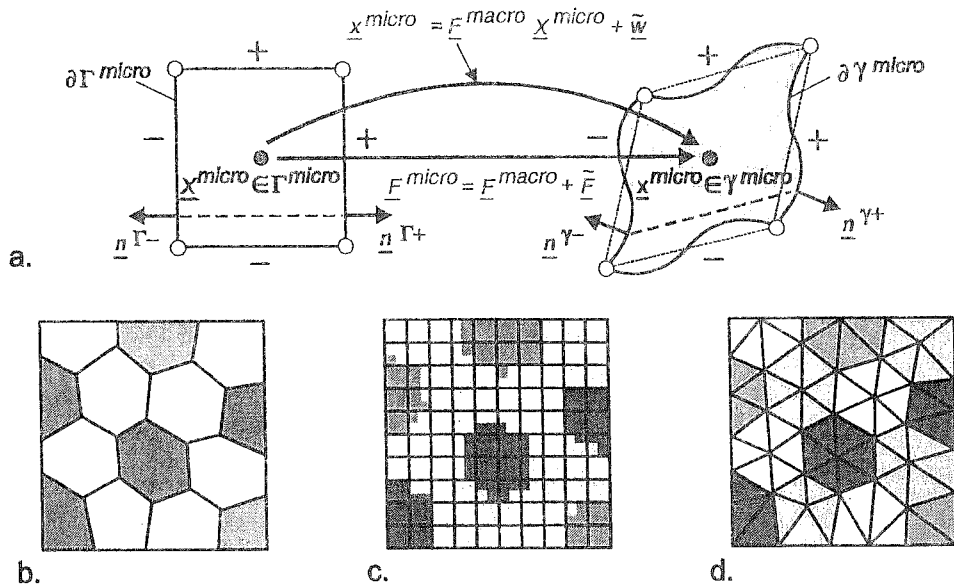


Figure 5-14 a. Deformation of the microstructure level
 b., c., d. Finite element meshes applied to the initial shape of the RVE, where
 crystals are identified by different grey colors
 (adapted from Miehe *et al.* 1999).

The deformation assumption in the RVE is related to macroscopic values by:

$$\underline{x}^{micro} = \underline{F}^{macro} \cdot \underline{X}^{macro} + \tilde{w} \quad (5-29)$$

$$\underline{F}^{micro} = \underline{F}^{macro} + \tilde{F} \quad (5-30)$$

The assumption (5-30) coupled with the previous average equation (5-26) leads to:

$$\frac{1}{V} \int_{\Gamma^{micro}} \tilde{\underline{F}} dV = \frac{1}{V} \int_{\partial\Gamma^{micro-}} \tilde{\underline{w}} \otimes \underline{n}^{\Gamma^-} dA + \frac{1}{V} \int_{\partial\Gamma^{micro+}} \tilde{\underline{w}} \otimes \underline{n}^{\Gamma^+} dA = 0 \quad (5-31)$$

with $\underline{N}^{\Gamma^+} = -\underline{N}^{\Gamma^-}$ at 2 associated points of the contour (Figure 5-14 a.).

This general mathematical frame shows that 3 alternative possibilities directly satisfy relation (5-31) :

- $\tilde{\underline{w}} = 0$ everywhere in Γ^{micro} : Taylor's assumption $\underline{F}^{micro} = \underline{F}^{macro}$ is recovered, no superimposed deformation field at the microscale;
- $\tilde{\underline{w}} = 0$ on the contour $\partial\Gamma^{micro}$: zero fluctuation of the superimposed deformation field $\tilde{\underline{w}}$ on the boundary but non zero fluctuation inside the RVE;
- $\tilde{\underline{w}}^+ = \tilde{\underline{w}}^-$ on the contour $\partial\Gamma^{micro}$: periodic fluctuation of the superimposed deformation field $\tilde{\underline{w}}$ on the boundary.

Set of representative crystals

All the examples presented in Mische *et al.* 1999 start from an isotropic texture easily represented by random crystal orientations. According to the size of the macroscopic mesh, the number of finite elements in the RVE varies.

For instance, in a validation test simulating a simple shear loading, one macroscopic element is used, coupled with 100 finite elements in the RVE. Each of them has one integration point associated with one crystal orientation. The texture predictions resulting from the 3 alternative choices for the $\tilde{\underline{w}}$ field are quite close to each other.

Another example of punch indentation was computed using 100 macroscopic finite elements, each of them linked with 400 crystal grains in the RVE.

Behavior model of each crystal

Mische *et al.* 1999 provides one of the most complete micro-macro models: it considers the anisotropic elasticity in each crystal coupled with a plastic or viscoplastic anisotropic behavior. This model takes into account thermomechanical behavior as well. The rate dependent plastic behavior is quite classical and the rate independent plastic approach proposes an extension of the work of Kothari & Anand 1996.

Conclusion

The advantages of this approach are that texture and grain shape or size effects are directly taken into consideration. Like in the self-consistent approach, both equilibrium and compatibility between crystals are reached in the RVE. The effects of 3 different assumptions at the microscopic scale (Taylor's, no fluctuation or periodic fluctuation on the boundary) are easily considered. One significant drawback is the amount of computations and memory requirements, which are even

worse than with self-consistent and Taylor's models coupled with macroscopic FEM simulations. For instance, the variables describing the microscopic FEM simulation (nodal positions, state variables at every microscopic integration point: crystal orientation, reference CRSS or CRSS for each slip systems...) associated to every macroscopic integration point must be stored. So far, no industrial examples were simulated with this approach.

5.4. Macroscopic FEM simulations with microscopic models

Micro-Macro Link

Nakamachi & Dong 1997, Nakamachi *et al.* 1999a, Nakamachi *et al.* 1999b, propose a very nice simplification of the simulations presented in section 5.3.1. A macroscopic mesh is defined to model the investigated process (Limiting Dome Height test, see Figure 1-1, cup deep drawing, see Figure 1-2). For instance in Nakamachi & Dong 1997, the quarter of the 180 x 100 mm blank used in the NUMISHEET'96 LDH benchmark test (Lee *et al.* 1996) is simulated by 1125 eight-node SRI (Selected Reduced Integration) solid elements. At every macroscopic interpolation point, the behavior law of a single crystal characterized by its orientation and the hardening state of each of its slip system is adopted. This approach is in fact a macroscopic extension of the microscopic FEM computation described in section 5.2. It can be considered as an inhomogeneous material modeling and it appears as the limit ($N=1$) of the models presented in section 5.3. In the macroscopic examples (LDH test, cup deep drawing) described in Nakamachi & Dong 1997, Nakamachi *et al.* 1999, Nakamachi *et al.* 1999b, no grain size effect is considered. However, the same approach applied on small scale simulations (rectangular sheet of 0.1mm x 0.3 mm in Nakamachi *et al.* 1999) allows to study grain size effect like in section 5.2.2.

A dynamic explicit finite element code is used with an elastic/crystalline viscoplastic constitutive law. Details on the crystalline viscoplasticity model are given hereafter. No special assumption as Taylor's, self-consistent or homogenization is needed as one single crystal orientation is given per macroscopic integration point. The strain heterogeneity between interpolation points directly follows from the nodal displacements. The equilibrium is assumed but not checked since an explicit finite element scheme is used.

Representative crystals orientation

The initial crystal orientation assigned to each interpolation point is randomly selected from a crystal population chosen to be representative of the measured ODF (Nakamachi & Dong 1997).

Behavior model of each crystal

The elastic/crystalline viscoplastic constitutive law is detailed in Nakamachi *et al.* 1999. Here, only the evolution of the CRSS associated with the slip system s is presented. Relation (5-32) takes into account the hardening process between slip systems as already done by relation (4-16) but it adds a softening aspect:

$$\dot{\tau}^s = \sum_{u=1}^N (h^{su} - s^{su}) |\dot{\gamma}^u| \quad (5-32)$$

The hardening coefficient matrix h^{su} is related to the grain size, to the increase of dislocation density, to the shear slip and to the interaction matrix between self and latent hardening:

$$h^{su} = \left\{ h_1 - h_2 \tanh\left(\frac{D}{h_3}\right) \right\} n \{C(\gamma_0 + \gamma)\}^{n-1} q^{su} \quad (5-33)$$

where h_1, h_2, h_3 parameters related to the grain size D ,
 n, C parameters related to the increase of dislocation density,
 γ_0 initial shear slip,
 q^{su} interaction matrix of self and latent hardening.

The softening coefficient matrix s^{su} is related to the grain size, to the decrease of dislocation density, to the shear slip, to the CRSS level and to the cross slip:

$$s^{su} = \left\{ s_1 + s_2 \tanh\left(\frac{D}{s_3}\right) \right\} \left(\frac{I}{I + r/r_0} \right) s_0 \tau_c^s \tau^u p^{su} \quad (5-34)$$

with

s_1, s_2, s_3 parameters related to the grain size D ,
 r actual distance between the adjacent slip systems,
 r_0 initial distance between the adjacent slip systems,
 s_0 parameters related to the decrease of dislocation density due to glide work, and thermomechanical effect,
 p^{su} parameter of dynamic recovery due to cross slip.

Conclusion

From Nakamachi's oral presentation at NUMISHEET 1999, it is known that his model has been applied with success to the simulations of cup deep drawing. However, in the written version, Nakamachi *et al.* 1999 only present the theory but not yet the Numisheet 99 benchmark applications.

The interest of such an approach is the decrease in computation time and variables storage as a set of representative crystals per integration point is replaced by a single crystal. Each integration point behaves like a single crystal characterized by a

different orientation; the material response must therefore be quite heterogeneous and it is not sure that an implicit FEM approach would converge. However, this approach gives a possible direct application of the micro-macro approach.

5.5. FEM analysis applied on both ODF evolution and macroscopic process

The discrete set of representative crystals used in FEM simulations as described in section 5.2 suffers from shortcomings because the characterization comes with few analytical tools. No direct means are available, for instance, to develop quantitative measures to differentiate between textures associated with distinct discrete aggregates. As a result, considerations on differences between textures are often qualitative, or obtained through projections onto alternate representations. In dealing with spatially inhomogeneous textures, there is often a need to interpolate or to project across textures. This requirement appears when initializing from experiment, or computing spatial gradients of texture as measures of the inhomogeneity degree. Such measures are important when the considered material is initially inhomogeneous and when substantial inhomogeneities develop over the course of the process. In rolling, for instance, highly localized regions of inhomogeneity develop through the thickness of the sheet due to roll induced shearing.

Kumar & Dawson 1995a, 1995b and 1996 and Dawson & Kumar 1997 propose a quite complex approach that uses directly the ODF without relying on discrete sets of representative crystals. This approach offers the advantage of an easier and more accurate possibility to compare and interpolate textures. 2 FEM simulations applied in different spaces are connected to each other :

- **in the crystal orientation space**, a finite element mesh describes the ODF representing the material; a microscopic finite element analysis is used to solve the ODF conservation equation presented in section 5.5.3;
- **in the classical geometrical space**, a spatial steady state simulation using Eulerian finite elements is applied to an industrial process such as rolling for instance.

It is fundamentally different from the approach proposed in section 5.3.3 which consists of 2 coupled FEM simulations in the classical geometrical space but performed on different scales: microscopic and macroscopic.

Of course, in Kumar and Dawson's work, both FEM simulations are coupled:

- the microscopic FEM requires the strain evolution to compute texture evolution;
- the macroscopic FEM uses the up-dated texture as well as crystal plasticity with Taylor's or Sachs' assumption to get the macroscopic constitutive behavior.

5.5.1. Crystal orientation representation

The crystal orientation is defined as the rotation \underline{R} required to align the crystal lattice frame with a fixed sample reference frame. Three independent parameters are sufficient to describe such a rotation. Euler's angles are a frequent choice (see section 3.2, Figure 3-4). An alternative class of representation uses an axis of rotation \underline{n} and an angle of rotation ϕ . In this case :

$$\underline{R}(\underline{n}, \phi) = \underline{n} \otimes \underline{n} + (\underline{I} - \underline{n} \otimes \underline{n}) \cos \phi + \underline{I} \wedge \underline{n} \sin \phi \tag{5-35}$$

where \underline{I} is the second order unit tensor. A particular representation of the crystal orientation is defined by Rodrigues' parameters which are the components r^1, r^2, r^3 of vector \underline{r} :

$$\underline{r} = \underline{n} \operatorname{tg} \phi \tag{5-36}$$

The parameters r^1, r^2, r^3 define the so-called Rodrigues' space.

The advantages of this choice are the following ones :

- A simple *fundamental region* can be computed in the orientation parameters space. Rodrigues' proposal defines all the possible crystal orientations without redundancy due to crystal symmetry. For instance, the case of f.c.c crystal leads to the fundamental region represented on Figure 5-15.

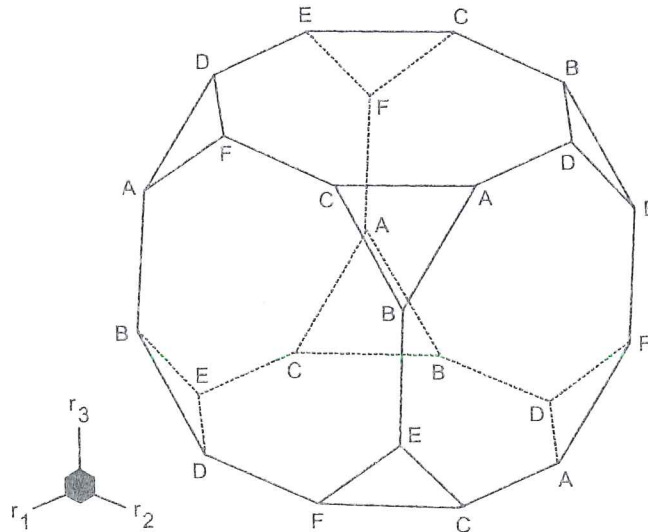


Figure 5-15 f.c.c fundamental region for Rodrigues' space (from Kumar & Dawson 1995).

- The space distortion is limited and there is no singularity in this space. This can be deduced from the form of the invariant volume element:

$$dv = \cos^2\left(\frac{\phi}{4}\right) dr^1 dr^2 dr^3 \tag{5-37}$$

The quantity $\cos^2 \frac{\phi}{4}$ is plotted in Figure 5-16 versus the angle ϕ , the range of which increases as the crystal degree of symmetry decreases from cubic to orthorhombic lattice.

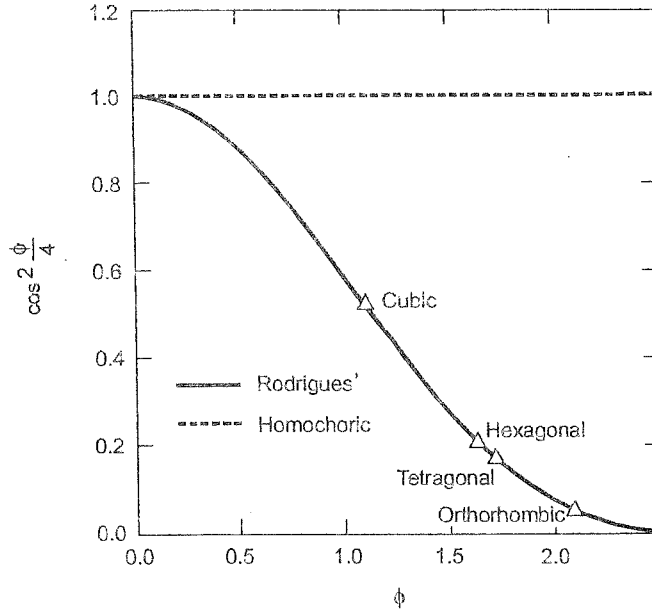


Figure 5-16 Volumetric scaling factor for Rodrigues' parameters (from Kumar & Dawson 1995).

With this parametrization, the *Orientation Distribution Function (ODF)* is defined by the *probability density* $f(\underline{r})$. The volume fraction V^* of crystals whose orientations belong to a subset Ω^* of the orientation space is given by:

$$V^* = \int_{\Omega^*} f(\underline{r}) d\Omega \tag{5-38}$$

The whole domain Ω of orientation space depends on symmetries exhibited by the crystal. $f(\underline{r})$ is scaled in such a way that:

$$1 = \int_{\Omega} f(\underline{r}) d\Omega \tag{5-39}$$

5.5.2. Micro-macro links

The macroscopic behavior is the average of the behavior of the individual crystallites of the aggregate. If x^{micro} is an arbitrary crystal quantity, its macroscopic value x^{macro} is given by:

$$x^{macro} = \int_{\Omega} x^{micro}(\underline{r}) f(\underline{r}) d\Omega \tag{5-40}$$

Here is a difference with respect to approaches using a discrete sample of orientations and simply computing a weighted average of the crystal quantities (see relations (5-18) and (5-19)). Dawson and Kumar apply a visco-plastic constitutive law at the crystal level as proposed in section 4.2., with identical rate sensitivity and CRSS for all slip systems and for all the crystallites related to one interpolation point. Coupling this crystal behavior law with the crystal velocity gradient (4-2) and the definition of the resolved shear stress (3-2), an invertible relationship between the crystal deformation rate and the deviatoric stress in this crystallite is obtained:

$$\underline{\underline{\hat{\sigma}}}^{micro} = \underline{\underline{D}}^{micro} : \underline{\underline{\hat{\epsilon}}}^{micro} \quad (5-41)$$

where $\underline{\underline{D}}^{micro}$ is the microscopic stiffness. Then, either Taylor's assumption of equality between micro and macro plastic strain rates or the assumption of micro and macro stress equality (Prantil *et al.* 1995) is applied. Both assumptions allow to reach $\underline{\underline{D}}^{micro}$ and its average value, computed by (5-40). This gives upper and lower bounds to macroscopic stiffness.

5.5.3. Evolution rule of the Orientation Distribution Function

Restricting his attention to the lattice reorientation caused by crystallographic slips, Clement 1982 proposes to model texture evolution by integrating an equation for the rate of change of the probability density $f(\underline{r}, t)$. This equation results from requiring that the material derivative of relation (5-39) vanishes.

$$\frac{\partial f}{\partial t} + \underline{v} \cdot \text{grad } f + f \text{ div } \underline{v} = 0 \quad (5-42)$$

where \underline{v} is the reorientation velocity. Note that Arminjon 1988 provides a demonstration of this type of equation using physical hypotheses. The above formulation is an Eulerian representation in which f is associated to particular locations in the orientation space, rather than to particular crystals whose orientations change. Alternatively, a reference texture f_0 can be specified, for instance f at time t_0 . Then, this reference position remains fixed for all times and is used to define initial Lagrangian coordinates for crystals. Relation (5-42) can be written either with respect to current Eulerian coordinates $f(\underline{r}, t)$ or with respect to the Lagrangian coordinates $\hat{f}(\underline{r}_0, t)$. The two representations are related through the mapping of coordinates from reference to current configurations:

$$f(\underline{r}, t) = \hat{f}(\underline{r}_0, t) \quad (5-43)$$

and

$$\hat{f}(\underline{r}_0, t) J(\underline{r}_0, t) = f_0(\underline{r}_0) \quad (5-44)$$

where $J(\underline{r}_0, t)$ is the determinant of the mapping, which corresponds to the trajectories of crystals in the orientation space due to plastic deformation:

$$\underline{r}(t) = \hat{\underline{r}}(\underline{r}_0, t) \quad (5-45)$$

In Lagrangian representation, relation (5-42) becomes:

$$\frac{\partial f}{\partial t} + \hat{f} \operatorname{div} \hat{\underline{v}} = 0 \quad \text{where } \hat{\underline{v}}(\underline{r}_0, t) = \underline{v}(\underline{r}, t) \quad (5-46)$$

Euler's choice (5-42) leads to difficulties in the FEM formulation because of the convective contribution associated with the term $\underline{v} \cdot \operatorname{grad} f$. This still remains a problem, even if some solutions are proposed in computational fluid mechanics. The alternative is to use the Lagrangian representation (5-46). However, this adds the cost of an explicit computation of crystal trajectories in the orientation space. Both approaches are described in Kumar & Dawson 1996.

Another difficulty is the extreme behavior of the ODF. The ODF can evolve exponentially, sometimes tending asymptotically to Dirac's function. Clearly, inaccuracies are inevitable as the finite element size cannot tend to 0. An effective strategy applied by Kumar and Dawson is to moderate the evolution of the ODF by the following transformation :

$$p = \ln f \quad (5-47)$$

5.5.4. Computation of the reorientation velocity field

Relations (5-42) and (5-46) to compute the new ODF make use of the reorientation velocity field \underline{v} , which is linked to crystal plasticity and to the relationship between the crystal velocity gradient and its macroscopic counterpart. As explained in section 4.1.1 related to single crystal plasticity, the rate of crystal lattice rotation $\underline{\Omega}^L$ can be expressed by (4-12):

$$\underline{\Omega}^L = \underline{\Omega}^{micro} - \sum_s \underline{Z}^s \dot{\gamma}^s \quad (5-48)$$

where the first term on the right side of (5-48) is directly given by the macroscopic spin if Taylor's assumption is chosen. The second term is the spin due to the slip rates on the different slip systems.

The relationship between $\underline{\Omega}^L$ and \underline{v} depends on the specific parametrization employed for rotations. For Rodrigues' parameters, Kumar & Dawson 1995a or Dawson & Kumar 1997 establish:

$$\underline{v} = \frac{1}{2} (\underline{\Omega}^{Lv} + (\underline{\Omega}^{Lv} \cdot \underline{r}) \underline{r} + \underline{\Omega}^{Lv} \wedge \underline{r}) \quad (5-49)$$

where $\underline{\Omega}^{Lv}$ is a vector form of the rate of crystal lattice rotation $\underline{\Omega}^L$.

5.5.5. Texture prediction under monotonic deformations

The following example shows a FEM analysis applied to solve the texture conservation relation under the assumption of plane strain compression of f.c.c polycrystals. In Figure 5-17, the 3D FEM mesh of 28672 - 4 nodes tetrahedral elements is showed.

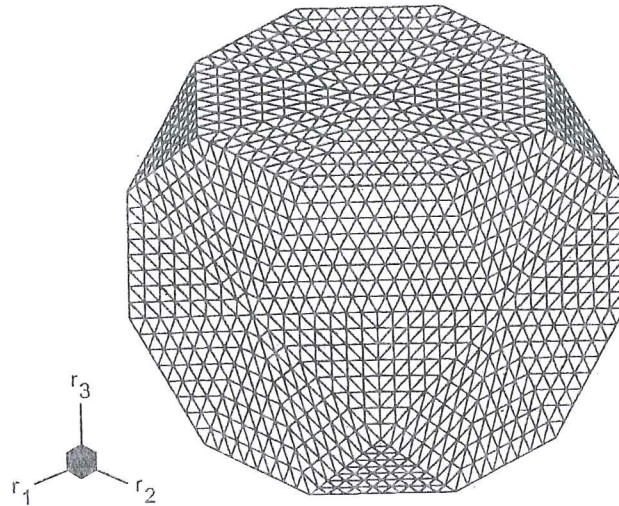


Figure 5-17 FEM mesh used for f.c.c fundamental region (from Kumar & Dawson 1995b).

As Taylor's hypothesis is applied, the reorientation velocity, developed under a monotonic deformation, is invariant with strain. So crystal computations are done only once. The developed texture is adequately represented by the ODF on the boundaries of the fundamental region; consequently only outside views of the ODF are represented. The ideal components of f.c.c plane strain compression texture are compared with the computed results on Figure 5-18.

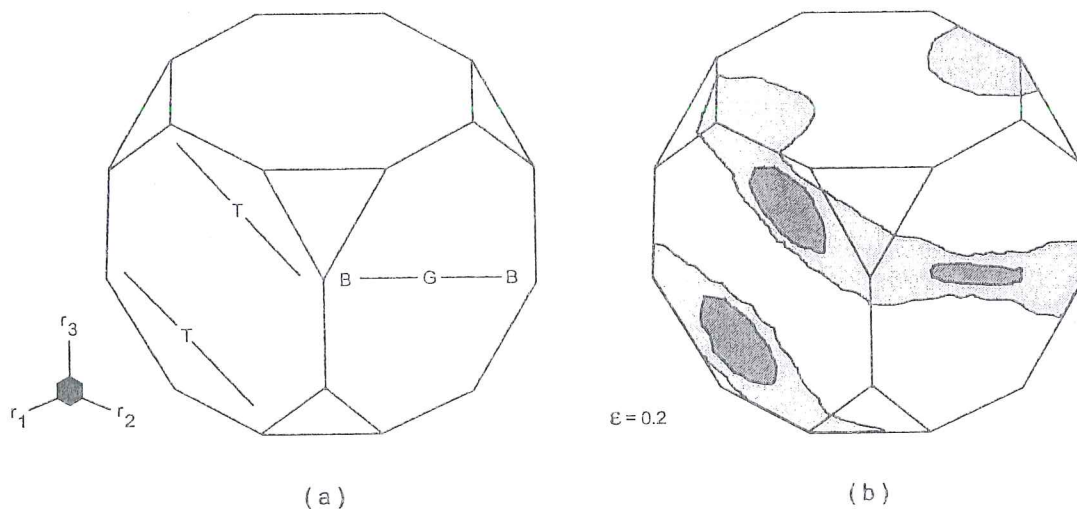


Figure 5-18 Ideal (a) and computed (b) components of plane strain compression texture of an f.c.c polycrystal (from Kumar & Dawson 1995b).

Texture development is dominated by two fibers:

- an α fiber connecting the ideal Goss and Brass' orientations;
- the β fiber connecting Brass and Taylor's orientations.

5.5.6. Application to aluminum rolling

The flat rolling of a 1100 aluminum (Figure 5-19) being a steady state process, a macroscopic Eulerian FEM approach is applied to model the macroscopic mechanical problem (Figure 5-20).

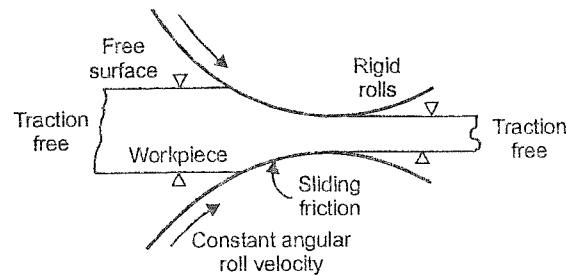


Figure 5-19 Schematic diagram of flat rolling (from Dawson & Kumar 1997).

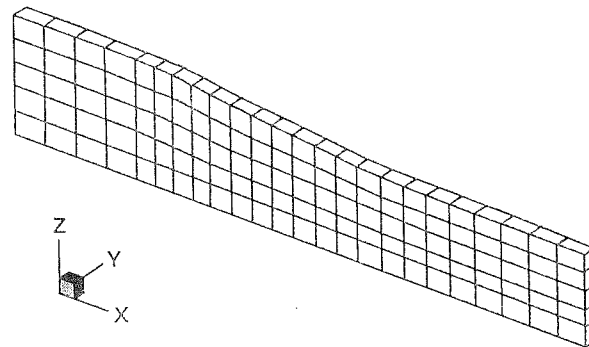


Figure 5-20 Finite element discretization of the workpiece (from Dawson & Kumar 1997).

In fact, the FEM analysis of texture evolution is coupled with the macroscopic FEM computation. Two FEM scales are present and the details on their parallel implementation can be found in Kumar & Dawson 1995b. Figure 5-21 shows the equivalent plastic deformation rate, the reference CRSS and the scalar measure of the spatial gradients of the ODF defined by :

$$\nabla A = \int_{\Omega} |\text{grad } f(\underline{r}, \underline{x})| d\Omega \quad (5-50)$$

where \underline{x} identifies a material point of the workpiece.

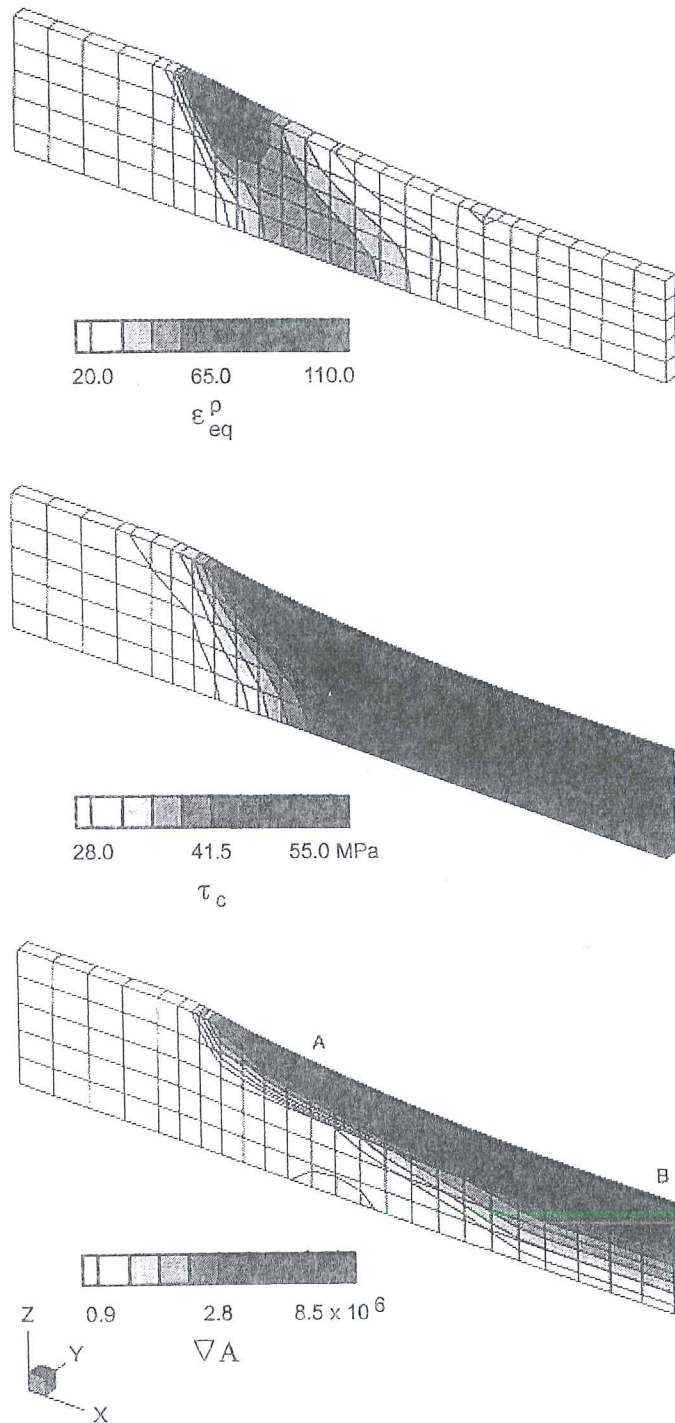


Figure 5-21 Contour plots of the equivalent plastic deformation rate ϵ_{eq}^p ,
 the reference CRSS τ_c ,
 a scalar measure of the spatial gradients of the ODF ΔA ,
 (from Kumar & Dawson 1995).

As expected, the microstructure hardens primarily within the deformation zone under the roll. Hardening and texture gradients appear through the workpiece thickness. It is observed that the texture gradients are rather important.

5.5.7. Conclusion

This approach developed by Kumar and Dawson is interesting from a scientific point of view. It shows another proposal for the micro-macro coupling, not limited to the mechanical point of view. Here the FEM formulation is directly applied for texture prediction and, hence, provides metallurgical information. However, the amount of computations seems to be even greater than in section 5.2 since the mesh discretization of the texture problem is already of large size.

5.6. Conclusion

Section 5.1 demonstrates the interest of FEM microscopic simulations to check the microscopic models and to investigate the effect of microscopic parameters such as the influence of grain sizes on the macroscopic mechanical behavior.

Clearly, with parallel computers, the above selection of scientific works (sections 5.3., 5.4. and 5.5) shows that micro-macro approaches attract a great interest and become closer to practical problems. However, for each type of applications, it appears that more efforts should be devoted estimating the size of the set of representative crystals or the RVE or the texture discretization. This is directly linked to the accuracy of the results and to the CPU time.

From this review, it appears that a visco-plastic formulation is very often used at the crystal level with the advantage of avoiding the choice between the multiple solutions of Taylor's model. However, at room temperature, the strain rate sensitivity coefficient is very low, which leads to numerical difficulties and explains the further research dedicated to the strain rate independent approach (Anand & Kothari 1996, Miehe *et al.* 1999). Finally both models can be chosen according to their availability.

The use of a common CRSS evolution rule (5-20) for all the slip systems in a crystal or even for all crystallites in a polycrystal at an integration point, seems a logical simplification to limit the number of state variables. However, a clear information on the accuracy benefit of choosing a distinct CRSS for each slip system seems unavailable.

The effect of the micro-macro links which have been used (FC or RC or modified Taylor's model, self-consistent model, homogenization method) has been the most studied problem. The choice clearly depends on the number of available slip systems, the desired accuracy and the CPU requirements. For b.c.c or f.c.c materials, Taylor's model already seems to give interesting results from a mechanical point of view

(stress, strain) but it also gives qualitative texture prediction with the lowest CPU time.

The simple approach proposed by Nakamachi 1999b offers a solution to reduce the CPU time of micro-macro approaches. However further results comparison with an implicit micro-macro FEM approach should be performed.

References

- Acharya, A., Bassani, J.L. (2000) Lattice incompatibility and a gradient theory of crystal plasticity, *J. Mech. Phys. Solids*, **48/8**, 1565-1595.
- Acharya, A., Beaudoin, A.J. (2000) Grain-size effect in viscoplastic polycrystals at moderate strains, *J. Mech. Phys. Solids*, **48/10**, 2213-2229.
- Anand, L., Kothari, M. (1996) A Computational Procedure for Rate-Independent crystal plasticity, *J. Mech. Phys. Solids*, **44/4**, 525-558.
- Anand, L., Balasubramanian S., Kothari, M. (1997) Constitutive Modeling of Polycrystalline Metals at Large Strains : Application to Deformation Processing, *Large plastic deformation of crystalline aggregates*, International Centre for Mechanical Sciences, Courses and Lectures n° 376, Springer Ed, 109-172.
- Arminjon, M. (1988) Lois de comportement homogénéisées pour la plasticité des polycristaux, Mém. d'habilitation, Univ. Paris-Nord, Villetaneuse.
- Asaro, R.J., Needleman, A. (1985) Texture development and strain hardening in rate dependent polycrystals, *Acta Metallurgica*, **33**, 923-953.
- Beaudoin, A.J., Dawson, P.R., Mathur, K.K., Kocks, U.F., Korzekwa, D.A. (1994) Application of polycrystal plasticity to sheet forming, *Comp. Methods Appl. Mech. Eng.*, **117**, 49-70.
- Beaudoin, A.J., Dawson, P.R., Mathur, K.K., Kocks, U.F. (1995) A hybrid finite element formulation for polycrystal plasticity with consideration of macrostructural and microstructural linking, *Int. J. Plasticity*, **11/5**, 501-521.
- Becker (1990) An analysis of shear localization during bending of a polycrystalline sheet, *Microstructural Evolution in Metal Processing*, **46**.
- Bertram, A., Böhlke, T., Kraska, M. (1997) Numerical simulation of texture development of polycrystals undergoing large plastic deformations, *Computational Plasticity, Fundamentals and Applications*, Owen D.R.J., Onate, E., Hinton E. Eds.
- Canova, G.R., Lebensohn, R. (1995) Micro-macro modelling, *Computer Simulation in Materials Science, NATO ASI, Ile d'Oleron, France, June 6-16*.
- Chastel, Y., Loge, R., Perrin, M., Lamy, V. & Zaefferer, S. (1998) Microscopic and macroscopic length scales in hot extrusion of Zircaloy 4, *First ESAFORM Conference on Material Forming*, Sophia-Antipolis, France.
- Clément, A. (1982) Prediction of Deformation Texture Using a Physical Principle of Conservation. *Mater. Sci.&Eng.*, **55**, 203-210.
- Dawson, P.R., Beaudoin, A.J., Mathur, K.K. (1992) Simulating deformation-induced texture in metal forming, *Num. Meth. in Ind. Form. Proc.*

- Dawson, P.R. & Kumar, A. (1997) Deformation Process Simulations Using Polycrystal Plasticity, *Large plastic deformation of crystalline aggregates*, International Centre for Mechanical Sciences, Courses and Lectures n° 376, Springer Ed, 247.
- Feyel; F., Chaboche, J.L. (2000) Multiscale non linear FE analysis of composite structures : damage and fiber size effects, *Euromech 417*, 2-4 October 2000, University of Technology of Troyes, France.
- François, D., Oineau, A. Zaoui, A (1992) *Elasticité et Plasticité*, Hermes, Paris.
- Geers, M.G.D., Kouznetsova, V., Brekelmans, W.A.M. (2000) Constitutive approaches for the multi-level analysis of the mechanics of microstructures, 5th National Congress on Theoretical and Applied Mechanics, Louvain-La-Neuve, May 23-24, 2000.
- Hacquain A., Montmitonnet, P., Guillerault J.P. (1995) Coupling of roll and strip deformation in three-dimensional simulation of hot rolling, *Simulation of Materials Processing : Theory, Methods and Applications*, 921.
- Kalidindi, S.R., Bronkhorst, C.A., Anand, L. (1992) Crystallographic texture evolution during bulk deformation processing of FCC metals, *J. Mech. Phys. Solids*, **40**, 537-579.
- Kalidindi, S.R., Anand, L. (1994) Macroscopic shape change and evolution of crystallographic texture in pre-textured FCC metals, *J. Mech. Phys. Solids*, **42/3**, 459-490.
- Kallend, J.S., Kocks, U.F., Rollett, A.D., Wenk, H.R. (1991) popLA – an integrated software system for texture analysis. *Text. microstruct.*, **14-18**, 1203-1208.
- Kumar, A., Dawson, P.R. (1995a) The simulation of texture evolution during bulk deformation processes using finite elements over orientation space, *Simulation of Materials Processing : Theory, Methods and Applications*, Shen & Dawson Eds., Balkema.
- Kumar, A., Dawson, P.R. (1995b) Polycrystal plasticity modeling of bulk forming with finite elements over orientation space, *Comp. Mech.*, **17**, 10-25.
- Kumar, A., Dawson, P.R. (1996) The simulation of texture evolution with finite elements over orientation space, I. Development, II. Application to planar crystals, *Comp. Methods Appl. Mech. Eng.*, **130**, 227-261.
- Lebensohn, R.A., Tome, C.N. (1993) A self-consistent anisotropic approach for the simulation of plastic deformation and texture development of polycrystals : application to Zirconium alloys, *Acta Metall. Mater.*, **41**, 2611-2624.
- Lee, J.K., Kinzel, G.L., Wagoner, R.H. (1996) Numerical Simulation of 3-D Sheet Metal Forming Processes - Verification of Simulations with Experiments, *Proceedings of the 3rd International Conference NUMISHEET'96*, Dearborn, USA, September 29-October 3, 1996.
- Mathur, K.K., Dawson, P.R. (1989) On modeling the development crystallographic texture in bulk forming processes, *Int. J. Plasticity*, **5**, 67-94.
- Miehe C., Schröder J., Schotte J. (1999) Computational homogenization analysis in finite plasticity, simulation of texture development in polycrystalline materials, *Computer methods in applied mechanics and engineering*, **171**, 387-418.

- Molinari, A. (1997) Deformation Process Simulations Using Polycrystal Plasticity, *Large plastic deformation of crystalline aggregates*, International Centre for Mechanical Sciences, Courses and Lectures n° 376, Springer Ed, 173-246.
- Nakamachi, E., Dong, X.H. (1997) Study of Texture Effect on Sheet Failure in a Limit Dome Height Test by Using Elastic/Crystalline Viscoplastic Finite Element Analysis, *J. Appl. Mech. Trans. ASME(E)*, **64**, 519-524.
- Nakamachi, E., Onate, E., Bergan, P., Boduroglu, M.H., Kaykayoglu, C.R. (1999a) The study of crystalline morphology effects on sheet metal forming, *IACM Expressions*, **7**, Spring-Summer 1999.
- Nakamachi, E., Xie C.L., Hiraiwa, K., Harimoto, M. (1999b) Development of elastic/crystalline viscoplastic finite element analysis code based on the meso-phenomenological material modeling, *Numisheet'99*, 13-17 September 1999, vol. 1, Besançon, France, 79-84.
- Nikolov, S., Doghri, I. (2000) A micro-macro constitutive model for the small deformation behavior of polyethylene, *Polymer*, **41**, 1883-1891.
- Neale, K.W. (1993) Use of Crystal Plasticity in Metal Forming Simulations, *Int. J. Mech. Sci.*, **35/12**, 1053-1063.
- Prantil, V., Dawson, P., Chastel, Y. (1995) Comparison of equilibrium based plasticity models and a Taylor like hybrid formulation for deformations of constrained crystal systems, *Modeling Simul. Mater. Sci. Eng.* **3**, 215-234.
- Smit, R.J.M., Brekelmans, W.A.M., Meijer, H.E.H. (1998) Prediction of the mechanical behavior of nonlinear heterogeneous systems by multi-level finite element modeling, *Comp. Meth. Appl. Mech. Eng.*, **155**, 181-192.
- Teodosiu, C., Raphanel, J.L., Tabourot, L. (1992) Finite Element Simulation of the Large Elastoplastic Deformation of Multicrystals, *Large Plastic Deformations. Fundamentals and Applications to Metal Forming (Proc. MECAMAT'91)*, Teodosiu C., Sidoroff F., Raphanel, J.L. Eds, Balkema, Rotterdam, 153-168.

6. FEM MICRO-MACRO MODELS WITH YIELD LOCUS

6.1. Introduction

In the preceding chapter, the drawback of high CPU time to compute the state of representative crystals, then to reach, by an averaging operation, the macroscopic behavior has often been mentioned. Scientists have investigated other micro-macro approaches that are less greedy from a CPU time point of view.

A first option is to develop new macroscopic elasto-plastic or elasto-visco-plastic models with general features imbued from plasticity models in single crystals. Such approaches are described in section 6.2.

Another option is presented in section 6.3. In this case, outside any FEM code, models at crystal level and micro-macro links are applied to estimate an accurate expression of the yield locus in polycrystal materials. Then, this accurate yield locus function is used during macroscopic FEM computations. The evolution of the size and position of this yield locus during the process is defined by macroscopic isotropic and kinematic hardening rules. As explained in chapter 3, such hardening models can be macroscopic but with strong links to microscopic phenomena. Even if their accuracy can be quite high (see Teodosiu & Hu 1998 and Miller & Mc Dowel 1996), such models generally neglect the "texture hardening", i.e. the fact that due to texture evolution, the yield locus shape should be updated. In some cases, this phenomenon is really negligible and using an accurate description of the initial yield locus conjugated with elaborate hardening models yields a very good accuracy at low CPU cost. The time reduction of such approaches as compared to FEM codes directly coupled with microscopic calculations (see section 5.3) is difficult to estimate. However we do not speak of a ratio of 2 or 3 but rather 10, 100 and even greater, if no parallel computation is applied.

About the memory requirement, such approaches spare all the variables needed at every interpolation point to store the orientation and the average CRSS (or even the CRSS associated to each slip system) of each crystal of the representative set. This explains why, even if some yield locus description and their hardening behavior need 100 or more constants and 50 internal variables, they are still much more economical than the micro-macro approaches presented in chapter 5.

Of course these FEM models predict only the mechanical behavior. If the texture evolution is an interesting result, the strain history during the process must be stored and used in post-processor modules to predict the final texture. Such an approach is proposed by Winters 1996, who simulates a cup drawing with the LAGAMINE code using the yield locus described in section 6.3.4. Then he uses the strain history to

predict the texture evolution and compares it to texture measurements. His simulation results are quite accurate. Another example is the work by Schoenfeld & Asaro 1996. They study the texture gradients through thickness in rolled polycrystalline alloys by means of FEM rolling simulations using a phenomenological constitutive law. Once the displacement time history of the roll gap has been calculated, Taylor's model is applied at locations of interest through the thickness of the workpiece to predict the final texture and material anisotropy.

Finally, section 6.4 describes the model developed by MSM department. It stands between the models of section 5.3 and the accurate yield locus functions deduced from texture (section 6.3). As the aim is to model the effect of texture updating on the shape of the yield locus, a function accurately describing the whole yield locus and adjusted from computations on a set of representative crystals would be too expensive to fit each time the texture needs to be updated. A function limited to a "small local zone" of the yield locus has been chosen and the position of this zone is adapted according to the stress or strain rate state of each integration point. The identification of this function requires a limited number of calls to Taylor's model applied on a set of representative crystals. As for memory storage, this approach is equivalent to FEM models coupled with microscopic computations, described in section 5.3. However, concerning the constitutive law, generally no call to microscopic computations is needed. Some calls exist if it appears that the local zone of the yield locus does not fit with the new material state. After a few increments or time steps, texture updating is taken into account by using a Taylor's model to compute the new orientations of the set of representative crystals and to update the local zone of the yield locus. Details and examples are given in sections 6.4. and 6.5.

Such analysis where some microscopic computations still appear in the FEM code, is slower than the totally decoupled approaches described in section 6.3. Its interest is to take into account the texture updating effect on the yield locus, without the microscopic computations necessary to compute a complete updated yield locus.

6.2. Macroscopic models imbued from single crystal plasticity

6.2.1. 3G Model

The "Centre de Recherches Métallurgiques" of Liège has developed the so-called "3G model" (Montfort *et al.* 1991, Montfort & Defourny 1993, Montfort & Defourny 1994). It is a non-associated visco-plastic model. The planar isotropic version has been studied and validated in the Ph.D. by Hage Chegade 1990, before the proposal of an orthotropic version by Montfort & Defourny 1993.

To understand this approach, first consider the plane stress state in a planar isotropic material as described on Figure 6-1.

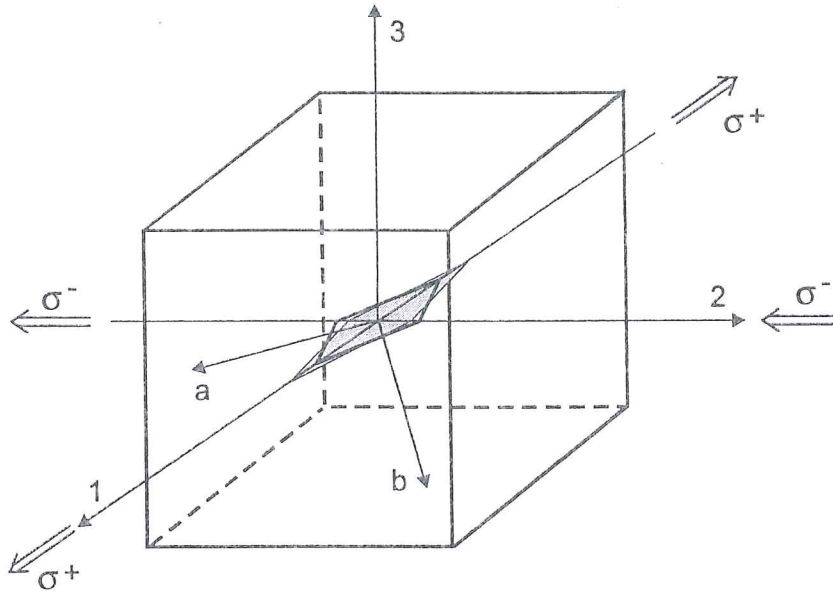


Figure 6-1 Plane stress state resulting in a pure shear state in axes a, b , rotated by 45° from the principal stress axes 1,2 (adapted from Hage Chehade 1990).

The strain tensor associated to this loading state is defined by (6-1) where G_{12} is associated to the shear stress τ_{12} applied on the planes oriented at 45° from directions 1 and 2.

$$\underline{\underline{\epsilon}}^P = \begin{pmatrix} G_{12} & 0 & 0 \\ 0 & -G_{12} & 0 \\ 0 & 0 & 0 \end{pmatrix}_{ref\ axes\ 1,2,3} \quad \underline{\underline{\epsilon}}^P = \begin{pmatrix} 0 & G_{12} & 0 \\ G_{12} & 0 & 0 \\ 0 & 0 & 0 \end{pmatrix}_{ref\ axes\ a,b,3} \quad (6-1)$$

The extension of this simple state to general cases assumes that plastic strains happen by plastic slips on planes oriented at 45° from principal axes and along directions where shear stresses are maximal. As in b.c.c metals, 24 families of slip planes exist, one can assume that there is always a crystallographic plane oriented nearly along a direction of maximum shear stress. This generalisation is represented by Figure 6-2 and by relation (6-2) where axes λ, μ, ν are not orthogonal axes.

The plastic strain tensor is expressed by:

$$\underline{\underline{\epsilon}}^P = \begin{pmatrix} 0 & G_{12} & G_{13} \\ G_{12} & 0 & G_{32} \\ G_{13} & G_{32} & 0 \end{pmatrix}_{ref\ axes\ \lambda,\mu,\nu} \quad (6-2)$$

where the 3 G shear strains, responsible for the model name, appear.

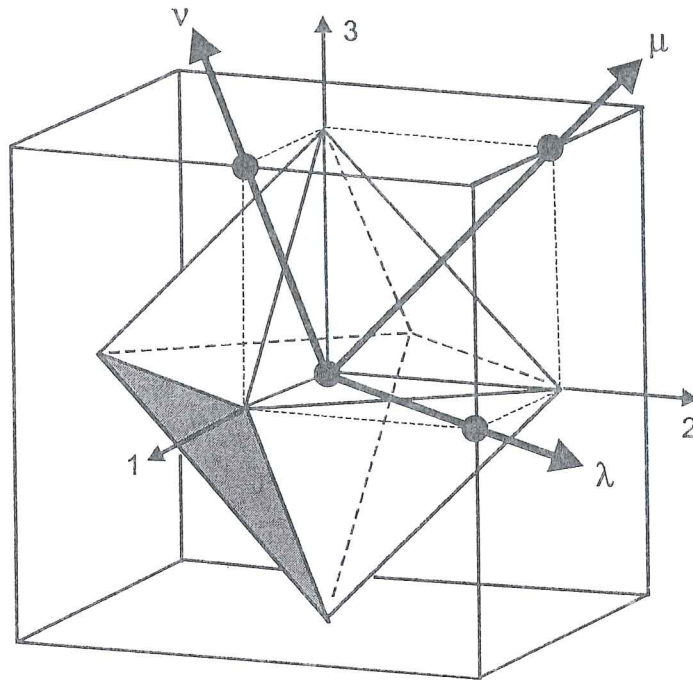


Figure 6-2 General view of assumed slip planes in general cases (adapted from Hage Chehade 1990).

For simplicity, relation (6-2) is written in principal axes 1,2,3:

$$\underline{\varepsilon}^p = \begin{pmatrix} \varepsilon_{11} & 0 & 0 \\ 0 & \varepsilon_{22} & 0 \\ 0 & 0 & \varepsilon_{33} \end{pmatrix} = \begin{pmatrix} G_{12} - G_{13} & 0 & 0 \\ 0 & G_{23} - G_{12} & 0 \\ 0 & 0 & G_{31} - G_{23} \end{pmatrix}_{ref\ axes\ 1, 2, 3} \quad (6-3)$$

Shear stresses acting on octahedral planes are associated to the 3 G shear strains:

$$\tau_{12} \rightarrow G_{12}, \tau_{23} \rightarrow G_{23}, \tau_{13} \rightarrow G_{13} \quad (6-4)$$

With the previous concepts in mind, the isotropic planar version of the 3G model applies to a thin sheet where the principal stress σ_3 in the thickness direction is low. It assumes that any plastic strain results from the superposition of plastic shears oriented at 45° from principal stresses directions as represented on Figure 6-3.

If the material presents a planar anisotropy, more crystals are oriented in specific directions for which a macroscopic deformation is easier or more difficult. In other words, the resistance to deformation varies with the direction in the sheet plane. Extending the isotropic planar approach, macroscopic strain occurs in families of planes presenting the most favourable ratio between the applied shear stress and the intrinsic resistance to deformation. In general, such planes are deviated from the 45° directions to principal stresses. The shift angle strongly depends on the Lankford coefficient. It can be mathematically determined as well as its incidence on the total deformation.

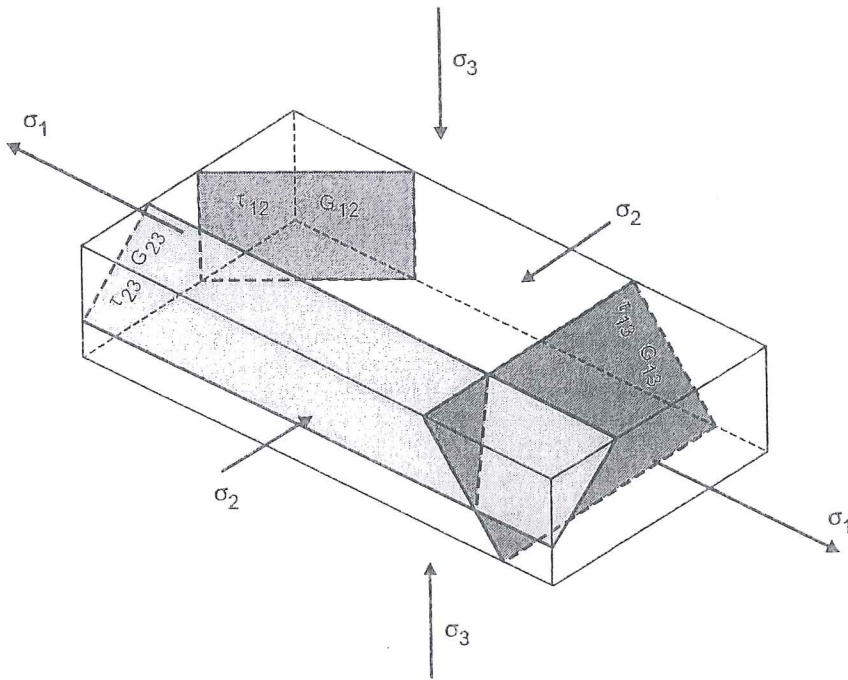


Figure 6-3 Sheet strains decomposed into plastic slips in planes oriented at 45° from principal stresses (from Hage Cheade, 1990).

As far as the hardening rule is concerned, the 3G model applies a generalization of Bergström's model presented in section 3.5.1 (Bergström 1969). Using the 3 G as strain measures allows to extend Bergström's work on a more physical basis for any stress and strain state. It is demonstrated (Monfort & Defourny, 1994) that the plastic shear stress τ used in Tresca's theory can be related to the 3G strain measures:

$$2\tau = A + B \left[1 - \exp \left(-a r_{45+\beta} (|G_{12}| + r_{90+\beta} |G_{23}| + r_{\beta} |G_{31}|) \right) \right]^{1/2} \quad (6-5)$$

where A, B and a are material constants, r_{α} is Lankford's coefficient for a direction at an angle α from the Rolling Direction, β is the angle between the first principal stress and the Rolling Direction and τ is the stress limit in Tresca's criterion, ($2\tau = \sigma_F$ is the yield stress in uniaxial tension test). For simplicity, Lankford's coefficient for any direction α is approximated by a simple function :

$$r_{\alpha} = C + D \sin^2 \alpha + E \sin^2 2\alpha \quad (6-6)$$

with 3 material constants C, D, E .

These constants can be determined from the values of r_0, r_{45} and r_{90} . As the 3G model is based on stresses acting on the maximum shear planes, a Tresca-like criterion is used, which is consistent with the mechanism taken into account:

$$|\sigma_1 - \sigma_2| + |\sigma_2 - \sigma_3| + |\sigma_3 - \sigma_1| - 2\tau = 0 \quad (6-7)$$

However the exact shape of the plasticity criterion is of secondary importance, since it only specifies the limiting stress level of plasticity initiation. The subsequent plastic behavior, in terms of stresses and strains is obviously more important with this non associated visco-plastic model. It is described by the flow rule presented hereafter. Returning to the physics, the evolution of the shear strain dG_{ij} is due to the creation and the propagation of mobile dislocations. It is proportional to:

- the time increment dt ;
- the rate of mobile dislocation creation¹, itself proportional to the total amount of immobile dislocations and to a thermal activation factor;
- the path free of mobile dislocations, which is assumed constant and equal to the average dimension of the dislocation cell as in Bergström's model;
- the inverse of Lankford's coefficient²;
- the probability that a dislocation moves along a given shear plane, which is a function of the shear stresses.

Finally, the flow rules proposed by Monfort & Defourny, 1994 for the shear strains dG_{ij} are given hereafter:

$$dG_{12}^1 = \frac{d\lambda(\sigma_1 - \sigma_2)\cos(2\alpha_1)}{2r_{(\beta-45-\sigma_1)}}$$

$$dG_{12}^2 = \frac{d\lambda(\sigma_1 - \sigma_2)\cos(2\alpha_2)}{2r_{(\beta+45-\sigma_2)}}$$

$$dG_{23} = \frac{d\lambda(\sigma_2 - \sigma_3)}{r_1 r_{(90+\beta)}}$$

$$dG_{31} = \frac{d\lambda(\sigma_3 - \sigma_1)}{r_1 r_\beta} \quad (6-8)$$

with :

$$tg(2\alpha_1) = \frac{-D \cos(2\beta - 2\alpha_1) - 2E \sin(4\beta - 4\alpha_1)}{2C + D(1 - \sin(2\beta - 2\alpha_1)) + 2E \cos^2(2\beta - 2\alpha_1)}$$

$$tg(2\alpha_2) = \frac{D \cos(2\beta - 2\alpha_2) - 2E \sin(4\beta - 4\alpha_2)}{2C + D(1 + \sin(2\beta - 2\alpha_2)) + 2E \cos^2(2\beta - 2\alpha_2)} \quad (6-9)$$

1 The rate of mobile dislocation creation is related to a potential function of stresses (Mecking & Lucke 1970).

2 The texture effect responsible for Lankford's coefficient value directly modifies the flow rule.

$$\frac{1}{r_1} = \frac{\cos(2\alpha_1)\cos(45-\alpha_1)\cos(45+\alpha_1)}{2r_{(\beta+45-\sigma_1)}} + \frac{\cos(2\alpha_2)\cos(45-\alpha_2)\cos(45+\alpha_2)}{2r_{(\beta+45-\sigma_2)}}$$

$$d\lambda = K \cdot dt \cdot s \cdot \left[\frac{2\tau - A}{B} \right]^2 \frac{\exp\left[\frac{|\sigma_1 - \sigma_2| + |\sigma_2 - \sigma_3| + |\sigma_3 - \sigma_1| - 4|\tau|}{W} \right]}{|\sigma_1 - \sigma_2| + |\sigma_2 - \sigma_3| + |\sigma_3 - \sigma_1|}$$

where K : material constant,
 s : average free path of dislocations,
 W : viscosity constant,
 α_1, α_2 : angles measuring the deviation of G_{12} gliding planes from the directions at 45° from the principal stresses (planar anisotropy effect).

Recall that all the computations are performed in the axes of principal stresses. For the orthotropic cases, the basic strain relations are:

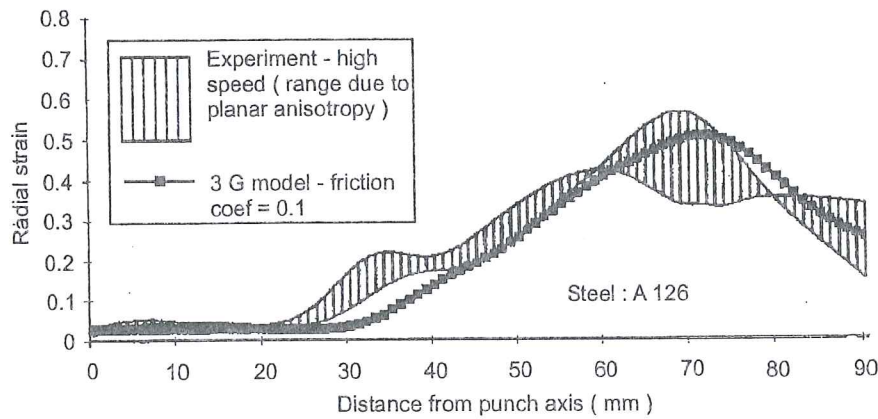
$$\begin{aligned} d\epsilon_{11} &= dG_{12}^1 \cos(45 - \alpha_1) \cos(45 + \alpha_1) + dG_{12}^2 \cos(45 + \alpha_2) \cos(45 - \alpha_2) - dG_{31} \\ d\epsilon_{22} &= dG_{12}^1 \sin(45 - \alpha_1) \sin(45 + \alpha_1) - dG_{12}^2 \sin(45 + \alpha_2) \sin(45 - \alpha_2) + dG_{23} \\ d\epsilon_{33} &= dG_{31} - dG_{23} \\ d\epsilon_{12} &\cong \alpha_1 dG_{12}^1 - \alpha_2 dG_{12}^2 \end{aligned} \quad (6-10)$$

The parameter identification is well described in Monfort & Defourny 1994:

- the parameters A, B and a of the hardening rule (6-5) are determined by means of a uniaxial tensile test, a tensile test on a wide specimen test and an equiaxial stretching (bulge test);
- the parameters C, D, E defining Lankford's coefficient function are reached thanks to classical tensile tests in 3 directions;
- with s incorporated in K , the flow rule is defined by K and W constants. The parameter W can be considered as nearly constant for all steels ($W=16 \text{ Mpa}$); the fitting of the K factor is more complicated: the interested scientist should read Monfort & Defourny 1994.

With its parameters related to fundamental physics, the $3G$ model potentially has the ability to take into account the main macroscopic features of deformation under complex strain paths. For instance, pre-strain effect, or change in dislocation cell shapes and sizes can be handled with simple modifications. This advantage appears for any model based on Bergström's extension. The interesting feature of the $3G$ model is to take directly into consideration changes in Lankford's coefficients; however their evolution is not provided in the present version of the model, so it neglects texture evolution effect.

Comparisons between simulation results and experiments, such as bulge test, hemispherical and cylindrical cup deep drawings, show the interest of the 3G model. The experimental observations due to different materials properties or different friction coefficients are correctly reproduced by the implementation of the 3G model in the ABAQUS code. For instance, experiments of cylindrical cup deep drawing at various speeds on a deep drawing steel are well predicted by simulations performed with different friction coefficients. The fracture occurring during medium to very low speed experiments is predicted (Figure 6-4). Axisymmetrical FEM simulations are performed, so the planar anisotropy is neglected.



(a) High speed = low friction
 (b) Medium speed = high friction

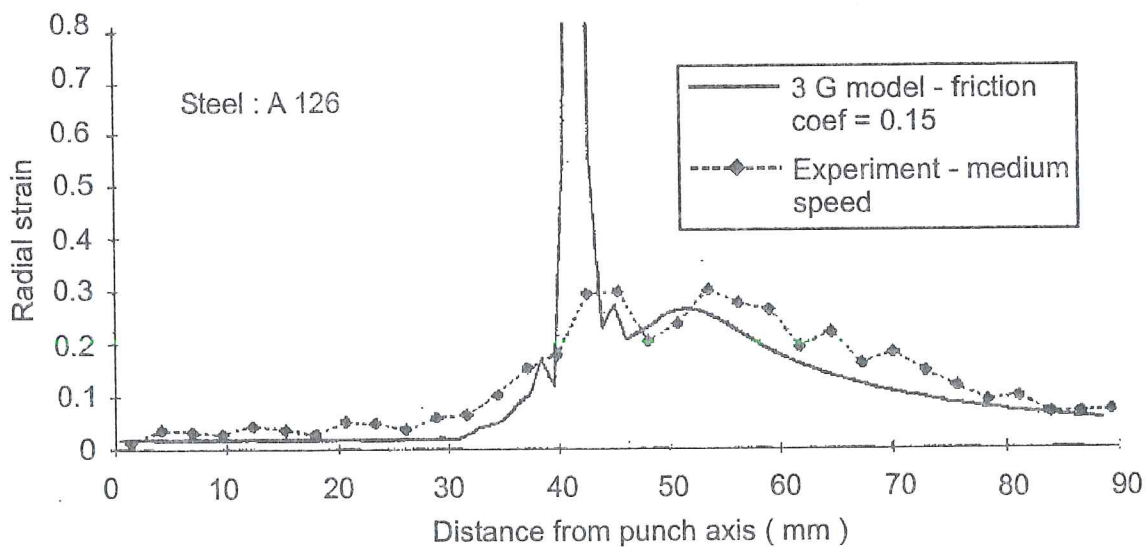


Figure 6-4 Comparisons between experiment and simulation for radial strains in cup drawing of a Deep Drawing steel (from Montfort & Defourny 1994).

The planar anisotropic behavior of the 3G model is checked by theoretical and experimental considerations on the fracture of cylindrical cups (Montfort & Defourny 1994).

In conclusion, along simple strain paths, the 3G model gives slightly more accurate results than the classical theory but its main advantage is to give a metallurgical background to the mathematical formulation of the material behavior. It has the basic ingredients to model the events happening in complex loading paths but specific improvements are needed to predict texture evolution or pre-strain effects. Its identification is not too heavy and its FEM implementation is not straightforward but tractable.

6.2.2. Khan & Cheng's model

Compared with a single crystal, a polycrystal contains a much larger number of slip systems, which are randomly distributed in the polycrystal. Khan & Cheng 1996's model applies the above idea to transfer the plasticity model of a single crystal to polycrystal level. Due to grain boundary effect, all slip systems interact. Describing the behavior of polycrystal implies formulating the interactions of all slip systems.

A single crystal yield locus is extended to a polycrystal yield locus by simply assuming a larger number of slip systems s . The macroscopic phenomenological approach of isotropic hardening is transferred to slip systems by equation (6-11), with the initial value of the plastic radius R_0 and its increment R^s . The backstress α^s modifies the center of the yield locus.

$$|\tau^s - \alpha^s| \leq R^s + R_0 \quad (6-11)$$

The projection already presented at microscopic level in relation (3-2) is applied here to get the resolved shear stress:

$$\tau^s = A_{ij}^s \sigma_{ij}^{macro} \quad (3-2)$$

Isotropic and kinematic hardening rules affect each slip system; their evolution is defined by relations :

$$\dot{\alpha}^s = \sum_j^N b_\alpha \dot{\gamma}^j \left(X_0 + X_1 A_{kl}^s A_{kl}^j + X_3 (A_{kl}^s A_{kl}^j)^3 - \alpha^s \right) \quad (6-12)$$

$$\dot{R}^s = \sum_j^N b_R \dot{\gamma}^j \left(R_0 + R_2 (A_{kl}^s A_{kl}^j)^2 - R^s \right) \quad (6-13)$$

The first terms on the right hand side of relations (6-12) and (6-13) respectively correspond to classical isotropic and kinematic models. The next terms take into account the shape change of the yield surface. The final feedback terms account for the dependence of the plastic behavior of slip systems on deformation history. The constants X_0, X_1, X_3, R_0, R_2 are the saturated values of the corresponding hardening and b_α, b_R are the shape-control parameters.

To show the credibility of the extension from single crystal to polycrystal by simply increasing the number of slip systems, an alternative analysis of the self-consistent method is proposed to consider the effect of grain boundaries on the behavior of polycrystals. The analysis concludes that the effect of grain boundaries could be incorporated in the interactions of slip systems. Unfortunately, further comparisons with experiments announced in the paper I (Khan & Cheng 1996) could not be found.

6.2.3. Aifantis' models

Aifantis 1987 is a typical macroscopic model imbued from single crystal plasticity. It is based on a *scale invariance concept*, which assumes that the structure of the resulting equations is preserved during a transition from the micro-scale to the macro-scale.

The single crystal model proposed by Aifantis considers a single family of dislocations moving along a slip system identified by two vectors, n_j^s (normal unit vector to the slip plane for the slip system s) and b_j^s (unit vector in the slip direction for the slip system s). The associated Schmid's tensor K_{ij}^s (relation 3-1), its symmetric part A_{ij}^s and its skew-symmetric part Z_{ij}^s also appear. Hereafter the superscript s is dropped as only one slip family is taken into account.

The microscopic state is represented by two sets of equations specifically representing conservation rules and constitutive relations. The mass and momentum balance equations are :

$$\frac{\partial \rho}{\partial t} + \text{div } \underline{j} = \hat{c} \quad (6-14)$$

$$\text{div } \underline{\alpha} = \hat{f} \quad (6-15)$$

with ρ the dislocation density, \underline{j} the dislocation flux, $\underline{\alpha}$ the dislocation stress (associated to the classical back stress in macroscopic models), t the time. The source terms \hat{c} and \hat{f} measure the mass and momentum exchanges between dislocations and lattice. Specifically \hat{c} represents the generation, immobilisation or annihilation of dislocations and \hat{f} includes the effect of lattice friction, damping and Peach-Koehler's force acting on a dislocation as a result of the applied stress.

The constitutive equations are assumed to be of the form:

$$\underline{\alpha} = t_A \underline{A} + t_b \underline{b} \otimes \underline{b} + t_n \underline{n} \otimes \underline{n} \quad (6-16)$$

$$\underline{\hat{f}} = (a_{1b} - a_{2b} \tau_{effective} - a_{3b} j_b) \underline{b} + (a_{1n} - a_{2n} \tau_n - a_{3n} j_n) \underline{n} \quad (6-17)$$

$$\hat{c} = \hat{c}(\rho, j_b, j_n, \tau_{effective}, \tau_n) \quad (6-18)$$

where $a_{1b}, a_{2b}, a_{3b}, a_{1n}, a_{2n}, a_{3n}, t_A, t_b, t_n$ are assumed functions of ρ . The coefficients t_A, t_b, t_n measure the interaction forces between dislocations and are responsible for the development of internal stresses. The coefficients a_{1b}, a_{1n} measure the lattice-dislocation interactions and are responsible for yielding. The coefficients a_{2b}, a_{2n} measure the effect of Peach-Koehler's force, while a_{3b}, a_{3n} measure the drag associated with dislocation motion and are responsible for internal damping and viscoplastic flow. The other variables are defined by:

$$\begin{aligned} \tau_{effective} &= (\sigma_{ij}^{micro} - \alpha_{ij}) A_{ij} \\ \tau_n &= (\sigma_{ij}^{micro} - \alpha_{ij}) (n_i n_j) \\ j_b &= \underline{j} \cdot \underline{b} \\ j_n &= \underline{j} \cdot \underline{n} \end{aligned} \quad (6-19)$$

where subscript b identifies glide components and subscript n climb components. Such a microscopic model helps to predict heterogeneity of plastic flow such as shear bands or Portevin-Le Chatelier bands (Aifantis 1987).

As macroscopic plasticity smoothes out plastic micro-heterogeneities, it is assumed that, at macroscopic level, the divergence terms of relations (6-14) and (6-15) have no influence and can be dropped. The macroscopic plasticity theory neglecting volume changes, the climb process appearing in (6-17) and (6-18) is neglected. In (6-16), the stress $t_n \underline{n} \otimes \underline{n}$, which accounts for presence of dislocation dipole and decomposition, can be kept but is often neglected as in Prager's kinematic hardening rule. Consequently, the macroscopic relations chosen by Aifantis are:

$$\dot{\rho} = \hat{c}(\rho, j_b, \tau_{effective}) \quad (6-20)$$

$$a_{1b} - a_{2b} \tau_{effective} - a_{3b} j_b = 0 \quad (6-21)$$

$$\underline{\sigma}^{effective} = \underline{\sigma}^{macro} - \underline{\alpha}^{macro} \quad (6-22)$$

$$\underline{\alpha}^{macro} = t_A \underline{A} + t_n \underline{N} \quad (6-23)$$

with $\underline{N} = \underline{n} \otimes \underline{n}$. The microscopic stress quantities $\underline{\sigma}^{micro}, \underline{\sigma}^{micro} - \underline{\alpha}, \underline{\alpha}$ are assumed to preserve their character and interrelationship during the transition to macro scale. They are respectively identified with the macroscopic total stress $\underline{\sigma}^{macro}$, the macroscopic effective stress $\underline{\sigma}^{effective}$ and the macroscopic back stress $\underline{\alpha}^{macro}$. The yield condition is directly deduced from (6-21) and the macroscopic plastic strain is

assumed to be linked to an orientation tensor A_{ij} "equivalent" to the symmetric part of Schmid's tensor in the microscopic analysis:

$$\underline{\dot{\epsilon}}^{p\ macro} = \dot{\gamma}^p \underline{A} \quad (6-24)$$

In Aifantis 1987, the macroscopic \underline{A} tensor results from the macroscopic principle of maximum dissipation for maximum entropy production. This is related to the power associated with a dislocation motion along its slip plane:

$$\tau^{effective} j_b > 0 \quad \Leftrightarrow \quad (\underline{\sigma}^{macro} - \underline{\alpha}^{macro}) : \underline{\dot{\epsilon}}^{p\ macro} > 0 \quad (6-25)$$

This leads to a maximization problem:

$$\text{maximum of } (\sigma_{ij}^{effective} A_{ij})$$

with applied constraints :

$$\text{tr } \underline{A} = 0 \quad ; \quad \text{tr } \underline{A}^2 = \frac{1}{2} \quad (6-26)$$

by analogy to the microscopic analysis where \underline{A} is the symmetric part of Schmid's tensor.

The solution found by Aifantis is:

$$\underline{A} = \frac{\underline{\hat{\sigma}}^{effective}}{2\sqrt{\frac{1}{2}(\underline{\hat{\sigma}}^{effective})^2}} \quad (6-27)$$

where $\underline{\hat{\sigma}}^{effective}$ is the deviatoric part of stress tensor $\underline{\sigma}^{effective}$. This solution allows to retrieve Prandtl-Reuss' flow rule and von Mises' yield criterion:

$$\underline{\dot{\epsilon}}^p = \frac{\dot{\gamma}^p}{2\sqrt{J_2}} \underline{\hat{\sigma}}^{effective} \quad \sqrt{J_2} = \frac{a_{1b}}{a_{2b}} = \sigma_F \quad (6-28)$$

$$\text{with } J_2 = (1/2) \underline{\hat{\sigma}}_{ij}^{effective} \underline{\hat{\sigma}}_{ij}^{effective} .$$

Using standard kinematic arguments in conjunction with relation (6-24), Aifantis obtains, at the microscopic level, the plastic spin formulation. His result is equivalent to the expression adopted in usual theories of crystal plasticity for the plastic spin if only one slip system is considered (see relation 4-3b):

$$\underline{\Omega}^p = \dot{\gamma}^p \underline{Z} \quad (6-29)$$

where \underline{Z} is the non-symmetric part of Schmid's tensor. By analogy to the microscopic state, the practical macroscopic relation for the plastic spin is derived by eliminating tensor \underline{Z} from (6-29) thanks to the use of expressions (6-23) and (6-24):

$$\underline{\Omega}^p = -t_n^{-1} (\underline{\alpha}^{macro} \underline{\dot{\epsilon}}^p - \underline{\dot{\epsilon}}^p \underline{\alpha}^{macro}) \quad (6-30)$$

The above relations (6-20 to 6-24), (6-27), (6-30), define Aifantis' macroscopic model, when a random texture results in an isotropic macroscopic behavior. Its interest is to be able to predict the development of axial strain due to torsion in free-end cylindrical specimens and the development of axial stress due to torsion in fixed-end cylindrical specimens (Swift effect, see section 3.5.4).

In cases where the effect of grain orientations cannot be neglected, Ning & Aifantis 1996 propose another version of the above model. The simplified relations (6-20 to 6-24), (6-27), (6-28), (6-29) are assumed here to be the constitutive relations for a single crystal.

Their model applies Taylor's assumption of equality of the velocity gradient at microscopic and macroscopic levels. It introduces an additional "texture spin" $\underline{\underline{\Omega}}^t$ not mentioned in section 4.1.1, where the material rotation was only subdivided into a plastic spin $\underline{\underline{\Omega}}^p$ and a crystal lattice rotation $\underline{\underline{\Omega}}^L$:

$$\underline{\underline{\Omega}}^{micro} = \underline{\underline{\Omega}}^{macro} = \underline{\underline{\Omega}}^p + \underline{\underline{\Omega}}^L \quad (4-3b)$$

Ning & Aifantis' texture spin $\underline{\underline{\Omega}}^t$ results from grain boundary constraints to maintain deformation compatibility. The final local material spin $\underline{\underline{\Omega}}^L$ is derived as the difference between the global spin ($\underline{\underline{\Omega}}^{micro} = \underline{\underline{\Omega}}^{macro}$), related to the macroscopic velocity gradient, and two types of plastic spins, the usual plastic spin $\underline{\underline{\Omega}}^p$ due to crystal slip given by relation (6-29) and the texture spin $\underline{\underline{\Omega}}^t$ due to grain boundary effects:

$$\underline{\underline{\Omega}}^L = \underline{\underline{\Omega}}^{macro} - \underline{\underline{\Omega}}^p - \underline{\underline{\Omega}}^t \quad (6-31)$$

Ning & Aifantis define a crystal orientation by a unit vector \underline{a} oriented in the crystal direction, expressed as a function of the slip system identifiers \underline{n} , \underline{b} and of the angle between \underline{a} and \underline{b} . Then, they use the classical concept of Orientation Distribution Function f , which represents the probability for a grain to be oriented along \underline{a} at time t . The evolution of the ODF is prescribed by a conservation rule as already presented in section 5.5.3, which can be solved analytically in the case of an initial random texture and simple deformation gradient tensor.

Ning & Aifantis' micro-macro link differs from the classical volume average procedure expressed in its integrated form by (5-40), or in its discrete form by (5-18 or 5-19). Such a classic average procedure does not consider the effect of morphological texture. For instance, the fact that the orientation of large grains may have a more pronounced effect than that of small grains. The following improved average relation is proposed:

$$\underline{\underline{x}}^{macro} = \oint \underline{\underline{K}}(\underline{a}) : \underline{\underline{x}}^{micro} f(\underline{a}, t) d\underline{a} \quad (6-32)$$

where \underline{x}^{micro} is either the deviatoric Cauchy stress or the back stress at the crystal level and \underline{x}^{macro} is the associated macroscopic value. The fourth order tensor \underline{K} , called “texture” tensor, is a function of \underline{a} . Due to the stress symmetry, it is a transversely isotropic tensor finally defined by only three independent material parameters. The overall plastic flow rule and yield condition are then obtained by combining the flow rule and yield condition assumed at the crystal level (see 6-28) and the average stress relation (6-32). This results in the flow rule:

$$\underline{\dot{\epsilon}}^p = \frac{\dot{\gamma}^p}{2\sigma_F(\gamma^p)} \langle \underline{K} \rangle^{-1} : \underline{\hat{\sigma}}^{effective} \quad (6-33)$$

and the yield condition:

$$\sqrt{\frac{1}{2} \underline{\hat{\sigma}}^{effective} \langle \underline{K} \rangle^{-1} \langle \underline{K} \rangle^{-1} \underline{\hat{\sigma}}^{effective}} = \sigma_F(\gamma^p) \quad (6-34)$$

where the overall texture tensor $\langle \underline{K} \rangle$ is defined by the average formula:

$$\langle \underline{K} \rangle = \oint \underline{K} f(\underline{a}, t) d\underline{a} \quad (6-35)$$

Relation (6-33) is similar to the previous phenomenological relations for the description of the yield behavior of metallic materials, based on the introduction of “modified” stress tensors as, for instance, in Karafillis & Boyce 1993, presented in section 2.1.2.

The evolution of the macroscopic back stress and the plastic spin $\underline{\Omega}^p$ are deduced from their microscopic value, Taylor’s assumption and the same averaging procedure.

The macroscopic counterpart of the additional spin $\underline{\Omega}^i$ describes the overall average grain rotation. Thus, it cannot be expressed in terms of the average slip processes alone. The average procedure (6-32) is slightly modified and applied now to a vector associated with the skew-symmetric tensor $\underline{\Omega}^i$. The fourth order tensor \underline{K} is reduced to a second order tensor, isotropic function of vector \underline{a} , taking into account 2 material parameters related to plastic strain history and temperature as well as to grain size and shape.

Like the above isotropic macroscopic model, this anisotropic macroscopic model has been applied to the prediction of Swift’s effect. This is a simple case as it is possible to find an analytical form of the ODF function. Analytical and experimental results are very close as shown on Figure 6-5.

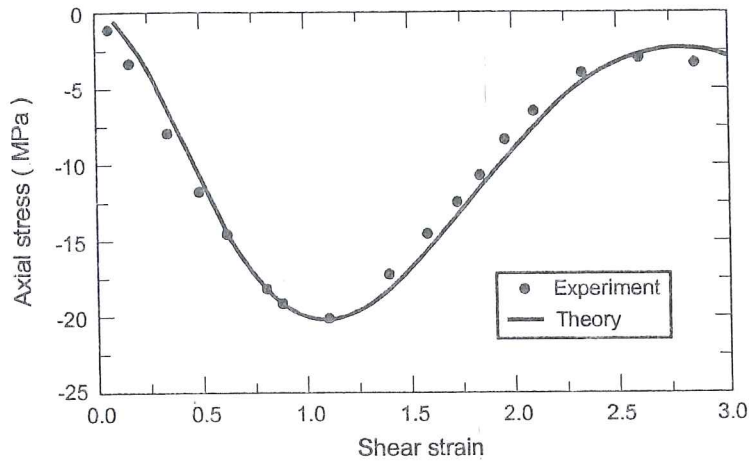


Figure 6-5 Comparison between theoretical predictions and experimental data for the non-monotonic evolution of the axial stress in a copper bar under fixed-end torsion (from Ning & Aifantis 1996).

As reported by Ning & Aifantis, these predictions were much less straightforward in previous attempts with other macroscopic models.

The yield behavior in tension coupled to torsion has been further studied for a theoretical material. For instance, Figure 6-6 and Figure 6-7 show the evolution of the initial yield locus. They respectively correspond to a tension dominated deformation state and a shear dominated deformation mode. The results show that the texture development causes both rotation and distortion of the yield surface, the shear mode having a more pronounced effect than the tension mode.

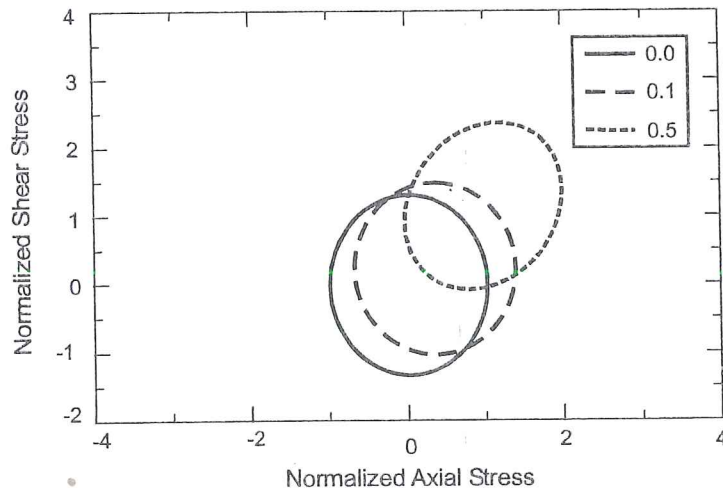


Figure 6-6 Evolution of yield surface in tension-torsion for different tensile strains: 0, 0.1, 0.5, and a ratio shear/axial strain of 1 (from Ning & Aifantis 1996).

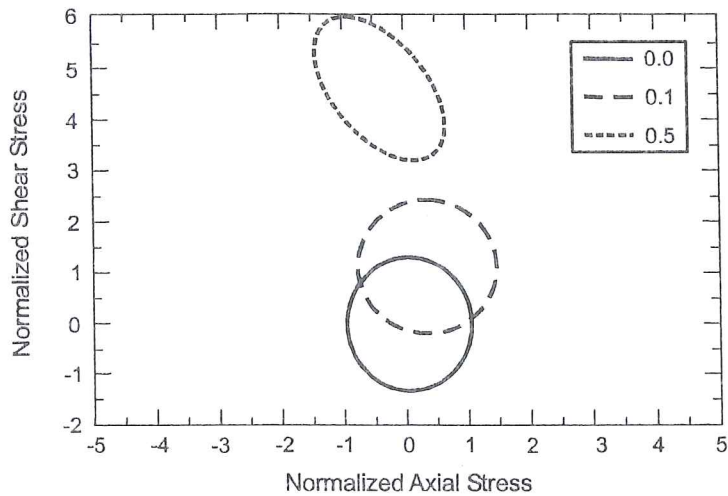


Figure 6-7 Evolution of yield surface in tension-torsion for different tensile strains: 0; 0.1; 0.5 and a ratio shear/axial strain of 5 (from Ning & Aifantis 1996).

A comparison of model predictions with available experimental data in small deformations (effect of plastic spin neglected) is presented on Figure 6-8 for 304 stainless steel in tension-torsion.

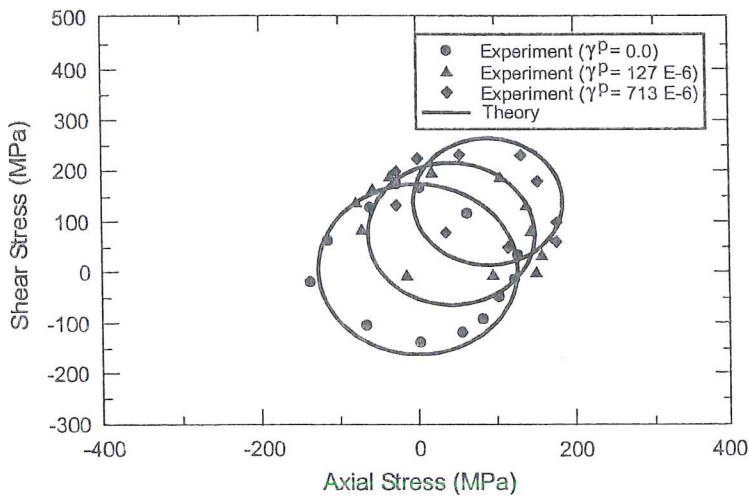


Figure 6-8 Comparison between theoretical predictions and experimental data for the yield surface of 304 stainless steel in tension-torsion, γ^p means here equivalent plastic strain (from Ning & Aifantis 1996).

In short, these macroscopic models imbued from single crystal plasticity can predict mechanical behavior quite accurately. Ning & Aifantis 1996 analytically compute the ODF evolution in some simple cases. However, the extension of this model to a general velocity gradient seems heavy from both computational and theoretical points of view. The latter model has the advantage of giving microscopic fundamental bases for phenomenological models, which propose the same form for the yield locus function.

6.2.4. Conclusion

3G or Aifantis' models propose macroscopic plasticity models based on the knowledge of crystal plasticity. Each one makes some assumptions to provide "simple" useful macroscopic constitutive laws. Their applications verify that the actual behavior under complex loading paths can be predicted. It is however clear that each specific path (tension + torsion, pre-straining...) may need some adjustments of the models.

Such models are neither straightforward to implement in FEM code nor to identify. So it is not surprising that they generally seem to be used only by the teams that have developed them. They provide more accurate results than simple phenomenological approaches. Aifantis's model also gives a theoretical justification for more advanced phenomenological models such as Karafillis & Boyce 1993.

6.3. Analytical yield loci computed from texture data

First, section 6.3.1 presents the classical way to obtain a macroscopic yield locus thanks to classical single crystal plasticity combined with texture description. As this approach does not give an analytical formulation easy to implement in FEM codes, different ways to derive an analytic function for the flow surfaces have been proposed. Some are described in sections 6.3.2 to 6.3.4.

6.3.1. Polycrystal yield locus obtained by Taylor's approach

Let us recall the important notions of Taylor's factor and average Taylor's factor, as the latter appears as a material parameter able to express the response of a textured material submitted to a given strain rate.

$M(g, \underline{U}_{\dot{\epsilon}^p})$ is the Taylor's factor associated to a crystal of orientation g for a given strain mode $\underline{U}_{\dot{\epsilon}^p}$ (plastic strain rate tensor divided by the equivalent plastic strain rate, relation 4-7). It is conventionally derived from the single crystal plastic power dissipation per unit volume \dot{W}^p by the following relation:

$$M(g, \underline{U}_{\dot{\epsilon}^p}) = \frac{\dot{W}^p}{\dot{\epsilon}_{eq}^p \tau_c} = \sum_s \alpha_s |\dot{\gamma}_{scaled}^s| = \frac{1}{\tau_c} \sigma_{ij}^{micro}(U_{\dot{\epsilon}^p})_{ij} \quad (4-14)$$

Physically, it represents a certain amount of dislocation glide rate associated with a crystal orientation and an applied strain mode.

At the level of a polycrystal, the average plastic work dissipation per unit volume has been established in section 4.5.2 as a function of the ODF $f(g)$, which effect is then hidden in the average Taylor's factor $\overline{M}(\underline{U}_{\dot{\epsilon}^p})$:

$$\overline{\dot{W}^p}(\underline{\dot{\epsilon}}^{p\ macro}) = \oint \dot{W}^p(\underline{\dot{\epsilon}}^{p\ micro}, g) f(g) dg = \dot{\epsilon}_{eq}^{p\ macro} \overline{\tau}_c \overline{M}(\underline{U}_{\underline{\dot{\epsilon}}^p}) = \sigma_{eq}^{macro} \dot{\epsilon}_{eq}^{p\ macro} \quad (4-33)$$

$$\overline{M}(\underline{U}_{\underline{\dot{\epsilon}}^p}) = \oint M(\underline{U}_{\underline{\dot{\epsilon}}^p}, g) f(g) dg \quad (4-34)$$

Taylor's assumptions of equality between the strain rates at the crystal level and at the macroscopic level as well as a common CRSS for all slip systems and all grains are both used in relation (4-33). Studying this equation :

$$\dot{\epsilon}_{eq}^{p\ macro} \overline{\tau}_c \overline{M}(\underline{U}_{\underline{\dot{\epsilon}}^p}) = \sigma_{eq}^{macro} \dot{\epsilon}_{eq}^{p\ macro} = \underline{\sigma}^{macro} : \underline{\dot{\epsilon}}^{p\ macro} \quad (6-36)$$

one can see that, if the macroscopic strain rate $\underline{\dot{\epsilon}}^{p\ macro}$ is known, $\overline{M}(\underline{U}_{\underline{\dot{\epsilon}}^p})$ can be computed and all stress tensors $\underline{\sigma}^{macro}$ * that satisfy (6-36) constitute hyperplanes in stress vectors space. The strain rate vector $\underline{\dot{\epsilon}}^{p\ macro}$ are perpendicular to these hyperplanes. In practice, as already explained, only the deviatoric stress tensors are considered in the plastic state, so the stress space is a 5 dimensional space. The deviatoric stress $\underline{\hat{\sigma}}^{macro}$ corresponding to $\underline{\dot{\epsilon}}^{p\ macro}$ is one point of the hyperplane. According to the normality rule, the yield locus must be tangent to the hyperplane at the location of $\underline{\sigma}^{macro}$ (see Figure 6-9). Since the yield locus must be convex, it is the inner envelope of the hyperplanes associated with all possible strain modes.

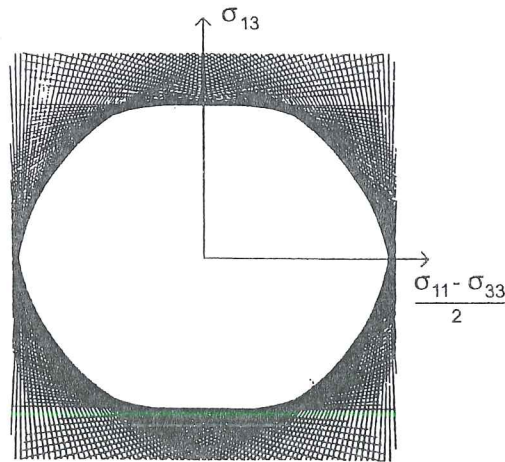


Figure 6-9 Example of projection of the yield locus onto the subspace

$$\frac{\sigma_{11} - \sigma_{33}}{2}, \sigma_{13} \text{ (from Canova } et\ al\ 1985).$$

The practical way to build 2-dimensional projections of the yield surface is described in Canova *et al.* 1985, Lequeu *et al.* 1987a, van Houtte 1992. Some details on van Houtte's approach will be given in section 6.3.4.

6.3.2. Proposals applying concepts from Montheillet

Lequeu *et al.* 1987b follow the approach of Montheillet *et al.* 1985, where the principal axes of anisotropy are chosen to coincide with the $\langle 100 \rangle$ axes of the studied texture component, rather than with the symmetry axes of the workpiece. Another characteristic of this method consists in the determination of the coefficients of the yield function only from crystallographic considerations. According to Montheillet *et al.* 1985, the yield locus of a highly textured f.c.c or b.c.c polycrystal, containing a dispersion of orientations about a single ideal orientation (cube textures) is given by :

$$F_p(\underline{\hat{\sigma}}) = \alpha \left\{ |\hat{\sigma}_{11} - \hat{\sigma}_{22}|^n + |\hat{\sigma}_{22} - \hat{\sigma}_{33}|^n + |\hat{\sigma}_{33} - \hat{\sigma}_{11}|^n \right\} + 2\beta \left\{ |\hat{\sigma}_{12}|^n + |\hat{\sigma}_{23}|^n + |\hat{\sigma}_{31}|^n \right\} = (\sqrt{6} \tau_c)^n \quad (6-37)$$

where $\hat{\sigma}_{ij}$ are the components of the macroscopic deviatoric stress tensor. The coefficient n must be equal or greater than 1 to satisfy convexity requirement. The values of α and β depend on n . The parameters are identified from the best fit between (6-37) and the single crystal yield locus computed by Schmid's law and Taylor-Bishop-Hill's. Figure 6-10 and Figure 6-11 respectively show the π -plane section and the shear plane section of the yield loci computed by (6-37) and by Taylor-Bishop-Hill's formulation.

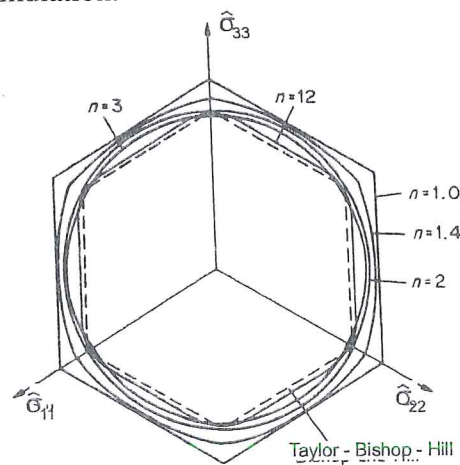


Figure 6-10 π -plane sections of Taylor-Bishop-Hill's single crystal yield locus and yield surfaces defined by (6-37) for 5 values of the exponent n (from Lequeu *et al.* 1987b).

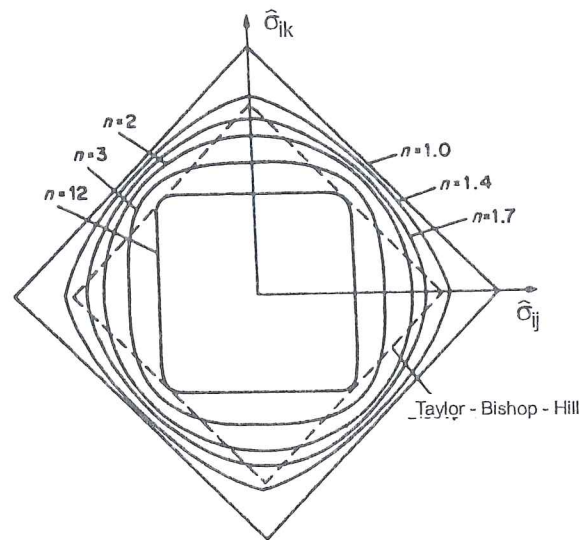


Figure 6-11 Shear plane sections of Taylor-Bishop-Hill's single crystal yield locus and yield surfaces defined by (6-37) for 6 values of the exponent n (from Lequeu *et al.*, 1987b).

The best overall fit with respect to the single crystal yield locus is obtained with $n = 1.7$, $\alpha = 0.47$, $\beta = 0.54$. The final objective is of course not an analytical yield surface describing a material with a sharp cube texture. The goal is to develop analytical models for any textured material containing one or more arbitrary orientations. Therefore the comparisons between the relation (6-37) and crystallographic yield loci should be interpreted as concerning individual texture components, which in reality are cube textures oriented along particular directions in the material. Lequeu *et al.* 1987b introduce a transformation matrix between crystallographic axes and workpiece axes, that is used to adapt the yield surface (6-37) to any texture component. When more than one texture component is involved, a Sachs' approach is used. Some comparisons between experimental and computed yield loci are shown on Figure 6-12, where σ_0 and σ_{90} are the yield stresses in uniaxial tension along rolling and transverse directions respectively. The angle ω_0 , called the scatter width, expresses the misorientation about the ideal orientation associated with one texture component. Lequeu *et al.* 1987a study the effect of increasing the scatter width on π -plane and shear stress cross-sections of the yield locus.

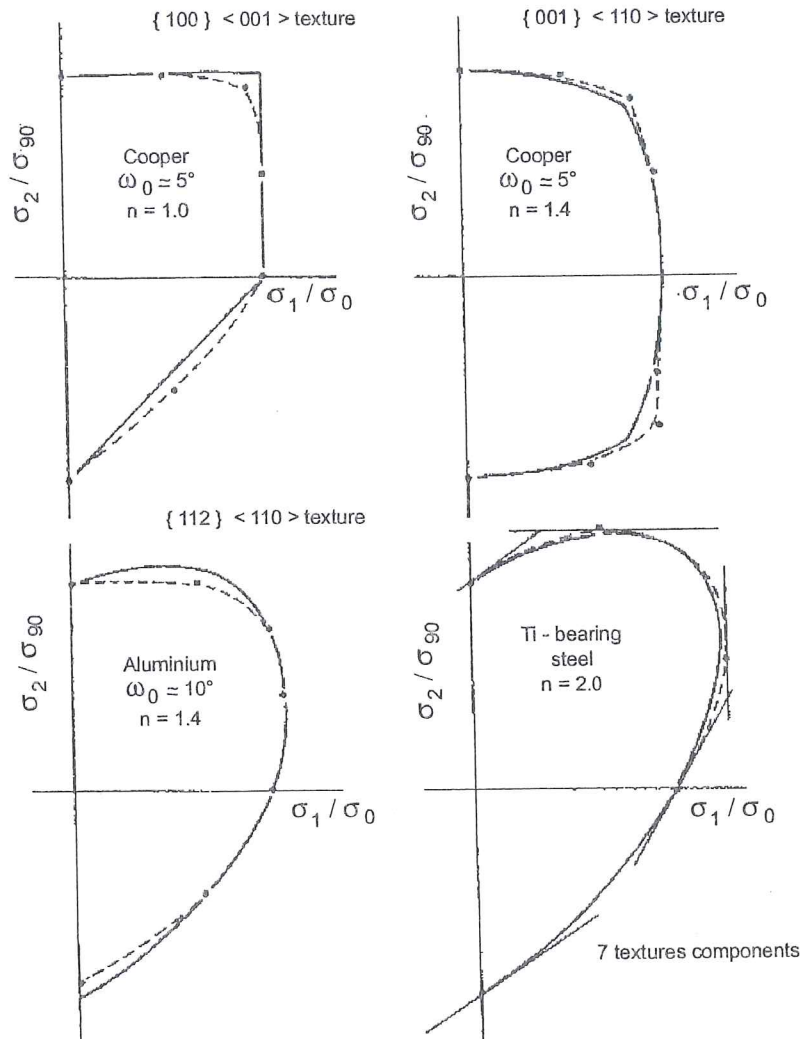


Figure 6-12 Comparison between experimental yield loci (dotted lines) reported in literature and the predictions by Lequeu's approach (straight lines), (from Lequeu *et al.* 1987b).

In summary, this approach adjusts an analytical function on Taylor-Bishop-Hill's single crystal locus; then, by rotation, adapts it according to macroscopic axes and uses a Sachs' approach when the material has more than one texture component.

Darrieulat & Piot 1996 apply the same type of approach to f.c.c materials characterised by 12 slip systems. However, they consider a more accurate representation of the microscopic behavior and take into account the ODF function to represent the texture effect.

Beginning also with the plastic behavior at the single crystal level, Darrieulat & Piot 1996 express Schmid's law by an analytical form obtained through a classical mathematical property of power averages already proposed by Arminjon 1988:

$$F_p(\underline{\hat{\sigma}}) = \left(\sum_{s=1}^{12} \left| \frac{\underline{\hat{\sigma}} : \underline{A}^s}{\tau_c^s} \right|^n \right)^{\frac{1}{n}} = 1 \quad (6-38)$$

where \underline{A}^s is the symmetric part of Schmid's tensor (3-1) associated with the slip system s . Function (6-38) is differentiable, strictly convex and is arbitrarily close to the inner envelope of the hyperplanes of equations:

$$\left| \frac{\underline{\hat{\sigma}} : \underline{A}^s}{\tau_c^s} \right| = 1 \quad s = 1, \dots, 12 \quad (6-39)$$

Applying the normality rule to the yield surface, the plastic strain rate is computed by:

$$\underline{\hat{\epsilon}}^p = \dot{\lambda} F_p^{\frac{1-n}{n}} \sum_{s=1}^{12} \text{sgn}(\underline{\hat{\sigma}} : \underline{A}^s) \left| \underline{\hat{\sigma}} : \underline{A}^s \right|^{n-1} \underline{A}^s \quad (6-40)$$

It is interesting to note that this form is close to the macroscopic flow rule derived when the rate sensitive approach is applied at the crystal level (see relation (4-15)).

Figure 6-13 compares yield loci based on expression (6-38) for different values of n with results from Lequeu *et al.* 1987a.

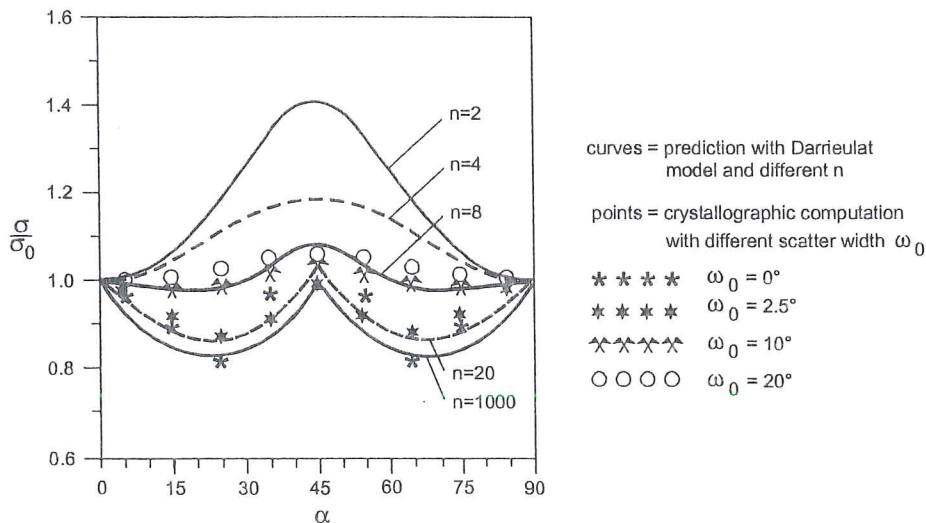


Figure 6-13 For cube orientation, yield stress versus the angle to the Rolling Direction by Darrieulat & Piot and crystal models assuming different scattering width angles ω_0 (Darrieulat & Piot 1996).

When an orthotropic material is known through its N crystallographic components, relation (6-38) provides a differentiable representation of the mechanical behavior that can be attributed to each component. The macroscopic behavior is some average between them. A simple physical assumption close to Khan & Cheng's 1996 proposal (see section 6.2.2) is that polycrystals behave like crystals possessing not 12

slip systems but $12 \times N$ slip systems, the orientations of which are given by the texture data. Each of the N sets contributes proportionally to its volume fraction.

Let the texture be defined by an ODF $f(g)$ function of Euler's angles $\varphi_1, \Phi, \varphi_2$ (Figure 3-4). If Euler's space is covered by a step Δ , one value f_i of the ODF represents the average intensity of the orientations in the solid angle $\left[\varphi_1 - \frac{\Delta}{2}, \varphi_1 + \frac{\Delta}{2} \right] \times \left[\Phi - \frac{\Delta}{2}, \Phi + \frac{\Delta}{2} \right] \times \left[\varphi_2 - \frac{\Delta}{2}, \varphi_2 + \frac{\Delta}{2} \right]$. It is also the volume fraction of crystals belonging to this orientation space sector. The number of crystallographic orientations N directly depends on the size of Δ .

Using the same power average as in relation (6-38), the plastic behavior of the polycrystal is given by:

$$F_p = \left(\sum_{i=1}^N f_i \sum_{s=1}^{12} \left| \hat{\sigma}_i^{micro} : \underline{A}_i^s \right|^n \right)^{\frac{1}{n}} = \bar{\tau}_c \quad (6-41)$$

where Taylor's assumption of a common value of CRSS is adopted for all the slip systems and all the crystals. The subscript i identifies the texture component. This tensorial expression being the average of strictly convex and differentiable terms, it is also strictly convex and differentiable. It can be easily computed no matter what the chosen axes are.

If $n = 2$, relation (6-41) is a quadratic criterion similar to Hill's 1948 yield locus. Darrieulat & Piot 1996 give the 6 coefficients of Hill's 1948 criterion as functions of f_i and \underline{A}_i^s .

The macroscopic mechanical behavior $(\underline{\hat{\sigma}}^{macro}, \underline{\hat{\epsilon}}^{p macro})$ of a polycrystal can be predicted from each of its component $(\underline{\hat{\sigma}}_i^{micro}, \underline{\hat{\epsilon}}_i^{p micro})$ if :

- either a uniform stress $(\underline{\hat{\sigma}}_i^{micro} = \underline{\hat{\sigma}}^{macro})$ or a uniform strain $(\underline{\hat{\epsilon}}_i^{p micro} = \underline{\hat{\epsilon}}^{macro})$ assumption is accepted. Here, Darrieulat and Piot choose the stress uniformity;
- a condition of homogenisation is applied:

$$\sum_{i=1}^N f_i \underline{\hat{\sigma}}_i : \underline{\hat{\epsilon}}_i = \underline{\hat{\sigma}}^{macro} : \underline{\hat{\epsilon}}^{macro} \quad (6-42)$$

The details are given in Darrieulat & Piot's 1996 paper, where a slightly modified relation (6-41) using two exponents instead of one is also checked. Their conclusions are that proposal (6-41) gives good results for low values of n (up to 10) but assigns a too large influence to crystallographic texture when n increases. Their validations consist in predictions of uniaxial yield stresses and Lankford's coefficients as functions of the angle with the rolling direction. This is done for a single component texture or real materials such as aluminium 3004 or 5182.

6.3.3. Arminjon, Bacroix, Imbault... 's potential formulation

Arminjon 1988, Arminjon & Bacroix 1991, Arminjon *et al.* 1994 propose an identification of the plastic work rates to derive a yield criterion applied to polycrystalline materials. When a quadratic form is assumed, the macroscopic anisotropy parameters become explicit functions of the texture coefficients. Their approach is summarized hereafter.

In visco-plastic models, the existence of two dual convex potentials E and E_c is usually assumed. They define the relationship giving the stress tensor as function of the plastic strain rate tensor as well as the inverse relation:

$$\underline{\sigma} = \frac{\partial E}{\partial \underline{\dot{\epsilon}}^p} \quad \underline{\dot{\epsilon}}^p = \frac{\partial E_c}{\partial \underline{\sigma}} \quad (6-43a,b)$$

where functions E and E_c exchange by Legendre's transformation. In case of rate-independent standard plasticity, function E is simply the rate of plastic work \dot{W}^p . The complementary function E_c cannot be defined, since the strain rate $\underline{\dot{\epsilon}}^p$ is only determined by the stress tensor $\underline{\sigma}$ up to the plastic multiplier $\dot{\lambda}(\underline{\dot{\epsilon}}^p)$ and relation (2-3) of associated flow rule is used:

$$\underline{\dot{\epsilon}}^p = \dot{\lambda}(\underline{\dot{\epsilon}}^p) \frac{\partial F_p}{\partial \underline{\sigma}} \quad (6-44)$$

In this section, the yield locus is expressed as:

$$F_p(\underline{\sigma}) = \bar{\tau}_c \quad (6-45)$$

Following Hill 1987, F_p can be formulated as an homogeneous function of order one with respect to positive multipliers. This property implies :

$$F_p(\underline{\sigma}) = \underline{\sigma} : \frac{\partial F_p}{\partial \underline{\sigma}} \quad (6-46)$$

Relations (6-44) to (6-46) allow to give the following expression of the rate of plastic work:

$$\dot{W}^p = \underline{\sigma} : \underline{\dot{\epsilon}}^p = F_p(\underline{\sigma}) \dot{\lambda}(\underline{\dot{\epsilon}}^p) = \bar{\tau}_c \dot{\lambda}(\underline{\dot{\epsilon}}^p) \quad (6-47)$$

In practice, using (6-43a) and (6-47), Arminjon writes:

$$\underline{\sigma} = \frac{\partial \dot{W}^p}{\partial \underline{\dot{\epsilon}}^p} = \frac{\partial (\bar{\tau}_c \dot{\lambda}(\underline{\dot{\epsilon}}^p))}{\partial \underline{\dot{\epsilon}}^p} = F_p(\underline{\sigma}) \frac{\partial \dot{\lambda}(\underline{\dot{\epsilon}}^p)}{\partial \underline{\dot{\epsilon}}^p} \quad (6-48)$$

Compare the macroscopic expression of the plastic power dissipation (6-47) with the micro-macro one (4-33), presented as an average value and recalled here:

$$\overline{\dot{W}^p}(\underline{\dot{\epsilon}}^{p\ macro}) = \oint \dot{W}^p(\underline{\dot{\epsilon}}^{p\ micro}, g) f(g) dg = \dot{\epsilon}_{eq}^{p\ macro} \bar{\tau}_c \overline{M}(\underline{U}_{\underline{\dot{\epsilon}}^p}) = \sigma_{eq}^{macro} \dot{\epsilon}_{eq}^{p\ macro} \quad (4-33)$$

One can find physical interpretations for each term. $\bar{\tau}_c$ is the average CRSS in the polycrystal. $\hat{\lambda}$ is naturally expressed from the texture alone and is characterized by the average Taylor's factor defined by relation (4-34) :

$$\overline{M}(\underline{U}_{\dot{\varepsilon}^p}) = \oint M(\underline{U}_{\dot{\varepsilon}^p}, g) f(g) dg \quad (4-34)$$

The above relations assume the equality between the macroscopic strain rate and the microscopic one. So, all the further analytical formulation is based on this so-called Taylor's hypothesis.

Arminjon & Bacroix 1991 define four requirements that functions $\hat{\lambda}(\underline{\dot{\varepsilon}}^p)$ in strain rate space, or F_p in stress space, have to fulfil:

- convexity,
- respect of orthotropic material symmetry,
- homogeneity,
- use of deviatoric tensors only.

If one chooses a polynomial function, the convexity must be checked. The hereafter defined 4th order homogeneous function F of plastic strain rate (which is a deviatoric tensor) respects also the 3 other characteristics. Let us define the function in plastic strain rate space:

$$F = \sum_{k=1}^{22} \alpha_k X_k \quad (6-49)$$

$$\begin{aligned} X_1 &= (\dot{\varepsilon}_{11}^p)^4 & X_2 &= (\dot{\varepsilon}_{22}^p)^4 & X_3 &= (\dot{\varepsilon}_{23}^p)^4 & X_4 &= (\dot{\varepsilon}_{13}^p)^4 \\ X_5 &= (\dot{\varepsilon}_{12}^p)^4 & X_6 &= (\dot{\varepsilon}_{11}^p)^3 \dot{\varepsilon}_{22}^p & X_7 &= (\dot{\varepsilon}_{22}^p)^3 \dot{\varepsilon}_{11}^p & X_8 &= (\dot{\varepsilon}_{11}^p)^2 (\dot{\varepsilon}_{22}^p)^2 \\ X_9 &= (\dot{\varepsilon}_{11}^p)^2 (\dot{\varepsilon}_{23}^p)^2 & X_{10} &= (\dot{\varepsilon}_{11}^p)^2 (\dot{\varepsilon}_{13}^p)^2 & X_{11} &= (\dot{\varepsilon}_{11}^p)^2 (\dot{\varepsilon}_{12}^p)^2 & X_{12} &= (\dot{\varepsilon}_{22}^p)^2 (\dot{\varepsilon}_{23}^p)^2 \\ X_{13} &= (\dot{\varepsilon}_{22}^p)^2 (\dot{\varepsilon}_{13}^p)^2 & X_{14} &= (\dot{\varepsilon}_{22}^p)^2 (\dot{\varepsilon}_{12}^p)^2 & X_{15} &= (\dot{\varepsilon}_{23}^p)^2 (\dot{\varepsilon}_{13}^p)^2 & X_{16} &= (\dot{\varepsilon}_{23}^p)^2 (\dot{\varepsilon}_{12}^p)^2 \\ X_{17} &= (\dot{\varepsilon}_{13}^p)^2 (\dot{\varepsilon}_{12}^p)^2 & X_{18} &= \dot{\varepsilon}_{11}^p \dot{\varepsilon}_{22}^p (\dot{\varepsilon}_{23}^p)^2 & X_{19} &= \dot{\varepsilon}_{11}^p \dot{\varepsilon}_{22}^p (\dot{\varepsilon}_{13}^p)^2 & X_{20} &= \dot{\varepsilon}_{11}^p \dot{\varepsilon}_{22}^p (\dot{\varepsilon}_{12}^p)^2 \\ X_{21} &= \dot{\varepsilon}_{11}^p \dot{\varepsilon}_{23}^p \dot{\varepsilon}_{13}^p \dot{\varepsilon}_{12}^p & X_{22} &= \dot{\varepsilon}_{22}^p \dot{\varepsilon}_{23}^p \dot{\varepsilon}_{13}^p \dot{\varepsilon}_{12}^p \end{aligned}$$

where symmetry $\varepsilon_{ij} = \varepsilon_{ji}$ is assumed and only $i \leq j$ terms are present.

A scaled function is used in practice as function $\hat{\lambda}$:

$$\hat{\lambda}(\underline{\dot{\varepsilon}}^p) = \frac{\dot{W}^p}{\tau_c} = F(\underline{\dot{\varepsilon}}^p) / (\dot{\varepsilon}_{eq}^p)^3 = \sum_{k=1}^{22} \alpha_k \psi_k(\underline{\dot{\varepsilon}}^p) \quad (6-50)$$

with $\psi_k(\underline{\dot{\epsilon}}^p) = X_k(\underline{\dot{\epsilon}}^p) / (\dot{\epsilon}_{eq}^p)^3$.

Note that symmetry $\sigma_{ij} = \sigma_{ji}$ is not assumed in (6-48) but taken into account in (6-49). So the stresses are computed by :

$$\begin{aligned} \sigma_{ij} &= \frac{1}{\tau_c} \frac{\partial \dot{\lambda}}{\partial \dot{\epsilon}_{ij}^p} \quad \text{if } i = j \\ \sigma_{ij} &= \frac{1}{2} \frac{1}{\tau_c} \frac{\partial \dot{\lambda}}{\partial \dot{\epsilon}_{ij}^p} \quad \text{if } i < j \end{aligned} \quad (6-51)$$

As explained hereafter, the choice (6-50) leads to represent the coefficients α_k by a linear function of coefficients C_i , equivalent to the well-known $C_i^{\mu\nu}$ coefficients of the ODF. Here for simplicity, a single index notation is adopted to identify C_i coefficients. So, the relation (3-5) defining $C_i^{\mu\nu}$ coefficients is adapted:

$$\begin{aligned} f(g) &\cong \sum_{l=0}^{l_{max}} \sum_{\mu=1}^{\mu_{max}(l)} \sum_{\nu=1}^{\nu_{max}} C_i^{\mu\nu} \dot{T}_i^{\mu\nu}(g) \\ f(g) &= \sum_{i=1}^I C_i T_i(g) \end{aligned} \quad (3-5)$$

where l_{max} is the maximum degree of the series expansion;
 I is the maximum index of Fourier's coefficients identified by a single index notation;
 $\dot{T}_i^{\mu\nu}(g)$ or $T_i(g)$ are harmonic functions of Euler's angles;
 $C_i^{\mu\nu}$ or C_i are Fourier's coefficients describing the texture.

Looking at the above relations (6-51), (3-5), (4-33) and (4-34), one can express the function $\dot{\lambda}$, after algebraic manipulations, by a linear function of coefficients C_i :

$$\dot{\lambda} = \frac{\dot{W}^p}{\tau_c} = \frac{\overline{\dot{W}^p}}{\tau_c} = \sum_{i=1}^I C_i M_i^*(\underline{\dot{\epsilon}}^p) \quad (6-52)$$

where function M_i^* is computed from Taylor's factor and the harmonic function T_i .

The identification of the material parameters α_k , introduced in relation (6-50), directly results from the 2 expressions (6-52) and (6-50) of function $\dot{\lambda}$:

$$\alpha_k = \sum_{i=1}^I \beta_k^i C_i \quad k = 1, \dots, 22 \quad (6-53)$$

Arminjon *et al.* 1994 have found that, for a given i , the best approximation of coefficients β_k^i is based on a set of 16200 values of $\underline{\dot{\epsilon}}^p$ and the comparison between:

$$M_i^{**}(\underline{\dot{\epsilon}}^p) = \sum_{k=1}^{22} \beta_k^i \psi_k(\underline{\dot{\epsilon}}^p) \quad \text{and} \quad M_i^*(\underline{\dot{\epsilon}}^p)$$

Such computation is done only once with a Taylor's model and it has been checked that for steel texture, I = 12 is enough. This fact means that the 22 coefficients α_k are not independent because relation (6-52) uses 13 coefficients to describe plastic dissipation (12 coefficients C_i and the value of τ).

The above process of parameters identification is independent of the C_i values and hence independent of texture. This is why it can be done only once.

The above explanations give the procedure to start from the choice of a scaled fourth order polynomial function $\hat{\lambda}(\underline{\dot{\epsilon}}^p)$ and to finally provide an expression of this function as a linear relation of coefficients C_i . The same approach can be used if one choose $\hat{\lambda}$ as a second order polynomial function or Hill's yield locus. The application of this method will give a direct computation of 2nd order series or Hill's coefficient from C_i coefficients.

The validation of this approach can be checked on Figure 6-14 and Figure 6-15. Let us note that Figure 6-14 and Figure 6-16 give sections of the yield locus for $\sigma_{12} / \bar{\tau}_c = 0, 0.5, 1$ and 1.5 and, at the center, the value of $\sigma_{12} / \bar{\tau}_c$ for $\sigma_{11} = \sigma_{22} = 0$.

The above approach as well as Lequeu or Darrieulat's work compute an analytical yield locus from the initial texture. Figure 6-16 for steel I1 (A1 killed) shows Lankford's coefficients and yield loci deduced from texture measurements in the initial state and after biaxial tension stopped at two different levels of deformation. In Figure 6-16, one observes that the effect of texture evolution cannot always be neglected. Imbault & Arminjon 1993 propose a semi-analytical method to take it into account in their analytical expression of the yield locus. In fact, the principle is simple. They assume that a linear operator, which is adjusted by comparison with a polycrystal model, can express the evolution with strain of the $C_i^{\mu\nu}$ coefficients from ODF. Of course, this linear operator depends on strain rate, which means that numerous strain rate tensors (1800) must be used to establish it. Once the $C_i^{\mu\nu}$ coefficients are known, the above identification process of the analytical expression for the yield locus can be activated.

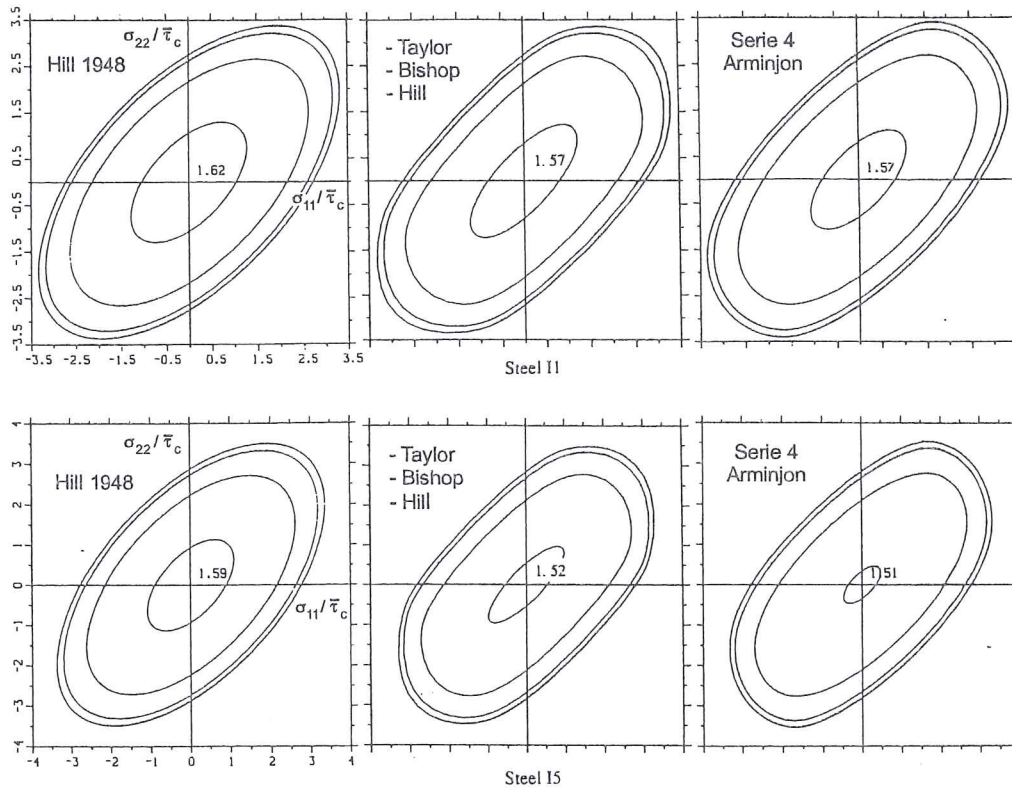


Figure 6-14 Yield locus sections computed by classical Hill's model, crystallographic Taylor-Bishop-Hill's model or Arminjon's 4th order series, for 2 industrial steels I1 (Al killed) and I5 (IF, Ti) (from Arminjon *et al.* 1994).

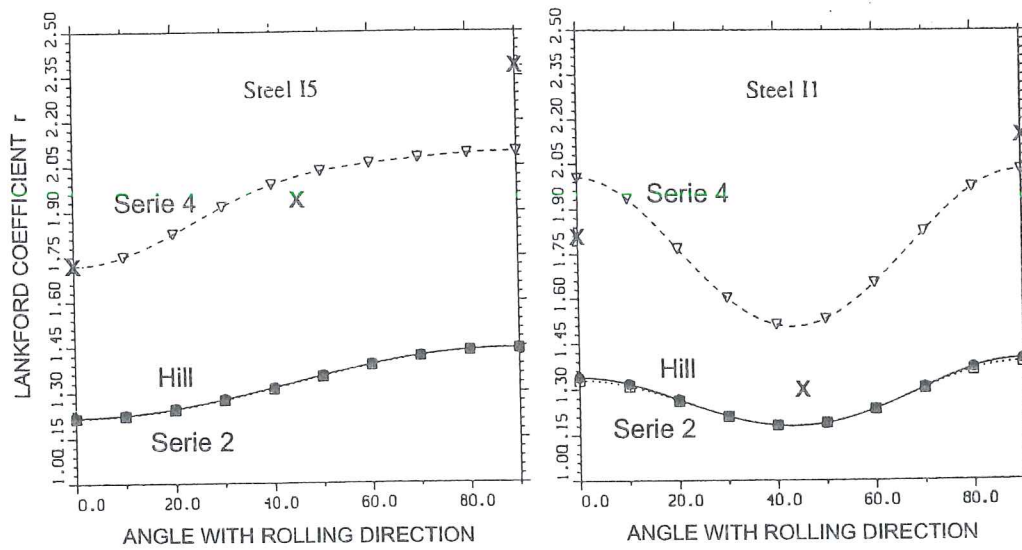


Figure 6-15 Measured (X) and computed Lankford's coefficients for 2 industrial steels I1 (Al killed) and I5 (IF, Ti) (from Arminjon *et al.*, 1994).

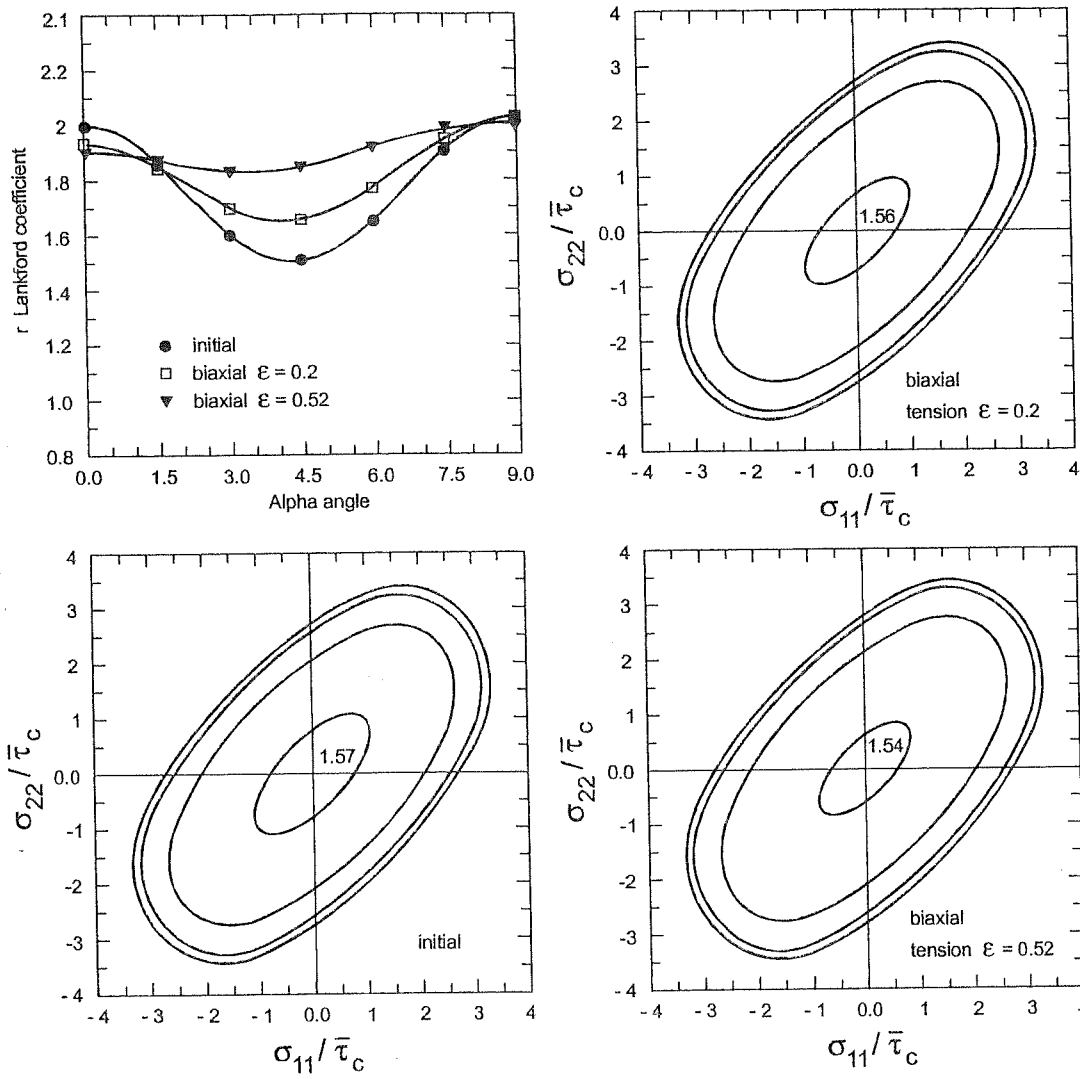


Figure 6-16 Lankford's coefficients and yield loci computed from texture measurements for a steel in its initial state and after biaxial tests performed up to 2 different levels (from Imbault & Arminjon 1993).

6.3.4. Van Houtte's potential formulation

As Arminjon, van Houtte 1994 uses the method of the dual plastic potentials to derive convenient formulae for calculating yield loci of rate insensitive anisotropic materials. In practice, the implementation in FEM code of such yield loci in strain space has been performed by one of his Ph.D. student, van Bael 1994, in collaboration with the university of Birmingham (Wang *et al.* 1989). The yield locus in stress space has been implemented in the LAGAMINE code by Winters 1996, another Ph.D. student in collaboration with MSM team (Munhoven *et al.* 1995a and b). Further developments such as the coupling with Teodosiu's hardening model (Hiwatashi *et al.* 1997) and the formulation in strain rate space in the LAGAMINE

code (Hoferlin *et al.* 1998, Hoferlin *et al.* 1999b) is described in details in Hoferlin's Ph.D. thesis (2001). The hereafter description summarizes van Houtte and co-workers' approach. It also explains what has been implemented in LAGAMINE code.

For rate-independent standard plasticity and formulation in strain rate space, the relation (6-43) computes the stress tensor:

$$\underline{\sigma} = \frac{\partial E}{\partial \underline{\dot{\epsilon}}^p} = \frac{\partial \dot{W}^{p\ macro}}{\partial \underline{\dot{\epsilon}}^p} \quad (6-54)$$

In practice, as already suggested by Lequeu *et al.* 1987, van Houtte's team works in the five dimensional space. The plastic strain rate is classically assumed to be deviatoric and only the deviatoric stress tensor matters with regard to plastic deformation (van Houtte *et al.* 1989). So, the tensors have only 5 independent components and are replaced by 5-dimensional vectors. This transformation, "tensor V_{ij} -vector v_p ", can be defined in different ways. The version implemented in LAGAMINE by Winters 1996 assumes, as van Houtte 1988:

$$\begin{aligned} v_1 &= \frac{1}{\sqrt{2}}(V_{11} - V_{22}) & v_2 &= \sqrt{\frac{3}{2}}(V_{11} + V_{22}) = -\sqrt{\frac{3}{2}} V_{33} \\ v_3 &= \sqrt{2} V_{23} & v_4 &= \sqrt{2} V_{31} & v_5 &= \sqrt{2} V_{12} \end{aligned} \quad (6-55)$$

This vector representation has the following property:

$$\underline{V} : \underline{W} = V_{ij} W_{ij} = \underline{v} \cdot \underline{w} = v_p w_p \quad (6-56)$$

The vector forms of plastic strain rate and deviatoric stress tensors are respectively noted $\underline{\dot{\epsilon}}$ and \underline{s} and their components $\dot{\epsilon}_p$ and s_p .

Using the potential relation (6-54), Taylor's hypothesis and micro-macro relations (4-33), (4-34), the deviatoric stress is computed by:

$$\underline{\hat{\sigma}} = \frac{\partial}{\partial \underline{\dot{\epsilon}}^p} \left(\oint \dot{W}^{p\ micro}(\underline{\dot{\epsilon}}^{p\ micro}, g) f(g) dg \right) = \frac{\partial}{\partial \underline{\dot{\epsilon}}^p} \left(\dot{\epsilon}_{eq}^{p\ macro} \bar{\tau}_c \bar{M}(\underline{U}_{\underline{\dot{\epsilon}}^p}) \right) \quad (6-57a)$$

$$\underline{\hat{\sigma}} = \bar{\tau}_c \frac{\partial}{\partial \underline{\dot{\epsilon}}^p} \left(\dot{\epsilon}_{eq}^{p\ macro} \bar{M}(\underline{U}_{\underline{\dot{\epsilon}}^p}) \right) \quad (6-57b)$$

where $\underline{U}_{\underline{\dot{\epsilon}}^p} = \underline{\dot{\epsilon}}^{p\ macro} / \dot{\epsilon}_{eq}^{p\ macro}$ is a strain mode as defined in Chapter 4. The relation (6-57b) assumes that the average CRSS is independent of further applied strain rate modes. It helps to understand how van Houtte and co-workers completely dissociate the size ($\bar{\tau}_c$) and the shape of the yield locus $\frac{\partial}{\partial \underline{\dot{\epsilon}}^p} \left(\dot{\epsilon}_{eq}^{p\ macro} \bar{M}(\underline{U}_{\underline{\dot{\epsilon}}^p}) \right)$.

In practice, Winters 1996 proposes an isotropic hardening model. He updates $\bar{\tau}_c$ via a simple Swift's law (3-11) applied at the macroscopic stress strain level. The transfer to $\bar{\tau}_c(\bar{\Gamma})$ is based on the first term of the relation (4-40):

$$\frac{d\sigma}{d\varepsilon} = \bar{M}^2 \frac{d\bar{\tau}_c}{d\bar{\Gamma}} + \bar{\tau}_c \frac{d\bar{M}}{d\varepsilon} \quad (4-40)$$

where $\bar{\Gamma}$ is the total polycrystal slip. The stress σ and the strain ε are those of a uniaxial test. Neglecting the second term of (4-40) means that the texture evolution is dropped. This will be assumed in further developments, except when clearly specified.

Hiwatashi *et al.* 1997 applies a kinematic hardening assumption and slightly modifies the relation (6-57b) which becomes:

$$\underline{\hat{\sigma}} - \underline{\alpha} = \bar{\tau}_c \frac{\partial}{\partial \underline{\hat{\varepsilon}}^p} \left(\dot{\underline{\hat{\varepsilon}}}_{eq}^{p, macro} \bar{M}(\underline{U}_{\underline{\hat{\varepsilon}}^p}) \right) \quad (6-58)$$

where $\underline{\alpha}$ is the back-stress and defines the updated center of the yield locus. The evolutions of $\underline{\alpha}$ and $\bar{\tau}_c$ follow the model proposed by Teodosiu, already described in section 3.5.5.

The size and position of the yield locus being defined by the choice of the hardening model, what about its shape? Relation (6-57b) clearly shows the role of the texture via the average Taylor's factor $\bar{M}(\underline{U}_{\underline{\hat{\varepsilon}}^p})$. \underline{u} or u_p are the vector forms of this strain mode. The average Taylor's factor can be approximated by an analytical function $Q(u_p)$ of the components u_p :

$$\bar{M}(\underline{U}_{\underline{\hat{\varepsilon}}^p}) = \bar{M}(\underline{u}) \approx Q(\underline{u}) = F_{p_1 p_2 p_3 \dots p_N} u_{p_1} u_{p_2} u_{p_3} \dots u_{p_N} \quad (6-59)$$

$N = \text{order of series expansion} \quad p_i = 1, \dots, 5 \quad i = 1, \dots, N$

For instance, if N is reduced to 2, there are 15 coefficients:

$$Q(\underline{u}) = F_{11} u_1 u_1 + F_{12} u_1 u_2 + F_{13} u_1 u_3 + F_{14} u_1 u_4 + F_{15} u_1 u_5 + F_{22} u_2 u_2 \dots + F_{55} u_5 u_5 \quad (6-60)$$

van Bael 1994 has extensively described the symmetry properties of such an analytical expression, the main drawback of which is its lack of convexity. He explains that an odd order choice gives a non centro-symmetrical yield locus, which allows to model stress differential effects. It has been checked by van Bael *et al.* 1996 and Munhoven *et al.* 1997 that the 6th order is required to reproduce, with an analytical description, the accuracy of polycrystal approaches.

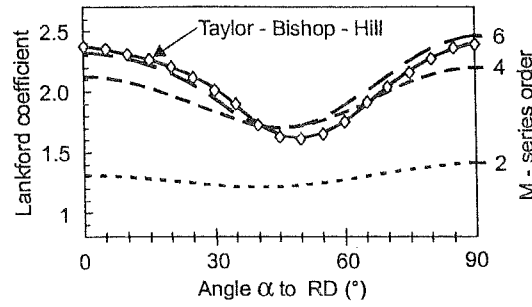


Figure 6-17 Lankford's coefficient of a classical interstitial steel computed by a polycrystal model or by means of 2nd, 4th, 6th order series in strain rate space (from Munhoven *et al.* 1997).

This choice of $N=6$ leads to 210 coefficients $F_{p_1 \dots p_6}$. To identify them, it is interesting to note that any strain mode tensor can be represented by means of 4 independent parameters and not 5 because $\underline{U}_{\dot{\epsilon}^p} : \underline{U}_{\dot{\epsilon}^p} = \frac{3}{2}$. van Houtte 1994 demonstrates:

$$\underline{U}_{\dot{\epsilon}^p} = \begin{pmatrix} U_{11} & U_{12} & U_{13} \\ & U_{22} & U_{23} \\ \text{SYM} & & U_{33} \end{pmatrix} \quad \underline{U}_{\dot{\epsilon}^p} = \underline{R}^T \underline{U}_{\dot{\epsilon}^p}^X \underline{R} \quad (6-61)$$

with :

$$\underline{R} = \underline{R}(\beta_1, \beta_2, \beta_3) \text{ and } (\beta_1, \beta_2, \beta_3) \in (0, 2\pi) \times (0, \pi/2) \times (0, \pi) \quad (6-62)$$

$$\underline{U}_{\dot{\epsilon}^p}^X = \begin{pmatrix} U_{11}^X & & \\ & U_{22}^X & \\ & & U_{33}^X \end{pmatrix} \text{ but } \text{tr}(\underline{U}_{\dot{\epsilon}^p}^X) = 0 \text{ and } \underline{U}_{\dot{\epsilon}^p}^X : \underline{U}_{\dot{\epsilon}^p}^X = \frac{3}{2} \quad (6-63)$$

$$U_{11}^X = \cos(\beta_4 - \frac{\pi}{3}), \quad U_{22}^X = \cos(\beta_4 + \frac{\pi}{3}), \quad U_{33}^X = -\cos(\beta_4) \quad (6-64)$$

The 3 Euler's angles $\beta_1, \beta_2, \beta_3$ define the orientation of the strain rate mode principal directions with respect to the sample reference system. The fourth angle gives the deviation of the current strain rate mode with respect to an axisymmetric compression along the third principal axis. Finally discrete variations of β_i , for instance $\Delta\beta_1 = \Delta\beta_2 = \Delta\beta_3 = 10^\circ$ and $\Delta\beta_4 = 7.5^\circ$ define a discrete set of strain rate modes (around 70300). The average Taylor factor is computed by the texture and crystalline approach (full Constrained Taylor-Bishop-Hill's model) for each of these modes. Then, the coefficients of the series expansion are provided by a least square fit of Q function (6-59).

Relation (6-57b) calculating the stress from the dissipation, is modified to take into account both the vector formulation and the analytical expression of the average Taylor's factor:

$$s_p = \tau_c \frac{\partial(\dot{\epsilon}_{eq}^p Q(\underline{u}))}{\partial \dot{\epsilon}_p} \quad (6-65)$$

In FEM, one usually needs the yield locus point corresponding to a given stress direction \underline{s}^* . So, Legendre's transformation must be applied. Let $s\underline{s}^*$ describe one stress vector belonging to the yield locus : the scalar factor s is the vector norm $\sqrt{s_p s_p}$ of the stress point, it is called stress radius, and \underline{s}^* is its unit vector direction. Assuming that \underline{u} is the strain rate mode associated with this stress direction \underline{s}^* and using the average Taylor's factor definition, one gets :

$$\overline{M}(\underline{u}) = \min_{\underline{u}'} \frac{s \underline{s}^*}{\tau_c} \cdot \underline{u}' = \text{minimum in strain rate space} \quad (6-66)$$

where \underline{u}' represents all the possible strain modes of the strain rate space.

As \underline{u} is actually unknown, one has to minimize the ratio:

$$\frac{s}{\tau_c} = \min_{\underline{u}'} \frac{\overline{M}(\underline{u})}{\underline{u}' \underline{s}^*} \quad (6-67a)$$

$$\frac{s}{\tau_c} = \min_{\underline{u}'} \frac{Q(\underline{u}')}{\underline{u}' \underline{s}^*} \quad (6-67b)$$

The scaled factor $\overline{\tau}_c$ clearly shows that the shape does not depend on the size of the yield locus. If a formulation in strain rate space is adopted, $Q(\underline{u})$ is known and (6-67b) is used to perform the minimization. Figure 6-18 explains this procedure graphically. As reported above, the field of strain rate modes can be covered by 4 independent parameters, which limits the operation duration. Additionally, Hoferlin *et al.* 1999a propose a way to speed up significantly the minimization : with a BFGS type method instead of a classical Newton's method and by splitting the minimization process.

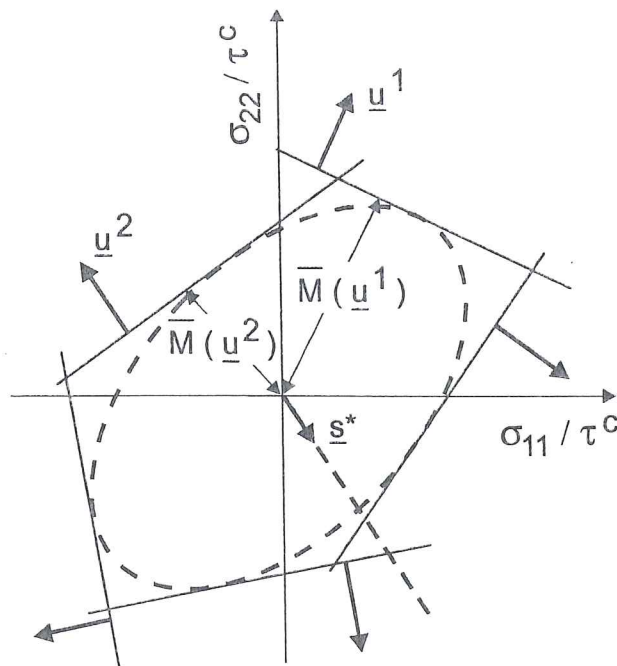


Figure 6-18 Graphical view of the minimization procedure to find a point on the yield locus (adapted from Hoferlin *et al.* 1999a).

As the convexity of the function $Q(\underline{u})$ in strain rate space is not perfect, gathering all stress points computed by (6-67b) does not produce a convex yield locus in stress space. Some fishtails appear as demonstrated by Figure 6-19. This drawing applies to an almost single f.c.c. crystal texture generated around the Goss' orientation (Gaussian distribution with 11° spread around $(011)[100]$). The left figure shows the π - section of one yield locus in strain rate space. For a pure single crystal, linear segments compose this locus. The series expansion reproduces linear segments by oscillating around them. The application of the minimization (6-67b) provides a yield locus in stress space with fishtails: see figure on the right.

Real materials generally present a less sharp texture; so their yield loci are smoother and the 4th or 6th order series expansions should be convex descriptions. However as non convex loci fail to bring convergence in FEM simulations, some secure approach should be implemented. Hoferlin's proposal consists in repeating the minimization (6-67b) with different starting guesses for \underline{u}' and choosing the smallest result s , as the one giving the point on the yield locus. This procedure cuts off the fishtails and prevents convergence problems due to lack of convexity.

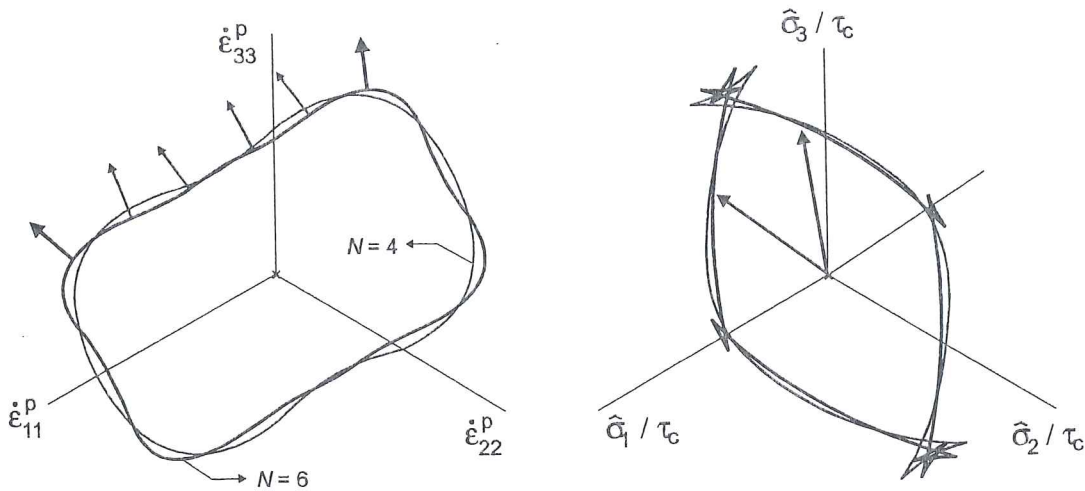


Figure 6-19 π -plane sections of the yield loci expressed in strain rate space (left) and in deviatoric stress space (right) for a f.c.c polycrystal with Goss' texture component (from Hoferlin *et al.* 1999a).

Another choice can be to implement an analytical yield locus in stress space, computed from texture and crystal plasticity approaches. The above presentation explains how to find points belonging to the yield locus. For a set of directions \underline{s}^* in stress space, (6-67a) or (6-67b) provide the stress radius s . These two ways to obtain sets of yield points are not exactly equivalent.

The first way uses relation (6-67a), where $\overline{M}(\underline{u}')$ has no analytical expression and is computed for a certain number of strain rate modes. It is similar to the polycrystal method to get yield locus sections (see section 6.3.1.). By analogy, this method is called "geometrical approach". These yield points generally describe a nearly convex yield locus.

The second way uses relation (6-67b) and gives a set of points defining an approximate yield locus, not necessarily convex as shown by Figure 6-19.

In both cases, one has not yet reached an analytical yield formulation of the stress yield locus F_p . To reach this goal, one must fit an analytical function on these points. By analogy to the work in strain rate space, a series expansion is applied. Relations (6-68) and (6-69) present two possible choices:

$$\frac{s}{\tau_c} = Q(\underline{s}^*) \rightarrow F_p = \frac{s}{Q(\underline{s}^*)} - \tau_c = 0 \rightarrow u_p^* = \lambda \frac{\partial(s / Q(\underline{s}^*))}{\partial s_p^*} \quad (6-68a,b,c)$$

$$\frac{s}{\tau_c} = \frac{1}{Q(\underline{s}^*)} \rightarrow F_p = sQ(\underline{s}^*) - \tau_c = 0 \rightarrow u_p^* = \lambda \frac{\partial(s Q(\underline{s}^*))}{\partial s_p^*} \quad (6-69a,b,c)$$

where \underline{u}^* is chosen as a unit vector. Its relation with the previous identification of the strain modes in vector form is $\underline{u}^* = \underline{u} / \sqrt{\underline{u} \cdot \underline{u}}$. It defines the direction of the strain rate mode \underline{u} .

The third relations (6-68c), (6-69c) express a weak form of the normality rule in which the vector norms are not defined since both \underline{s}^* and \underline{u}^* are unit vectors. The scalar λ is computed to keep the norm of the strain rate mode tensor equal to unity.

In practice, Winters 1996 chooses (6-69) in order to use all the routines already developed to compute the formulation (6-65) in strain rate space. His function $Q(\underline{s}^*)$ is a 6th order series expansion, the coefficients of which are fitted to the inverse of the stress radii:

$$Q(\underline{s}^*) = G_{p_1 p_2 \dots p_N} s_{p_1}^* s_{p_2}^* \dots s_{p_N}^* = \frac{\bar{\tau}_c}{s} \tag{6-70}$$

This set of points $\frac{\bar{\tau}_c}{s}$ is provided by the first way presented above. So, the yield locus will exhibit no fishtail. However as illustrated by figure 6-20, it must be observed that this yield locus in stress space is not completely convex. The locus on the left in strain rate space results from the approximation (6-59) in strain rate space while the one in stress space on the right is computed by (6-69b) and the first way to get the set of stress points.

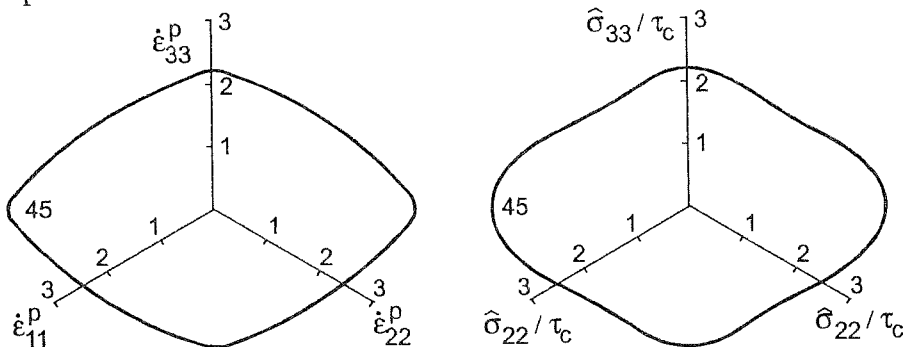


Figure 6-20 π -plane sections of the yield loci expressed in the strain rate space (left) and in deviatoric stress space (right), relative to a polycrystal with cube texture component and a Gaussian spreading of 16.5° (adapted from Winters 1996).

Further investigations have computed Lankford's coefficient: from (6-69) i.e. calculations in stress space, from (6-59) i.e. calculations in strain rate space and from Taylor-Bishop Hill's model. Both works from Winters 1996 and van Bael *et al.* 1996 reach the same conclusion that the yield locus in stress space is less accurate than the formulation in strain rate space.

Finally, is it better to use a formulation in strain rate or in stress space? The answer depends on your primary interest: accuracy, low CPU time, necessity of texture updating. Table 6-1 summarizes the advantages and drawbacks of each approach:

	Stress space $\frac{s}{\tau_c} = \frac{1}{Q(\underline{s}^*)}$	Strain-rate space $\dot{W}^P = \bar{\tau}_c \dot{\epsilon}_{eq}^P Q(\underline{u})$
Speed of FEM	faster	slower 4-dim. minimization
Texture evolution	Slower texture $\rightarrow \bar{M} \rightarrow$ 4-dim. minimization $\rightarrow Q$	faster texture $\rightarrow \bar{M} \rightarrow Q$
Sharp textures	one stress direction \rightarrow one stress point	one stress direction \rightarrow fishtails (extra cost)
Accuracy	Lower	Higher

Table 6-1 Comparison between stress and strain rate formulations for analytical yield loci implemented in FEM codes (adapted from Hoferlin *et al.* 1999a).

Two points are completely missing in this description: the integration scheme and the numerical way to identify the position of material axes. Both are described in Winters 1996. For material axes, the solution proposed by Munhoven *et al.* 1995 is applied: each step is characterized by a constant local velocity gradient, which determines the evolution of material axes. This method has been described in part C, section 7.3.1 of this thesis. Another explanation of the same mathematical approach is proposed by Hoferlin *et al.* 1999b, using Ponthot's 1995 constant co-rotational strain rate tensor.

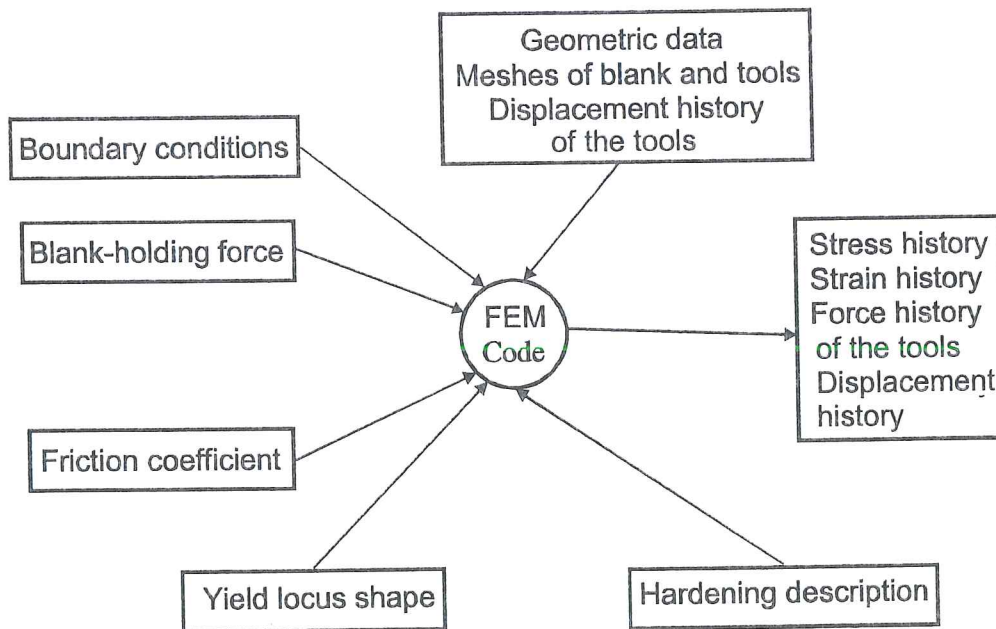


Figure 6-21 Schematic view of inputs and outputs of a FEM deep drawing simulation.

Figure 6-21 recalls the usual input and output of a FEM deep-drawing simulation when no texture updating is performed.

Figure 6-22 summarizes all the necessary steps to reach the yield locus shape expressed in stress or strain rate spaces.

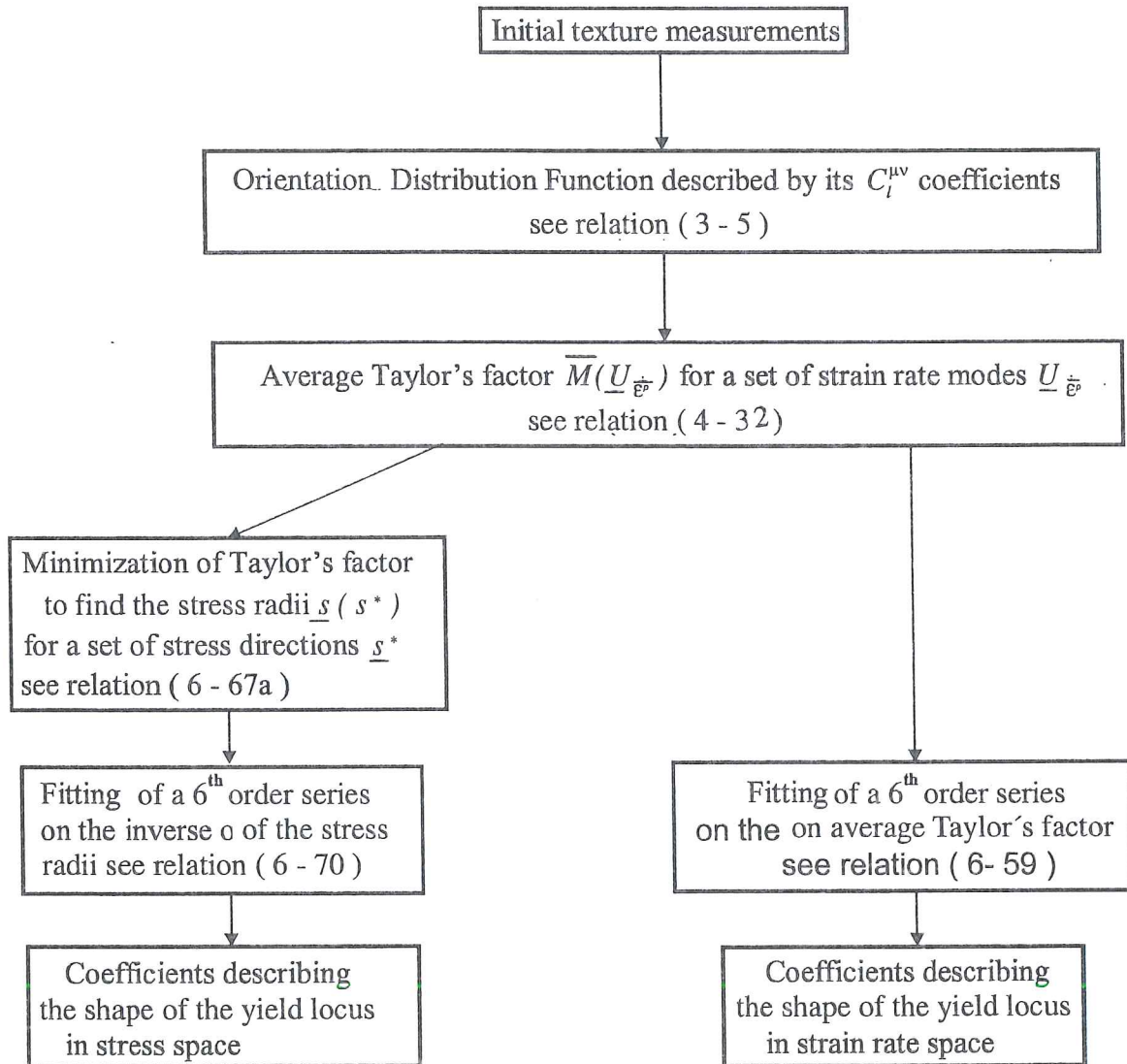


Figure 6-22 Successive operations to reach the shape description of the yield locus in stress or strain rate space.

6.3.5. Conclusion

Sections 6.3.2 to 6.3.4 propose models able to describe the behavior of real materials. They can be implemented in FEM codes and each one presents some advantages and drawbacks.

Darrieulat's micro-macro approach seems more accurate than Lequeu's. However, for real materials where important number of texture components are present, the FEM computations must be quite lengthy as their approach finally considers the yield locus associated to each component. Uniform stress approach must bring some difficulties in the FEM integration scheme.

The proposals from Arminjon, van Houtte and co-authors seem quite interesting. The identification of yield locus coefficients from texture coefficients can be optimized outside the FEM code. Taylor's assumption leads to a direct macroscopic stress-strain formulation.

Arminjon's semi-analytical method (shortly summarised at the end of section 6.3.3) to take texture updating into account is probably difficult to use for arbitrary velocity gradient. The approach proposed by Hoferlin (yield locus in strain rate space) seems more adapted in a FEM context. However, the CPU time is still important, as working in the strain rate space is slower than in stress space.

6.4. Models developed by MSM

6.4.1. First steps in coupling FEM with texture codes

Thanks to a collaboration with the team of Professor van Houtte, scientists of MSM department had, in 1995, the possibility to identify a 6th order series describing a yield locus in stress space from the $C_i^{\mu\nu}$ coefficients of an ODF (see Figure 6-22). The constitutive law called "ANI3VH" (ANIsotropic 3 dimensions Van Houtte law) described by (6-69) and (6-70) was implemented in LAGAMINE. It allows to simulate deep drawing experiments (Munhoven *et al.* 1995a, Munhoven *et al.* 1995b, Munhoven *et al.* 1996b) such as cup-drawing and to predict the earing profile. The 6th order polynomial series expansion defining the yield locus in the stress space is fitted once, from the initial ODF measurements and is not updated from the texture evolution. A simple isotropic hardening Swift's law (3-11) is applied at the microscopic level. This hardening law is fitted thanks to tensile test experiments and the micro-macro transition is done via (4-40) as explained in section 6.3.4.

From the collaboration with van Houtte's team, MSM department received a "Pascal version" of Taylor's model that allows texture evolution computations (see section 4.1). As inputs, such a module requires the initial texture approximated by a discrete set of orientations, the crystal slip systems identified by Schmid's tensors, the ratio between CRSS associated to slip systems and the macroscopic velocity gradient provided by the FEM analysis. With all these data, Taylor's model computes the updated crystal orientations, which can be used to retrieve the continuous ODF.

With these numerical tools, MSM team has simulated the experimental axisymmetric deep drawing of a cold-rolled interstitial free steel sheet, described on Figure 6-23.

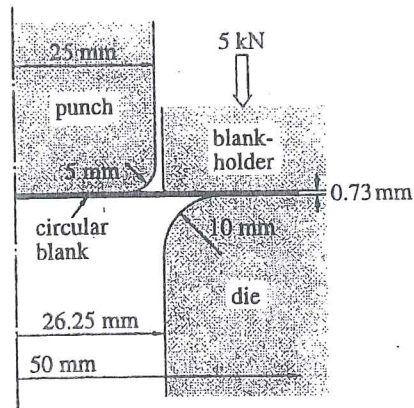


Figure 6-23 Radial section of the cup-drawing process (from Munhoven *et al.* 1995a).

The elastic part of the deformation is assumed to follow the isotropic Hooke's law. The total strain rate is split into elastic and plastic parts and an integration scheme developed by Winters 1996 is applied. Taking advantage of the orthotropic symmetry of the blank material, only one quarter is simulated. A single layer of 8-node hexahedral solid elements is used; they are of the assumed strain family with one-point quadrature and hourglass control (Zhu & Cescotto 1996). Figure 6-24 shows the blank mesh with an indication about the positions of the tools.

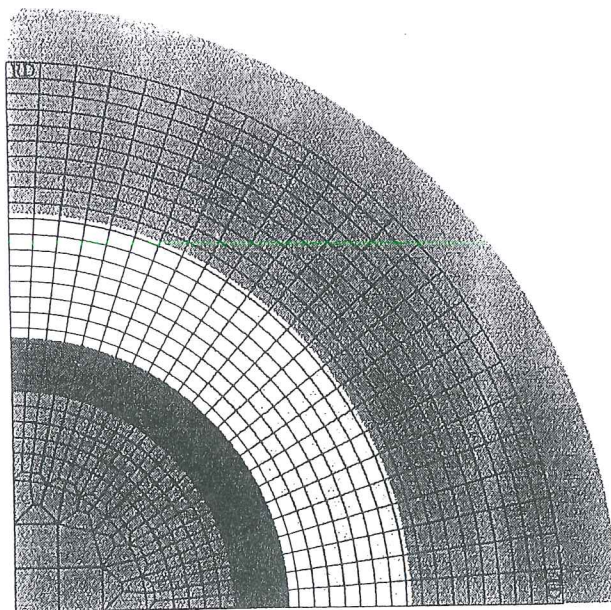


Figure 6-24 Discretization of the blank (656 elements, 1396 nodes) with an indication of tool positions (from Munhoven *et al.* 1996).

The die, punch and blank-holder are meshed by 1080 triangular elements and a Coulomb-type friction law (Charlier & Habraken 1990) is applied. The deformed mesh is presented on Figure 6-25, where the progressive earing of the drawn cup can be observed.

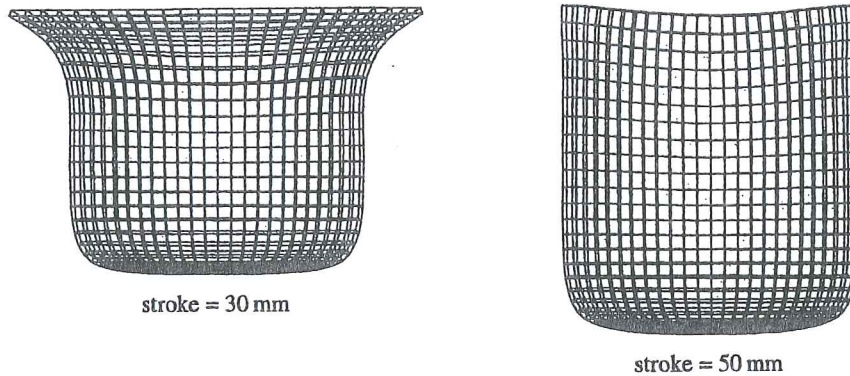


Figure 6-25 Orthogonal projections of the deformed mesh (from Munhoven *et al.* 1996).

The percentage of earing, defined as :

$$e = (h - h_{min}) / h_{min} \quad (6-71)$$

where h is the cup height depending on α angle with the initial rolling direction, and h_{min} is its minimal value, is plotted on Figure 6-26. Considering the absence of texture updating on the yield locus and the simple constant friction model, a quite good agreement is found.

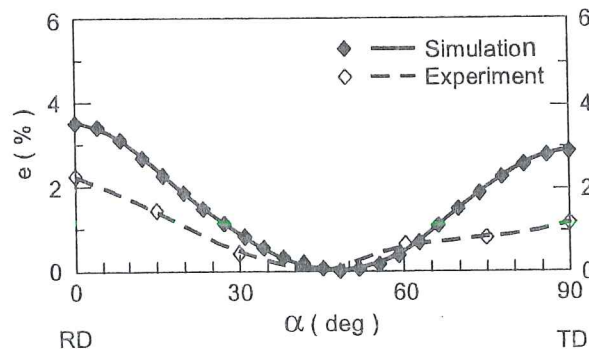


Figure 6-26 Simulated and experimental percentage of earing e (from Munhoven *et al.* 1996).

In general, a large portion of Euler's space angles ($\varphi_1, \varphi, \varphi_2$) has to be considered in order to get a correct idea of an ODF. In the present case, however, the symmetries of the material and the particular deformation history make a $\varphi_2 = \pi/4$ section very representative. Figure 6-27 a) shows some ideal texture features in such a plot. Comparison with Figure 6-27 b), corresponding to the cold-rolled steel before deep-

drawing, underscores the presence of a strong γ -fiber: many crystallites have a $\{111\}$ crystallographic plane parallel to the rolling plane, but no direction $\langle uvw \rangle$ within this plane has a preferential orientation.

After deep-drawing, samples are cut out of the cup at different positions and their textures are measured. Their texture evolution is also computed according to the FEM results using the "full constraints" Taylor's model of van Houtte, 1988. Experimental and numerical results are shown in Figure 6-27 c) to f) for two points (defined in Figure 6-24) near the cup rim, in the rolling (RD) and transverse direction (TD). In both cases, the initially strong γ -fiber has disappeared. Note that the texture sheet is measured at mid-thickness.

In RD, an E -component texture has appeared: $\{111\}$ planes are still parallel to the sheet-plane, but now direction $\langle 110 \rangle$ has become strongly aligned with the initial RD. This evolution is typically observed in a plane strain situation, with elongation along RD and compression along TD. Since it is not exactly the case here, the texture peaks are slightly shifted away from E , as it appears in both experimental and simulated results. Considering that the "full constraints" Taylor's model typically produces too sharp textures, satisfactory agreement is found.

In TD, the situation is similar, except that radial flow now occurs in TD instead of RD. Up to a rotation of 90° around the vertical direction, results should thus be quite analog: an F -component texture with $\{111\}$ planes still parallel to the sheet plane is expected but, this time, with $\langle 112 \rangle$ preferentially parallel to the initial RD. Again, up to a slight shift, this is obtained experimentally and numerically.

It is important to note that, in the present case, material flow is almost fully constrained. In addition, the rim undulations are very small. As a consequence, the flow pattern does not dramatically depends on texture and corresponding evolution of the yield locus.

In order to progress in the development of a model in which texture updating is coupled with the FEM simulation, Munhoven has written a new version of Taylor's model in "Fortran 90", better adapted to be efficiently linked with the LAGAMINE code (Munhoven 1997, Habraken 1998a, Habraken 1998b). Taylor's factors associated with each crystal are the direct results of the simplex linear programming of Taylor's model (van Houtte 1988). They are combined to give the average Taylor's factor. Another interesting point is the fact that the simplex multipliers are none but the components of the five-dimensional vector representation of the crystal scaled deviatoric yield stress $s_p / \bar{\tau}_c$. The macroscopic stress is reached by averaging crystal stresses, weighted by the volume fraction associated with each crystal orientation (see relation (5-19)). It is important to note that, for b.c.c crystals and orthotropic sheets, a lot of symmetries are present. If one is interested in scalar values such as average Taylor's factor, one can choose a set of representative crystals

with Euler's angles $\varphi_1, \phi, \varphi_2$ in the reduced space of $[0^\circ, 90^\circ] \times [0^\circ, 90^\circ] \times [0^\circ, 90^\circ]$. However, to reach tensor values such as macroscopic stresses, a less reduced space must be adopted: $[0^\circ, 360^\circ] \times [0^\circ, 90^\circ] \times [0^\circ, 90^\circ]$ (Pospiech 1982). The new Fortran 90 module has been checked by comparisons with van Houtte's module and gives entire satisfaction (Habracken 1998a).

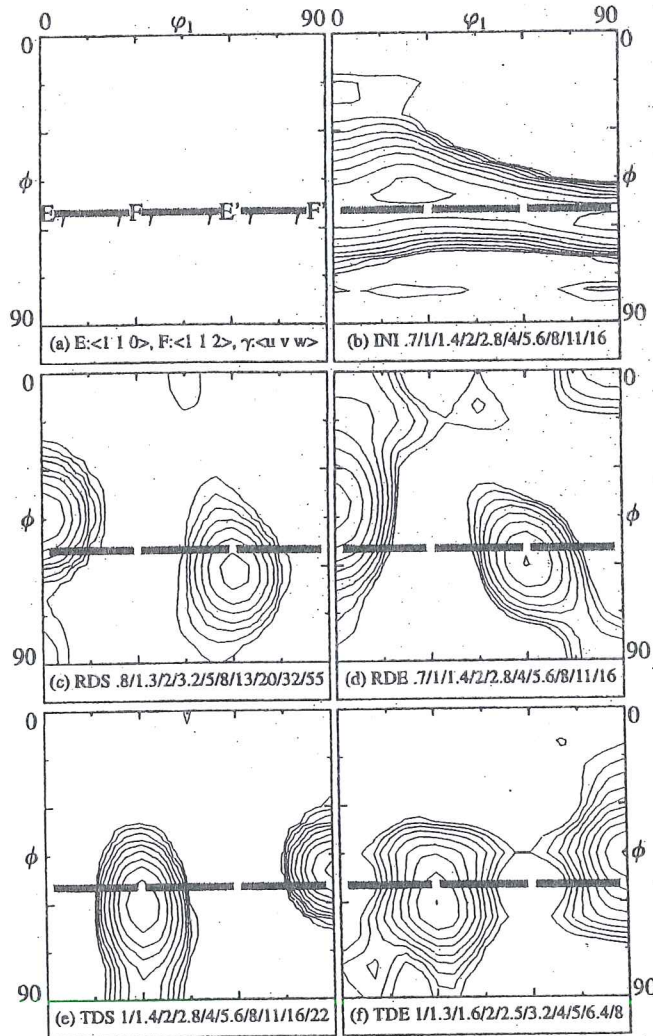


Figure 6-27 $\varphi_2 = 45^\circ$ sections of Euler's space (from Munhoven *et al.* 1996).

a) some b.c.c. texture components:

$$E = \{111\}\langle 110 \rangle \quad F = \{111\}\langle 112 \rangle \quad \gamma - \text{fiber} = \{111\}\langle uvw \rangle$$

b) initial texture

c) simulated texture at RD point located in Figure 6-24

d) measured texture at RD point

e) simulated texture at TD point located in Figure 6-24

f) measured texture at TD point.

Figure 6-28 summarizes inputs and outputs of Taylor's module used by LAGAMINE.

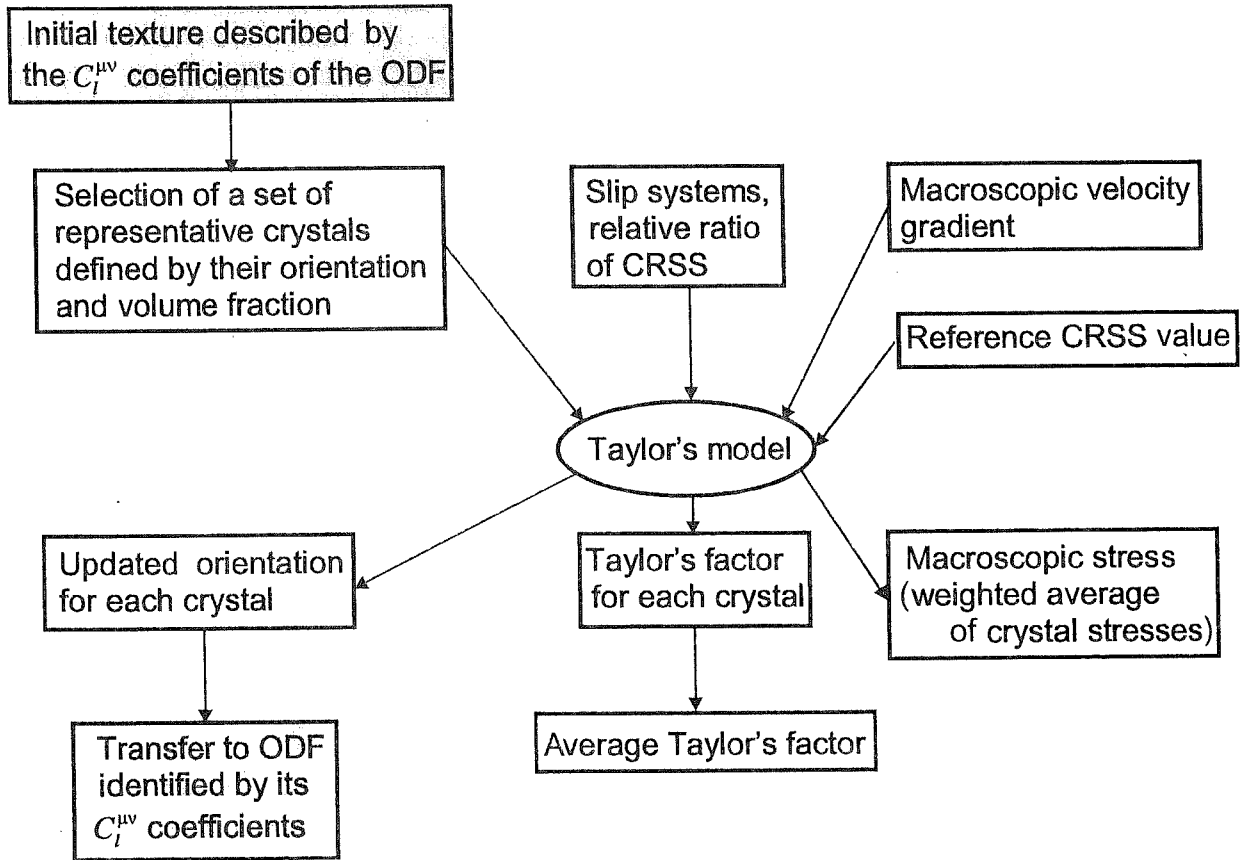


Figure 6-28 Texture updating by Taylor's model.

The "American way" of selecting a representative set of crystals has already been shortly described in section 5.3.1. However, here the approach called "STAT" from Tóth & van Houtte 1992 is applied. In practice, a 5°-grid in Euler' space is used to define N boxes in Euler' space. These boxes are given sequence numbers i ranging from 1 to N . Let us compute f_i the integral of the ODF in box i :

$$f_i = \int_{\text{box } i} f(g) dg \quad (6-72)$$

The property of the ODF yields:

$$\sum_{i=1}^N f_i = 1 \quad (6-73)$$

A kind of staircase function $F(j)$ is built with some smoothing between the steps:

$$F(j) = \sum_{i=1}^j f_i \quad (6-74)$$

If g_j represent Euler's angles at the center of box j , one can plot the diagram (g_j, F_j) in Figure 6-29.

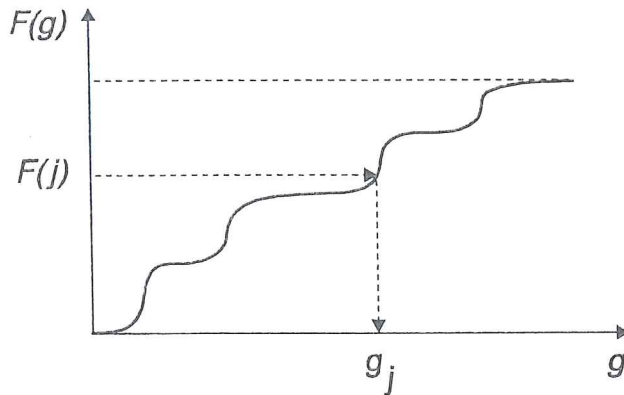


Figure 6-29 Staircase function of crystal orientation (adapted from Tóth & van Houtte 1992).

To discretize the ODF, a set of n numbers s_k , called selectors, is generated in the range $[0,1]$. They represent points of the vertical axis. By inverting function $F(g)$, one reaches, on the horizontal axis, the orientation g_k or the box k associated to s_k . The selectors s_k have a uniform probability distribution. The probability $p(i)$ of selecting a particular box i is f_i . Further details on the statistical properties of the STAT method are given in Tóth & van Houtte 1992.

In Degueldre *et al.* 1996, my co-workers and myself have applied the texture prediction module to an experiment of aluminium extrusion shown on Figure 6-30 and performed by the R&D Center of Hydro Aluminum in Norway.

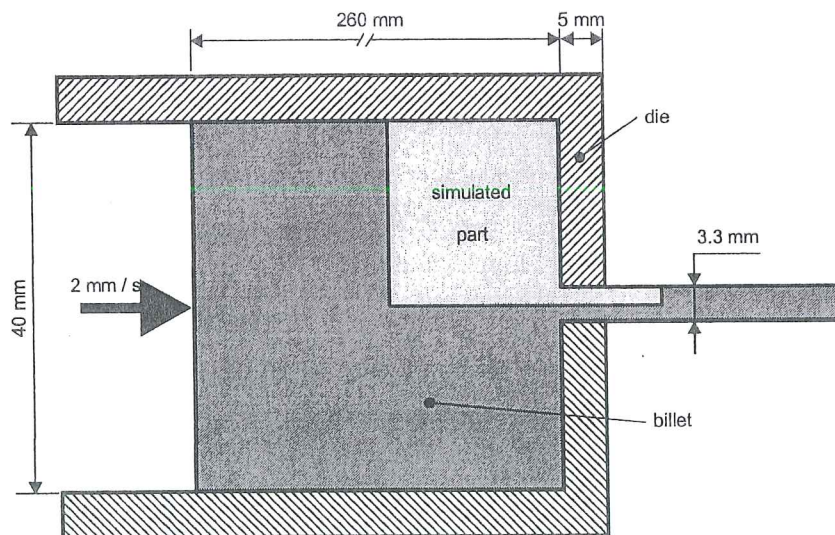


Figure 6-30 Cross section of the experimental set up (plane extrusion), adapted from Aukrust *et al.* 1994.

As the LAGAMINE code is Lagrangian, an automatic remeshing procedure (Dyduch *et al.* 1995) has been applied and the process is simulated until stationary conditions are reached. Three successive meshes are presented on Figure 6-31.

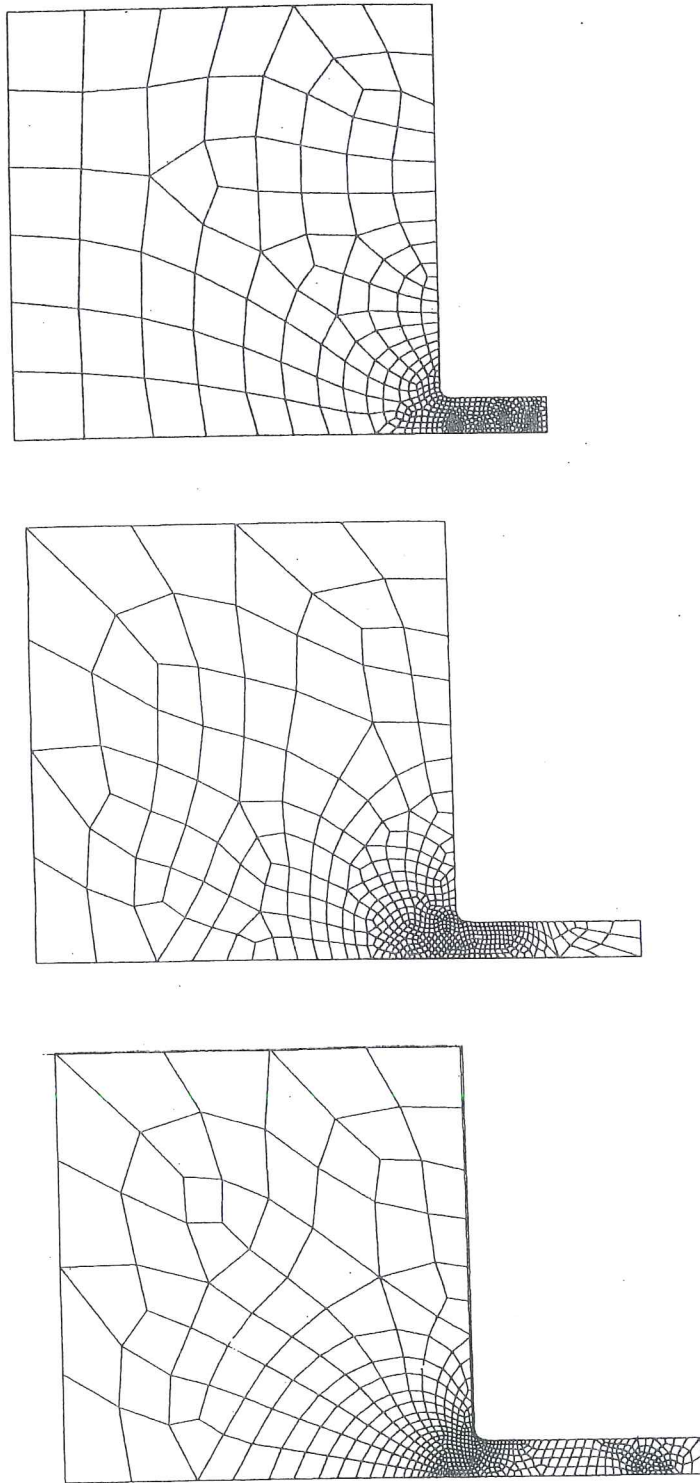


Figure 6-31 Three successive meshes in the extrusion simulation.

A macroscopic elasto-visco-plastic law (Cescotto et Grober, 1985) represents the isotropic behavior of the hot material. The experimental boundary conditions and particularly the friction coefficient to be used in Coulomb's friction model were not clearly identified. So, depending on contact conditions (case A or B) and on small variations of the parameters of the elasto-visco-plastic law (law 1 or 3), different velocity fields were computed. The material strain history was extracted from the FEM results thanks to a special post processing (Munhoven 1996) and used as data for Taylor's model. The material initial texture was isotropic and, after extrusion, different textures were observed according to the vertical position in the extruded section. The coordinate S identifies this location: $S=0$ at the center and $S=1$ at the surface. Figure 6-32 presents pole figures at the center and near the surface of the extruded section. The results, produced by the measurements, by a Norwegian team (Aukrust *et al.* 1997) using a FEM Eulerian code with Full Constraints (FC) or Relaxed Constraints (RC) Taylor's model and by our group, are plotted in Figure 6-32.

A good agreement is found at the center, while predictions close to the surface appear to be highly sensitive to simulation conditions. Comparisons of velocity fields near the surface also show a lot of scatter, depending on boundary conditions, material parameters and FEM codes. So it is not surprising that textures computed from these different strain histories vary.

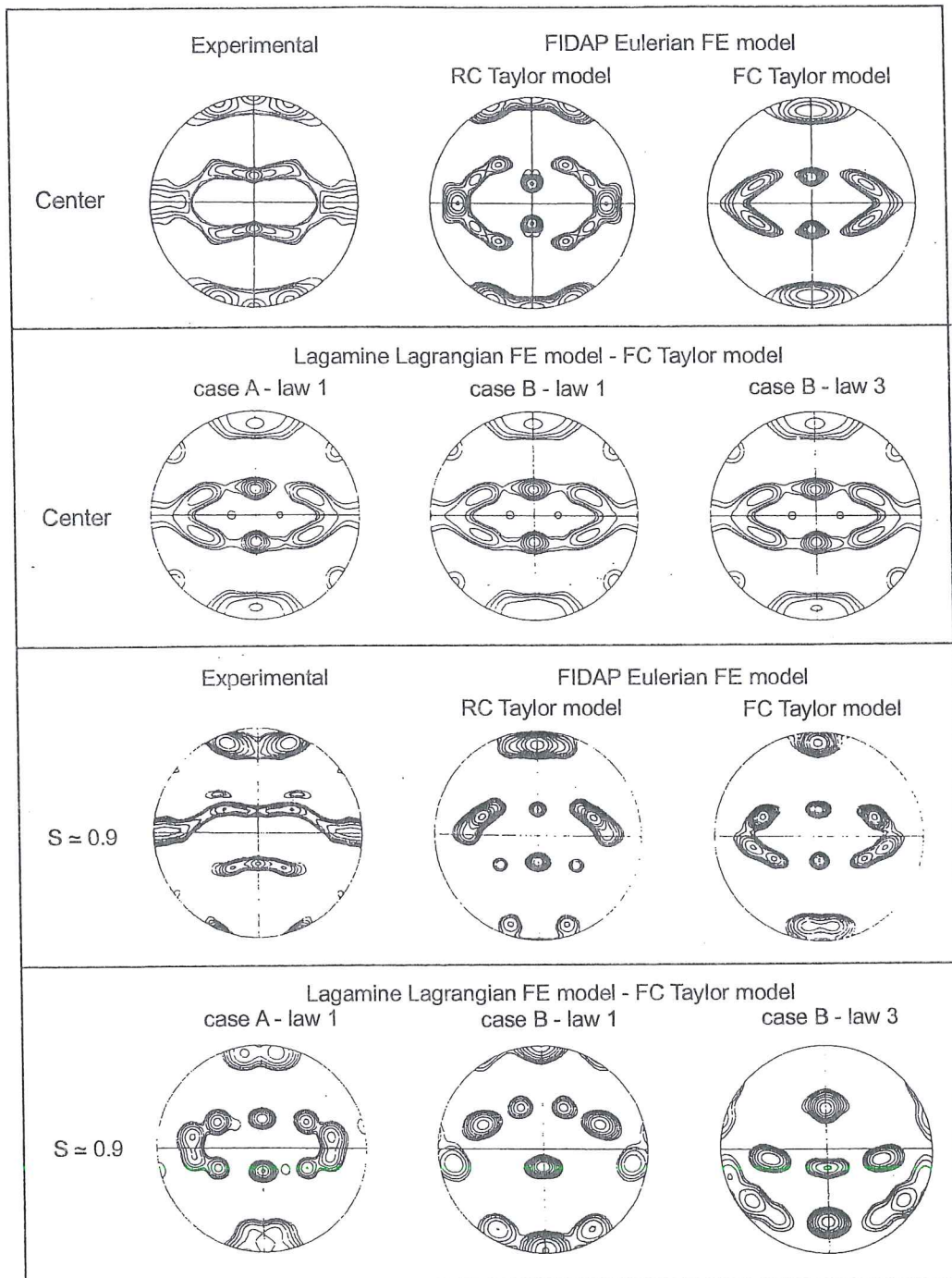


Figure 6-32 $\{111\}$ pole figures at the center and near the surface of the extruded section (from Degueudre *et al.* 1996).

6.4.2. Texture updating coupled with FEM simulations

As verified by Figure 6-27 and Figure 6-32, the texture evolution during a forming process is not always negligible. Material properties such as Lankford's coefficients and the yield locus computed from texture measurements before and after biaxial tension show a clear evolution (see Figure 6-16). So, to obtain FEM simulations that

really represent the material behavior during forming processes, it is interesting to couple a FEM code using a yield locus based on texture and a texture prediction module.

One possible global scheme is described by Figure 6-33. In this approach, every Interpolation Point of each finite element is associated with a representative set of crystal orientations. One yield locus in stress space is computed by a “Micro-Macro transition” as summarized by Figure 6-22. Then, the FEM code is run for a chosen number of loading steps and it computes the macroscopic velocity gradient that feeds a texture prediction module (Taylor’s model). This module provides the updated orientations of the set of representative crystal orientations and the loop goes on.

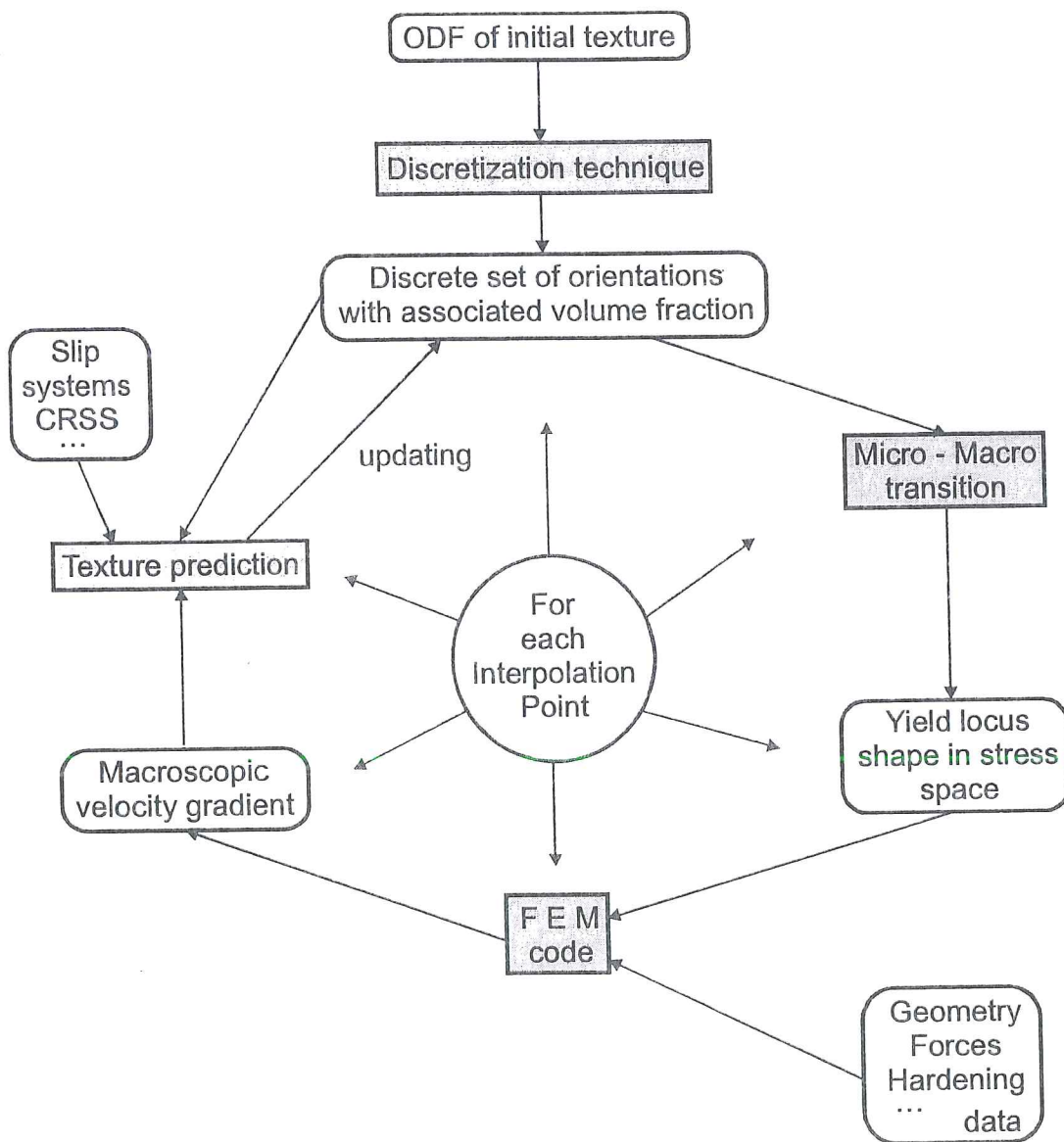


Figure 6-33 Complete flowchart for coupling yield locus and crystallographic texture.

Does such a scheme bring any economy compared with the simulations without yield locus presented in section 5.3?

Concerning memory requirement, certainly not. There are not only the parameters describing the set of representative crystals for each interpolation point to be stored but, in addition, the coefficients describing the shape of the yield locus.

Concerning CPU time, probably yes... In fact, in the models of section 5.3, Taylor's model is called each time the stress must be computed that is at each iteration of each loading step. In Figure 6-33, Taylor's model is called after a "few steps", when the strain history produces a significant texture evolution. If these "few steps" are reduced to one, the economy resulting of the proposal on Figure 6-33 is reduced but still exists: there is only one Taylor's call per step, after convergence of the equilibrium iterations. However, this advantage is counterbalanced by all the computations needed in the "Micro-Macro transition" box. If an important number of steps can be done between the phase of texture updating, the model described by Figure 6-33 is certainly more economical. So, a key point should be to find a criterion based on strain history to determine when a texture updating is necessary.

Other tracks can be studied to reduce CPU time of the coupling scheme on Figure 6-33. For instance, Hoferlin *et al.* 1999a and b prefer to use the yield locus in strain rate space instead of the one in stress space. They assume that the fact that this approach slows down the FEM code is compensated by a quicker identification of the shape of the yield locus from texture data. This choice should also increase accuracy.

As already summarized in the introduction (section 6.1), Cescotto, Munhoven, Radu and Habraken (MSM team) have chosen to use an incomplete yield locus, called "local yield locus zone", determined by only 5 or 6 calls to Taylor's model. This strongly reduces the time spent in the "Micro-Macro transition" box. Recall that, for the general case, 70300 Taylor's factors are computed in Figure 6-22. However, it increases the FEM computation time, because, sometimes during the simulation, the known part of the yield locus must be updated by means of additional calls to Taylor's model.

The implementation of the scheme on Figure 6-33 in the LAGAMINE environment is based on compatible software modules. So, if some day, one wants to replace Taylor's model by a self-consistent model, the rest of the coupling approach will not be modified.

The idea of a "local yield locus zone" and a long practice of the finite element discretization approach have first resulted in a discretized portion of the yield surface in stress space by hyperplanes. This discontinuous model introduces a lot of convergence difficulties and is now forgotten. It is however described in section 6.4.3 as it allows to identify the important properties of a local model description. The second approach, presented in section 6.4.4, gives entire satisfaction. It is rather

an interpolation scheme than a yield locus approach. However, such an interpolation is based on the existence of a yield locus in strain or stress space.

6.4.3. Hyperplane model

This model developed in 1996 and 1997 is described in reports of a Région Wallonne project (Habraken & Munhoven 1996, Radu *et al.* 1997, Habraken & Radu 1997). A lot of improvements have been implemented by Duchêne (Duchêne 1998a, b, c).

A. Principles

As in van Houtte's approach explained in section 6.3.4, this approach dissociates the shape and the size of the yield locus. The vector representation of deviatoric tensors described by (6-55) is applied and the same notations are adopted:

- \underline{s} vector form of $\underline{\hat{\sigma}}$, the deviatoric stress tensor, defined by its components s_p ,
- s size of the stress vector, computed by $\sqrt{s_p s_p}$,
- \underline{s}^* unit vector, direction of the stress vector, computed by \underline{s} / s .

Concerning the strain rate tensor $\underline{\dot{\epsilon}}^p$, the strain rate mode $\underline{U}_{\dot{\epsilon}^p} = \underline{\dot{\epsilon}}^p / \dot{\epsilon}_{eq}^p$ and its vector form \underline{u} or components u_p introduce scalar coefficients 3/2 in the formulation. So the unit vector form \underline{u}^* is preferred to describe the strain rate direction, with its components u_p^* .

The chosen definition of the yield function is very close to (6-69) but is slightly different. It is:

$$F_p = \frac{s}{\tau_c} Q(\underline{s}^*) - 1 = 0 \quad (6-75)$$

However here, no complete analytical function exists for $Q(\underline{s}^*)$, only a local discretization is available.

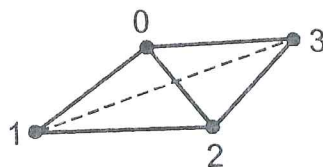


Figure 6-34 Approximation in 3 dimensional space X, Y, Z by 3 triangular facets of a surface described by a central point O and 3 neighbor points $1, 2, 3$ from Habraken & Munhoven 1996.

In three dimensions, triangular plane facets are the simplest discretization of complex surfaces. For instance, if a surface must be described around a central point 0 , three triangular facets $(0,1,2; 0,2,3; 0,1,3)$ defined on 3 neighbor points $1, 2, 3$ belonging also to the surface, approximate the surface. This is shown by Figure 6-34.

Each triangle can be described by the isoparametric concept recalled on Figure 6-35:

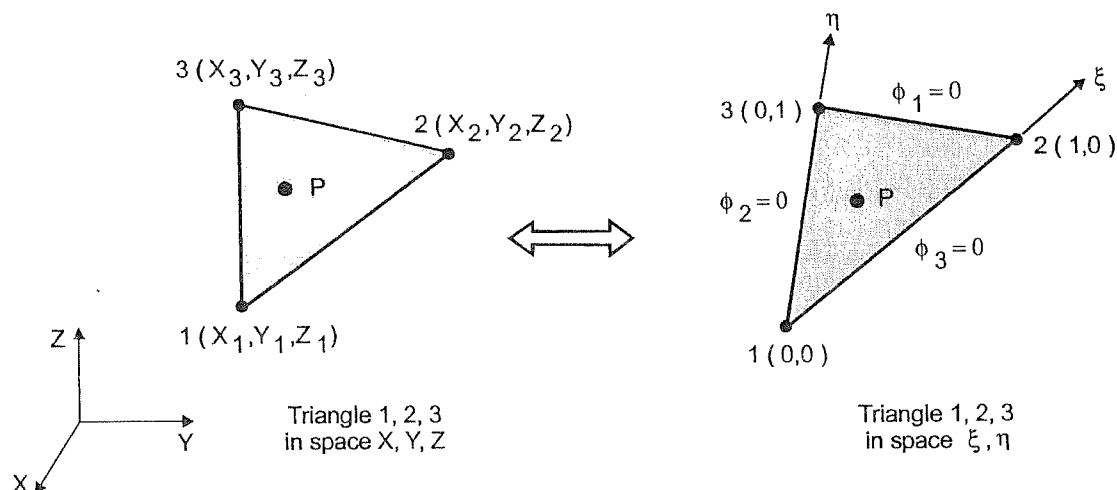


Figure 6-35 Concept of isoparametric triangle, adapted from Habraken and Munhoven 1996.

Each point P , defined by its coordinates X_P, Y_P, Z_P inside the triangle $1, 2, 3$, is associated with isoparametric coordinates ξ, η in the range $[0,1]$. These coordinates follow the relation:

$$\begin{Bmatrix} X_P \\ Y_P \\ Z_P \end{Bmatrix} = \sum_{i=1}^3 \Phi_i(\xi, \eta) \begin{Bmatrix} X_i \\ Y_i \\ Z_i \end{Bmatrix} \quad (6-76)$$

where interpolation functions are introduced:

$$\Phi_1 = 1 - \xi - \eta; \quad \Phi_2 = \xi; \quad \Phi_3 = \eta \quad (6-77)$$

The nodal points $1,2,3$ are characterized by isoparametric coordinates equal to 0 or 1, and the edges $12, 23, 31$ respectively correspond to $\Phi_3 = 0, \Phi_1 = 0, \Phi_2 = 0$.

The above concept, described in a three-dimensional space, is applied to the five-dimensional space related to the five components of the vector representation of deviatoric stress tensors. Six points belong to the stress yield locus: the central point 0 surrounded by five neighbors $1,2,3,4,5$. This local part of the yield locus is approximated by five hyperplane facets built on the central point and four neighbor points: $(0 1 2 3 4), (0 2 3 4 5), (0 1 3 4 5), (0 1 2 4 5), (0 1 2 3 5)$. The coordinates of

a point belonging to a hyperplane facet is computed by a relation analogous to (6-76):

$$s_p = \sum_{k=1}^5 \Phi_k s_p^{(k)} \text{ with } p=1,5 \quad (6-78)$$

where $s_p^{(k)}$ is the p^{th} component of the (stress) nodal point number k that determines the hyperplane facet. The interpolation functions are:

$$\begin{aligned} \Phi_1 &= 1 - \xi_1 - \xi_2 - \xi_3 - \xi_4 & \Phi_2 &= \xi_1 \\ \Phi_3 &= \xi_2 & \Phi_4 &= \xi_3 & \Phi_5 &= \xi_4 \end{aligned} \quad (6-79)$$

This approximation by hyperplane facets can only be accurate if the six points are quite close to each other. The five neighbor points must really surround the central point O . For instance, a good and a bad configuration are shown in three-dimensional space on Figure 6-36.

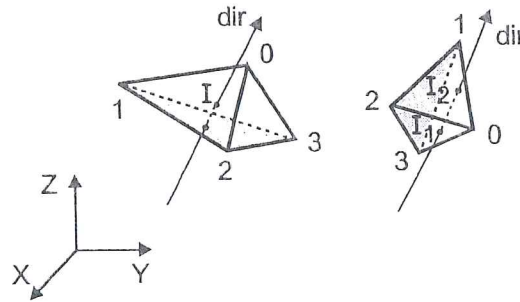


Figure 6-36 Disposition of surrounding points around central point in three-dimensional case, adapted from Radu *et al.* 1997.

Let dir define a direction for which the intersection I with the discretized surface is required. On the left of Figure 6-36, this direction first intersects the triangle 123 , which does not belong to the discretized surface but constitutes the base of the tetrahedral volume the other faces of which approximate the surface. Then, dir intersects only one triangle facet of the approximated surface and gives the requested point I . On the right of Figure 6-36, dir intersects 2 such facets and not the base triangle. The points I_1, I_2 are 2 potential solutions, which proves a bad approximation of the real surface.

So, transposed into the five-dimensional stress space, the set of five hyperplane facets built on the six points $0,1,2,3,4,5$ must give only one intersection in one direction $\underline{s}^* = \underline{s} / \bar{\tau}_c$. In practice, the following method allows to define six points, well distributed in stress space. The plastic strain rate direction \underline{u}^* associated with the central point O is assumed to be known. Let \underline{a} be a vector and \underline{v} its associate unit vector such as:

$$\underline{a} = (11111) \quad \underline{v} = \underline{a} / \sqrt{a_i a_i} \quad (6-80)$$

The perturbed vectors $\underline{a}^{(i)}$ and $\underline{v}^{(i)}$ are computed by:

$$\begin{aligned}\underline{a}^{(1)} &= \underline{v} + \beta(10000) \\ \underline{a}^{(2)} &= \underline{v} + \beta(01000) \\ \underline{a}^{(3)} &= \underline{v} + \beta(00100) \\ \underline{a}^{(4)} &= \underline{v} + \beta(00010) \\ \underline{a}^{(5)} &= \underline{v} + \beta(00001)\end{aligned}\quad (6-81)$$

$$\underline{v}^{(i)} = \underline{a}^{(i)} / \sqrt{a_p^{(i)} a_p^{(i)}} \quad \text{with no summation on } (i) \quad (6-82)$$

with β a parameter to be defined. Somehow it is a measure of the size of the local yield locus zone. Let \underline{R} be the rotation matrix linking the plastic strain rate direction \underline{u}^* and vector \underline{v} :

$$\underline{u}^* = \underline{R} \underline{v} \quad (6-83)$$

This matrix is used to find $\underline{u}^{*(i)}$:

$$\underline{u}^{*(i)} = \underline{R} \underline{v}^{(i)} \quad i = 1,5 \quad (6-84)$$

which constitute five perturbations of \underline{u}^* . Then, Taylor's module, described on Figure 6-28, computes the stress points associated with \underline{u}^* and its five perturbations $\underline{u}^{*(i)}$.

According to the idea of an associate plasticity model, using five hyperplane facets to approximate the yield locus should give five discrete values for the associate normals or plastic strain rate but undetermined normals at the hyperplane intersections. To try to increase the accuracy of the model and to prevent indetermination, it was decided to interpolate the normals separately. So, the hyperplane model is a non associate plasticity model. This aspect of the computation is now described. At a given instant of the FEM computation, for example during an equilibrium iteration, the local yield locus zone is known and one has to search its intersection with a stress direction dir , hopefully close to \underline{s}^* (the stress direction corresponding to point 0). If no intersection is found, this means that the local yield locus zone is not correctly located and a new one has to be computed.

If the intersection is found, $\xi_1^*, \xi_2^*, \xi_3^*, \xi_4^*$ are its isoparametric coordinates. They identify the scaled yield stress in direction dir . The associated normal $\underline{u}^{interpolated}$ is computed by:

$$\underline{u}_p^{interpolated} = \sum_{k=1}^5 \Phi_k(\xi_1^*, \xi_2^*, \xi_3^*, \xi_4^*)(\underline{u}_p)_k \quad \text{with } p = 1, \dots, 5 \quad (6-85)$$

where $(u_p)_k$ is the p^{th} component of the strain rate direction associated with the five nodal points, k identifies the five points determining the hyperplane facet in which the intersection has been found. Four strain rate directions correspond to the $\underline{u}^{(i)}$, resulting of the perturbation process described above and one to the central strain rate direction \underline{u}^* . The corresponding unit vector $\underline{u}^{interpolated}$ is then calculated since relation (6-85) does not produce a unit vector. Figure 6-37 shows, in a two-dimensional space, all the directions of “normals” to the stress yield locus. It is assumed that $\underline{u}^{interpolated}$ is a better approximation of the true strain rate direction \underline{u}^{true} than $\underline{u}^{hyperplane}$.

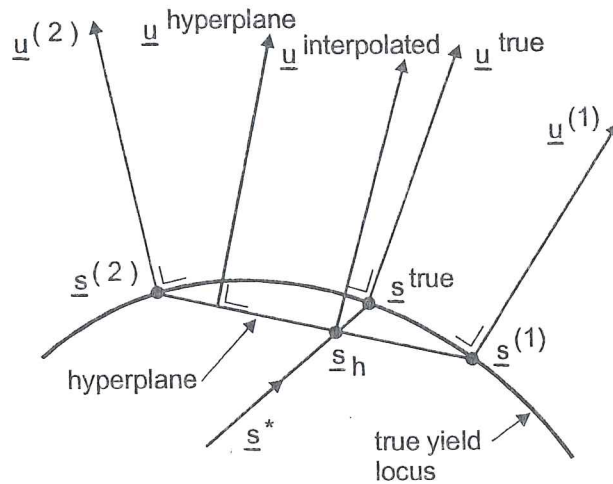


Figure 6-37 Normals to the stress yield locus, adapted from Habraken & Munhoven 1996.

The above description defines the hyperplane model except for the hardening evolution (factor τ) since only scaled values have so far been treated. The simple isotropic hardening approach proposed by Winters 1996 and already described in 6.3.4 is applied. Radu *et al.* 1997 and Habraken & Radu 1997 give all the details on the hyperplane approach.

The implementation in LAGAMINE of this constitutive law requires of course an integration scheme. Three different integration schemes were tested (Duchêne 1998a, Duchêne 1998c, Duchêne *et al.* 1999a). The first one is an application of the tangent cutting plane algorithm (Simo & Ortiz 1985). This procedure, already implemented by Li 1996 in LAGAMINE for the integration of Hill's constitutive law, can be visualized by Figure 6-38.

Its application to the hyperplane model introduces two iterative loops as summarized by the flowchart on Figure 6-39.

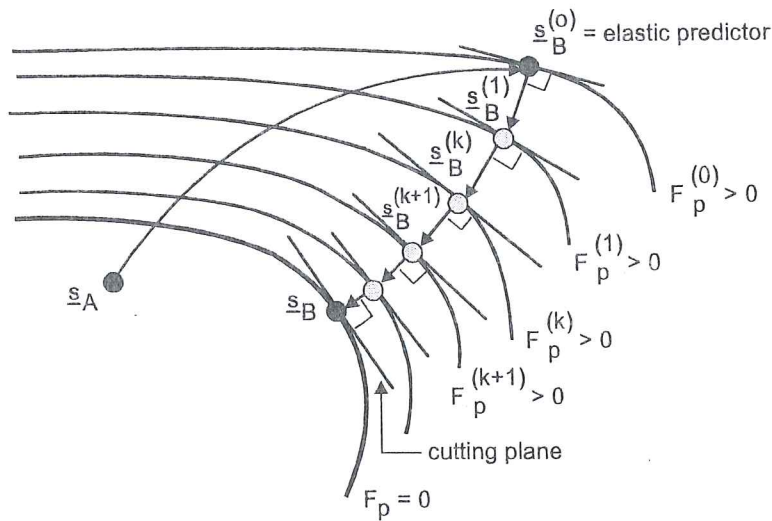


Figure 6-38 Tangent cutting plane algorithm, \underline{s}_A stress at the step start, \underline{s}_B stress at the step end (from Li 1996).

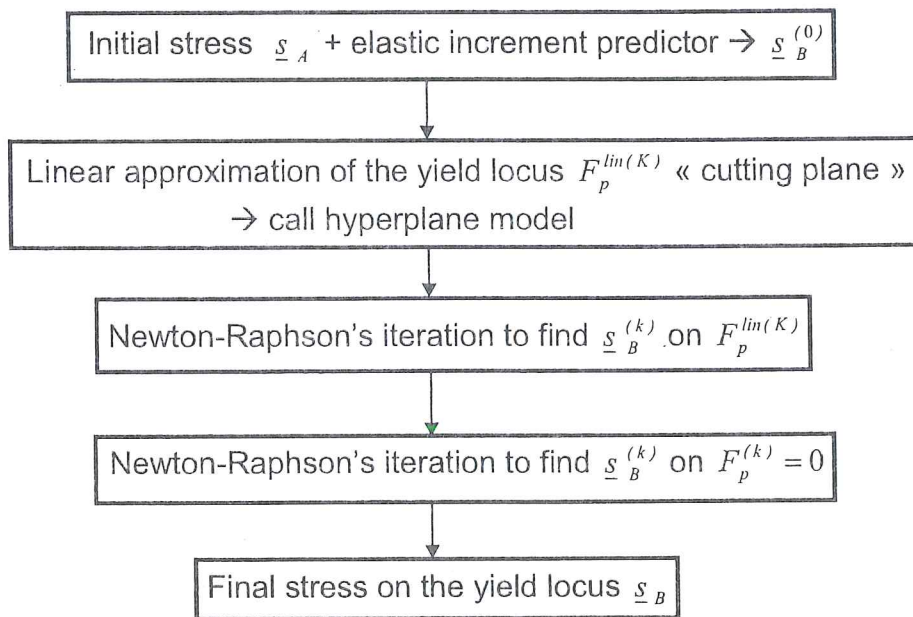


Figure 6-39 Flow chart of cutting plane algorithm (from slides used for Duchêne *et al.* 1999a's presentation).

The details can be found in Habraken & Munhoven 1996. This first scheme is quite expensive in CPU time. So, Duchêne 1998a has proposed a second integration scheme where only one iteration loop appears. Its principle is visualized in Figure 6-40, and Figure 6-41.

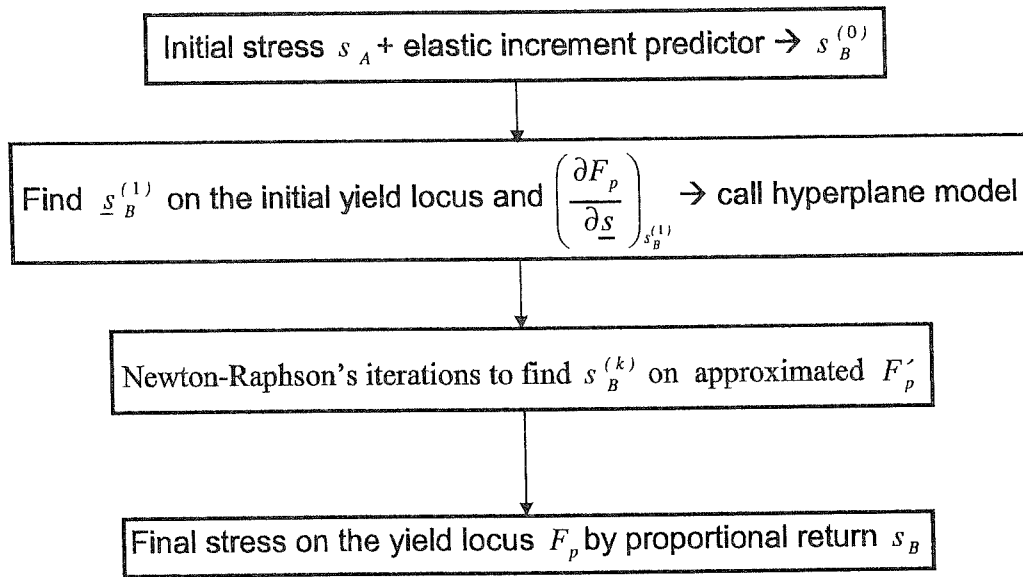


Figure 6-40 Flowchart of Duchêne's integration scheme (from slides used for Duchêne *et al.* 1999a's presentation).

The exact stress \underline{s}_B^{true} is located on the real yield locus updated by hardening. It differs slightly from the final stress \underline{s}_B provided by Duchêne's scheme. An improved solution could be reached by performing a radial return along the normal associated to \underline{s}_B . However, as this new iteration loop slows down the integration scheme, it has not been implemented.

Sometimes, the initial elastic trial can be very far from the initial yield stress at the step beginning and also very far from the final stress at the step end. In this case, the local yield locus zone must be updated a few times during the integration scheme to cover the interesting part of the yield locus. So, we decided to use an elasto-plastic predictor (Figure 6-41) to increase the life time of one set of hyperplanes.

The matrix used to compute the elasto-plastic predictor comes from the preceding converged step. This requires its storage or its computation. So, even if the scheme seems very simple, this method is not so direct.

These 3 integration schemes have been compared thanks to FEM simulations modeling a simple tensile test with one finite element. It appears (Duchêne *et al.* 1999a) that the elasto-plastic predictor scheme provides the best accuracy, convergence rate and lowest CPU time. It reduces the number of updates of the yield locus zones. Concerning CPU time, Duchêne's scheme comes in second position and provides the same accuracy as the other elastic predictor scheme (Li 1996). The size of hyperplane approximation has also been investigated. It is characterized by the scalar β (relation 6-81) or by the angle θ between the $\underline{u}^{(i)}$ directions, with

$\cos \theta = \underline{u}^* \cdot \underline{u}^{*(j)}$. This is a key parameter for both accuracy and CPU time. The smallest size gives the highest accuracy but also high CPU time. Table 6-2 shows the CPU time comparison with the time unit set to 1 for the fastest case.

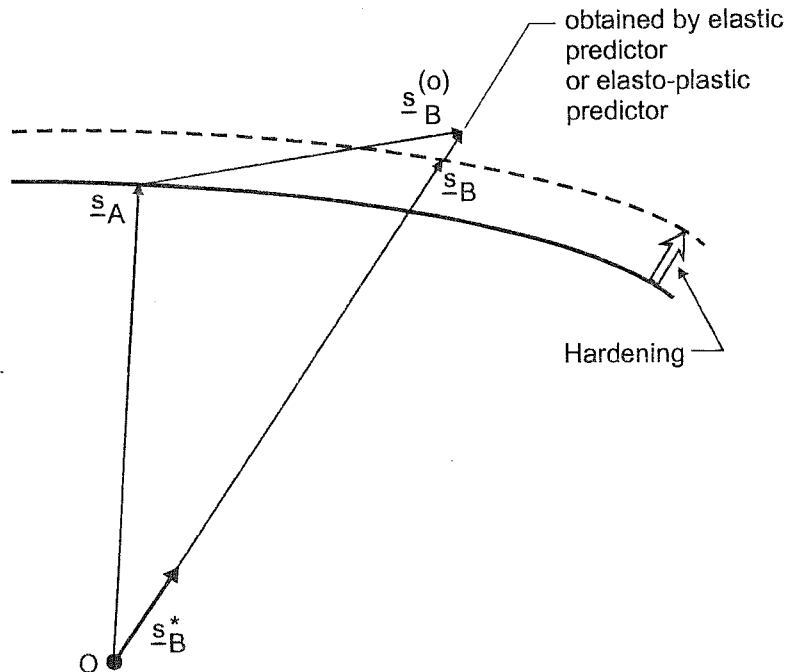


Figure 6-41 Schematic view of plastic predictor scheme (from slides used for Duchêne *et al.* 1999a's presentation).

Angle θ	1°	5°	10°	20°	30°
First method (elastic predictor 1)	-	98.9	1.40	1.27	1.15
Second method (elastic predictor 2)	-	89.8	1.34	1.22	1.05
Third method (plastic predictor)	1.92	1.15	1.14	1.01	1

Table 6-2 Comparison of the CPU time for tensile tests (from Duchêne *et al.* 1999a).

Eight different strain rate tensors, modeling situations more complex than uniaxial tension have been computed by "one finite element" simulations (Duchêne 1998c). It appears from these more complex strain states, that the elasto-plastic predictor scheme yields poor accuracy. It updates the local yield locus zone more often than the elastic predictor scheme proposed by Duchêne.

A tensile test of a plane sheet with a hole has also been simulated by 766 finite elements. The results confirm that elastic prediction of Duchêne's scheme is a better choice.

B. Stiffness matrix

The implicit finite element approach of the LAGAMINE code requires a global tangent stiffness matrix assembled from the local tangent stiffness matrices associated with each finite element. So, at each interpolation point, the \underline{C}^{ep} matrix linking the stress increment to the strain increment is necessary. Different evaluations (Li 1996) are possible:

- classical tangent matrix, which is directly obtained from the continuum rate constitutive equation:

$$\underline{\sigma}^{\nabla} = \underline{C}^{ep} \underline{\dot{\epsilon}} \quad (6-86)$$

- consistent tangent matrix, which is computed by consistent linearization of the integration scheme;
- numerical tangent matrix, which is evaluated by numerical perturbations. The stress at the end of the time step is first computed for the actual strain increment ($\dot{\epsilon} \Delta t$). Then, one at a time, each strain rate component is perturbed and the integration scheme provides a new perturbed stress. The difference between perturbed stress and actual stress, divided by the strain perturbation, yields one column of the tangent matrix.

These 3 approaches (Duchêne 1998a) have been implemented. The consistent tangent matrix is known to preserve the quadratic convergence of the global iteration scheme. However in the performed simulations, it does not clearly provide a better convergence than the classical tangent matrix. As the approximation of the tangent matrix by the numerical tangent matrix induces a higher convergence rate, it suggests that our linearization approach should be refined. The numerical tangent matrix suffers from two main drawbacks: the influence of the numerical perturbation amplitude and the CPU time required to compute it.

C. Yield locus section

The influence of the size of the local yield locus zone can be visualized as follows. The modules computing the stress are called for successive stress directions determining the π section of the yield locus.

Figure 6-42 results from different choices of hyperplane sizes, defined by angle θ . The parameter β , or its associated angle θ , strongly modifies the yield locus approximation and the number of necessary updates of the hyperplane approximation to cover a whole π section. One can verify on this figure that large hyperplane facets underestimate the yield stress and create very strong discontinuities when the local approximation of the yield locus is updated. From this figure and the convergence of different simulations, the size corresponding to 5° or 10° should be adopted.

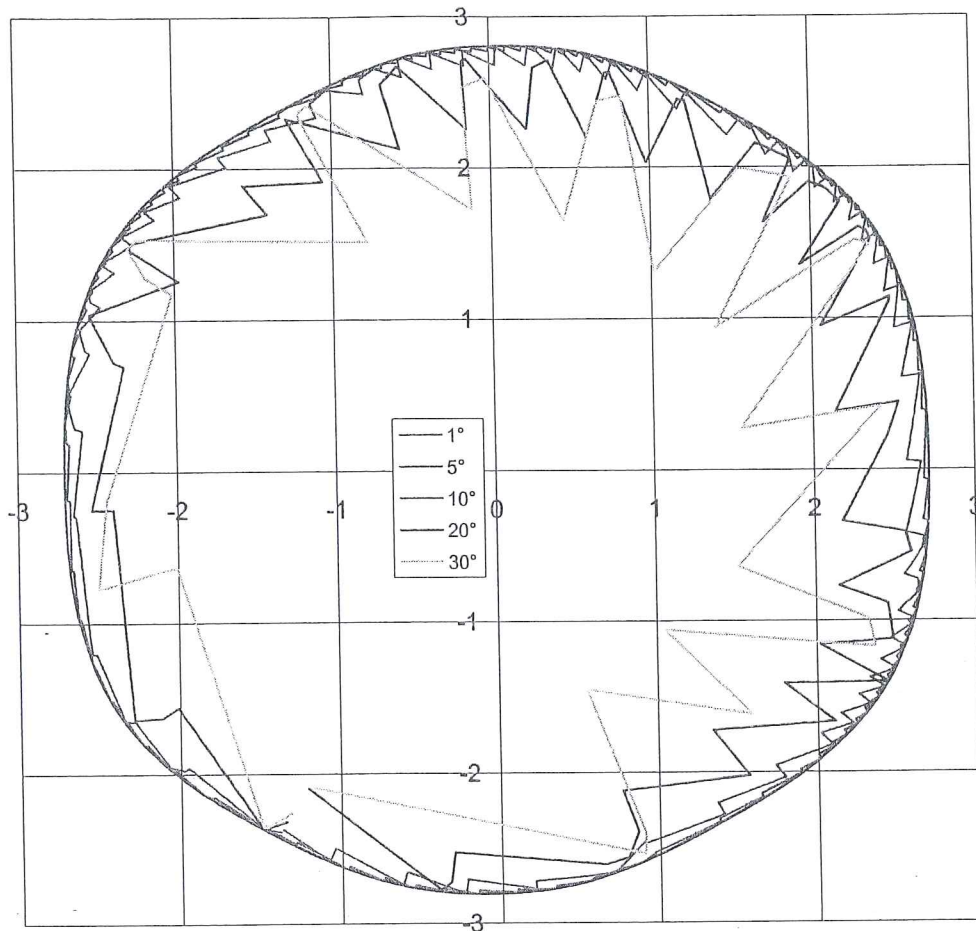


Figure 6-42 π section of the yield locus for different hyperplane sizes, SPXI steel sheet (from Duchêne *et al.* 1999c).

D. Conclusion

This local yield locus approach suffers from strong discontinuities that explain the convergence problems happening in finite element simulations with a large number of finite elements. It has been dropped in favor of a new method, more continuous, directly inspired from the investigations required to develop the hyperplane approach.

6.4.4. Interpolation approach

Developed thanks to a close cooperation of Godinas, Duchêne and Habraken, this method appears more stable and less expensive in CPU time than the hyperplane approach. Duchêne's Ph.D thesis, which should come to an end during 2001, will present numerous comparisons between deep drawing experiments, FEM simulations with and without texture updating and FLD predictions.

This method has already been described in Duchêne's master (Duchêne 2000). Its summary and some results have been published in ICOTOM, NUMISHEET, and ESAFORM proceedings (Duchêne *et al.* 1999b and c, 2000, 2001). Theory and applications are recalled here to give the reader a complete overview of the performed work. The text is adapted to the notations and principles introduced in previous chapters.

A. Local description of a scaled yield locus

The shape of the yield locus is our present goal. The size of the yield locus is defined by a simple hardening law, as already proposed by Winters 1996. The method proposed hereafter is more an interpolation approach than a local representation of a scaled yield locus. A "function" locally describing the plastic surface is not developed. Nevertheless, this interpolation method assumes the existence of a yield locus.

Keeping the notations of the previous sections, let \underline{s}^{*0} be a unit stress vector, corresponding to the direction of the central point of the local yield locus zone. $\underline{s}^{*(i)}$ are $N(=5)$ unit stress vectors surrounding \underline{s}^{*0} and determining the interpolation domain. They will be called the "domain limit vectors." In practice, the approach has been developed for a N dimensional space but it is directly applied to the five dimensional case as the goal is to define a local yield locus zone in deviatoric stress or strain rate space. Hereafter, the notation choice is adapted to stress space but the whole approach can be transposed to strain rate space. The six or $(N+1)$ vectors (five $\underline{s}^{*(i)}$ and one \underline{s}^{*0}) have the following properties:

-they are unit vectors:

$$\underline{s}^{*(i)} \cdot \underline{s}^{*(i)} = 1 \quad \text{and} \quad \underline{s}^{*0} \cdot \underline{s}^{*0} = 1 \quad (6-87)$$

-there is a common angle between all $\underline{s}^{*(i)}$:

$$\underline{s}^{*(i)} \cdot \underline{s}^{*(j)} = 1 + \beta^2 (\delta_{ij} - 1) \quad \text{with } i, j = 1, \dots, N \quad (6-88)$$

-there is a common angle between each $\underline{s}^{*(i)}$ and \underline{s}^{*0} :

$$\underline{s}^{*0} \cdot \underline{s}^{*(i)} = \cos \theta \quad \text{with } i = 1, \dots, N \quad (6-89)$$

-they determine a regular domain.

These choices induce that \underline{s}^{*0} , the central direction, can be computed as a scaled average of the five (N) limit vectors $\underline{s}^{*(i)}$:

$$\underline{s}^{*0} = \frac{1}{\cos \theta} \sum_{i=1}^N \underline{s}^{*(i)} \quad (6-90)$$

Both the angle θ and the parameter β determine the size of the interpolation domain. They are linked by the relation:

$$\beta^2 = \frac{N}{N-1} \sin^2 \theta \quad (6-91)$$

As the N $\underline{s}^{*(i)}$ vectors are linearly independent, they constitute a vector basis for the N -dimensional space. However, as they are not orthogonal, it is interesting to introduce N new vectors $\underline{ss}^{(i)}$ with the following orthogonal property:

$$\underline{ss}^{(i)} \cdot \underline{s}^{*(j)} = \delta_{ij} \quad (6-92)$$

These vectors are called "contravariant vectors". Relation (6-87) implies that they are not unit vectors and one can verify that they depend linearly on vectors $\underline{s}^{*(i)}$ and \underline{s}^* :

$$\underline{ss}^{(i)} = \frac{1}{\beta^2} \left(\underline{s}^{*(i)} - \frac{1-\beta^2}{\cos \theta} \underline{s}^{*0} \right) \quad (6-93)$$

The N η coordinates representing any vector \underline{v} in the $\underline{s}^{*(i)}$ vector basis:

$$\underline{v} = \sum_{i=1}^N \eta_i \underline{s}^{*(i)} \quad (6-94)$$

are determined thanks to the N $\underline{ss}^{(i)}$ vectors:

$$\underline{v} \cdot \underline{ss}^{(j)} = \sum_{i=1}^N \eta_i \underline{s}^{*(i)} \cdot \underline{ss}^{(j)} = \sum_{i=1}^N \eta_i \delta_{ij} = \eta_j \quad (6-95)$$

These N η coordinates are independent of each other. They determine both the length and the direction of vector \underline{v} . It is important to note that, for a unit vector \underline{v} equal to a domain limit vector $\underline{s}^{*(i)}$, the $\eta_j^{(i)}$ coordinates are:

$$\eta_j^{(i)} = \delta_{ij} \quad \text{with } j = 1, \dots, N \quad (6-96)$$

These vectors represent the domain vertices. Each of the N limit boundaries (or edges) of the interpolation domain correspond to a function such that:

$$\eta_i = 0 \quad (6-97)$$

In fact, the properties associated with isoparametric interpolations already recalled on Figure 6-35 are retrieved but extrapolated to N -dimensions. The above choices imply that any point belonging to the interpolation domain is associated with positive η coordinates.

A practical way to determine the 5 domain limit vectors $\underline{s}^{*(i)}$ is identical to the procedure described by 6-80 to 6-84. A particular central direction \underline{s}^{*0} is chosen in such a way that its N components are identical. To obtain associated domain limit vectors $\underline{s}^{*(i)}$, one successively computes a linear relation between the central direction and each vector of the Cartesian basis $\underline{e}^{(i)}$:

$$\underline{s}^{*(i)} = \alpha' \underline{s}^{*0} + \beta \underline{e}^{(i)} = \alpha' \underbrace{\frac{1}{\sqrt{N}}}_{=\alpha} \begin{pmatrix} 1 \\ 1 \\ 1 \\ 1 \\ 1 \end{pmatrix} + \beta \begin{pmatrix} 0 \\ \vdots \\ 1 \\ \vdots \\ 0 \end{pmatrix} \quad (6-98)$$

Using the conditions that $\underline{s}^{*(i)}$ and \underline{s}^{*0} must be unit vectors and relation (6-89), one obtains:

$$\alpha = \frac{\cos \theta}{\sqrt{N}} - \frac{\sin \theta}{\sqrt{N \cdot (N-1)}} \quad \text{and} \quad \beta^2 = \frac{N}{N-1} \sin^2 \theta \quad (6-99)$$

Then the rotation linking the actual required central point \underline{s}^{*0} and the particular one \underline{s}^{*0} is computed by:

$$\underline{R} = \underline{I} + 2 \underline{s}^{*0} \otimes \underline{s}^{*0} - \frac{(\underline{s}^{*0} + \underline{s}^{*0}) \otimes (\underline{s}^{*0} + \underline{s}^{*0})}{I + \underline{s}^{*0} \cdot \underline{s}^{*0}} \quad (6-100)$$

where \underline{I} is the second order unit tensor. This rotation applies \underline{s}^{*0} onto the real central vector \underline{s}^{*0} :

$$\underline{R} \cdot \underline{s}^{*0} = \underline{s}^{*0} \quad (6-101)$$

It also provides the domain limit vectors:

$$\underline{R} \cdot \underline{s}^{*(i)} = \underline{s}^{*(i)} \quad (6-102)$$

If \underline{s}^{*0} and \underline{s}^{*0} are opposite vectors, equation (6-100) is not valid; the domain limit vectors $\underline{s}^{*(i)}$ can be computed as the opposite of the $\underline{s}^{*(i)}$.

This interpolation domain is called a regular one because the angles between the domain limit vectors are identical (6-89) and the domain limit vectors are unit vectors. However, it is possible to define interpolation domains based on limit vectors that are non-uniformly located and are non unit vectors provided they are

linearly independent. With such non-regular domains, the η coordinates are still available and require the definition of \underline{ss}^i vectors (see relations 6-90, 6-92, 6-95).

The above considerations are sufficient to understand the interpolation approach finally implemented in the LAGAMINE code. However, it is interesting to note that further details and properties of such parameterization of a N dimensional space were investigated by Godinas 1998 and Duchêne 2000. They study different interpolation methods: linear interpolation in Cartesian coordinates or hyperplane model, linear interpolation in spherical coordinates, approach enriched by bubble mode...

Now, consider both five dimensional stress and strain rate spaces. A regular domain is built in strain rate space. It is defined by its five vertices $\underline{u}^{*(i)}$ (unit vectors). Thanks to five calls to Taylor's module (Figure 6-38), the associated stress vectors $\underline{s}^{(i)}$ can be defined. At this level, no hardening is assumed, so only a scaled yield locus is determined. These five stress vectors define a non-regular domain in stress space. In each space, the concept of contravariant vectors, from relation (6-92), is applied:

$$\underline{uu}^{(i)} \cdot \underline{u}^{*(j)} = \delta_{ij} \quad (6-103)$$

$$\underline{ss}^{(i)} \cdot \underline{s}^{(j)} = \delta_{ij} \quad (6-104)$$

The contravariant vectors $\underline{ss}^{(i)}$ and $\underline{ss}'^{(i)}$, respectively computed by (6-104) and (6-92), differ only because in (6-92) unit stress directions $\underline{s}^{*(i)}$ are used. Here the length of the stress vectors $\underline{s}^{(j)}$ is an important characteristic as it defines the yield locus anisotropy. These contravariant vectors $\underline{ss}'^{(i)}$ and $\underline{uu}^{(i)}$ give in each space, the η coordinates associated with any stress \underline{s} or unit strain rate \underline{u}^* :

$$\eta_i = \underline{uu}^{(i)} \cdot \underline{u}^* \quad (6-105)$$

$$\eta_i = \underline{ss}'^{(i)} \cdot \underline{s} \quad (6-106)$$

So any stress vector \underline{s} or strain rate direction \underline{u}^* can be represented according to the vector basis of their space and the η coordinates:

$$\underline{u}^* = \sum_{i=1}^5 \eta_i \underline{u}^{*(i)} \quad (6-107)$$

$$\underline{s} = \sum_{i=1}^5 \eta_i \underline{s}^{(i)} \quad (6-108)$$

Physically, a material state corresponds to a stress point and a strain rate direction. In a yield locus formulation, a point on the locus and its normal define both stress and

associated strain rate. Here, two interpolation domains are defined; they are physically linked because Taylor's model computes their domain limit vectors. Due to this close link between the two spaces, it is assumed that the η coordinates computed by (6-105) and (6-106) are equal when the stress \underline{s} and the strain rate direction \underline{u}^* are physically associated. This property is exactly fulfilled for the domain limit vectors. The stress $\underline{s}^{(i)}$ corresponds to the strain rate direction $\underline{u}^{*(i)}$ and their η coordinates are $\eta_i = 1$ and $\eta_j = 0 (i \neq j)$ in both spaces. Inside the domain, this property is extended by convenience. It is an assumption. The so-called interpolation approach directly derives from this hypothesis of equality and from relations (6-108) and (6-105). They provide the interpolation relation:

$$\underline{s} = \sum_{i=1}^5 (\underline{uu}^{(i)} \cdot \underline{u}^*) \underline{s}^{(i)} = \underline{uu}^{(i)} \otimes \underline{s}^{(i)} \cdot \underline{u}^* = \underline{C} \cdot \underline{u}^* \quad (6-109)$$

For each domain, the \underline{C} matrix is computed only once from the stress domain limit vectors $\underline{s}^{(i)}$ and the contravariant vectors $\underline{uu}^{(i)}$ associated with the 5 strain rate vertices $\underline{u}^{*(i)}$. Inside a domain, relation (6-109) provides the stress state if the strain rate direction is given. The η coordinates computed by relation (6-105) control the domain validity. If their values do not belong to the interval $[0,1]$, then a new local yield locus zone is required.

B. Updating of the scaled yield locus description

When the available local description of the scaled yield locus does not cover the interesting zone anymore, one has to find another local description enclosing the interesting part of the yield locus. Of course, the procedure described in previous section could be repeated using a new strain rate direction \underline{u}^* as central point. However, this would provide a new local description forgetting the previous information and the discontinuities observed with the hyperplane approach would appear again. Looking at the η coordinate that does not belong to $[0,1]$ anymore, one can identify the boundary that is not respected by the new explored direction. This boundary is identified by $N-1$ (4) domain limit vectors and can belong to two regular domains. A 3 dimensional analogy represented on Figure 6-43 helps to understand.

The two neighboring domains defined by their common boundary require only one additional domain limit vector to be completely defined. So, only one new vertex must be computed by Taylor's model to identify the neighboring domain that probably contains the new explored strain rate direction. This is the option adopted in the LAGAMINE code.

associated strain rate. Here, two interpolation domains are defined; they are physically linked because Taylor's model computes their domain limit vectors. Due to this close link between the two spaces, it is assumed that the η coordinates computed by (6-105) and (6-106) are equal when the stress \underline{s} and the strain rate direction \underline{u}^* are physically associated. This property is exactly fulfilled for the domain limit vectors. The stress $\underline{s}^{(i)}$ corresponds to the strain rate direction $\underline{u}^{*(i)}$ and their η coordinates are $\eta_i = 1$ and $\eta_j = 0 (i \neq j)$ in both spaces. Inside the domain, this property is extended by convenience. It is an assumption. The so-called interpolation approach directly derives from this hypothesis of equality and from relations (6-108) and (6-105). They provide the interpolation relation:

$$\underline{s} = \sum_{i=1}^5 (\underline{uu}^{(i)} \cdot \underline{u}^*) \underline{s}^{(i)} = \underline{uu}^{(i)} \otimes \underline{s}^{(i)} \cdot \underline{u}^* = \underline{C} \cdot \underline{u}^* \quad (6-109)$$

For each domain, the \underline{C} matrix is computed only once from the stress domain limit vectors $\underline{s}^{(i)}$ and the contravariant vectors $\underline{uu}^{(i)}$ associated with the 5 strain rate vertices $\underline{u}^{*(i)}$. Inside a domain, relation (6-109) provides the stress state if the strain rate direction is given. The η coordinates computed by relation (6-105) control the domain validity. If their values do not belong to the interval $[0,1]$, then a new local yield locus zone is required.

B. Updating of the scaled yield locus description

When the available local description of the scaled yield locus does not cover the interesting zone anymore, one has to find another local description enclosing the interesting part of the yield locus. Of course, the procedure described in previous section could be repeated using a new strain rate direction \underline{u}^* as central point. However, this would provide a new local description forgetting the previous information and the discontinuities observed with the hyperplane approach would appear again. Looking at the η coordinate that does not belong to $[0,1]$ anymore, one can identify the boundary that is not respected by the new explored direction. This boundary is identified by $N-1$ (4) domain limit vectors and can belong to two regular domains. A 3 dimensional analogy represented on Figure 6-43 helps to understand.

The two neighboring domains defined by their common boundary require only one additional domain limit vector to be completely defined. So, only one new vertex must be computed by Taylor's model to identify the neighboring domain that probably contains the new explored strain rate direction. This is the option adopted in the LAGAMINE code.

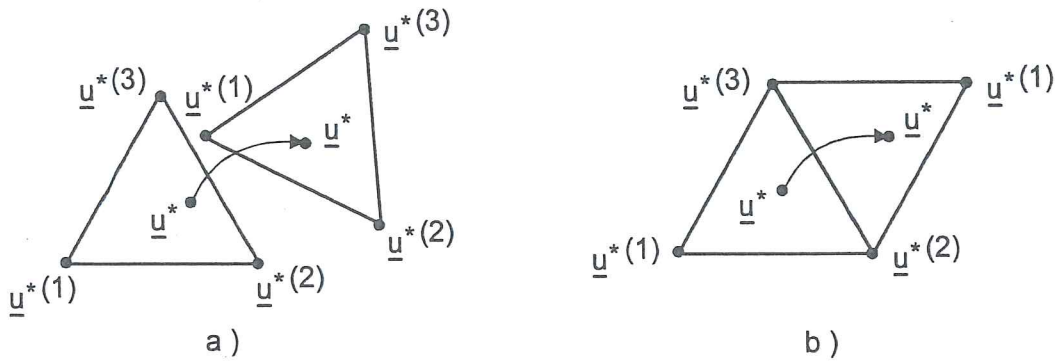


Figure 6-43 Updating of the local description
 a) Completely new local description b) Neighborhood domain,
 (from Duchêne 2000).

C. Integration scheme

The stress-strain interpolation relation (6-109) does not use the concept of yield locus in a classical way. So, a specific integration scheme has been developed. At this level, the actual stress and not the scaled one is aimed at, so the size and the shape of the yield locus cannot be dissociated anymore. As relation (6-109) expresses the shape and is assumed to model a reference level of hardening, an additional factor τ is introduced to represent hardening:

$$\underline{s} = \tau \underline{C} \cdot \underline{u}^* \quad (6-110)$$

It plays the same role as the hardening factor $\bar{\tau}_c$ in (6-57b) and is simply linked to the total polycrystal slip Γ by a Swift's law:

$$\tau = K(\Gamma_0 + \Gamma)^n \quad (6-111)$$

As in Winters 1996, this micro-macro hardening law is identified by a tensile uniaxial macroscopic test and the first term of relation (4-40) (see the summary of this approach in section 6.3.4.).

Relation (6-110) assumes plastic loading. Writing this equation at the step beginning, identified by subscript A, and at the step end, identified by subscript B, subtracting these two relations and neglecting higher order terms yields the incremental form:

$$d\underline{s} = \underline{C} \cdot (d\tau \underline{u}_A^* + \tau_A d\underline{u}^*) \quad (6-112)$$

with $d\underline{s} = \underline{s}_B - \underline{s}_A$; $d\tau = \tau_B - \tau_A$ and $d\underline{u}^* = \underline{u}_B^* - \underline{u}_A^*$.

During such a time step, Hooke's law links the stress and the elastic strain increments:

$$d\underline{s} = \underline{C}^e \cdot (d\underline{\varepsilon}^{tot} - d\underline{\varepsilon}^p) = \underline{C}^e \cdot (d\underline{\varepsilon}^{tot} - \dot{\varepsilon}_{eq}^p dt \underline{u}_A^*) \quad (6-113)$$

where it has been assumed that, during this time step, the direction of the strain rate \underline{u}_A^* tensor is not modified. This assumption induces an approximation on the final tangent stiffness matrix provided by following considerations.

Because \underline{u}_A^* and \underline{u}_B^* are unit vectors, one can find that:

$$d\underline{u}_A^* \cdot \underline{u}_A^* = 0 \quad (6-114)$$

Using (6-112) to (6-114), one can obtain :

$$d\tau = \underline{u}_A^* \cdot \underline{C}^{-1} \cdot \underline{C}^e \cdot d\underline{\varepsilon}^{tot} - \underline{u}_A^* \cdot \underline{C}^{-1} \cdot \underline{C}^e \cdot \underline{u}_A^* \dot{\varepsilon}_{eq}^p dt \quad (6-115)$$

The time derivative of relation (6-111) and the micro-macro relation established between the total polycrystal slip and the plastic strain (4-39) give:

$$d\tau = \frac{n\tau_A}{(\Gamma_0 + \Gamma_A)} \overline{M} \dot{\varepsilon}_{eq}^p dt \quad (6-116)$$

Both relations (6-115) and (6-116) allow to find an expression for $\dot{\varepsilon}_{eq}^p dt$:

$$\dot{\varepsilon}_{eq}^p dt = \frac{\underline{b} \cdot \underline{C}^e \cdot d\underline{\varepsilon}^{tot}}{\underline{a} \cdot \underline{b} + \frac{n\tau_A}{\Gamma_0 + \Gamma_A} \overline{M}} \quad (6-117)$$

with $\underline{a} = \underline{C}^e \cdot \underline{u}_A^*$ and $\underline{b} = \underline{u}_A^* \cdot \underline{C}^{-1}$.

Relation (6-117), introduced in equation (6-113), provides an estimation of \underline{C}^{tan} , the tangent operator:

$$d\underline{s} = \left(\underline{C}^e - \frac{\underline{a} \cdot \underline{b} \underline{C}^e}{\underline{a} \cdot \underline{b} + \frac{n\tau_A}{\Gamma_0 + \Gamma_A} \overline{M}} \right) \cdot d\underline{\varepsilon}^{tot} = \underline{C}^{tan} \cdot d\underline{\varepsilon}^{tot} \quad (6-118)$$

If an explicit integration scheme is chosen, \underline{s}_B , the deviatoric stress at the step end, is directly computed by (6-118) and a Jaumann correction because of large deformation context:

$$\underline{s}_B = (\underline{I} + \underline{\Omega}) \cdot \underline{s}_A + \underline{C}^{tan} \cdot \Delta\underline{\varepsilon}^{tot} \quad (6-119)$$

The hardening is also computed by an explicit formulation:

$$\tau_B = \tau_A + \frac{n\tau_A}{(\Gamma_0 + \Gamma_A)} \overline{M} \Delta\varepsilon_{eq}^p \quad (6-120)$$

This rather simple formulation yields poor accuracy unless very small time steps or large number of subintervals are used. Adding a radial return slightly improves this

simple scheme. In this case, relation (6-119) computes $\underline{s}_{B\text{trial}}$, a trial stress. Then, it is corrected in order to return on the yield locus approximation:

$$\underline{s}_B = k \underline{s}_{B\text{trial}} \quad (6-121)$$

The strain rate direction \underline{u}_B^* associated by (6-110) to this trial stress direction is assumed to be correct:

$$\underline{u}_B^* = \underline{C}^{-1} \cdot \underline{s}_{B\text{trial}} \frac{k}{\tau_B} \quad (6-122)$$

To respect the interpolation method, \underline{u}_B^* must be a unit vector. One can compute k in order to respect this condition:

$$\underline{u}_B^* \cdot \underline{u}_B^* = 1 \Rightarrow k = \frac{\tau_B}{\sqrt{\underline{b}_{\text{trial}} \cdot \underline{b}_{\text{trial}}}} \quad (6-123)$$

with $\underline{b}_{\text{trial}} = \underline{C}^{-1} \cdot \underline{s}_{B\text{trial}}$.

Finally, in order to allow large time steps while retaining accuracy, an implicit scheme has been implemented in the LAGAMINE code. The stress at the step end is computed by:

$$\underline{s}_B = (\underline{I} + \underline{\Omega}) \cdot \underline{s}_A + \underline{C}^e \cdot (\Delta \underline{\varepsilon}^{\text{tot}} - \Delta \underline{\varepsilon}^p) \quad (6-124)$$

The plastic strain increment during the step is decomposed into its length $\Delta \varepsilon_{eq}^p$ and its direction, which is classically computed by a linear interpolation between the initial direction \underline{u}_A^* and the final direction \underline{u}_B^* :

$$\Delta \underline{\varepsilon}^p = \Delta \varepsilon_{eq}^p k \left((1 - \theta) \underline{u}_A^* + \theta \underline{u}_B^* \right) \quad (6-125)$$

with $0 \leq \theta \leq 1$. Again, the fact that the direction of the plastic strain increment \underline{u}_B^* is a unit vector defines the value of k :

$$k = \frac{1}{\sqrt{1 + 2\theta(1 - \theta)(\underline{u}_A^* \cdot \underline{u}_B^* - 1)}} \quad (6-126)$$

If one replaces relations (6-126) and (6-125) into (6-124), this yields an equation with 2 unknown variables on the right side: \underline{u}_B^* and $\Delta \varepsilon_{eq}^p$. It will be solved thanks to the interpolation relation (6-110) and the fact that \underline{u}_B^* is a unit vector.

The following flowchart summarizes the implementation of the interpolation method as a constitutive law without sub-interval. More details can be found in Duchêne 2000, which proposes a description that conforms to the LAGAMINE routines. A sub-interval approach and the possibility to use an analytical tangent operator or a numerical one computed by a perturbation method are also described.

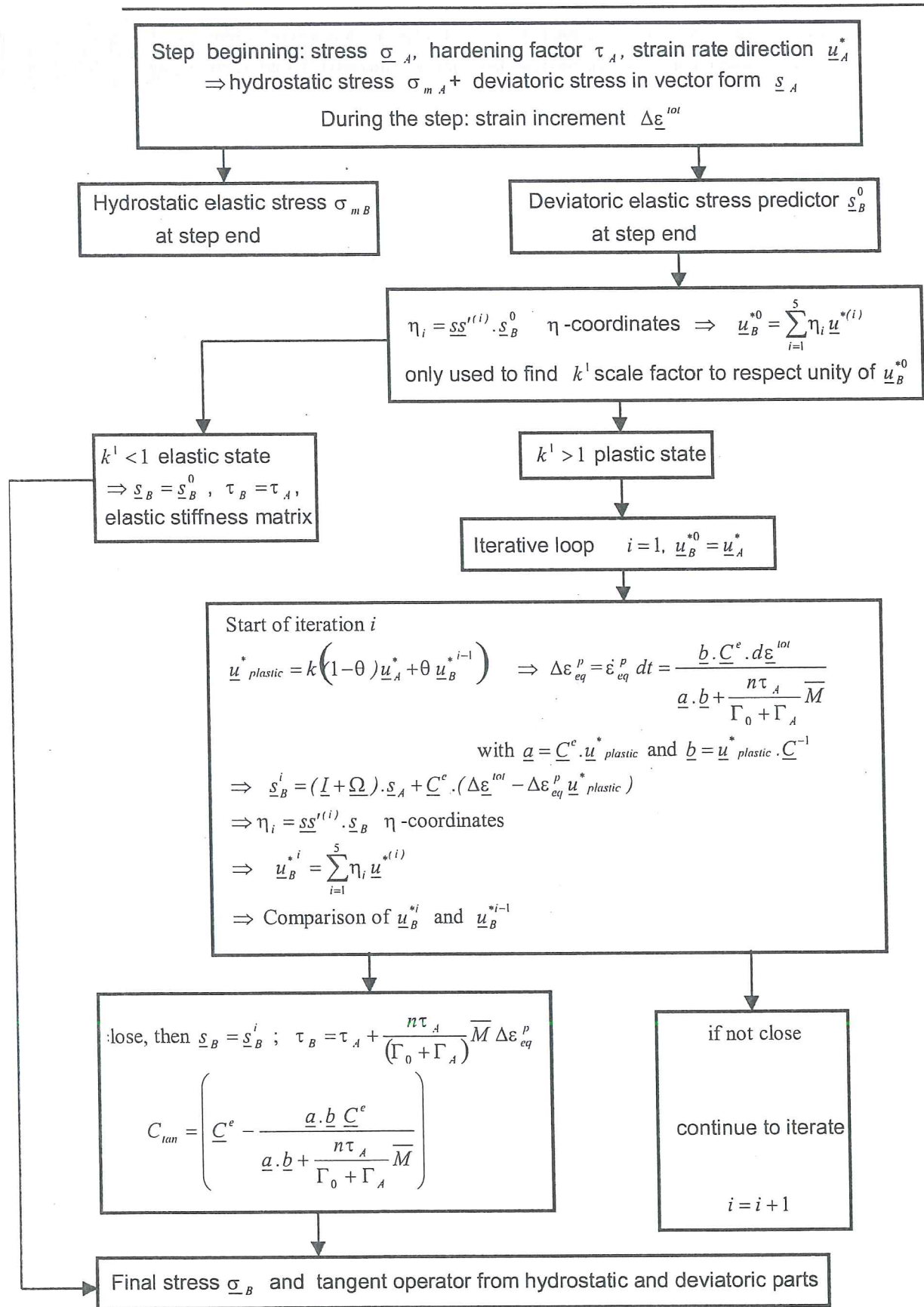


Figure 6-44 Flowchart of the interpolation method as constitutive law.

6.4.5. Conclusion

The hyperplane has been dropped to concentrate our research on the interpolation method. Key factors for its application are the number of crystal orientations, the size of the domain and the criterion to decide when texture updating is necessary. These questions are still under investigation and should be solved in Duchêne's Ph. D. thesis.

6.5. Validations of our models

6.5.1. Discrete sets of crystallographic orientations

In the developed constitutive laws, Taylor's model (see Figure 6-44) computes the domain limit stress vectors from the domain limit strain rate directions. So the number of discrete crystallographic orientations used to represent the texture is an important factor. It defines the accuracy of the domain limit stress vectors but also the CPU time. An estimation of the accuracy can be based either on ODF description or on stress computation.

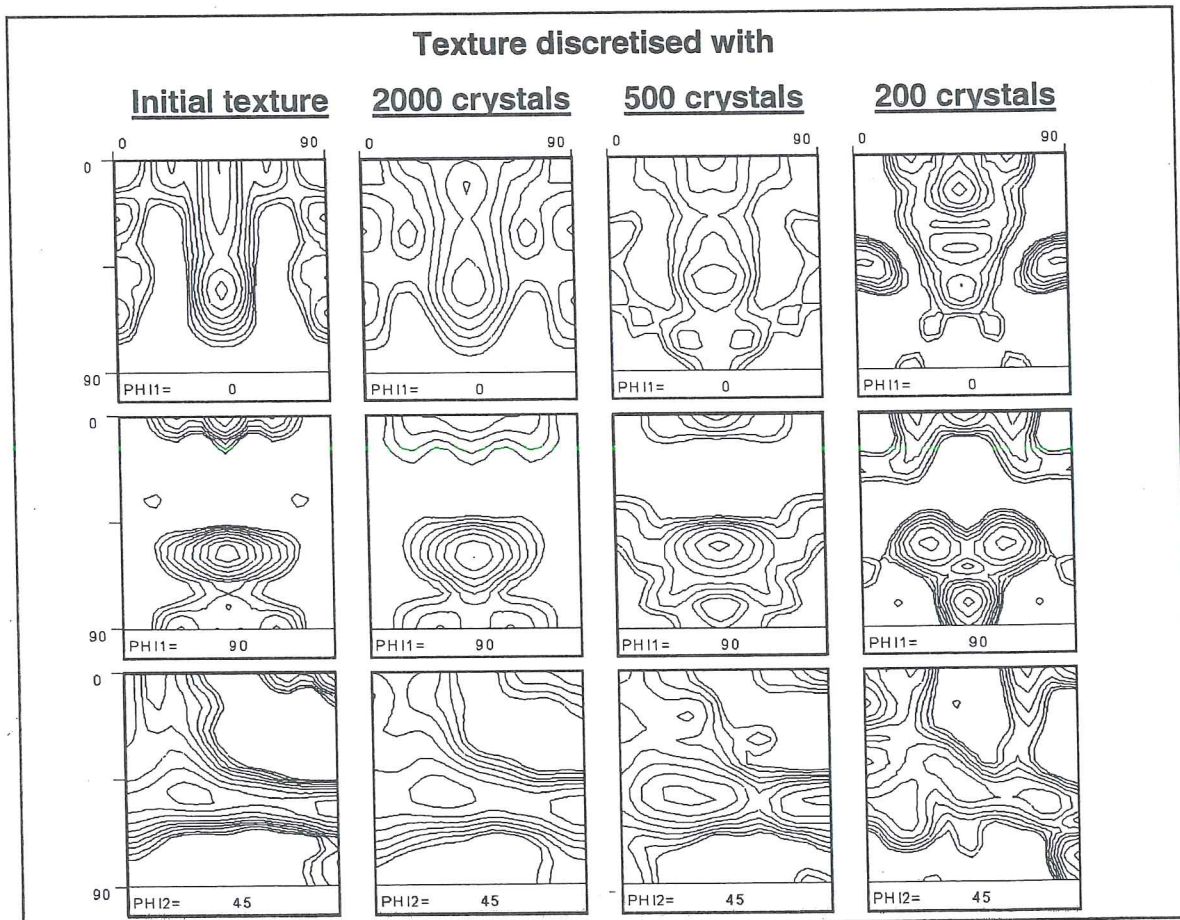


Figure 6-45 ODF sections before and after the use of discrete sets of orientations (from Duchêne *et al.* 2000).

For a SPXI steel sheet, Figure 6-45 shows sections of an ODF known by its coefficients after X-ray measurements. The method described in section 6.4.1 is applied to define 2000, 500 or 200 crystals that are representative of this texture. Then $C_i^{\mu\nu}$ coefficients are deduced from these 2000, 500 or 200 crystals respectively and sections of the ODF are drawn again on Figure 6-45. One can see that for 2000 crystals, the location of maxima is preserved as well as the section shape. However, with 200 crystals, there are still similitudes between ODF sections but a lot of features are lost.

Another way to compare the accuracy of discrete sets of orientations is to use them in Taylor's model to compute a stress tensor from different velocity gradients. Figure 6-46 computes the "error" due to a discrete representation of the texture for 2 different steel sheets (IF ULC Ti and SPXI) and 3 different velocity gradients. The reference response is provided by a Taylor's call using 40000 crystals. Here again one can check the important effect of the number of orientations on the result accuracy.

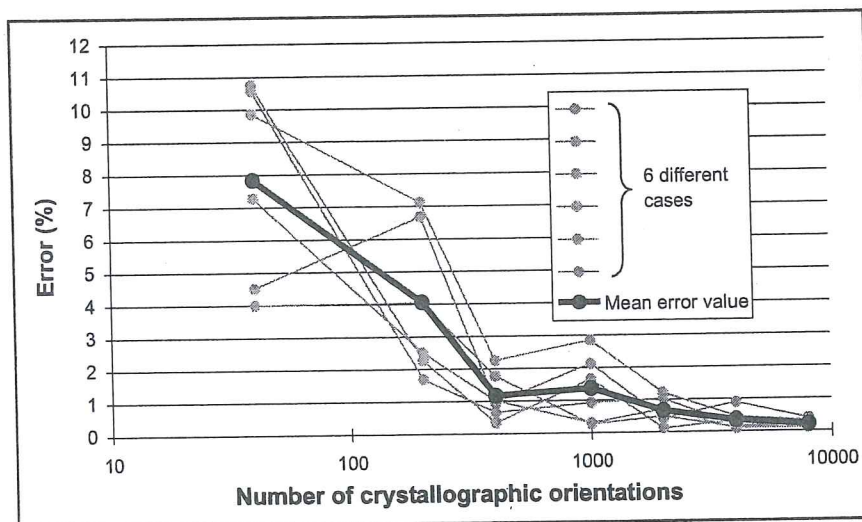


Figure 6-46 Error on stress computed by Taylor's model with different numbers of crystal orientations (from Duchêne *et al.* 2000).

A final means to estimate the effect of the number of crystal orientations is to use Taylor's model to compute π -sections of the yield locus. For the SPXI steel already described by its ODF on Figure 6-45, Figure 6-47 shows the effect of different ways to represent the texture.

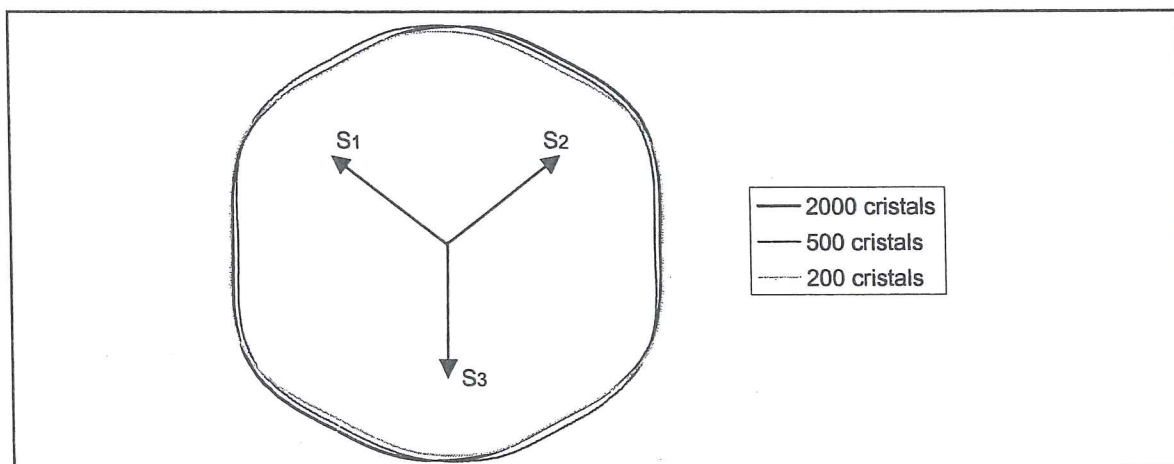


Figure 6-47 π -sections computed by Taylor's model for different representations of the texture, SPXI steel (from Duchêne *et al.* 2000).

In practice, a lot of our computations rely on 2000 crystals but further validations are necessary to know if this number can be decreased or not.

6.5.2. π -sections of the yield locus computed by local and non-local methods

For the SPXI steel sheet the texture of which is shown on Figure 6-45, the π -section has been computed by 5 different approaches:

- 6th order = global yield locus in stress space described by a 6th order series from van Houtte (see section 6.3.4).
- Hyp. 1° or 20° = Hyperplane approach with an angle of 1° or 20° between the strain rate directions used as domain limit vectors $\underline{u}^{*(i)}$ (see section 6.4.3).
- S-s I 1° or 20° = Stress-strain rate Interpolation approach with an angle of 1° or 20° between the strain rate directions used as domain limit vectors $\underline{u}^{*(i)}$ (see section 6.4.4)

The computational method to obtain π -sections has been described at the end of section 6.4.3. Figure 6-48 compares the π -sections obtained with the 5 investigated procedures. For the local approaches with large domains (Hyp. 20° and S-s I 20°), the associated yield locus normals, which represent the deviatoric plastic strain rates, are also plotted. Normals from the hyperplane approach are clearly discontinuous.

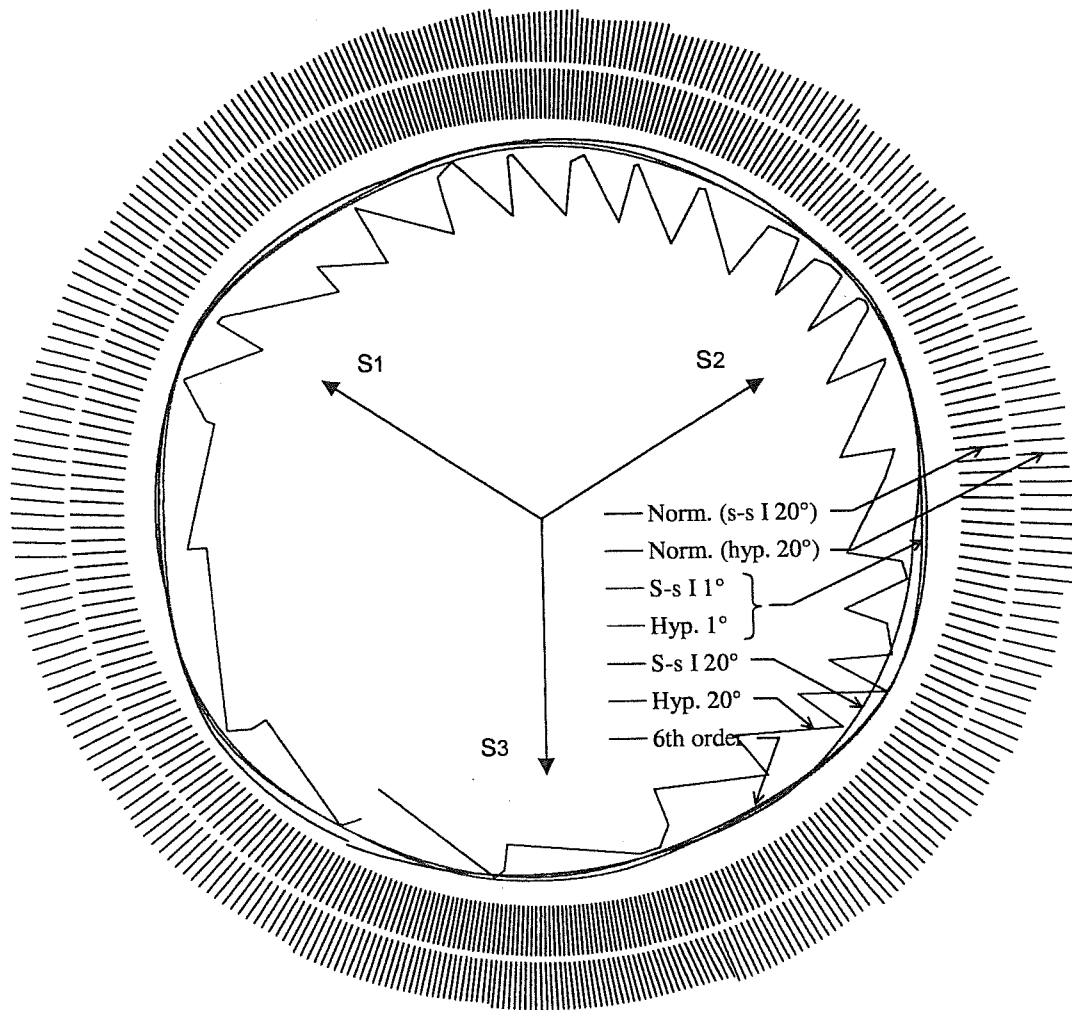


Figure 6-48 π -sections of the yield locus computed by 5 models, and normals to the yield loci computed by stress-strain rate interpolation and hyperplane method with a size of 20° (from Duchêne *et al.* 1999c).

When small local domains are used (1°), their associated yield loci are superposed and very close to the yield locus computed by the 6th order series. For larger domain size (20°), the results of the hyperplane and interpolation methods strongly differ: while the interpolation approach is continuous and close to the yield loci computed by more accurate methods, the hyperplane result is discontinuous and diverges from other results.

Figure 6-47 and Figure 6-48 show that both the number of crystal orientations used to describe the texture and the size of the local description adopted in the interpolation method are key factors for the accuracy.

6.5.3. Lankford's coefficient prediction

For the SPXI steel sheet and the deep drawing IF ULC Ti steel sheet already treated in previous sections, Lankford's coefficients have been investigated.

Two sets of experimental results are available, the ones performed by MSM laboratory (Exp. MSM) and the others from the Research and Development Cockerill Sambre center (Exp. RDCS). These results take into account the hardening and the evolution of the yield locus as they are computed by the average of instantaneous Lankford's coefficient measured at strains of 10, 12, 14, 16, 18 %. The MSM measurements are described in Wauters 2000. Tests are systematically repeated 3 or 5 times. Their agreement with a previous set of measures, limited to strains 0 and 10% and performed by Charles (Charles & Habraken 1996) is not perfect. So, even with the same equipment a different set of sheets present variation. So, different equipment and different sets of sheets can explain the differences in the measurements from RDCS and MSM.

J

All the predictions of Lankford's coefficient are based on the initial texture. The results identified by "Texture" are computed directly from the texture information and Taylor's model as explained in van Houtte 1995. The points characterized by "6th order" rely on a global yield locus in stress space described by a 6th order series. The curves identified by S-s I 1°, 5°, or 10° are computed thanks to the interpolation method with different domain sizes.

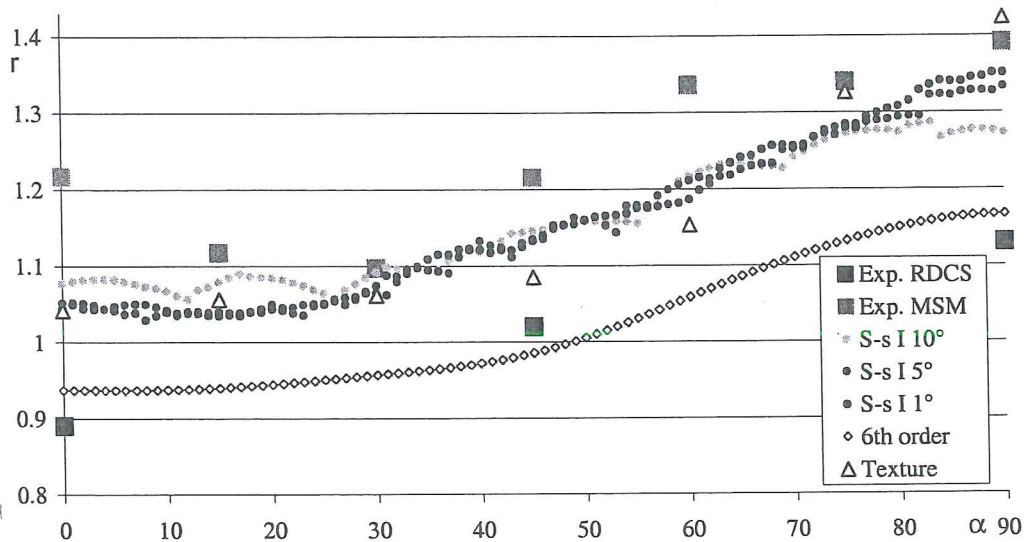


Figure 6-49 Measured and predicted Lankford's as a coefficient function of the angle with the Rolling Direction for SPXI steel (from Duchêne *et al.* 1999c).

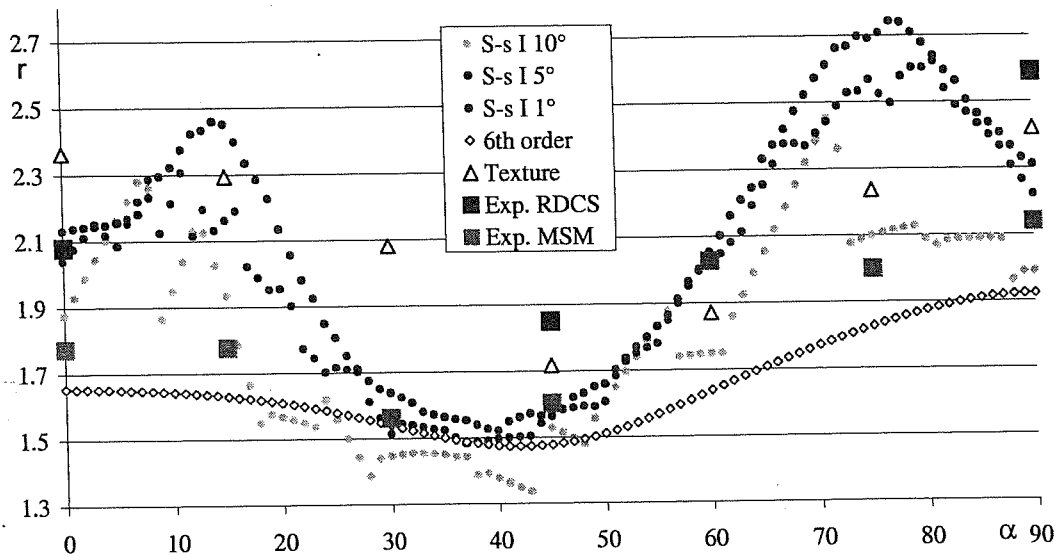


Figure 6-50 Measured and predicted Lankford's coefficient as a function of the angle with the Rolling Direction for IF ULC Ti steel (from Duchêne *et al.* 1999c).

The general shapes of the experimental and computed curves are rather similar; however, the levels differ.

The SPXI sheet is characterized by a relatively weak texture with a maximum ODF-value of 5.9 (van Houtte & van Bael 1997). This leads to a quite smooth yield locus. This fact is confirmed by continuous and close curves predicted by the S-s approach with different domain sizes (1°, 5°, 10°). The agreement between Texture and S-s method is good, recovering that both methods finally rely on identical Taylor's model. The results computed by the 6th order series yield locus are clearly underestimated by comparison to other predictions relying on crystal plasticity. This means that even a 6th order series is too poor to represent the actual anisotropic yield locus and that this analytical function smoothes the reality.

The IF ULC Ti sheet consists in a strong γ -fiber (maximum ODF-value of 11.4), which broadens towards α -fiber. The associated yield locus presents a high anisotropy and one can verify that the S-s results clearly show jumps corresponding to the updating of the local yield locus zone. These jumps are of course higher for domain size of 10°. The S-s results do not coincide with texture results, this could perhaps be explained by the fact that working in the stress space introduces some inaccuracy compared on direct use of Taylor's model. The global 6th order yield function is still not rich enough to catch the variation in Lankford's coefficient: the predicted curve seems too smooth as compared with other predicted curves and experimental values.

In conclusion, the prediction of Lankford's coefficient is very sensitive. It requires domain size smaller than 10° for the interpolation method. It has also been checked that small texture evolutions can induce large evolution in Lankford's values (Duchêne *et al.* 2001). So, the tensile test should be simulated until a strain of 18% and the predicted Lankford's coefficients should result from the average of instantaneous Lankford's values associated with the computed texture associated to each strain level. These simulations are planned but not yet achieved.

Such investigation shows that, while the trends are well predicted, the absolute values are still not reached. Different simplified assumptions can explain these differences, for instance:

- the use of Taylor's model that does not allow to take into account grain size and morphology and forgets grain equilibrium at the microscopic level;
- the results are based on initial yield locus shape, both material and geometric hardening (see definition in section 3.3) are neglected. At the present state, geometrical hardening could be introduced, however the simple isotropic Swift's hardening model is too poor to represent the reality with accuracy (see Chapter 3).

The measurement accuracy is far from perfect, so in short, it is not possible to use Lankford's coefficient as unique validation.

Remark: Another validation of the same type as the prediction of Lankford's coefficient could be the prediction of Forming Limit Diagrams (FLD). MSM team has already worked in this direction (Habraken *et al.* 1998). The Ph.D. theses by Duchêne and Wauters (to appear later on) will present some new results. However two remarks can already be done:

- If the goal is really to spare the experiments required to determine an FLD, then, **for classical steels**, the Cayssials' approach (Cayssials 1998) mixing mechanics, damage, metallurgy and statistic provides an interesting solution.
- If the goal is to validate a constitutive law using a Marciniak & Kuczynski 1967 type approach, then predictions are very sensitive. The results depend not only on the constitutive law under consideration but also on the **localization criterion and on the initial defect used in the computations**. Large modifications of FLD predictions can be obtained from very small variations of yield locus shape (see for instance Figure 2-20 and Figure 2-21 where Vegter modifies slightly the yield locus corner of biaxial stretching to achieve good FLD prediction). Hence, because of the many possible numerical adjustments, such kind of validation is of limited interest.

6.5.4. Academic rolling validation with texture updating

The rolling process is simply represented by one three-dimensional finite element in plane strain state as shown on Figure 6-51. The compressive force applied on direction z produces an expansion in the rolling direction x as the displacements in y direction are fixed.

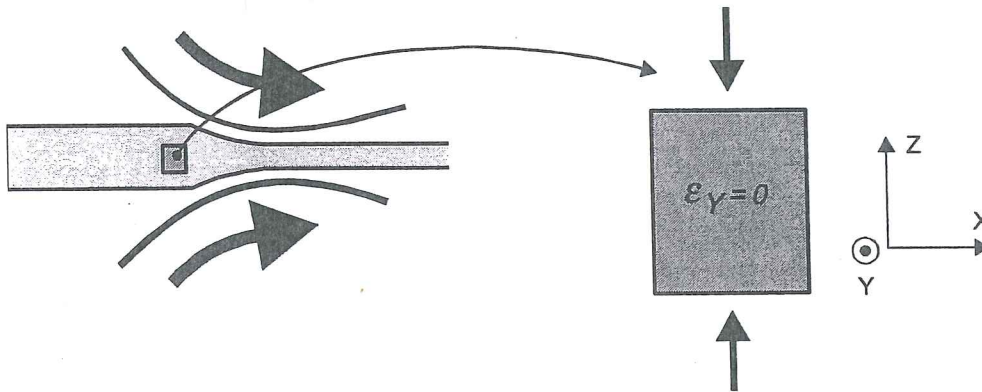


Figure 6-51 Rolling process represented by one finite element (from slides used for Duchêne *et al.* 1999c's presentation).

The initial texture, represented by a discrete set of 2000 crystal orientations, is isotropic. The finite element height is compressed until a reduction factor of two, which represents a 69% rolling reduction. Both cases of b.c.c and f.c.c materials are simulated with an arbitrary but identical hardening law. For each material, two simulations are performed, one with texture updating at each time step and one with the initial texture.

The final texture computed by the simulations with texture updating exhibits a typical rolling texture. For the b.c.c. material (Figure 6-52), the ODF maximum is 11.9 times the random texture level and is located at $\varphi_1 = 25^\circ$, $\Phi = 50^\circ$, $\varphi_2 = 55^\circ$. For f.c.c. material (Figure 6-53), the ODF maximum is 14.7 at $\varphi_1 = 40^\circ$, $\Phi = 70^\circ$, $\varphi_2 = 20^\circ$.

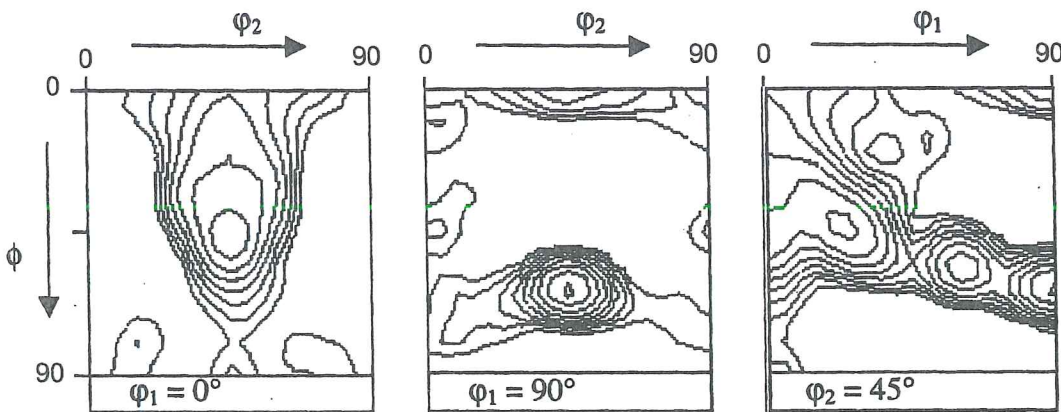


Figure 6-52 Sections $\varphi_1 = 0^\circ$, 90° and $\varphi_2 = 45^\circ$ in the final ODF of the b.c.c. material; curves levels = 0.7, 1.0, 1.4, 2.0, 2.8, 4.0, 5.6, 8.0, 11.0 and 16.0 (from Duchêne *et al.* 1999b).

In spite of an assumed common hardening behavior, a non-negligible influence of the crystal lattice is observed on the computed rolling forces (Figure 6-54). The larger stiffness observed for f.c.c. metals can be related to a lower number of slip systems to accommodate the imposed deformation. Even if the texture evolution is important, as shown on Figure 6-52 and Figure 6-53, no effect appears on the rolling force. As checked by Figure 6-55 which presents π -sections of the yield loci associated with random or rolling texture, it does not mean that these texture evolutions have no effect on the yield locus shape. It just happens that the point associated with the stress state in rolling is not affected by the shape evolution of the yield locus.

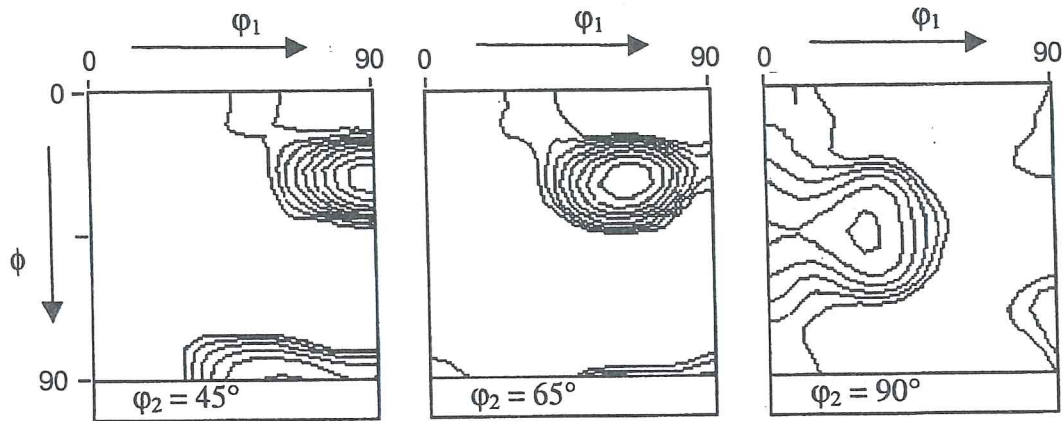


Figure 6-53 Sections $\varphi_2 = 45^\circ, 65^\circ,$ and 90° in the final ODF of the f.c.c. material; curves levels = 0.7, 1.0, 1.4, 2.0, 2.8, 4.0, 5.6, 8.0, 11.0 and 16.0 (from Duchêne *et al.* 1999b).

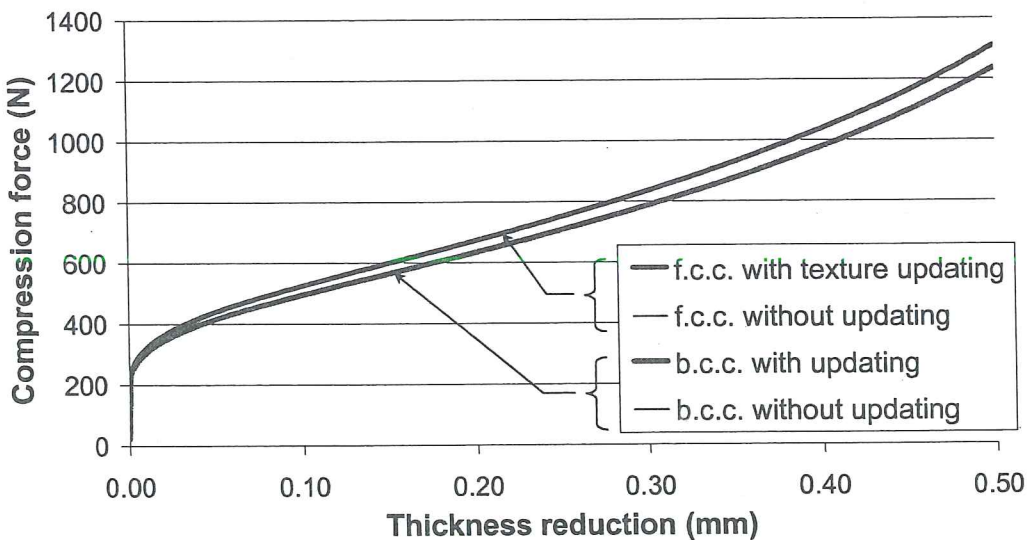


Figure 6-54 Rolling forces resulting of rolling simulations with or without texture updating for b.c.c. or f.c.c. materials (from Duchêne *et al.* 1999b.).

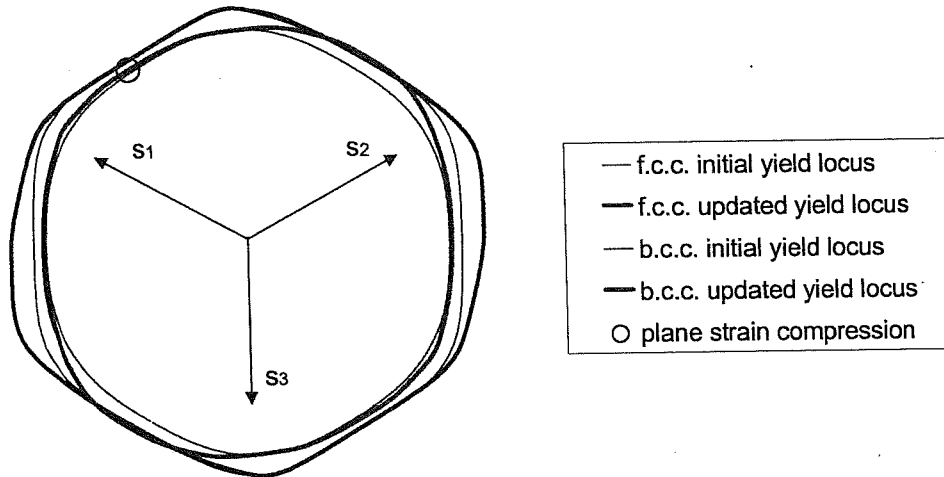


Figure 6-55 Initial and final π -sections of the yield locus computed from a random or a rolling texture for b.c.c. or f.c.c. materials (from Duchêne *et al.* 1999b).

The yield locus associated with a random texture in f.c.c. material is larger than the one corresponding to b.c.c. material. This explains the larger rolling force required to perform rolling from a mechanical point of view. The texture evolution creates, in both materials, a strongly anisotropic yield locus.

6.5.5. Conclusions of validation step

The interpolation model developed by MSM team stands between the models without yield locus (see Chapter 5), where a set of representative crystals is called upon to determine the macroscopic constitutive laws, and the models relying on a yield locus, computed thanks to texture information (see section 6.3). Its advantage is to keep an accurate description of plastic behavior by using a local description of the yield locus that allows the updating of its shape due to texture evolution. The CPU time reduction of such an approach has not yet been accurately estimated but does exist.

Applications to actual deep-drawing processes are in progress as well as the investigation of important parameters such as the size of the yield locus zone and the number of crystals necessary to represent the material behavior. Duchêne's thesis (to appear later on) will present comparisons between deep drawing experiments and simulations performed with classical Hill 1948 yield locus, the van Houtte's yield locus (6th order series in stress space) and the interpolation method with or without texture updating. Initial and final texture measurements will allow checking the prediction of texture evolution.

Another thesis begins this year in MSM department to implement an improved kinematic hardening law coupled with the interpolation method. As numerical

developments are quite useless without experimental data, half of the thesis will be dedicated to the development of a tensile experiment coupled with shear deformation.

6.6. Conclusion

Clearly all the models described in this chapter are not straightforward for implementation into a FEM code. However their identification require less macroscopic mechanical experiments than accurate phenomenological models such as Karafillis's law, since the yield locus shape is deduced from texture measurements. In this case, experiments must "only" be used to define the hardening behavior. This chapter shows that constitutive laws with yield locus are available if one is interested in modelling sheet metal forming without forgetting all the microscopic events happening during deep drawing processes. The models presented here are more complex than those of Chapter 5. Their analytical formulation attempts to recover the micro-macro transfer performed by simple averaging of the behavior of sets of representative crystals in Chapter 5.

As long as texture updating during the sheet forming process can be neglected, it is clear that the models described in section 6.3 are interesting. They rely on accurate yield loci, which are computed once, outside the FEM code. This thesis proposes a summary of the methods used to estimate such yield loci according to texture description, crystal plasticity and the Taylor's assumptions.

This state of the art helps to understand the context of our proposals, which the originality of which lies in the concept of a local part of the yield locus instead of global one. This choice is motivated by our final goal of taking into account texture updating.

6.7. References

- Aifantis, E.C., (1987) The physics of Plastic Deformations, *Int J Plasticity*, **3**, 211-247.
- Arminjon, M. (1988) Lois de comportement homogénéisées pour la plasticité des polycristaux, Mém. d'habilitation, Univ. Paris-Nord, Villetaneuse.
- Arminjon, M., Bacroix, B. (1991) On plastic potentials for anisotropic metals and their derivation from the texture function, *Acta Mechanica*, **88**, 219-243.
- Arminjon, M., Bacroix, B., Imbault, D. and Raphanel, J.K. (1994) A fourth-order plastic potential for anisotropic metals and its analytical calculation from texture function, *Acta Mechanica*, **107**, 33-51.
- Aukrust, T., Tjøtta, S., Skauvik, I., Vatne, H.E., Van Houtte, P. (1994) Modelling of texture development in aluminium extrusion, Proceedings of the 15th Riso Int. Symposium on Material Science, Anderson *et al.* editors, Denmark.

- Aukrust, T., Tjøtta, S., Vatne, H.E., Van Houtte, P. (1997) Coupled FEM and texture modelling of plane strain extrusion of an Aluminium alloy, *Int. J. of Plasticity*, **13**, 1/2.
- Bergström, Y. (1969) A dislocation model for the stress strain behaviour of polycrystalline α -Fe with special emphasis on the variation of the densities of mobile and immobile dislocations, *Mat. Sci. Eng.*, **5**, 179-192.
- Canova, G.R., Kocks, U.F., Tomé, C.N., (1985), The yield surface of textured polycrystals, *Mech. Phys. Solids*, vol. 33, 4, 371-397.
- Cayssials, F. (1998) A new method for predicting FLC, *IDDRG*, Conference Genval.
- Cescotto, S. Grober, H. (1985) Calibration and application of an elastic-visco-plastic constitutive equation for steels in hot-rolling conditions, *Eng. Comp.* **2**, June, 101-106.
- Charles, J-F, Habraken, A.M. (1996), Dépouillement des essais de traction nécessaires à la calibration de la loi anisotrope élastoplastique avec endommagement de Y.Y. Zhu, rapport intermédiaire n° 9, Convention 2748, Micro-Macro, Université de Liège, Département MSM, Région Wallonne.
- Charlier, R., Habraken, A.M. (1990), Numerical model of contact with friction phenomena by the finite element method, *Computers and Geotechnics*, **9**, 59-72.
- Darrieulat, M., Piot, D. (1996), A method of generating analytical yield surfaces of crystalline materials, *Int. J. Plasticity*, **12/10**, 1221-1240.
- Degueldre, A., Habraken, A.M., Munhoven, S., Aukrust, T., Van Bael, A., Karhausen, K. (1996) Texture prediction and aluminium extrusion. General Workshop COST 512, *MMSP 96 Davos : Modelling in Materials Science and Processing*, COST 512, Action Management Committee, Rappaz, M., Kadro M., editors, European Commission Directorate General XII Science Research Development, 260-265.
- Duchêne, L., (1998a) Modifications et améliorations apportées à la loi MIPAY 3, rapport intermédiaire n° 26, Convention 2748, Micro-Macro, Université de Liège, Département MSM, Région Wallonne.
- Duchêne, L., (1998b) Description de la programmation de la méthode d'interpolation de la relation de Taylor, rapport intermédiaire n° 30, Convention 2748, Micro-Macro, Université de Liège, Département MSM, Région Wallonne.
- Duchêne, L., (1998c) Etude de la précision, de la convergence et de la stabilité de la méthode des hyperplans et de la méthode d'interpolation, rapport intermédiaire n° 31, Convention 2748, Micro-Macro, Université de Liège, Département MSM, Région Wallonne.
- Duchêne, L., Habraken A.M., Cescotto S., (1999a) Elastoplastic Anisotropic Model Based on Texture Analysis to Simulate Steel Sheet Behaviour. *7th Int. Symp. on Plasticity*, Cancun, Mexico, January 5-13, 1999, Akthar S. Khan Ed., Neat Press, 325-328.
- Duchêne, L., Godinas, A., Habraken, A.M. (1999b) Texture effects on steel sheet behaviour under large strain simulations, *12th Int. Conf. on Textures of Materials (ICOTOM-12)*, Montreal, Canada, 9-13 August 1999, J.A. Szpunar, Ed. NRC Research Press Ottawa, pp. 286-291.

- Duchêne L., Godinas A., Habraken, A.M.(1999c) Metal Plastic Behaviour linked to Texture Analysis and FEM Method, *NUMISHEET '99, 4th Int. Conf. and Workshop on Numerical Simulation of 3D Sheet Forming Processes*, Besançon, France, 13-17 September 1999, Edité par J.C. Gélina, P. Picart, Université de Franche-Comté et ENSMM, 97-102.
- Duchêne, L. (2000), Implementation of a Yield Locus Interpolation Method in the Finite Element Code Lagamine, DEA Graduation Work, Université de Liège MSM Département, Belgium.
- Duchêne, L., Habraken, A.M., Godinas, A. (2000), Validation of a FEM model coupled with texture applied to deep drawing process. *ESAFORM*, Stuttgart, Fritz Editor, Inst. Für Kunststofftechnologie, IV-3, IV-6.
- Duchêne, L., Habraken, A.M., Godinas, A. (2001), Influence of steel sheet anisotropy during deep-drawing processes, *Proceedings of the 4th ESAFORM Conference*, Habraken, A.M. Ed.
- Dyduch, M., Cescotto, S., Habraken, A.M., (1995) Efficient error estimates for adaptive remeshing in 2D metal forming modelling, *Numiform'95, Simulation of Materials Processing: Theory, Methods and Applications*, Shen, S.-F., Dawson, P., editors, Belkema, Rotterdam, 419-424.
- Godinas, A., (1998) Définition locale de la surface de plasticité. Partie 1 : théorie, rapport intermédiaire n° 22, Convention 2748, Micro-Macro, Université de Liège, Département MSM, Région Wallonne.
- Habraken, A.M. (1996) Description du module d'évolution de texture, rapport intermédiaire n° 4, Convention 2748, Micro-Macro, Université de Liège, Département MSM, Région Wallonne.
- Habraken, A.M. Munhoven, S., (1996) Schéma d'implantation d'une version simplifiée du couplage micro-macro, texture éléments finis., rapport intermédiaire n° 10, Convention 2748, Micro-Macro, Université de Liège, Département MSM, Région Wallonne.
- Habraken, A.M., Radu, J.P., (1997) Tests de la loi MIPAY, implantation des surfaces de plasticité série du $\sigma^{ème}$ ordre et du modèle de Taylor, rapport intermédiaire n° 21, Convention 2748, Micro-Macro, Université de Liège, Département MSM, Région Wallonne.
- Habraken, A.M. (1998a) Taylor Ulg A : rapport de programmation, tests, rapport intermédiaire n° 19, Convention 2748, Micro-Macro, Université de Liège, Département MSM, Région Wallonne.
- Habraken, A.M. (1998b) Taylor Ulg B : rapport de programmation, tests, rapport intermédiaire n° 20, Convention 2748, Micro-Macro, Université de Liège, Département MSM, Région Wallonne.
- Habraken, A.M., Radu, J.P., Duchêne, L., Wauters, M., Munhoven, S. (1998) Comparison of Anisotropic Elastoplastic Laws Applied to Steel Sheet. *NUMIFORM 98, Simulation of Materials Processing : Theory, Methods and Applications*, Huetink, Baaijens Ed., Balkema, Enschede, The Netherlands, 769-774.
- Hage Chehade, I. (1990) Simulation de l'emboutissage des tôles anisotropes par éléments finis avec prédiction des risques de striction, Thèse de doctorat, Institut National des Sciences Appliquées de Lyon.

- Hill, R. (1948) A theory of the yielding and plastic flow of anisotropic materials. Proc. Royal Soc. London, A193, 281-297.
- Hill, R. (1987) Constitutive dual potentials in classical plasticity, *J Mech. Phys. Solids*, 35, 23-33.
- Hiwatashi, S., Van Bael, A., Van Houtte, P., Teodosiu, C. (1997) Modelling of plastic anisotropy based on texture and dislocation structure, *Computational materials science*, 9, 274-284.
- Hoferlin, E., Van Bael A., Van Houtte P., (1999a) Comparison between stress-based and strain-rate based elasto-plastic finite element models for anisotropic metals, *Plasticity'99, Constitutive and damage modelling of inelastic deformation and phase transformation*, Khan, A.S. editor, Neat Press Fulton, Maryland.
- Hoferlin, E., Van Bael A., Van Houtte P., Teodosiu C. (1999b) An accurate model of texture and strain-path induced anisotropy, *Numisheet'99, Numerical Simulation of 3D Sheet Forming Processes*, Gelin, J.C., Picart, P., editors, Université de Franche Comté, Besançon, France.
- Hoferlin, E. (2001) Incorporation of an accurate model of texture and strain-path induced anisotropy in simulations of sheet metal forming, Ph. D thesis Katholieke Universiteit Leuven.
- Imbault, D., Arminjon, M. (1993) Theoretical and numerical study of the initial and induced plastic anisotropy of steel sheets, using a texture-based methodology, Final report of contract Univ. J. Fourier n° 17191401, Laboratoire 3S, Université Joseph Fourier, France.
- Karafillis, A.P., Boyce, M.C. (1993) A general anisotropic yield criterion using bounds and a transformation weighting tensor, *J. Mech. Phys. Solids*, 41/12, 1859-1886.
- Khan, A.S., Cheng, P. (1996) An anisotropic elastic-plastic constitutive model for single and polycrystalline metals. I – theoretical developments, *Int. J. Plasticity*, 12/2, 147-162.
- Lequeu, Ph., Gilormini, P., Montheillet, F., Bacroix, B., Jonas, J.J. (1987a) Yield surfaces for textured polycrystals, I. Crystallographic Approach, *Acta Metall.*, 35/2, 439-451.
- Lequeu, Ph., Gilormini, P., Montheillet, F., Bacroix, B., Jonas, J.J. (1987b) Yield surfaces for textured polycrystals, II. Analytical Approach, *Acta Metall.*, 35/5, 1159-1174.
- Li, K. (1996) Contribution to the finite element simulation of three-dimensional sheet metal forming, Ph. D. thesis, Université de Liège, département MSM.
- Marciniak, Z., Kuczynski, K., (1967) Limit strains in the processes of stretch-forming sheet metal. *Int. J. Mech. Sci.*, 9, 609-620.
- Mecking, H., Lücke, K. (1970) A new aspect of the theory of flow stress of metals, *Scripta Metallurgica*, 4, 427-432.
- Miller, M.P., Mc Dowell, D.L. (1996) Modeling large strain multiaxial effects in FCC polycrystals, *Int. J. of Plasticity*, 12/7, 875-902.
- Monfort, G., Adriaens, J. P., Defourny, J., Jodogne, P., Brunet, M., Detraux, J.M. (1991), FEM simulation of non-axisymmetric press formed parts using anisotropic constitutive laws for steel, *IDDRG*, Pisa.

- Monfort, G., Defourny, J., (1993) A new orthotropic plasticity model for complex sheet forming, *Centre for Theoretical Physics – External activities. (ICTP-OEA)*, Conference on interface between physics and mathematics. Hangzhou, China.
- Monfort, G., Defourny, J., (1994) The 3G plasticity model, Metallurgical bases – Mechanical evaluation - Application to finite element simulation of steel forming, 14 septembre, Centre de recherches métallurgiques, Liège.
- Montheillet, F., Gilormini, P., Jonas, J.J.(1985) Relation between axial stresses and texture development during torsion testing : a simplified theory. *Acta Metall.*, **33/4**, 705-717.
- Munhoven, S., Habraken, A.M., Winters, J., Schouwenaars, R., Van Houtte, P. (1995a) Application of an anisotropic yield locus based on texture to a deep drawing simulation, *NUMIFORM 95, Simulation of Materials Processing: Theory, Methods and Applications*, Shen&Dawson editors, Balkema, 767-772.
- Munhoven, S., Winters J. Habraken, A.M., (1995b) Finite element applications of an anisotropic yield locus based on crystallographic texture, *Computer simulations in materials science Nano / Meso / Macroscopic Space and time scales*. Nato Advanced study Institute, Ile d'Oléron France 6-16 juin, Université de Liège, Département MSM.
- Munhoven, S., (1996), Deformation history from 2D Lagrangian FEM results, Internal report n°226, MSM department, University of Liège.
- Munhoven, S., Habraken, A.M., Van Bael A., Winters J. (1996) Anisotropic finite element analysis based on texture. *Proc. 3rd Int. Conf.: Numerical Simulation of 3-D Sheet Metal Forming Processes. NUMISHEET'96*, Ed. L.K. Lee, G.L. Kinzel, R.H. Wagoner, The Ohio State University, Columbus, 112-119.
- Munhoven, S., Habraken, A.M. (1996) Anisotropic finite element analysis based on texture, rapport intermédiaire n° 3, Convention 2748, Micro-Macro, Université de Liège, Département MSM, Région Wallonne.
- Munhoven, S. (1997) Taylor ULg A, rapport intermédiaire n° 4, Convention 2748 Micro-Macro, Région Wallonne, Université de Liège, Département MSM.
- Munhoven, S., Habraken, A.M., Radu, J.P.(1997), Anisotropic plasticity based on crystallographic texture, 4ème Congrès de Mécanique théorique et appliquée, Leuven.
- Ning, J., Aifantis, E.C. (1996) Anisotropic yield and plastic flow of polycrystalline solids, *Int. J. of Plasticity*, **12/10**, 1221-1240.
- Ponthot, J.Ph., (1995) Traitement unifié de la mécanique des milieux continus solides en grandes déformations par la méthode des éléments finis, Ph.D. thesis, LTAS, Université de Liège.
- Pospiech, J., (1982) Symmetry Analysis in the Space of Euler Angles, *Quantitative Texture Analysis*, Bunge, H.J., Esling, C. editors, Deutsche Gesellschaft fur Metallkunde.
- Radu, J.P., Munhoven, S., Habraken, A.M., (1997) Amélioration de la version simplifiée du couplage micro-macro : texture-éléments finis, rapport intermédiaire n° 11, Convention 2748, Micro-Macro, Université de Liège, Département MSM, Région Wallonne.

- Schoenfeld, S.E., Asaro, R.J., (1996) Through thickness texture gradients in rolled polycrystalline alloys, *Pergamon, Int. J. Mech. Sci.*, vol 38, 6, 661-683.
- Simo, J.C., Ortiz, M. (1985) A unified approach to finite deformation elastoplastic analysis based on the use of hyperelastic constitutive equations, *Comp. Meth. Appl. Mech. Eng.*, 49, 221-245.
- Teodosiu, C., Hu, Z. (1998) Microstructure in the continuum modelling of plastic anisotropy, *Proceedings of the 19th Riso Int. Symp. on Materials Science : Modelling of Structure and Mechanics of Materials from Microscale to Products*, Carstensen, J.V., Leffers, T. Eds.
- Tóth, L.S., Van Houtte, P. (1992) Discretization techniques for orientation distribution functions, *Textures and Microstructures*, 1992, 19, 229-244.
- van Bael, A. (1994) Anisotropic yield loci derived from crystallographic data and their application in finite element simulations of plastic forming processes, proefschrift voorgedragen tot het behalen van het doctoraat in de toegepaste wetenschappen, Katholieke Universiteit Leuven.
- van Bael, A., Winters, J., Van Houtte, P. (1996) A semi-analytical approach for incorporating crystallographic data into elasto-plastic finite element formulations, *Textures of Materials*, Proceedings of the 11th Int. Conf. on Textures of Materials, vol. 1, ICOTOM-11, Sept. 16-20, Liang Z., Zuo L., Chu Y. Eds.
- van Houtte, P. (1988) A comprehensive mathematical formulation of an extended Taylor-Bishop-Hill model featuring relaxed constraints, the Renouard-Wintenberger theory and a strain rate sensitivity model, *Textures and Microstructures*, 8-9, 313-350.
- van Houtte, P. (1992) Anisotropic Plasticity, *Numerical Modelling of Material Deformation Processes, Research, Development and Applications*, Hartley, P., Pillinger, I., editors, Springer-Verlag.
- van Houtte, P. (1994) Application of plastic potentials to strain rate sensitive and insensitive anisotropic materials, *Int. J. Plasticity*, 10, 719-748.
- van Houtte, P. (1995) Micromechanics of polycrystalline materials, Chaire Francqui, Université de Liège.
- van Houtte, P., van Bael, A. (1997) Texture measurements, Report EX/97/009/1
- Wang, N., Hall, F.R., Pillinger, I., Hartley, P., Sturgess, C.E.N. (1992) Finite-element prediction of texture evolution in material forming, *Numerical Methods in Industrial Forming Processes*, Chenot, Wood&Zienkiewicz Eds, 193.
- Wauters, M. (2000), Calibration of an anisotropic elasto-plastic damage model for sheet metal forming, Master thesis, MSM department, University of Liège.
- Winters, J. (1996) Implementation of a texture-based yield locus into an elastoplastic finite element code. Application to sheet forming. Ph.D. thesis, Katholieke Universiteit Leuven, MTM department.
- Zhu, Y.Y., Cescotto, S. (1996) Unified and mixed formulation of the 8-node hexahedral elements by assumed strain method, *Comput. Methods Appl. Mech. Engrg.*, 129, 177-209.

References

- Beaudoin, A.J., Dawson, P.R., Mathur, K.K., Kocks, U.F.(1995), A hybrid finite element formulation for polycrystal plasticity with consideration of macrostructural and microstructural link, *Int J. of Plasticity*, **11/5**, 501-521.
- Garikipati, K., Hughes, J.R.T. (to appear) Embedding a Micromechanical Law in the Continuum Formulation-A Multiscale Approach Applied to Discontinuous Solution, *Int. J. for Computational Civil and Structural Engineering*.

7. CONCLUSIONS

This overview work provides an idea of the main models implemented today in FEM codes to represent macroscopic plastic anisotropic material behavior. Both plastic yield locus and hardening laws are important features for capturing the actual metal response at various loading.

Some examples, such as the microscopic finite element simulations from Teodosiu (section 5.2.1) or Acharya & Beaudoin (section 5.2.2) also show the interest of FEM simulations to check the validity of the microscopic models in representing macroscopic behavior.

Some care has been brought to provide not only the theoretical models, but their identification methods as well. Whenever possible, links between models are presented, such as, for instance, Aifantis's proposal that gives physical basis to von Mises and Karafillis' laws.

In the future, hardware development and parallel computation will reduce problems of CPU time. However, each time that this happens, engineers increase the sizes of the problems that they want to solve by finite elements... So, simple phenomenological laws described in chapter 2 or yield loci presented in chapter 6 that allow escaping to microscopic computations in the macroscopic FEM simulations, retain their interest. This also forces researchers to identify the important features necessary to capture material behavior. For instance, it is clear that texture evolution effects on yield locus are not necessary in all deep-drawing simulations.

The actual question is: what is really useful to take into account? The answer is not the same according to the goal of the simulations: shape prediction after spring back, texture prediction, residual stress field, wrinkling and necking prediction. It is clear that criteria exist to predict necking and wrinkling, but they rely on accurate stress and strain field computations. The spring back prediction is quite hard if your model neglects elasticity. The final shape and size of the yield locus after forming processes is important if your goal is to apply accurate fatigue models to predict the life of the pieces. The model descriptions provided in this thesis should help to choose the adapted model to fit one's requirements.

One direction not investigated in this overview is the formulation of the Finite Element itself. Going from a simple displacement formulation to a mixed or hybrid formulation can already provide a better convergence and a smoother stress answer, even if a low number of crystals is used per integration point (Beaudoin *et al.* 1995). Another possibility is to apply a simple macroscopic analysis coupled with a micro-macro analysis only where some event, such as strain localization, appears and requires a finer scale. For instance, Garikipati & Hughes (to appear) propose such a so-called variational multiscale approach.